NEWCASTLE UNIVERSITY

DOCTORAL THESIS

Using Theoretical Chemistry to understand the Properties of Polyoxometalates and their potential as energy storage materials

---

Author:
Emanuele FALBO

Supervisor:
Dr. Thomas PENFOLD

A thesis submitted in fulfilment of the requirements for the degree of Doctor of Philosophy

on the

2021/06/28

Declaration of Authorship

I, Emanuele FALBO, declare that this thesis titled, “Using Theoretical Chemistry to understand the Properties of Polyoxometalates and their potential as energy storage materials” and the work presented in it are my own. I confirm that:

- This work was done wholly or mainly while in candidature for a research degree at this University.
- Where any part of this thesis has previously been submitted for a degree or any other qualification at this University or any other institution, this has been clearly stated.
- Where I have consulted the published work of others, this is always clearly attributed.
- Where I have quoted from the work of others, the source is always given. With the exception of such quotations, this thesis is entirely my own work.
- I have acknowledged all main sources of help.
- Where the thesis is based on work done by myself jointly with others, I have made clear exactly what was done by others and what I have contributed myself.

Signed:

Date:

NEWCASTLE UNIVERSITY

Abstract

Chemistry
School of Natural and Environmental Sciences

Doctor of Philosophy

Using Theoretical Chemistry to understand the Properties of Polyoxometalates and their potential as energy storage materials

by Emanuele FALBO

Polyoxometalates (POMs) are very appealing compounds as these transition metal oxide nanoclusters exhibit the ability to store multiple electrons in a reversible manner. Recently, POM-based energy storage devices, like redox flow batteries (RFBs) and alkali-ion batteries, have been extensively employed, since they meet equally the need of higher energy demand and low impact on the environment. However, POM-based technologies are still at early stage of development, mostly because of the difficulties to understand POM electronic behaviour.

In this PhD thesis, it has been presented a theoretical study of POMs in different environments in order to understand the basic mechanisms behind their behaviour. In the first part, a general overview of electronic structures of POMs is given. Furthermore, the advantages and limits of POM-based batteries are discussed in detail. In Chapter 2 the state-of-the-art theoretical approaches used to study POMs are discussed, in particular, strong emphasis is given to the density functional theory (DFT), and both classical and quantum molecular dynamics (MD). In the third Chapter, the redox properties of POMs are investigated by means of simulations in an implicit and explicit environment. The implicit solvation is semiquantitative, and uncertainties arise due to the limit of the model. Quantum MD simulations reveal that an explicit environment can improve the calculated redox potentials of POMs, providing useful insights into their molecular nature. A spectroscopic study of x-ray absorption near-edge spectra (XANES) and extended x-ray absorption fine structure (EXAFS) is presented in Chapter 4. These techniques alongside with first-principles calculations have shown to be powerful tools to unveil the structure-property relationships of super reduced POMs. Chapter 5 is devoted to the study of self-assembly process of POMs. Classical MD simulations show that a rich network of hydrogen bonds mediates the POM-POM interaction, and their agglomeration strongly depends on total charge. Furthermore, first-principles calculations illustrate the effect of POM agglomeration on their redox potential, and catalytic efficiency towards the hydrogen evolution reaction.

The results from this study show that it is now possible to adopt a range of computational approaches to understand the properties of POMs in different physical contexts. Specifically, the advantages and limits of DFT have been highlighted when computing the redox potentials of POMs, showing that further accuracy and insights into their electronic structure can be achieved by explicitly including the solvent molecules. For instance, it has been shown that the POM ability to undergo multiple redox reductions is due to possibility of delocalizing further electron density over all metallic atoms, regardless of the POM type. This behaviour is linked to their molecular structure, which undergoes an elongation of metal-oxygens bond lengths and formation of metal-metal bonds when further electrons are added to POMs. Furthermore, the inclusion of an explicit environment was shown to be an important factor to understand other properties of POMs, like the profile of their x-ray spectra or the self-assembly process. In the first case, QM/MM calculations shows that the polariazation of POM electron density returns more realistic molecular structures with respect to static DFT calculations, thus influencing the sensitivity of their simulated x-ray spectra. On the other hand, MD simulations revealed that the dynamical behaviour of POMs and the formation of long-lived agglomerates depends on several factors, like the total charge of POM, its counter ions, and solvent.

Acknowledgements

I would like to thank Tom Penfold from whom I have learned how to carry out professional scientific research without loosing the joy for this profession.

A special thanks goes to the whole Computational Chemistry group for their company and tremendous help throughout the PhD. Julien Eng, Thomas Northey, Stuart Thompson, Jamie Gibson, Beth Laidlaw, Thomas Pope, Yvelin Giret, Conor Rankine, Marwah Madkahli, Miriam Fsadni, Shawana Ahmad, Cao Yang, and Josh Littlefair.

Last but not the least, I would also like to thank my family and Dalila, whose support has been fundamental throughout this long journey.

Contents

List of Figures

List of Tables

List of Abbreviations

AIMD	*ab initio* Molecular Dynamics
AMBER	Assisted Model Building with Energy Refinement
B3LYP	Becke, 3-parameter, Lee-Yang-Parr: hybrid density functional
BE	Bulk-Electrostatic effect
BO	Born-Oppenheimer
BS	Basis Set
CASSCF	Complete Active Space Self Consistent Field
CASPT2	Complete Active Space Second-order Perturbation Theory
CDF	Combined Distribution Function
CGTOs	Contracted GTOs
CHE	Computational Hydrogen Electrode
CV	Cyclic Voltammogram
DE	Delocalization Error
DFT	Density Functional Theory
DNN	Deep Neural Network
EA	Electronic Affinity
ECP	Effective Core Potentials
EEs	Electrical Energy Storages
EOM	Equations Of Motion
ET	Electron Transfer
EXAFS	Extended X-ray Absorption Fine Structure
FEP	Free Energy Perturbation
FF	Force Field
FFT	Fast Fourier Transform
FMOs	Frontier Molecular Orbitals
GB	Generalized Born
GEA	Generalized Expansion Approximation
GGA	Generalized Gradient Approximation
GHO	Generalized Hybrid Orbital
GTOs	Gaussian Type Orbitals
HER	Hydrogen Evolution Reaction
HH	Half-and-Half
HF	Hartree-Fock
HOMO	Highest Occupied Molecular Orbital
IP	Ionisation Potential
ISM	Implicit Solvent Model
KS	Khon-Sham
LDA	Local Density Approximation
LIB	Lithium-Ion Battery
LR	Linear Response

LSCF	Localized Self-Consistent-Field
LSDA	Local Spin Density Approximation
LUMO	Lowest Unoccupied Molecular Orbital
MC	Monte Carlo
MCB	Molecular Cluster Batteries
MCSCF	Multi-Configurstional Self-Consistent Field
MD	Molecular Dynamics
MEP	Molecular Electrostatic Potential
MO	Molecular Orbital
NB	Non-Bulk effect
NIB	Na-Ion Battery
NPBC	Non-Periodic Boundary Conditions
NPE	Nonhomogeneous-dieletric Poisson Equation
OER	Oxygen Evolution Reaction
PBC	Periodic Boundary Conditions
PBE	Perdew-Burke-Ernzerhof: density functional
PBE0	Perdew-Burke-Ernzerhof: hybrid density functional
PCET	Proton-Coupled Electron Transfer
PME	Particle-Mesh Ewald
POMs	Polyoxometalates
PT	Proton Transfer
QM/MM	Quantum Mechanical/Molecular Mechan- ics
RFB	Redox Flow Battery
SASA	Solvent-Accessible Surface Area
SCF	Self-Consistent Field
SD	Slater Determinant
SE	*Schrödinger* Equation
SHAKE	Constraint algorithm
SHE	Standard Hydrogen Electrode
SIC-DFT	Self-Interaction Corrected DFT
SIE	Self Interaction Error
SRCF	Self-Consistent Reaction Field
STOs	Slater Type Orbitals
TDDFT	Time-Dependent Density Functional Theory
TI	Thermodynamic Integration
TPSSh	Tao, Perdew, Staroverov, and Scuseria: hybrid density functional
UFF	Universial Force Field
VEG	Vertical Energy Gap
VRFB	all-Vanadium Redox Flow Battery
wACSF	weighted Atom-Centered Symmetry Functions
WT	Wavelet
XANES	X-ray Absorption Near-Edge Structure
XAS	X-ray Absorption Spectroscopy

List of Publications

[1] Emanuele Falbo, and Thomas J. Penfold. Redox Potentials of Polyoxometalates from an Implicit Solvent Model and QM/MM Molecular Dynamics *J. Phys. Chem C* 2020, 124, 28, 15045-15056 :

Contribution:

E.F. conceived and designed the presented idea. E.F. performed the computations. E.F. collected the data. E.F. and T.J.P. verified the analytical methods. E.F wrote the paper. T.J.P. supervised the findings of this work, and the final look of the text. This work is shown in Chapter 3, where further findings and contributions, absent in the original article, have been added.

[2] Emanuele Falbo, Conor Rankine, and Thomas J. Penfold. On the Analysis of X-ray Absorption Spectra for Polyoxometalates. This is work has been submitted in Chem. Phys. Lett., and its status is in peer review.

Contribution:

E.F. conceived and designed the presented idea. E.F. performed the computations. C.R. wrote the deep neural network program that has been used by E.F.. E.F. collected the data. E.F. , C.R. , and T.J.P. verified the analytical methods. E.F. wrote the paper. T.J.P. supervised the findings of this work, and the final look of the text. This work is shown in Chapter 4.

[3] Emanuele Falbo, and Thomas J. Penfold. Theoretical insights into the self-assembly process of Wells-Dawson Polyoxometalates. This is work has been submitted *J. Phys. Chem C*, and it is undergoing an initial assessment.

Contribution:

E.F. conceived and designed the presented idea. E.F. performed the computations. E.F. collected the data. E.F. and T.J.P. verified the analytical methods. E.F. wrote the paper. T.J.P. supervised the findings of this work, and the final look of the text. This work is presented in Chapter 5, where further findings and contributions, absent in the original article, have been added.

[4] Nathan Davison, Emanuele Falbo, Paul G. Waddell, Thomas J. Penfold and Erli Lu. A Monomeric Methyllithium Complex: Synthesis and Structure. This is work has been published in Chem. Comm., DOI: 10.1039/d1cc01420j .

Contribution:

N.D. conceived and designed the presented idea. N.D., P.W, and E.U. performed the experimental work, while the computational part has been done by E.F.. N.D. collected the experimental data. E.F. and T.J.P. verified the computational methods. N.D. and E.U. wrote the paper, apart from the computational section which was written by E.F. . E.U. and T.J.P. supervised the findings of this work, and the final look of the text. This work is due to a recent collaboration with E.U group and it is not presented here.

[5] Emanuele Falbo, Conor Rankine, and Thomas J Penfold. Theoretical study of spin state energetics in ferric hemes. This work has not been published yet.

Contribution:

E.F. conceived and designed the presented idea. E.F. performed the computations. C.R. wrote the deep neural network program that has been used by E.F.. E.F. collected the data. E.F. , C.R. , and T.J.P. verified the analytical methods. E.F. wrote the manuscript. T.J.P. supervised the findings of this work, and the final look of the text. This is work is still in progress, and it is not presented here.

Chapter 1

Introduction

1.1 Introduction to Polyoxometalates

Polyoxometalates (POMs) are large molecular clusters with highly symmetric structure. They are mostly composed of d^0 early transition metals (V^{5+}, Mo^{6+}, V^{6+}, W^{6+}) sharing oxo ligands. Typically, each metal occupies the center of an ideal six-fold coordinated octahedral with the oxygens located at vertices. In reality, the polyhedra points towards a more likely C_{4v} symmetry. Due to their ability to aggregate, POM molecular structures go from relatively small nano-clusters containing up to hundreds of atoms to approaching the size of small protein molecules. [10] Thanks to their high nuclearity, POMs have been employed for many different applications, for example, as biomedical materials or catalysts. [11] However, despite all the efforts, the underlying mechanism of POM self-assembly is still poorly understood, and the prediction of formation of specific species is usually only dictated by their thermochemistry. [12] Experimental data illustrates that an initial step involves the protonation of terminal M=O metal oxygen bonds of a six- or four-fold transition metal complex, leading to the formation of a hydroxo ligand, and thus to a more electrophilic metal. [13, 14] A theoretical study revealed that the energy barrier for the conversion from hydrated tetrahedral anions to a hydrated hexacoordinated species is almost negligible 1-10 kcal/mol. [15] The hydrated complex can then be attacked by an oxo ligand of another oxometalate anion, followed by a condensation reaction. [13] This process leads to the formation of a dinuclear species (Fig. 1.1.1), which can undergo further oligo-condensations leading to larger molecular clusters.

One of the first attempts to elucidate the mechanism of formation of POMs has been performed by the groups of Poblet and Cronin, who combined theoretical calculations and mass spectrometry experiments. [12,15] They postulate that, once dinuclear species are formed, successive steps of protonation

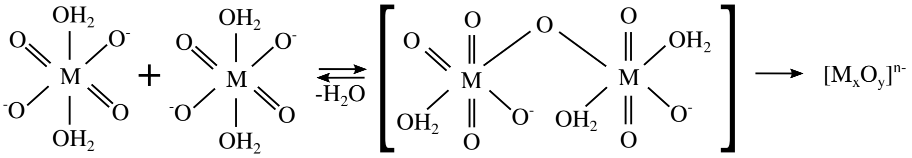

Figure 1.1.1: Schematic representation of formation of POMs via self-assembly process.

and water condensation with subsequent aggregation occur, with this last step being the most exothermic. [12]

POMs can be mainly classified in two families depending on whether an internal cation, or heteroatom (X), is present or not: (i) isopolyanions (IPAs) with formula $[M_xO_y]^{n-}$ (M = metal) without heteroatom X and (ii) heteropolyanions (HPAs) with formula $[X_zM_xO_y]^{n-}$ (with heteroatom X = P, Si, Al, B, z < x). A polyhedral representation of these species is illustrated in Fig. 1.1.2.

The most representative of the IPAs is the Lindqvist anion, $[M_6O_{19}]^{n-}$ with M = W, Mo, or Nb. These clusters are often structurally less stable than their HPA counterparts, they show high basicity, which makes them ideal building blocks to construct larger POMs. [16] As result of this, these ions are often only stable in their protonated forms. Another interesting application comes from substituting the hexamatelates with organic ligands, $[(M'L)_xM_{6-x}O_{19-y}]^{n-}$ ($M' \neq M$), in order to form versatile POM-organic hybrids. [17] Hexavandates have been hardly isolated, [13] however, single-addenda vanadates, like $[V_{10}O_{28}]^{6-}$ and $[V_{12}O_{32}]^{4-}$, have been experimentally studied. Their experimental importance is due to their ability to undergo fast multiple redox reactions, and therefore, they could actually be used as high-performing electrodes in ion batteries. [16] Some of these applications are discussed in more detail in the next section. From a theoretical perspective, all Lindqvist ions share the same electronic distributions. Essentially, the LUMO orbital of fully oxidized species consists of non-bonding p orbitals and d orbitals. [18] The HOMO-LUMO gap is relatively large, which confirms their structural stability. [14]

The ions of the HPA family are the Anderson, Keggin, Wells-Dawson, and Preyssler species, with respectively formula $[XM_6O_{24}]^{n-}$, $[XM_{12}O_{40}]^{n-}$, $[X_2M_{18}O_{62}]^{n-}$, and $[X_5M_{30}O_{110}]^{n-}$, (this latter is for phosphotungastates). [14] The most representative ions are the Keggin and Wells-Dawson, which have largely been employed in several fields due to their electronic properties and molecular stability. Here, we give a brief description of their electronic and molecular properties, while their relative applications are discussed in

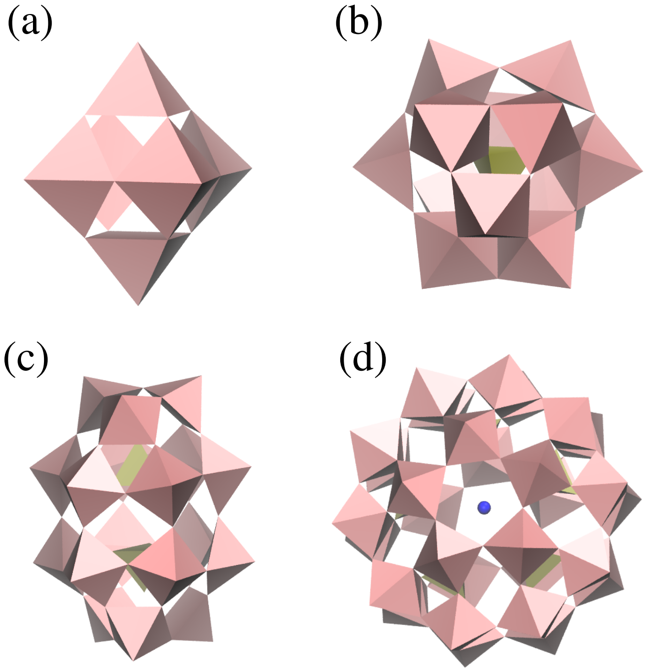

Figure 1.1.2: Illustration of **(a)** Lindqvist, **(b)** Keggin, **(c)** Wells-Dawson, and **(d)** Preyssler polyoxometalates. The pink polyhedrals are around the metallic atoms.

more detail in the next section.

Keggin compounds have an electronic structure similar to that of Lindqvist compounds, i.e., the character of inner doubly occupied orbitals are exclusively due to oxygens (often called *oxo band*), [14] whereas their frontier orbitals are a mix of metallic d orbitals and antibonding oxygen p orbitals (Figure 1.1.3). Thanks to this composition, the electron reductions occuring in the metallic orbitals generate the typical blue color of reduced POMs. In contrast to simple transition metal complexes, reduced POMs hardly show significant change in their molecular structure, since the strong electron-electron repulsion is lessened by delocalising the electrons over all metallic centres. This is particularly true for highly symmetric anions such as the Lindqvist and Keggin ions. Indeed, for Keggin polyanions the HOMO and LUMO orbitals are distributed over all metallic centres. As result, the Keggin ions are able to undergo multiple redox reactions, since further addition of electrons would be delocalised over the whole cluster or at least over a large part of it. The HOMO-LUMO gap is large enough so that these ions are stable under different chemical conditions. Indeed, conversely to the IPAs, Keggin ions are stable in solution in their dehydrated forms.

By rotating of 60° the $[M_3O_{10}]$ triads, it is possible to obtain the five isomers of Keggin anions: the α and β isomers contain zero and one rotated

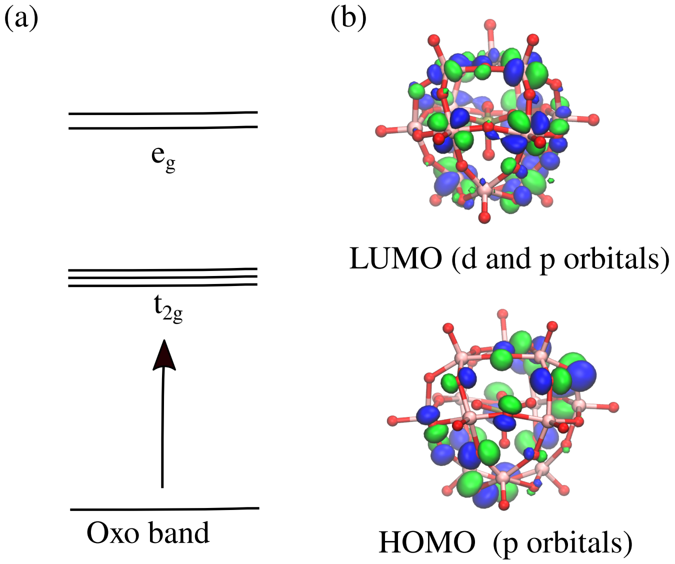

Figure 1.1.3: (a) Molecular orbital diagram of an idealised octahedral Keggin ion. **(b)** HOMO and LUMO orbitals of Keggin $[PMo_{12}O_{40}]^{3-}$ ion.

triad respectively, while the γ, δ, and ε contain respectively two, three, and four rotated triads. The α isomer is the most stable, and it is normally the only species isolated experimentally. These observations were also supported by theoretical results, which showed that the order stability is as follow: $\alpha > \beta > \gamma > \delta > \varepsilon$. [19] This energetic trend is extremely important, since it reduces a lot the number of simulations to be performed when studying POMs. Indeed, if any of the other isomers was as stable as the α one, a theoretical chemist would always need to consider the role of this for any property under study. For example, if one is interested in the computation of the redox potentials of a Keggin ion, the reduction on the other isomers should be also taken into account, doubling the number of calculations.

It is, however, worth mentioning that further reductions can change the stability of isomers according to the elemental composition of the Keggin type. [20] Poblet *et al.* showed that the β isomer of Keggin ions becomes more stable with respect to the α one after the second and third reduction. However, there are no further gain in stability for additional reductions.

In the Wells-Dawson anions, each metal atom possesses an idealised D_{3h} symmetry. There exist two different regions, namely, the equatorial region (or belt region) formed by two rings containing 6 metal atoms each, and the two cap regions, which have 3 metal atoms per cap. Both Keggin and Wells-Dawson ions are structurally similar, however, their electronic structures differ slightly. For instance, in contrast to the Keggin-type $[PW_{12}O_{40}]^{3-}$, where the HOMO and LUMO orbitals are distributed over all metals, regardless of the redox state of the POM, the frontier orbitals of Wells-Dawson $[P_2W_{18}O_{62}]^{6-}$ anions tend to be more localized over only certain metal atoms. This is a consequence of the presence of two different molecular regions, and it can be distinguished by observing the location of frontier orbitals. In Wells-Dawson types, the LUMO is mainly composed of d_{xy} and d_{yz} orbitals of the equatorial metals, whose energy becomes similar to that of the orbitals on the capping atoms when reducing the POM, and therefore, making the capping orbitals more likely to be filled. [20]

The Wells-Dawson anion has six isomers that are obtained by rotating the cap regions and keeping at the same time the belt regions eclipsed or staggered. As for the Keggin ions, the most stable form is the α isomer, whereas the remaining isomers are more difficult to synthesize. [21]

1.2 POM-based Technologies

In recent decades, there has been a growing interest in the development of new forms of energy storage materials due to the increasing worldwide energy demand. It is nowadays commonly accepted that the conventional production plants, such as those from fossil fuels or nuclear power plants, can not longer be the main source of energy due to their large contribution to the worldwide pollution and increasing temperature. In this regard, in the Paris Agreement (2016), the biggest economies in the world agreed to stop the future increase of world temperature below the 2 °C . To this end, economical investments have been devolving to a larger distribution of renewable resources. Renewable energies, like solar and wind sources, have largely been employed as alternatives to fossil fuels throughout the world, however, their intermittent nature cannot always meet the actual energy demand. For instance, both wind and solar power strongly depend on the weather or geographical position of where power plants are located. To smooth out such intermittency, there has been an increasing interest in new form of low-cost electrical energy storages (EESs). [1,22]

The EESs should be able to have high energy density, and at the same time provide a quick response according to the energy demand. They also need to have long-cycle life, i.e., the discharge time needs to be as high as possible (usually up to hours or even more). Another crucial aspect is the safety of EESs. Indeed, EESs are devices with high energy density, and the breakdown of their components can lead to a rapid explosive discharge of energy. [23]

Following these technical considerations, different technologies have been proposed for both stationary or more target applications. Among all of them, electrochemical storages and batteries are probably the most versatile EESs to meet equally the need of high energy demand and having a low impact on the environment. The main mechanism of such devices is to store electrical current in chemical energy when it is not needed, and vice versa, convert this latter in current on demand. In the following, two types of most promising electrochemical EES devices are discussed.

1.2.1 Redox Flow Batteries

Redox Flow Batteries (RFBs) are rechargeable batteries that convert electrical energy into chemical energy, and vice versa. A typical RFB is composed of large tanks containing the liquid electrolytes. A flow from the tanks to the electrodes permits the reduction (discharge) of the redox couples, while the reverse process (charge) converts chemical energy into electrical current. Thanks to such structural composition, it is possible to address separately the energy density and power density variables. Indeed, for stationary applications, it is possible to increase the energy density of a RFB by simply increasing the size of its tanks. [2]

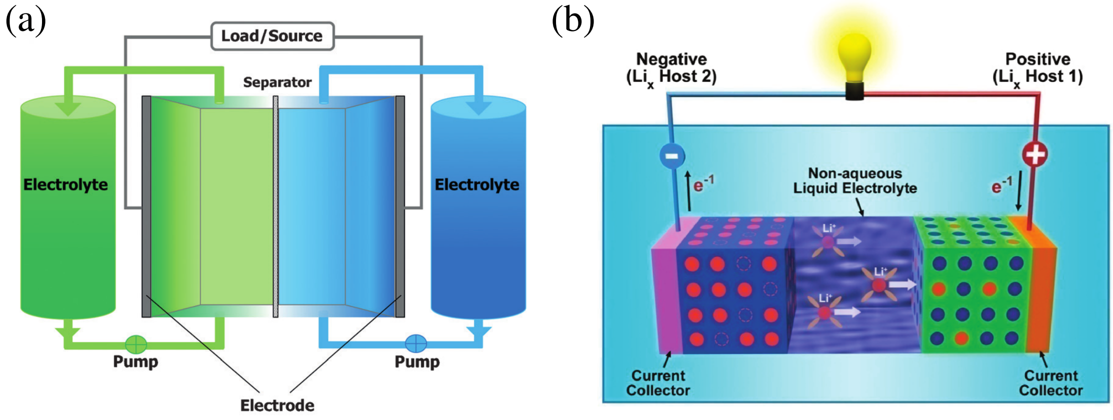

Figure 1.2.1: Schematic representation of **(a)** all-vanadium RFB and **(b)** LIB. These images were taken from Ref. [1,2]

Currently, the best performing RFB is the all-vanadium redox flow battery (VRFB). [1] The VRFB exploits the fact that the vanadium can go through several oxidation states in a reversible manner without loosing the stability of the cell, which permits the production of high energy density. The main drawback of the VRFB is the slow kinetics of V^{2+}/V^{3+} and VO^{2+}/VO_2^+ couples, which limits the flowing current and therefore the power density of the battery. [9]

Further challenge is the relatively low volumetric energy density compared to lithium ion/polymer and lead-acid batteries. For example, commercial VRFB systems feature an energy density of 25 Wh L^{-1}, which is lower than that of conventional storage technologies such as lead-acid (100 Wh L^{-1}) and lithium ion/polymer (100 Wh L^{-1}). [2] Therefore, larger volumes of electrolyte need to be used to make RFBs competitive in the field of batteries. [1,2] Another important aspect is the price of vanadium, which is strongly dependent on the amount of steel produced, and it is relatively high compared to lead and lithium. A solution is to utilize organic charge-storage materials, which have an important cost benefit over metal-based RFBs. Many organic redox couples have been presented in the recent years, among these, the anthraquinone derivatives are probably the most studied, since these compounds are also used as organic cathode materials for lithium-ion batteries. [2, 24] One disadvantage of organic redox couples is their long-term stability. In contrast to metals, which form stable ions, organic compounds tend to undergo side reactions when they are either oxidized or reduced. Furthermore, most studies of organic-based RFBs have been restricted to laboratory, and insights into scale-up with larger cell areas are currently not available. [9]

Besides increasing the size of tanks, and thus consuming larger volume of electrolyte, higher energy density can be obtained by increasing the number of electrons per molecule involved in the discharge/charge. On the other hand, the power density depends on the rate at which the chemical energy can be converted into electrical current, [2] and therefore, fast electron transfers can push forward the current power density limits.

In this regard, POMs have gained great interest, since they can undergo multiple electron reductions, and thus they could ideally give very high energy density. Recently, Pratt *et al.* developed a POM-based RFB, with a three-substituted W-based Keggin ion ($[SiW_9W_3O_{42}]^{4-}$) as electrolyte, in both aqueous and non-aqueous solvents. [25]. This system was demonstrated to produce a small capacity (4 mA h) at a low POM concentration (20 mM). [25] A higher capacity (13.4 A h L^{-1}) was reached by using higher concentration of $[CoW_{12}O_{40}]^{-6}$ as anolyte and catholyte. Note that the relationship between Wh and Ah per 1 L of solution is: Ah = Wh/V with V operating voltage of the cell. So, the operating voltage of the cell, which mainly depends on the redox couples, must be mentioned when expressing the capacity of a cell. While the $[CoW_{12}O_{40}]^{6-}$ was well suited as anolyte, since the the tungsten atoms undergo four electrons reduction at an average potential of -0.1 V vs. SHE, the cobalt heteroatom transfers only one electron at 1.1 V vs. SHE. Therefore, to balance the charges in the two tanks the catholyte volume had to be four times larger than the anolyte volume. [26] It is must be underlined that, in contrast to the $[SiW_9W_3O_{42}]^{4-}$, this system exploits the reduction of the internal cobalt heteroatom. However, both of these systems are symmetric RFBs, i.e. the same POM is reduced (catholyte) and oxidized (anolyte) in two separate tanks.

To overcome the limit of the performance of a symmetric RFB, and the difficulty to prepare specific substituted POMs such that the number of electrons during reduction and oxidation are the same, Jochen *et al.* developed an asymmetric POM-based RFB composed of $SiW_{12}O_{40}$ (**SiW**$_{12}$) as anolyte and the $PV_{14}O_{42}$ (**PV**$_{14}$) as catholyte. **SiW**$_{12}$ is a typical Keggin ion, while PV_{14} is a modified Keggin type with the addition of two VO units in the cap regions of the POM. The vanadium atoms of these units are defined as cap atoms to distinguish them by the remaining atoms. They showed that the **SiW**$_{12}$ and **PV**$_{14}$ can be reduced by respectively four and seven electrons, thus producing a high capacity of 10.7 A h L^{-1}. The authors claimed that the actual number of electrons used during battery operation is two and four for respectively **SiW**$_{12}$ and **PV**$_{14}$. This restriction is due to the fact that the third redox wave of **SiW**$_{12}$ irreversibly modifies the electrode which leads to its decomposition and catalysis of the hydrogen evolution reaction. On the other hand, the author highlighted the difficulty to individuate the exact number of electrons for the **PV**$_{14}$ reduction, despite four electrons were assigned. An important aspect is that **SiW**$_{12}$ undergoes simply electron reductions, while ^{51}V NMR specta revealed that the reduction of **PV**$_{14}$ is coupled to proton transfers, and therefore, it is pH dependent. The ^{51}V NMR analysis gave further insights into its electronic behaviour illustrating that both cap atoms and the remaining twelve vanadium atoms take part in the reduction. [9]

In addition, it has been shown that the electron transfer rate is four times faster than in the common VRFB. [9] This translates into the possibility to have higher power density (150 mW cm^{-2}) than commercial VRFB power densities (60-100 mW cm^{-2}). [9] Inspired by the above work of Jochen *et al.*, and its promising efficiency compared to earlier attempts of POM-based RFBs, we decide to theoretically investigate the **SiW**$_{12}$ and **PV**$_{14}$ POMs in order to understand their electrochemical behaviour, and where possible to provide general guidelines to predict their properties. This work is presented in Chapter 3, and a brief description of its objectives and theoretical methods are given in the next sections.

Another example of POM-based RFB was provided by Cronin *et al.*, who demonstrated that the Wells-Dawson $[P_2W_{18}O_{62}]^{6-}$ ($\mathbf{P_2W_{18}}$) is able to store up to 18 protons and electrons in acidic aqueous solution, returning an energy density of 225 W h l^{-1}. [27] They showed that this high energy density is due to the synergistic combination of two factors: the lowering of the pH, and the increase of POM concentration. At pH = 7, the redox peaks in the cyclic voltammogram are simple one-electron reductions, whereas when the pH is lowered to 4, the peaks below 0 V become two-electron processes. On the other hand, the increase of POM concentration leads to the formation of agglomerates, which would facilitate the acceptance of a high number electrons in solution. Inspired by these two observations, the authors showed that POMs can be reduced by 18 electrons (protons) by further lowering the pH to 1, and increasing the concentration from 2 mM to 100 mM. Thus, the authors believe that this system will be able to yield a flow battery with an energy density breaking the 1,000 Wh l^{-1} barrier, potentially allowing electric vehicles to be powered by POMs. Moreover, this will lead to new flexible energy devices with the ability to switch between hydrogen or electrical power. [27]

Although these POM-based switchable batteries possess a great potential, their basic mechanism is still not clear. For instance, at low pH and high concentration the cyclic voltammogram (CV) of $\mathbf{P_2W_{18}}$ shows a more complex scenario, with multiple peaks which are not easily assigned to the 18 electrons transferred to POMs. In addition, it is not clear what factors would be responsible for the aggregation process in solution. Therefore, the understanding of all these features would grant access to the modulation of POM properties in solution for experimental applications. For this reason, we decided to use theoretical chemistry to help determining the key factors that influence the self-assembly process, and at same time to define the connection between the aggregation and POM electrochemistry. The results from this study are presented in Chapter 5.

1.2.2 Alkali-ion Batteries

Since the discovery of intercalation compounds (Li_xMO_2, M= Co, Ni), the Lithium-ion batteries (LIBs) have become the champion of all batteries for portable devices, or vehicle applications. [1,28] Thanks to their high energy and power density, LIBs have indeed shaped the new technological era in which we now live, and this is the reason why the Nobel committee assigned the chemistry prize to J. Goodenough and colleagues. [29]

A typical LIB is shown in Fig. 1.2.1. During the discharge (charge) Li^+ ions go from one host electrode to another and they are reduced (oxidized). The electrolyte is usually a liquid containing Li salt, while the cathode and the anode are respectively made by Li-intercalation compounds and graphite. Here, we briefly mention some of the most commonly used LIB, and comment their advantages and limits.

$LiCoO_2$ (LCO) cathode has been the first and most successful battery of layered transition metal oxides. Its structure consists of alternating layers of Co and Li sites which form a hexagonal symmetry. [28] LCO is a attractive cathod material because of its high specific capacity of 274 mAh g^{-1}, high discharge voltage, and sufficiently good cycle life. [1] The main limits of LCO batteries are their high cost, low thermal stability, and the fast decay of capacity at high current rates. Their cost strongly depends on the Co prize, which is quite expensive. The thermal instability refers to the release of oxygen when the cathode is overheated, resulting in a runway reaction that can lead to a fast explosion. This is the major concern for the application of LIBs in hybrid or electric vehicles. For example, repeated events of fire on board of aircrafts, caused by LIBs, resulted in the grounding of all Boeing 787. [30] $LiNiO_2$ (LNO) has the same structure of LCO and similar capacity, however, the lower cost of the Ni compared to Co is the main driving force of LNO batteries. [28] However, the efficiency of LNO cathodes is limited because Ni^{2+} ions substitute the Li^+ ions during the synthesis and delithiation process, which results in a block of the Li^+ diffusion. [28] It has been shown that the thermal stability and electrochemical performance of LCO and LNO can be improved by adding a small amount of Al. This lead to the construction of the $LiNi_{0.8}Co_{0.15}Al_{0.05}O2$ (NCA) cathodes which are currently employed in the electrical vehicles of Tesla company. [28]

Other attractive alternatives to the common LIBs are the sulfur-based LIBs (Li-S). In Li-S, the sulfur (S_8) is reduced to produce lithium sulfide by accepting the lithium ions and electrons at the positive electrode (anode). These have an extremely high theoretical capacity of about 1675 mAh g^{-1} (almost ten times the capacity of common LIBs), and a low cost due to the abundance of sulfur sources. [28] However, the S-based cathodes suffer from low potential vs. Li/Li$^+$, dissolution of intermediate reaction products (polysulfides) in electrolyte, and significant volume change, which might destroy the electrical contacts in the battery. [28] To mitigate these effects, sulfur can be encapsulated in a hollow structure with excess internal void space. Alternatively, Li_2S in combination with carbon can be utilized as anode, and since the fully lithiated Li_2S does not expand, no void spaces are necessary in the battery. [28]

The safety of above LIBs is endangered by the use of the liquid electrolyte. Recently, solid-state batteries (SSBs), which uses a solid-state electrolyte (SE), are becoming the best option to satisfy the requirement for high energy density in a safer way. The cathode materials for SSBs are the same as those currently employed in the commercial LIBs, for example, LCO, LNO and NCA, since these reach high energy and power densities. [31] Several types of SSBs exist, here, we only focus on some of the commercially used. Lithium Superionic Conductors (LISICONs) was one of the first reported SSBs, with chemical formula $Li_{4\pm x}SI_{1-x}XO_4$ (X = P, Al, and Ge). [31] LISICONs are stable with water and their thermal stability make them efficient at high temperatures. The main drawback is associated to their low ionic conductivity at room temperature, which however can be improved by a strategic substitution of the elements. [31] Common materials are also the perovskites ABO_3 (A = Li, Ca, Sr, La, and B = Al, Ti). In these materials the Li ions hop from one site to another through the face sharing dodecahedra. Their ionic conductivity depends on many factors, like the nature of ions, their size, and content of vacancies. One of the most promising system is the LLTO ($Li_xLa_{y\gamma}TiO_3$, with x and γ varying), which shows an high conductivity at room temperature owing to the large radius and higher valence of La. [32] Generally, the low ionic conductivity is due to the change of composition of the interfacial layer between the electrode and the solid electrolyte, representing one of the big challenges associated to SSBs. [33] Other alternatives to LIBs have been proposed, such as alloys, inter-metallic materials, or even Na-ion batteries (NIBs). [1] These batteries are much cheaper than the expensive Lithium-based materials but their performances are still too poor compared to LIBs. However, it is worth noting that research on these alternatives lags behind that of LIBs by about 15 years or more because of the interest in developing only the more powerful LIBs.

As outlined in the previous sections, POM can undergo multiple electron reductions, and therefore, they have become promising electrode active materials for supercapacitors, either LIB or NIB. [34–36] Recently, Yoshikawa *et* *al.* showed that a LIB using Keggin anions $[PMo_{12}O_{40}]^{3-}$ (**PMo**$_{12}$) can achieve a high capacity of about 270 mA h g^{-1}, which is comparable or even higher than that in common LIBs (for example the LCO and LNO). [8] This high capacity is due to the ability of the $[PMo_{12}O_{40}]^{3-}$ to be reduced by 24 e$^-$ in a reversible manner, which translates into the reduction of each of the twelve Mo atom from Mo^{6+} to Mo^{4+}. In operando Mo K-edge extended x-ray absorption fine structure (EXAFS) and X-ray absorption near edge (XANES) measurements on this POM molecular cluster battery (MCB) revealed that the electronic rearrangements is followed by a simultaneous formation of Mo-Mo bonds which go from 3.6 Å to 2.6 Å, and an elongation of Mo=O bond lengths (from 1.6 Å to 2.0 Å), resulting in a slight shrinkage of **PMo**$_{12}$ molecular size. To better understand the structural changes, Irle *et al.* performed a theoretical study in which they showed that a linear relationship exists between the number of Mo-Mo and the electrons transferred to the POM. [37] In addition, their electronic analysis revealed the existence of a three-center two-electron bond at the center of each triangular Mo site, and it was found that Mo-Mo bonds mix with Mo-O antibonds, delocalizing electrons partially away from the Mo atoms to the O atoms, which in turn more likely interact with the Li$^+$ ions.

However, in their work ,more than the formal number of Li$^+$ were added to the POM to properly observe twelve Mo-Mo bonds. This is due to the current limits of many GGA functionals, which tend to overdelocalise electron density, and therefore might fail to properly describe highly charged systems like POMs. Furthermore, the POM-based battery of Yoshikawa *et al.* suffer from poor capacity retention due to the structural instabilities of the fully reduced $[PMo_{12}O_{40}]^{27-}$ during the operating time of the batteries. [8] This suggests that an explicit description of the solvent environment around them is likely to be important to properly treat the highly anionic nature of POMs. Therefore, in order to shed light on the key factors controlling the reduction of **PMo**$_{12}$, we performed a theoretical study, which is presented in Chapter 4. Furthermore, from this investigation, we expect to provide a theoretical protocol that can be used to link the molecular and electronic properties of any highly charged state of any POM type.

Currently, most of the studies focused on the modulation of POM-based batteries to improve their energy density, while there has not been much effort to study the electron transfer rates, which are responsible for the power density of the battery. This is largely due to the high number of electrons involved in the reactions that make difficult the computation of accurate electron transfer rates both experimentally and theoretically. [16] Although there exist many possible theories, like the Marcus theory, the large number of electrons require that all possible intermediate steps of the reduction must be taken into account, which poses a strong barrier to the actual computation. [38] Alternatively, strong approximations must be taken to simplify the redox scenario. A brief discussion of the key factors controlling the rates is given in the next section. In this thesis, we did not focus on the investigation of the electron transfer rates, however, it will be worth mentioning few experimental examples. Friedl *et al.* investigated the electron transfer rates for a NIB using Lindqvist-type $Na_6[V_{10}O_{28}]$ as anode. $Na_6[V_{10}O_{28}]$ presents a high capacity of 240 mA h g^{-1} with a capacity retention of 87%. [16] As for the $[PMo_{12}O_{40}]^{3-}$, the reason for such a high performance is due to the reduction of POM by 10 electrons. By performing chronoamperometry experiments they showed that the electron transfer rate is thirty times faster than in the common olivine $LiFePO_4$ batteries, [16] and therefore, a high power density can be reached with this material.

1.3 Theoretical Overview

Theoretical studies of POMs started more than two decades ago, however, as happened for many other compounds, the number of studies on POMs started to grow exponentially with concomitant growth of applying computational chemistry to real physical problems and complex systems in the early 2000s.

In this section we present a brief summary of the current theoretical approaches to study the properties of POMs. In particular, we discuss the differences between several methods, and their limits when dealing with specific arguments. In addition, we outline the current challenges that need to be addressed to allow the use of more sophisticated methods, with particular attention for large scale simulations.

1.3.1 Theoretical Approaches and Challenges in Modelling POMs

The state-of-the-art approach in the modelling of POMs is density functional theory (DFT). As for many other large systems, DFT is the most sensible choice because of its good accuracy and low computational cost. To give an idea of the speed of DFT compared to wavefunction theories, we can analyse how these theories scale with the number of atoms (N) under study, which affects the computational time and its corresponding resources (memory and number of processors). The scaling of DFT is generally governed by several factors but it can be approximately estimated as $\approx N^3$. The origin of this scaling with N has to do with the diagonalization of Kohn-Sham equations (2.3.45), where the one-electron functions are expanded over a fixed basis set of size, say Q. Typically, the size of the basis set Q is larger than the number of electrons, and therefore the proper scaling is $\approx Q^3$. [39] In contrast, wavefunction methods typically scale with higher powers of N compared to the DFT, for instance, coupled cluster single-double (CCSD), and coupled cluster single-double-triple (CCSDT) scale respectively as $\approx N^6$ and $\approx N^8$. [39] The problem associated with these scalings is particularly pronounced due to the fact that, depending on the specific system under study, a very large basis set must be used to obtain converged results. Therefore, the relatively low scaling factor and the inclusion of nondynamical and dynamical correlation effects (see 2.3) into the DFT functionals has made this theory the most reliable option to study both medium and large systems. On these grounds, DFT is the only feasible option to study large systems like POMs, and this has been used throughout.

As outlined in the text, the main drawback of DFT is the choice of the exchange-correlation functional E_{xc}^{DFT} (xc functional). In practice, better results are generally obtained by including Hartree-Fock exchange in the E_{xc}^{DFT}, however, there is not a universal receipt about which E_{xc}^{DFT} would give the best answer for a specific problem. The reason is due to the fact that the exact form of the E_{xc}^{DFT} functional is not known yet, and therefore, approximations must be used (see Section 2.3) This lead to the exploration and parametrization of different families of E_{xc}^{DFT}, which are not always valid for any type of systems. Among these, pure GGAs and hybdrid-GGAs are the most commonly used functionals, thanks to their low computational cost and performance. In this regard, both pure GGA and hybrid-GGA functionals return good equilibrium geometries in most cases, showing very subtle differences. However, care must be taken in some situations, such as for open-shell systems. In this latter case Buhl *et al.* showed that GGAs perform relatively good for first-row transition metals, whereas a slight improvement is obtained by hybrid-GGAs when going down the periodic table. [40, 41] In that work, they found that the for second- and third-row transition-metal complexes, the standard deviation of optimized bond lengths decreases in the following order of functionals: LSDA > BLYP > BP86 > B3LYP ≈ TPSSh > PBE0. A reason of this improvement is due the inclusion of exact exchange into the xc functionals, which should reduce in principle larger delocalisation errors present in heavy atoms.

On the other hand, care must be taken when describing the electronic structure of POMs. For example, for anions, the excess of electrons on localized or strong donor sites can lead to a wrong evaluation of electron affinity (EA) and frontier orbitals due to a strong self-interaction error (SIE). Indeed, a net negative charge gives a large upward bump in the Kohn-Sham potential so that the last electron of the compound is completely unbound. [42] One of the reason of the large SIE is due to the behaviour of the Kohn-Sham potential at large distances. The Kohn-Sham potential is written as the sum of three contributions: the external, the Coulomb, and the exchange-correlation (E_{xc}^{DFT}) potential (Eq. 2.3.43). Far from a nucleus, the Coulomb potential decays as N/r, where N is the number of electrons, and therefore, the exact Kohn-Sham potential should decay as -1/r. For a neutral atom, N equals the atomic number Z, and the Kohn-Sham potential approaches -1/r exactly. However, almost all local and gradient-corrected functional approximations to E_{xc}^{DFT} decay incorrectly at large distances, typically exponentially. This has a small effect on the electron density, but might lead to a very wrong description of HOMO and LUMO orbitals, with errors in the range of several eV. [43,44] This effect is particularly evident for localized anionic or strongly electron donating sites. [43] As result, the EA, HOMO and LUMO energies turn out to be dependent on the type of E_{xc}^{DFT} used. [43,44] There is no general rule other than assessing the goodness of *xc-functionals* by testing it, but two cases are indicators of E_{xc}^{DFT} limits. The presence of a positive HOMO indicates that the *xc-functional* is not correct to describe it, and/or a virtual orbital has a lower energy than the HOMO, which indicates that a lower energy solution to the SCF problem exists. [44] However, Burke *et al.* showed that even if the FMOs are ill-described, it does not necessarily mean that the total energy of the system is wrong. [43]

Returning to POMs, since these are normally barely charged molecules, it means that large deviations can be obtained in the description of both HOMO and LUMO orbitals. In this regard, most of the early and even recent calculations on POMs were performed on barely charged states. These works indirectly established the influence of E_{xc}^{DFT} on the HOMO/LUMO orbitals by computing the redox potentials of POMs, rather than focusing on the direct values of their frontier orbitals. [11, 20] For instance, for a singly-substituted Wells-Dawson ion, Poblet *et al.* showed that GGA functionals put an extra electron over the belt region instead of correctly localizing it in the cap region. [45] This aspect influences not only the HOMO and LUMO position (energy) but also their computed redox potentials. Further tests with hybrid-GGAs revealed that the inclusion of 20 % exact exchange (B3LYP functional) gives the best results in comparison to the experimental data. A practical solution to overcome a large SIE is to add enough counter ions such that the full system (POM plus the counter ions) is neutral. In this direction, Kremleva *et al.* presented theoretical studies on a tri-Mn-substituted W-based Keggin ion, which was recently employed in an aqueous RFB. [46, 47], with the explicit addition of enough counter ions (Li^+) such that each final system was neutral. However, even in that work, significant deviations were found for neutral POMs [48] due to large (de)localization errors.

Alongside the use of an accurate *xc*-functional, the choice of the *basis set (BS)* is important. The double-zeta atomic BSs suffices to reproduce good POM geometries, however, at least a triple-zeta BS must be used if other specific properties, such orbitals or thermochemistry, are investigated. [45, 48] Unfortunately, since the large molecular size of POMs, larger BSs than triple-zeta turn out to be prohibitive for specific simulations, such as in *ab initio* molecular dynamics (AIMD) calculations. Another crucial element to effectively describe both electronic and redox properties of POMs is the inclusion of solvent effects. [49] This can be done in two ways: using an implicit, or explicit solvation model. The first type is easily done by any modern quantum chemistry codes, which treats the solvent as continuum dieletric (COSMO, CPCM, or SMD) which accounts for the polarization effects between the POM electron density and the solvent. Lopez *et al.* illustrated that the inclusion of an implicit solvent slightly improves the computed geometries, while it has largely positive effect on the electron density. [14] Indeed, non-bulk and bulk interactions between the POM electron density and the electrostatic potential, generated by the solvent, improves the realistic description of the density itself. A more detailed discussion of this is given in Section 2.7. A clear example of the importance of the solvent is illustrated by the protonated forms of W-based Keggin ions. Gas-phase calculations suggest that the protons would preferentially bind the terminal oxygens rather than the bridging oxygens. However, the inclusion of the implicit solvation in the same calculations reverse the gas-phase results, indicating that the bridging oxygens are more basic than the terminal ones. [14]

The other alternative to include the solvent effect is offered by molecular dynamics (MD) simulations. Several authors reported classical MD studies of POMs to study the effect of an explicit environment on their molecular as well as electronic properties. [14, 50–52] The MD results gives important insights into the understanding of POM aggregation process. A general trend is that the higher is the POM charge, the higher is the POM solvation, and therefore less aggregation is observed. [51,53] One of the major issue for these simulations is given by the definition of a general *force field (FF)* for POMs. MD runs are often applied to (bio)organic systems, whose FFs were the first to be developed. Unfortunately, the development of FFs for even simple inorganic systems is quite difficult, since the large number of oxidation states that these compounds can reach. In this regard, several authors have attempted to generate common FFs that works for Keggin-type POMs, [54–56] however, in most cases these FFs are not free-access or not implemented in common MD packages, and therefore, an ad-hoc FF development remains still the first valid option to simulate POMs dynamics. Another important issue is represented by the large number of local-minimum energy states. For example, during a canonical ensemble simulation our system can get trapped in one of these minima, and it will never reach the final conformation. The transfer from one conformation to another (*rare event*) can be elegantly solved by using the so-called *enhanced or bias sampling techniques*. One of these techniques is the umbrella sampling. Umbrella sampling yields a set of biased probability distributions, and to generate the free energy profile for the entire pathway, the results of the various windows are combined and unbiased. [7] This approach was, for instance, used by Parrinello *et al.* to investigate the influence of the distal pocket conformation on the structure and vibrations of the heme-CO bond in myoglobin. [57] They showed that, since the CO stretch frequency and the strength of heme-CO interaction depends on the orientation and tautomerization state of an hystidine residue of the heme, a biased approach is necessary to allow a correct description of heme-CO system. [57]

More accurate methods such as quantum mechanical/molecular mechanics (QM/MM) or AIMD can be used to study POMs in solution. [47, 48] In these simulations, the evaluation of forces and energy is usually the bottleneck of the runs. For example, in QM/MM simulations only the POM and/or the counter ions are included in the QM region in order to have good accuracy in the little times. This choice is justified by the fact that many of the interesting properties of POMs are extrapolated from their electron density, and therefore, if this latter is well described, we could expect to obtain accurate results. This means that all we need is to treat the POM quantum mechanically, while the solvent molecules are modelled by classical mechanics. If this is not sufficient, then the scenario becomes more complex because of the difficulty to reach converged results when including solvent molecules in the QM region. Therefore, further convergence tests must be performed to account for not only the correct types of solvation but also for the correct molecular shape of POMs.

In addition, a proper embedding approach that accounts for QM-MM interaction needs to be used: an electrostatic embedding works well for most common applications. [48] In contrast, for AIMD simulations the full system must be treated quantum mechanically, and its application to POMs is currently limited to the use of few solvent molecules because of the already large POMs size.

It must be mentioned that *ab initio* wavefunction methods, such as complete active space self consistent field (CASSCF) or complete active space second-order perturbation theory, (CASPT2) have been also applied to POMs. [58] Despite their computational cost, these methods can provide better accuracy due to the fact that correlation effects are not approximated but these are already included in the theories.

1.4 Thesis Outline

In the previous sections, we outlined the continuing great interest in the development of POM-based technologies due to their extraordinary electronic properties. However, these technologies are still at an early stage, mostly because of the difficulties to understand POM electronic behaviour. Therefore, further improvements are needed to make them competitive with respect to the modern commercial energy devices.

Computational chemistry offers a way to understand and tackle the common challenges in any real-world system. Motivated by the urge of solving the current POM-related questions, in this PhD thesis, we present theoretical studies of POMs in different environments in order to understand the basic mechanisms behind their behaviour, and where possible to offer a guideline to systematically improve POM-based devices.

In the previous section, a brief introduction to the current theoretical methods employed to study POMs has been given. A more detailed discussion of such approaches is given in Chapter 2. There, the advantages and limits of theoretical methods can be grasped when dealing with large systems like POMs.

In Chapter 3, we study two POMs, i.e. **SiW_{12}** and **PV_{14}**. As previously mentioned, these two POMs have been used in asymmetric RFBs. [9] The ability of these two POMs to undergo multiple reduction allows the battery to reach high capacity in a reversible way, and therefore, make the POM-based RFB very competitive compared to the commercially used LIBs. However, while the number of electrons involved in the reduction of **SiW_{12}** is known with certainty, it is not clear how many electrons are involved in the reduction of **PV_{14}**. Their number is important, because they are related to their corresponding redox potentials, and thus to the operating voltage of the battery.

To this end, we investigate the redox properties of POMs by computing their redox potentials in two ways: (i) using an implicit solvent model, and (ii) explicit solvation. We show that the deviations of redox potentials are within the uncertainties predicted by the implicit model. Further improvement can be obtained by an explicit solvation, however, large deviations are observed when a large number of electrons are involved in the reduction process. Jochen *et al.* did not investigate the evolution of the molecular structure of POMs at high charge states. This is extremely important, because it allows to understand the connection between their structure and electrochemistry. The explicit treatment of the solvent offers a way to understand the effect of the solvent molecules on POM molecular geometry and on the energy required for the reductions. Our simulations show that the structure of **SiW_{12}** is not affected by the two-electron reduction, whereas the **PV_{14}** geometry undergoes a change after the simultaneous four proton-coupled electron transfer.

In Chapter 4, we discuss the electronic properties of the super-reduced phosphomolybdate **$PMo_{12}{}^{3-}$**. This has shown to give the highest capacity ever measured for a POM-based battery. [8] Despite this, it is not clear what molecular factors control the super reduction. Therefore, we investigated the structures of POM at low and high charge state by performing both static DFT and QM/MM simulations. Our results confirm the formation of metal-metal bonds in the fully reduced state, however, in contrast to previous findings, [37] these latter do not increase linearly with number of electrons transferred to the POM. Furthermore, a good agreement between experimental findings and x-ray spectroscopy simulations, namely XANES and EXAFS simulations, illustrates that it is possible to grasp the subtle structural changes of POMs from these simulations. For example, these show that the reduction of $\mathbf{PMo}_{12}{}^{3-}$ by 24 e^- occurs in a stepwise way.

Chapter 5 is devoted to investigate the self-assembly process of Wells-Dawson type $\mathbf{P}_2\mathbf{W}_{18}$, which was recently employed in a POM-based RFB by Cronin *et al.* We show that POM agglomeration strongly depends on their total charge, namely, inorganic micro-phases are formed at low charge, whereas the solvation increases as the POM charge increases. This study also highlights the importance of a rich network of hydrogen bonds, which mediate the POM-POM interaction. In addition, first-principles results illustrate the effect of POM agglomeration on their redox potential, and catalytic efficiency towards the hydrogen evolution reaction.

Concluding remarks and an outlook on future studies are presented in the last Chapter. In the first part, final outcomes obtained in the previous chapters are linked together, giving a clearer picture of the whole thesis work. In doing so, we hope that the reader might gain a better understanding of what approaches best describe the properties of POMs according to the desired functionality. Furthermore, we give a summary discussion of the future simulations to be performed in order to further expand the analysis of different POM types as well as to overcome the current limits of the used approaches.

Chapter 2

Theory and Methodology

2.1 The Many-body Problem

The motion of a system of N particles (N-body) in quantum mechanics is obtained by solving the time-dependent non-relativistic *Schrödinger* equation (SE). However, in most quantum mechanical applications, one is interested in the electronic structure of atoms and molecules without taking into account their time dependence. In these cases, the time variable is neglected, and the SE can be simply expressed as

$$\hat{H}\psi = E\psi \tag{2.1.1}$$

where E is the total energy of the system, $\psi = \psi(x_1, x_2, ..., x_n)$, (x stands for both 3N spatial and N spin coordinates) is the wavefunction. The $\hat{H}$ is the Hamiltonian operator, whose expression is the following

$$\hat{H} = -\frac{1}{2}\sum_{i}^{N}\nabla_i^2 - \frac{1}{2}\sum_{a}^{M}\nabla_a^2 - \sum_{i}^{N}\sum_{a}^{M}\frac{Z_a}{r_{ia}} + \sum_{i}^{N}\sum_{j>i}^{N}\frac{1}{r_{ij}} + \sum_{a}^{M}\sum_{b>a}^{M}\frac{1}{r_{ab}} \quad .(2.1.2)$$

Here, the first and second term represent respectively the kinetic energy of the N electrons and M nuclei. The third and fourth terms are respectively the electron-electron repulsive potential and attractive potential between electron and nuclei, while the last term indicates the repulsive interactions between nuclei. Note that atomic units are used throughout the thesis.

The SE can be further simplified if we distinguish the electron motion from those of the nuclei. The mass of the lightest nuclei, i.e., of the proton, is thousand times heavier than the electron mass, therefore, the electron moves much faster than the nuclei, and the first ones see these latter as if they were fixed in the space. This assumption is the basis of the famous *Born-Oppenheimer (BO)* approximation. The two motions can then be separated, and Eq. 2.1.2 is reduced to the electronic Hamiltonian

$$\begin{aligned}\hat{H} &= -\frac{1}{2}\sum_{i}^{N}\nabla_i^2 - \sum_{i}^{N}\sum_{a}^{M}\frac{Z_a}{r_{ia}} + \sum_{i}^{N}\sum_{j>i}^{N}\frac{1}{r_{ij}} \\ &= \hat{T} + \hat{V}_{ne} + \hat{V}_{ee} \quad .\end{aligned} \tag{2.1.3}$$

The nuclear-electron term ($\hat{V}_{ne}$) is often called *external potential* as we shall see later. The wavefunction ψ is not an observable, but its physical interpretation can be understood by the *Born interpretation*, which states that its square $|\phi|^2$ gives the probability of finding a particle at given place (or having a specific momentum). The wavefunction must respect some boundary conditions, such as being well-behaved everywhere, i.e, it is single-valued, continuous, and finite. This last condition is enforced by requiring that the wavefunctions are orthonormal $\langle\psi_i|\psi_j\rangle = \delta_{ij}$. In addition, the wavefunctions are antisymmetric, since electrons are fermions. This means that the interchange of two coordinates leads to a change of sign of the wavefunction

$$\psi(x_1, x_2, ..., x_n) = -\psi(x_2, x_1, ..., x_n) \quad . \tag{2.1.4}$$

For any observable A, its expectation values is given by

$$\langle\hat{A}\rangle = \frac{\langle\psi|\hat{A}|\psi\rangle}{\langle\psi|\psi\rangle} \tag{2.1.5}$$

So, for example, if the ψ is normalized, the kinetic and potential energy can be measured as

$$T[\psi] = \langle\hat{T}\rangle = \int \psi^*\hat{T}\psi dx \quad , \quad V[\psi] = \langle\hat{V}\rangle = \int \psi^*\hat{V}\psi dx \tag{2.1.6}$$

where the square brackets indicates that the ψ determines the T and V, namely, we say that $T[\psi]$ and $V[\psi]$ are functionals of ψ. In contrast to the concept of function, which relates a number to another number, a functional maps a function into a number.

The access to the total energy can then be obtained by the *variational principle*, which states that the total energy, computed via Eq. 2.1.5, is an upper bound of the real energy of the ground state

$$\frac{\langle\psi|\hat{E}|\psi\rangle}{\langle\psi|\psi\rangle} = E[\psi] \geq E^0 \quad . \tag{2.1.7}$$

Eq. 2.1.7 is central in the solution of the electronic problem, indeed, it elegantly offers a strategy to obtain the ground state energy: the E[ψ] functional needs to be minimized with respect to all possible N-electron wave functions

$$E^0 = \min_{\psi} E[\psi] = \min_{\psi} \langle \psi | \hat{T} + \hat{V}_{ne} + \hat{V}_{ee} | \psi \rangle \quad . \tag{2.1.8}$$

The search can be performed with the method of Lagrange multipliers respecting the constraint that the wavefunction is normalized $\langle \psi | \psi \rangle = 1$. The variational procedure is at basis of modern electronic calculations to solve Eq. 2.1.1.

2.2 The Hartree-Fock Approximation

Before discussing the concepts behind the *Hartree-Fock (HF) approximation*, it is worth explaining the *spin orbitals* functions. A spin orbital wavefunction is the product between the spatial and the spin function

$$\chi(x) = \phi(r)\sigma(s) \quad , \quad s = \alpha, \, or \, \beta \quad . \tag{2.2.1}$$

As the spatial function takes 3N coordinates, the spin function takes only spin up (α) or spin down (β). The spin functions are orthonormal between each other, therefore, if the spatial functions are also orthonormal, so are also their corresponding spin orbitals.

As discussed in the previous section, the variational principle offers a way to solve Eq. 2.1.1 by minimizing the energy with respect to N-electron wave function. Unfortunately, the exact wavefunction of the ground state is not known but trial wavefunctions respecting the conditions outlined above can be used as an approximation to the real ψ. One of the simplest approximation is the *Slater determinant* (SD), which is a product of antisymmetric spin orbitals $\chi(x)$

$$\psi_{SD}(x_1, x_2, ..., x_n) = \frac{1}{\sqrt{N!}} \begin{vmatrix} \chi_i(x_1) & \chi_j(x_1) & \dots & \chi_n(x_1) \\ \chi_i(x_2) & \chi_j(x_2) & \dots & \chi_n(x_2) \\ & \vdots & & \\ \chi_i(x_n) & \chi_j(x_n) & \dots & \chi_n(x_n) \end{vmatrix} \quad . \tag{2.2.2}$$

The SD is composed in such way that along columns there is the same spin orbital, while on the rows the same electron. The $(\sqrt{N!})^{-1/2}$ is a normalization constant. It is convenient to use a short-hand notation for the ψ_{SD}, which includes the normalization factor and only shows the diagonal elements of the matrix

$$\psi_{SD}(x_1, x_2, ..., x_n) = |\chi_i(x_1)\chi_j(x_2)\chi_n(x_n)\rangle \quad . \tag{2.2.3}$$

Recalling the variational principle, we can use the SD as our wavefunction to search the lowest energy values. Minimizing the total energy under the normalization constraint means

$$\delta E_{HF} = \langle\psi_{SD}|\hat{H}|\psi_{SD}\rangle \quad . \tag{2.2.4}$$

The procedure of minimization leads to the final results that HF energy is

$$E_{HF} = \sum_i^N h_i + \frac{1}{2}\sum_i^N\sum_j^N (J_{ij} - K_{ij}) \tag{2.2.5}$$

where

$$\begin{aligned} h_i &= \int \chi_i^*(x)\Big[-\frac{1}{2}\nabla^2 - \frac{Z_a}{r_{ia}}\Big]\chi_i(x)dx \\ J_{ij} &= \int |\chi_i(x_1)|^2\frac{1}{r_{12}}|\chi_i(x_2)|^2 dx_1 dx_2 \\ K_{ij} &= \int \chi_i^*(x_1)\chi_j^*(x_1)\frac{1}{r_{12}}\chi_i(x_2)\chi_j(x_2)dx_1 dx_2 \quad , \end{aligned} \tag{2.2.6}$$

and the first term in Eq. 2.2.6 is the kinetic energy and the electron-nucleus contribution, while J$_{ij}$ and K$_{ij}$ are respectively the Coulomb and exchange integral, and they account for the electron-electron interactions. The minimization of Eq. 2.2.5 under the orthonormalization constraints leads to the single-electron *Hartree-Fock (HF) equations*

$$\hat{f}_i\chi_i = \varepsilon_i\chi_i \tag{2.2.7}$$

where the ε_i corresponds to the energies of different electronic states. Therefore, the main idea behind the HF method is to reduce the complicated N-variables SE into N single-electron equations. The $\hat{f}$ operator is named *Fock operator*

$$\hat{f}_i = -\frac{1}{2}\nabla^2 + \sum_a^{nuclei}\frac{Z_a}{r_{ia}} + V_{HF} \tag{2.2.8}$$

where the V$_{HF}$ is the Hartree-Fock potential. It represents the mean potential felt by the ith electron due to the N-1 remaining electrons. The advantage of such formulation is that the two-electron operators in Eq. 2.1.3 are now reduced to a one-electron operator V_{HF}

$$V_{HF} = \sum_{i}^{N} (\hat{J}_i - \hat{K}_i) \quad . \tag{2.2.9}$$

The V_{HF} then contains all electron-electron interaction, i.e, the classical Coulomb repulsion term, and the non classical exchange integral, which is the result of the antisymmetric behaviour of Slater determinant

$$\begin{aligned} \hat{J}_i f(x) &= \sum_{i}^{N} \int |\chi_i(x_2)|^2 \frac{1}{r_{12}} f(x_1) dx_2 \\ \hat{K}_i f(x) &= \sum_{i}^{N} \int \chi_i^*(x_2) \frac{1}{r_{12}} \chi_i(x_1) f(x_1) dx_2 \quad . \end{aligned} \tag{2.2.10}$$

Eq. 2.2.6 can not be solved analytically, on the contrary, it is solved using a *self-consistent field (SCF)* procedure. [59] In practice, one guesses a certain wavefunction so that integrals of the Fock operator are constructed, then a better wavefunction is obtained by the solution of Eq. 2.2.6, and this new wavefunction is used to construct the new Fock matrix. This procedure is repeated until a certain threshold of convergence is reached. The HF method is not employed in any relevant chemical applications, however, its ideas are at the basis of all modern quantum chemistry theories and codes. Indeed, as outlined in section 2.3, density functional methods also use an SCF procedure.

Another important aspect of HF theory is that the unphysical self-interaction of one electron with itself is elegantly sorted. [39, 59] This can be seen in the one electron system (hydrogen atom), where the Coulomb and the exchange integral in Eq. 2.2.6 are equal, and they then cancel out in Eq. 2.2.5.

2.3 Density Functional Theory

2.3.1 Electron Density

The wave function methods, like HF, provides useful insights into the description of electronic configurations through the use of the molecular orbitals (MOs) concept. However, one of the disadvantages of wave function methods is that we have to deal with a quantity that can not be experimentally observed, which leaves the computational chemist to adopt intuitive approximations to describe the real state of studied system. One example is the concept of frontier molecular orbitals (FMOs) analysis. Indeed, chemists often describe the molecular behaviour by using only valence electrons, which works for many organic cases, but it can not be sufficient for inorganic compounds where the contribution from inner electrons might be important.

An alternative way of describing physical systems is given by invoking the electron density concept. From early quantum mechanics laws, the Born interpretation of wavefunction states that the probability of finding a particle at a specific position is proportional to the square of its wavefunction. This postulate lays the foundations to the use of the electron density as variable in modern quantum chemistry. For an electron, such probability is indeed given by its electron density. For a N electron system, the electron density of finding any of the N electron within the volume element dr_1 with arbitrary spin while the other N-1 electron have arbitrary position and spin can be expressed as

$$\rho(r) = N \int ... \int |\phi(x_1, x_2, ..., x_N)|^2 ds_1 dx_2 ... dx_N \tag{2.3.1}$$

where the x variable represents both spatial and spin variables x = (r, σ(s)). The great advantage of using the electron density as variable is that it is a physical observable, for example, it can be measured by x-ray experiments. In addition, $\rho(r)$ possesses many properties which fully describe any physical system. Firstly, it is always a non negative function, and its integration gives the total number of electrons in the system

$$\int \rho(r) dr_1 = N \quad . \tag{2.3.2}$$

Since the nuclei are treated as positive point charges, they exert an attractive force that lets $\rho(r)$ reach local maxima on each atomic position (these are actually cusps because of the singularity in the V_{ne} term in the Hamiltonian), and it is recognized that the cusps are strictly related to the nuclear charge Z as follow

$$\lim_{r_A \to 0} \left[\frac{\partial \bar{\rho}(r)}{\partial r_A} - 2 Z_A \rho(r) \right] = 0 \quad , \tag{2.3.3}$$

where $\bar{\rho}(r)$ is the spherical average of the electron density.

2.3.2 Density Matrices and Holes

The usual Hamiltonian operator of Eq. 2.1.2 is the sum of one-electron operators and a two-electron operators, and its expectation value can be simplified by integrating the $\phi^*\phi$ product over the N-2 coordinates (the Hamiltonian is spin independent). This procedure gives rise to the concept of *reduced density matrices*. In particular, an important element in the development of the density functional theory is the *pair density (or 2nd order reduced diagonal spin-summed density matrix)*

$$\rho_2(x_1, x_2) = N(N-1) \int ... \int |\phi(x_1, x_2, ..., x_N)|^2 dx_3...dx_N \quad . \tag{2.3.4}$$

Eq. 2.3.4 gives the probability of finding a pair of two electrons of arbitrary spins within a dr_1dr_2 volume element while all the remaining N-2 electrons move around them. The use of the pair density allows us to better understand the consequences of the antisymmetry wave function and the Coulombic repulsion among electrons. To this end, let us introduce the *2nd order reduced density matrix* $\gamma(x_1^{'}x_2^{'}, x_1x_2)$

$$\gamma_2(x_1^{'}x_2^{'}, x_1x_2) = \\ N(N-1) \int ... \int \phi^*(x_1^{'}, x_2^{'}, ..., x_N)\phi(x_1, x_2, ..., x_N)dx_3...dx_N \quad . \tag{2.3.5}$$

Eq. 2.3.5 is nothing more than the full matrix form of Eq. 2.3.4. This density is antisymmetric with respect to the change of two coordinates

$$\gamma_2(x_1^{'}x_2^{'}, x_1x_2) = -\gamma_2(x_1^{'}x_2^{'}, x_2x_1) \tag{2.3.6}$$

and its diagonal form, i.e, when $x_1^{'} = x_1$ and $x_2^{'} = x_2$, leads to the pair density $\rho_2(x_1, x_2)$. In the particular case where $x_1 = x_2$, the antisymmetric condition returns the following expression

$$\rho(x_1, x_1) = -\rho(x_1, x_1) \tag{2.3.7}$$

which means that $\rho(x_1, x_1) = 0$, and thus the probability of finding two electrons with the same spatial and spin coordinates is zero. This condition derives directly from the Pauli exclusion principle , and it is usually referred to as *exchange (or Fermi) correlation*. For example, the exchange correlation is also included in Hartree-Fock theory due to the use of an antisymmetric Slater determinant. We now show that HF does not account for any Coulomb correlation, which, on the contrary, is included in the density functional theories.

Let us compute the pair density for a two-electron system with spin orbitals χ_1(x$_1$) = ϕ(r$_1$)σ_1(s$_1$) and χ_2(x$_2$) = ϕ(r$_2$)σ_2(s$_2$). This is equal to the quadrature of its SD

$$\rho_2^{HF}(x_1, x_2) = [|\chi_1(x_1)\chi_2(x_2)\rangle]^2 \tag{2.3.8}$$

which in expanded form is

$$\begin{aligned}\rho_2^{HF}(x_1, x_2) &= \chi_1(x_1)^2\chi_2(x_2)^2 \\ &+ \chi_1(x_2)^2\chi_2(x_1)^2 \\ &- 2\chi_1(x_1)\chi_2(x_2)\chi_1(x_2)\chi_2(x_1) \quad .\end{aligned} \tag{2.3.9}$$

The integration over the spins returns the probability of finding one electron at r$_1$ while the second one is simultaneously at r$_2$. Since the spin functions are orthonormal $\sigma_1(s_1)\sigma_2(s_2) = \delta_{12}$, in case the two electrons have different spin, the last term in Eq. 2.3.9 will be zero, and ρ_2^{HF}(r$_1$,r$_2$) = ρ_2(r$_1$)ρ_2(r$_2$), i.e., it is simply the product of the electron densities of the independent electrons. On the contrary, when $\sigma_1(s_1) = \sigma_2(s_2)$, the last term of Eq. 2.3.9 will not vanish, and the motion of the two electron is not totally uncorrelated from each other. Therefore, we have shown that within HF theory the motion of electrons with antiparallel spins is completely correlated because of the exchange correlation, whereas electrons with same spins do not possess any Coulombic correlation , i.e., in this last case the pair density would not vanish even if the two electrons had the same coordinates.

On the basis of the results obtained so far, we can intuitively think of the actual pair density as a quantity that is between the two extremes, i.e, the simple product of independent electron densities plus a factor that accounts for all the correlation corrections

$$\rho_2(x_1, x_2) = \rho_1(x_1)\rho_2(x_2)[1 + f(x_1, x_2)] \quad . \tag{2.3.10}$$

The $f(x_1, x_2)$ is called *correlation factor*, and it essentially incorporates all the non classical effects. By introducing the conditional probability we show the actual effect of the $f(x_1, x_2)$ on the pair density. From probability theory, the conditional probability is the probability of finding any electron at x$_2$ if there is already one known to be at x$_1$ ($P(A|B) = P(A \cap B)/P(A)$, with A and B two events)

$$P(x_1, x_2) = \frac{\rho_2(x_1, x_2)}{\rho_1(x_1)} \quad . \tag{2.3.11}$$

Eq. 2.3.11 integrates to N-1 electrons

$$\int P(x_1, x_2)dx_2 = N - 1 \quad . \tag{2.3.12}$$

Inserting the definition of pair density given in Eq. 2.3.10 into Eq. 2.3.12, and recalling that the $\int \rho_2(x_2)dx_2 = N$, it can be shown the following important integral condition applies

$$\int \rho_2(x_2)f(x_1, x_2)dx_2 = -1 \quad . \tag{2.3.13}$$

This condition is often called "*sum rule*", and its integrand *exchange-correlation hole*

$$\int h_{xc}(x_1, x_2)dx_2 = -1 \quad . \tag{2.3.14}$$

Eq. 2.3.14 shows that the integration of h$_{xc}$ has exactly the charge of one electron, and therefore, it indicates that there is a depletion of electron density at x$_2$. Such loss of electron density is due to the exchange and correlation effects, which are now incorporated in the definition of pair density, and this can more explicitly be expressed as

$$\rho_2(x_1, x_2) = \rho_1(x_1)\rho_2(x_2) + \rho_1(x_1)h_{xc}(x_1, x_2) \quad . \tag{2.3.15}$$

In the following sections we will illustrate the importance that $h_{xc}(x_1, x_2)$ had in the strategic development of better approximated exchange-correlation functionals.

2.3.3 Exchange and Correlation Holes

We now show the effect of the exchange-correlation hole on the N-body Hamiltonian. Since no actual differences are generated for the kinetic energy and electron-nuclear potential when computing the expectation value of Eq. 2.1.8, we can focus only on the electron-electron interaction. This latter term can be expressed as

$$V_{ee} = \left\langle \psi \middle| \sum_{i}^{N} \sum_{j>i}^{N} \frac{1}{r_{ij}} \middle| \psi \right\rangle = \frac{1}{2} \int \int \frac{\rho_2(r_1, r_2)}{r_{12}} dr_1 dr_2 \tag{2.3.16}$$

where we made use of the spinless pair density. If one inserts the expression of pair density given in Eq. 2.3.15 into Eq. 2.3.16, we obtain

$$V_{ee} = \frac{1}{2}\int\int \frac{\rho(r_1)\rho(r_2)}{r_{12}} dr_1 dr_2 + \frac{1}{2}\int\int \frac{\rho(r_1)h_{xc}(r_1,r_2)}{r_{12}} dr_1 dr_2 \quad . \tag{2.3.17}$$

The first term is the classical Coulomb repulsion, while the last term incorporates all the exchange and correlation effects. To give a practical example, let us analyse a system with a single electron, i.e., the hydrogen atom. In this case, the Coulomb term does not vanish because the two electrons are indistinguishable (*self-interaction error (SIE)*). However, if we knew the exact expression of the exchange-correlation hole, and recalling that $h_{xc}(r_1, r_2) \leq 0$, the second term is subtracted to the J[ρ] returning the correct answer that $V_{ee} = 0$. We can now see the great importance of the exchange-correlation hole, indeed, if its expression was known, the electron motion would be correctly described. As outlined later, unfortunately the exact expression of the h$_{xc}$ is not known, and approximated formulations need to be built.

It is customary to think of the exchange-correlation holes as the sum of the independent contribution of the exchange and correlation hole

$$h_{xc}(r_1, r_2) = h_x(r_1, r_2) + h_c(r_1, r_2) \tag{2.3.18}$$

where the first term reflects the effect of the use of antisymmetric wavefunction, while the second term is due to the Coulombic repulsion. Thus, the last term of Eq. 2.3.17 can be formulated as (the use of E$_{xc}$ is motivated by the connection with the exchange-correlation functional in section 2.3.5)

$$E_{xc} = \frac{1}{2}\int\int \frac{\rho(r_1)h_x(r_1,r_2)}{r_{12}} dr_1 dr_2 + \frac{1}{2}\int\int \frac{\rho(r_1)h_c(r_1,r_2)}{r_{12}} dr_1 dr_2 \quad . \tag{2.3.19}$$

The electron-electron potential can be concisely written as

$$V_{ee}[\rho] = J[\rho] + E_x[\rho] + E_c[\rho] \tag{2.3.20}$$

where the second and third term represent respectively the potential energy due to the exchange and correlation effect. Let us now analyse the properties of the exchange and correlation holes. As for the exchange-correlation hole, it can be shown that the exchange hole respects the sum rule

$$\int h_x(r_1, r_2) dr_2 = -1 \tag{2.3.21}$$

This condition reflects the fact that the conditional probability integrates to N-1 instead of N, since there is already one electron at position r_1. In addition, in the case of two electrons with same spin, the exchange hole has to be equal to minus electron density when r_2 tends to r_1

$$\int h_x(r_1, r_2 \to r_1)dr_2 = -\rho(r_1) \tag{2.3.22}$$

This condition is a direct consequence of the Pauli exclusion principle. A further property to be mentioned is that the it is negative everywhere: $h_x(r_1, r_2) < 0$. As consequence of Eq. 2.3.22 and 2.3.14, the correlation hole must respect the following integral condition

$$\int h_c(r_1, r_2)dr_2 = 0 \quad . \tag{2.3.23}$$

This conditions tells us that, since electrons with antiparallel spins can occupy the same position, the probability of having a density depletion must be zero. An important consequence is that when $r_2 \to r_1$, the probability of finding two electrons with different spins at the same position is not zero, and therefore, the $h_c(r_1, r_2)$ does not have a prefixed value. However, electrons with same spins can not occupy the same position, which is the reason why the electron density has cusps at nuclei positions. In contrast to the $h_x(r_1, r_2)$, these physical cases allow h_c to assume either positive or negative values.

2.3.4 Hohenberg and Kohn Theorems

Despite the first models of Thomas, Fermi, and Dirac, DFT did not have a robust theoretical formulation until Hohenberg and Kohn postulated their two theorems, which are the pillars of DFT as we know it today. [60, 61] The first theorem states that all we need to describe any physical system is to know its electronic density $\rho(r)$, while the second one illustrates the way to compute $\rho(r)$. In the following we discuss the two theorems and the consequences of their statements.

For any multi-particle system the number of particles N and its potential $v(r)$ entirely defines its Hamiltonian. The first Hohenberg and Kohn theorem states that for "*a multi-particle system the potential is uniquely described, within a trivial additive constant, by the electronic density*". [60, 61] This statement is a direct consequence of the fact that the $v(r)$ fixes the Hamiltonian, and in turn this latter gives the ground state density $\rho(r)$. The proof of the theorem is disarmingly simple, and makes use of the reductio ad absurdum. Let us assume that two different potentials $v(r)$ and $v^{'}(r)$, which differ by more than a positive constant, produce the same ground state density $\rho(r)$ of non-degenerate N-particle system. As such, the two potentials define two different Hamiltonians H and H', whose wavefunctions ψ and ψ' are also different. Taking the ψ' wavefunction as basis to compute the ground state energy of H system, E$_0$, we have from the variational principle

$$E_0 < \langle\psi^{'}|H|\psi^{'}\rangle = \langle\psi^{'}|H^{'}|\psi^{'}\rangle + \langle\psi^{'}|H - H^{'}|\psi^{'}\rangle \tag{2.3.24}$$

where the $\langle\psi^{'}|H^{'}|\psi^{'}\rangle$ has been added and subtracted to the $\langle\psi^{'}|H|\psi^{'}\rangle$ term. Since the two Hamiltionians only differ by their external potential, Eq. 2.3.24 becomes

$$E_0 < E_0^{'} + \int \rho(r)(v - v^{'})dr \quad . \tag{2.3.25}$$

The same procedure can be applied by taking the ψ wavefunction as basis for the energy of the $H^{'}$ system, E$_0^{'}$, which gives

$$E_0^{'} < E_0 + \int \rho(r)(v - v^{'})dr \quad . \tag{2.3.26}$$

The addition of Eq. 2.3.25 to Eq. 2.3.26 then returns

$$E_0 + E_0^{'} < E_0^{'} + E_0 \tag{2.3.27}$$

which is absurd, and therefore, the two potentials are equal and give the same $\rho(r)$ for the ground state. Thus, the ground state density determines N and the $v(r)$, and all properties of the system. This means that it is possible to express the energy of N-particle systems as functional of the $\rho(r)$

$$\begin{aligned} E_0[\rho] &= T[\rho] + V_{ee}[\rho] + V_{ne}[\rho] \\ &= F_{HK}[\rho] + V_{ne}[\rho] \end{aligned} \tag{2.3.28}$$

where the Hohenberg-Kohn functional $F_{HK}[\rho]$ is introduced. The $F_{HK}[\rho]$ contains all the information relative to the electrons dynamics, i.e., the kinetic energy $T[\rho]$, and the electron-electron interaction $V_{ee}[\rho]$, and it can explicitly be expressed as

$$F_{HK}[\rho] = T[\rho] + J[\rho] + E_{ncl}[\rho] \quad . \tag{2.3.29}$$

The $J[\rho]$ is the classical Coulomb interaction, while the $E_{ncl}[\rho]$ represents all non classical interactions arising from the electron motion, such as electron self-interaction, exchange and Coulomb correlation. The $E_{ncl}[\rho]$ expression is yet unknown, and its determination remains the main challenge in the development of DFT theories.

The second Hohenberg-Kohn theorem states that *for a trial density $\rho^{'}(r)$, provided that $\rho^{'}(r) \geq 0$ and $\int \rho^{'}(r)dr = N$, the ground state energy can be obtained from the minimization principle*, [60,61]

$$E_0 \leq E[\rho^{'}(r)] \quad , \tag{2.3.30}$$

where $E[\rho^{'}(r)]$ is the energy functional. The variational principle is normally applied by requiring that the ground-state density returns the total number of particles in the system

$$\int \rho(r)dr = N \quad . \tag{2.3.31}$$

The constraint can be incorporated by employing the Lagrange multipliers method, which then requires that

$$\delta\Big\{E[\rho] - \mu\Big[\int \rho(r)dr - N\Big]\Big\} = 0 \tag{2.3.32}$$

with μ Lagrange multiplier. This expression gives the Euler-Lagrange equation

$$\mu = \frac{\partial E[\rho]}{\partial \rho(r)} = V_{ne}[\rho] + \frac{\partial F_{HK}[\rho]}{\partial \rho(r)} \quad . \tag{2.3.33}$$

The quantity μ is the *chemical potential*, and it is a fundamental property to describe bonding, since it is related to the electronegativity of atoms. If we knew the exact expression of $F_{HK}[\rho]$, Eq. 2.3.33 would give the exact ground state electron density.

The variational principle provides the way to compute the ground state energy as it occurs in HF theory. We will see in the next chapter that the actual computation of the energy is performed through as self-consistent field approach. However, despite its elegant formulation, DFT as formulated so far hides many limitations. Firstly, the theory would be exact only if the $F_{HK}[\rho]$ expression was known exactly. In addition, the employment of the variation principle theoretically limits DFT application only to the ground state energies, and for this reason, further theoretical implications must be taken into account to describe excited states. Another direct consequence of the Hohenberg-Kohn theorems is that only v-representable densities are eligible for DFT calculations. This concept refers to the use of densities which are associated with an antisymmetric wave function and a Hamilton operator with an external potential. Unfortunately, it occurs that common systems, like the Hamiltoninan with ground-state wavefunctions more than doubly degenerate, do not satisfy the v representability requirement. Despite its theoretical importance, this aspect is less important in practical applications, where the less stringent N-representability condition is used. This latter only requires that a density must be related to an asymmetric wavefunction, which is normally the case for any reasonable density.

The formulation of Hohenberg and Kohn theorems leaves one open question: "how can the ground state wavefunction be obtained from its corresponding density ?". The answer to such question is given by the Levy constrained-search approach. From the variational principle the ground state energy is

$$E_0 = \langle \psi_0 | H | \psi_0 \rangle \leq \langle \psi_\rho | H | \psi_\rho \rangle \tag{2.3.34}$$

where the ψ_0 is the ground state wavefunction, while ψ_ρ is an antisymmetric wavefunction computed from the trial density ρ. Since the external potential only depends on the density, then we have

$$\langle \psi_0 | T + V_{ee} | \psi_0 \rangle + \int V_{ne} \rho_0(r) dr \leq \langle \psi_\rho | T + V_{ee} | \psi_\rho \rangle + \int V_{ne} \rho_0(r) dr \tag{2.3.35}$$

or more concisely

$$\langle \psi_0 | T + V_{ee} | \psi_0 \rangle \leq \langle \psi_\rho | T + V_{ee} | \psi_\rho \rangle \quad . \tag{2.3.36}$$

Thus, among all wavefunctions, the one that minimizes the $\langle \psi_\rho | T + V_{ee} | \psi_\rho \rangle$, it also gives the ground state ρ. If the density belongs to the v-representable class, then the right-hand side of Eq. 2.3.36 is equal to the F$_{HK}[\rho_0]$ in Eq. 2.3.29

$$E_0 = \min_{\rho_0 \to N} \left(F_{HK}[\rho_0] + \int V_{ne} \rho_0(r) dr \right) \quad . \tag{2.3.37}$$

Eq. 2.3.37 is a further proof of the first theorem of Hohenberg and Kohn, and it also eliminates the requirement of non-degenerate ground state. It must be noted that, although its less stringent formulation, as for the Hohenberg and Kohn, the application of the constrained-search method finds no practical use in common computational algorithms. [62]

2.3.5 Kohn-Sham Approach

The practical approach to determine the ground state density and its energy comes from the Kohn-Sham (KS) idea of accounting the kinetic energy, correlation and exchange effects in an indirect way. [60] Kohn and Sham invoked a fictitious reference system due to non-interacting electrons, [60, 63] whose Hamiltonian can be simply expressed as

$$\hat{H}_s = \sum_i^N -\frac{1}{2}\nabla^2 + \sum_i^N V_{ne}(r) \tag{2.3.38}$$

where the first term is the kinetic energy operator, while the second term is the external potential due to the nuclei configuration on each particle. Here the subscript "s" indicates the non-interacting system. For such system, there exists an antisymmetric determinantal ground-state wavefunction ψ_s that gives the kinetic energy and the ground-state density

$$T_s = \langle\phi_s|\sum_i^N -\frac{1}{2}\nabla_i^2|\phi_s\rangle \tag{2.3.39}$$

$$\rho(r) = \sum_i^N \sum_s |\phi_i(r,s)|^2 \quad . \tag{2.3.40}$$

Despite $T_s[\rho]$ is defined for any density ρ, it is, of course, not the correct energy functional for the real interacting system. To account for corrections to the energy functional, Kohn and Sham expressed the Hohenberg and Kohn functional as

$$F[\rho] = T_s[\rho] + J[\rho] + E_{xc}[\rho] \tag{2.3.41}$$

with

$$E_{xc}[\rho] = T[\rho] - T_s[\rho] + V_{ee}[\rho] - J[\rho] \quad . \tag{2.3.42}$$

Note that the $F[\rho]$ is theoretically equal to the $F_{HK}[\rho]$ defined in Eq. 2.3.29, if the density of the non-interacting system is v-representable, however, this difference is not important from a practical prospective. The quantity $E_{xc}[\rho]$ is the *exchange-correlation functional* and, besides the exchange and correlation effects, it also accounts for the kinetic energy correction. Thus, the Euler-Lagrange equation 2.3.33 becomes

$$\begin{aligned}\mu &= v_{eff}(r) + \frac{\partial T_s[\rho]}{\partial \rho} \\ &= V_{ne} + \frac{\partial J[\rho]}{\partial \rho} + \frac{\partial E_{xc}[\rho]}{\partial \rho} + \frac{\partial T_s[\rho]}{\partial \rho}\end{aligned} \tag{2.3.43}$$

where the v_{eff} is the *KS effective potential*, and the last term of Eq. 2.3.43 is defined as *exchange-correlation potential*

$$v_{xc}(r) = \frac{\partial E_{xc}[\rho]}{\partial \rho} \quad . \tag{2.3.44}$$

Eq. 2.3.43 is exactly applied to a non-interacting system under the external potential V$_{ne}$ = v_{eff}. Therefore, for a given v_{eff}, the solution of one-electron SE is

$$\Big[-\frac{1}{2}\nabla^2 + v_{eff}(r) \Big] \phi_i = \epsilon_i \phi_i \quad , \tag{2.3.45}$$

and gives the density $\rho(r)$ (Eq. 2.3.40). The KS idea is to solve the electronic problem in a self-consistent way. A trial $\rho(r)$ is guessed to build the $v_{eff}(r)$ from Eq. 2.3.43, then Eq. 2.3.45 is solved to generate a new density into Eq. 2.3.40, this new density is used to better approximate the $v_{eff}(r)$, and this process is repeated until the density does not reach the convergence within a certain threshold. The ground state energy can be computed by Eq. 2.3.28 from knowing Eq. 2.3.41.

Once again, it is important to emphasize that if the E$_{xc}[\rho]$ was known, the Kohn-Sham procedure would lead to the exact ground state energy. This provides a main difference with Hartree-Fock theory, whose formulation is approximated by definition because of the use of single Slater determinant as wavefunction. In contrast, the way the Kohn-Sham approach has been proposed so far is free from approximations, and it is therefore exact. The approximation comes into play only when an explicit formulation of the exchange-correlation functional has to be built. And, the central objective of modern density functional theories is to actually provide better approximations to the E$_{xc}[\rho]$ so that the uncertainties related to this are as little as possible. In the next sections, we give further details on E$_{xc}[\rho]$ functionals highlighting also their role in the present context.

2.3.6 The Adiabatic Connection

In the previous section, we saw that the KS method provides a self-consistent way to solve the many-body problem by approximating the exact exchange-correlation functional. There is no clear procedure that can help us to reach this final goal, however, there are some conditions that the approximated exchange-correlation functionals need to obey in order to properly describe the physical behaviour of atoms and molecules. In this regard, the concept of exchange-correlation hole outlined in section 2.3.3 can be considered as a tool to assess the reliability of E_{xc}.

In KS formalism the exchange-correlation functional is given by Eq. 2.3.42, and recalling the role of the exchange-correlation hole in Eq. 2.3.17, one can understand that the information on the difference of kinetic energy between the non-interacting and real system must be incorporated into the $\mathrm{h}_{xc}(\mathrm{r}_1,\mathrm{r}_2)$. To explain this, let us connect the non-interacting and real system by a coupling constant λ so that the Hamiltonian can be expressed as

$$\hat{H}_\lambda = \hat{T} + \hat{V}^{\lambda}_{ne} + \lambda \sum_{i}^{N}\sum_{j>i}^{N} \frac{1}{r_{ij}} \quad . \tag{2.3.46}$$

The λ has the role to switch between the non-interacting system, $\lambda = 0$, to the full-interacting system, $\lambda = 1$. This method is often called the *adiabatic connection*. Let us now compute the change in energy for this Hamiltonian. The differentiation of energy gives

$$\frac{\partial E}{\partial \lambda} = \left\langle \phi \middle| \frac{\partial H_\lambda}{\partial \lambda} \middle| \phi \right\rangle \tag{2.3.47}$$

$$E_{\lambda=1} = E_{\lambda=0} + \int_0^1 \langle \phi | V^{\lambda}_{ne} + \sum_{i}^{N}\sum_{j>i}^{N} \frac{1}{r_{ij}} | \phi \rangle d\lambda \quad . \tag{2.3.48}$$

This result is the well-known *Hellmann-Feynman theorem*. Using the hole formalism, Eq. 2.3.48 can be formulated as

$$\begin{aligned} E_{\lambda=1} = E_{\lambda=0} + \int \rho(r) V^{\lambda=1}_{ne} + \int\int \frac{\rho(r_1)\rho(r_2)}{r_{12}} dr_1 dr_2 \\ + \frac{1}{2}\int\int \frac{\rho(r_1) h^{\lambda}_{xc}(r_1,r_2)}{r_{12}} dr_1 dr_2 d\lambda \end{aligned} \tag{2.3.49}$$

Note that the density is independent from λ. Recalling that for $\lambda = 0$ (s subscript refers to the non-interacting electrons), the Kohn-Sham energy is

$$E_{\lambda=0} = T_s + \int \rho(r) V_s dr \tag{2.3.50}$$

and defining the *coupling-strength integrated exchange-hole* $\bar{h}_{xc}$ as

$$\bar{h}_{xc} = \int_0^1 h_{xc}(r_1, r_2) d\lambda \quad , \tag{2.3.51}$$

we arrive to the final expression for the energy of the real system

$$\begin{aligned} E_{\lambda=1} = T_s + \int \rho(r) V_{eff} + \int \int \frac{\rho(r_1)\rho(r_2)}{r_{12}} dr_1 dr_2 \\ + \frac{1}{2} \int \int \frac{\rho(r_1)\bar{h}_{xc}(r_1, r_2)}{r_{12}} dr_1 dr_2 \quad . \end{aligned} \tag{2.3.52}$$

One can now see that the exchange-correlation functional, which contains all the non classical effects, can be expressed in terms of $\bar{h}_{xc}$. A direct comparison with Eq. 2.3.17 illustrates that the correlation energy due to the kinetic energy is now included in the coupled exchange-correlation hole, $\bar{h}_{xc}$. Within this formalism, only the kinetic energy of non-interacting electrons must be computed, which is a relatively simple task. Whereas, a further degree of complexity is added to the exchange-correlation functional, since it also needs to account for the kinetic correlation corrections.

In practice, exchange-correlation functionals are developed in way that the integral conditions on the exchange-correlation hole are fulfilled. Despite the sum rules dictate the way to improve $\text{E}_{xc}[\rho]$ functionals, these conditions are not so stringent, and it turns out that some empirical exchange-correlation functionals provide good approximations to the real E_{xc} even if they largely violate the sum rules.

2.3.7 Local Density Approximation

One of the earliest exchange-correlation functional comes from the *local density approximation (LDA)*. The LDA is the basis of most modern functionals, since it is possible to know exactly or at least with high accuracy the exchange and correlation energies. In the LDA, the main idea is to treat the real system as an uniform electron gas, and the exchange-correlation functional can be written as

$$E_{xc}^{LDA} = \int \rho(r)\varepsilon_{xc}(\rho(r))dr \quad . \tag{2.3.53}$$

The corresponding exchange-correlation potential can then ben computed from Eq. 2.3.44

$$v_{xc}(r) = \varepsilon_{xc}(\rho(r)) + \rho(r)\frac{\partial\varepsilon_{xc}(\rho)}{\partial\rho} \quad . \tag{2.3.54}$$

The $\varepsilon_{xc}(\rho(r))$ can be further divided into the exchange and correlation contribution:

$$\varepsilon_{xc}(\rho(r)) = \varepsilon_{x}(\rho(r)) + \varepsilon_{c}(\rho(r)) \quad . \tag{2.3.55}$$

This approximation is particularly useful, since the exact exchange energy for a uniform electron gas had already been computed by Dirac in the 1930s

$$\varepsilon_x = -C_x\rho(r)^{1/3} \quad , \quad C_x = \frac{3}{4}\left(\frac{3}{\pi}\right)^{1/3} \quad . \tag{2.3.56}$$

Unfortunately, there is not analytical expression for the correlation energy, however, its accurate values are available thanks to quantum Monte Carlo (MC) simulations. [64] Further accuracy can be obtained by accounting for the spins polarization, which is particularly important for unrestricted systems. In this case the LDA energy functionals are computed for both spins $\rho_\alpha(r)$ and $\rho_\beta(r)$, and the LDA takes the name of *local spin density approximation (LSDA)*, and the exchange-correlation is

$$E_{xc}^{LSDA}[\rho_\alpha, \rho_\beta] = \int \rho(r)\varepsilon_{xc}(\rho_\alpha(r), \rho_\beta(r))dr \tag{2.3.57}$$

Eq. 2.3.57 differs from Eq. 2.3.53 only for the introduction of the densities for the different spins, while the exchange and correlation terms are the same for both $\rho_\alpha(r)$ and $\rho_\beta(r)$. Despite their crude approximation the local approximations (more generally the LSDA) work surprisingly well for many systems, whose density does not vary significantly, as for example in metals or single atoms. For instance, Lopez *et al.* showed that LDA functionals produce relatively good POM geometries due to their similar structure to extended metallic solids. [65] In this perspective, Wen *et al.* carried out LDA calculations to reveal the interaction between graphene and W-based Keggin POM, [66] showing that accurate binding energies can be extracted with this functional. More generally, the reason is due to the fact that in these systems the LDA exchange-correlation hole meets the integral conditions outlined in section 2.3.3, and therefore, h_{xc}^{LDA} is very close to the real exchange-correlation hole.

2.3.8 Generalized Gradient Approximation

From the previous section we see that the addition of corrections from taking into account both α and β densities improves the LDA energy. This idea paves the way to a strategic procedure to improve the approximation of the E$_{xc}$, and it is at basis of a concept coined by J. Perdew, i.e., the so-called *Jacob's ladder*. [3] This is shown in Fig. 2.3.1. Following this idea, the logic further step in the improvement of density functionals is the inclusion of the gradient of the electron density. If we image to expand the electron density in Taylor series and stop to the gradient term, the resulting exchange-correlation functional looks like

$$E_{xc}^{GEA} = \int \rho(r)\varepsilon_{xc}(\rho(r))dr + \int b_{xc}(\rho)\frac{|\nabla\rho(r)|^2}{\rho^{4/3}}dr \quad , \qquad (2.3.58)$$

where b$_{xc}$ is a parameter. This expression is called *Generalized Expansion Approximation (GEA)*. It can be proven that the GEA provides the good E$_{xc}$ for slow-varying density systems. However, the real density quite never behaves in this way, and the GEA performs even worse than the LDA approaches. The actual reason of GEA failure is largely due to the fact that the exchange-correlation hole related to Eq. 2.3.58 violate two of the three sum rules outlined in the section 2.3.3.

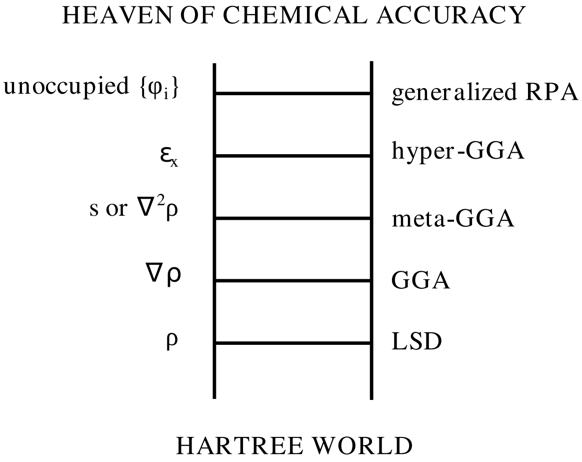

Figure 2.3.1: Jacob's ladder for DFT functioanals as described in Ref. [3]

In order to respect the hole constraints, the GEA exchange-correlation functionals are truncated. These new types of functionals are named *Generalized Gradient Approximations (GGA)*, and take the following form

$$E_{xc}^{GGA} = \int \varepsilon_{xc}(\rho(r), F_{xc}(s))dr \quad , \quad s = \frac{|\nabla\rho(r)|}{\rho^{4/3}} \qquad (2.3.59)$$

where the F_{xc} is the *reduced density gradient*, and s is a measure of the inhomogeneity of the system. From Fig. 2.3.2, one can visually grasp the difference due to the truncation. It can be seen that the h_x^{GEA} becomes positive at high value of z, while this is avoided in the GGA by truncating it so that the sum rules are respected. Also, since the truncation of the GGA slices out some hole region, the GGA hole becomes more negative than the GEA at small z because its normalization integral needs to be -1. The s variable assumes

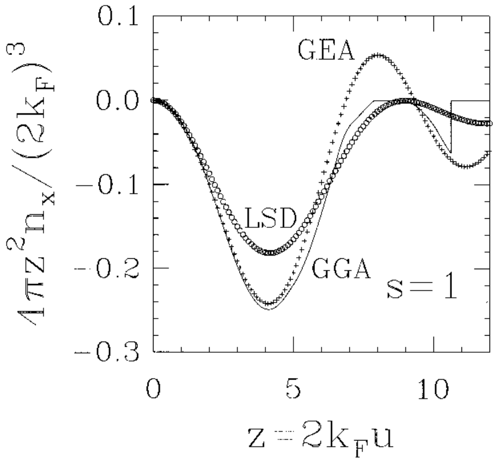

Figure 2.3.2: Spherically averaged exchange hole density h_x (here indicated as n_x) as function of dimensionless separation, z = $2k_F$u (u = r-r'), for s = 1 in LSD (circles), GEA (crosses), and GGA(solid line). This image was taken from Ref. [4]

large values for large gradients, as for example, near the nuclei, while it gets small values in bonding regions, where gradient is small. It is important to understand that there is not exact form for the F_{xc}, however, two main formulations are currently supported. The first class is related to first works of Becke (B88), [67] and they make use of empirical parameters to be fitted, while the second types do not need any parameters. Among these latter the PBE functional is one of most famous ones. [4] It is worth mentioning that the form of the reduced gradients is not easy to understand in terms of physical observations.

Lopez *et al.* showed that GGA functionals provide an accurate description of electron density as well as of reduction potentials for pure and substituted Keggin POM. [14, 49] Similarly, GGAs predict good geometries and redox potentials for pure Wells-Dawson POMs. [20] However, they showed that, since GGA functionals tend to overdelocalize electron density by nature, they cannot correctly describe extra electrons in substituted Wells-Dawson POMs. Therefore, the redox potentials computed with GGAs are far from reproducing the experimental data. [45] In contrast to Wells-Dawson types, Kremleva *et al.* showed that redox potentials of a tri-Mn-substituted W-based Keggin ion are better described by PBE compared to hybrid-GGA functionals (discussed below). However, the author claims that the reason of this good performance is due to fortuitous error cancellation. [46] From the above arguments, it can be understood that, despite GGAs might give accurate responses, it is advisable to test them against more accurate functionals.

2.3.9 Hybrid Functionals

A direct look to the adiabatic connection method, Eq. 2.3.48, suggests that the correct exchange-correlation functional can be obtained by computing it over all intermediate λ states

$$E_{xc} = \int_0^1 E_{ncl}^{\lambda} d\lambda \quad . \tag{2.3.60}$$

This task is not simple due to the fact that we can only approximate the exchange and correlation energies at end points (λ = 0, and 1). However, at λ = 0, we know exactly the exchange energy, since this is purely due to the non-interacting electrons, and at the same time we are able to approximate the E$_{xc}$ at λ = 1 by any DFT functionals, such as those from LDA or GGA methods. Eq. 2.3.60 can then be computed by assuming that the E$_{ncl}^{\lambda}$ has some empirical dependence on λ. A better understanding can be grasped from a geometric representation, as illustrated in Fig. 2.3.3. In this picture, the correct exchange-correlation functional corresponds to the exact E$_{xc}^{HF}$ (black box on the bottom) plus a fraction of the difference between the E$_{xc}^{DFT}$ and E$_{xc}^{HF}$.

$$E_{xc} = E_x^{HF} + z(E_{xc}^{DFT} - E_x^{HF}) \quad . \tag{2.3.61}$$

Usually, such fraction is expressed through $a = 1 - z$, and Eq. 2.3.61 turns into

$$E_{xc} = (1 - a)E_{xc}^{DFT} + aE_x^{HF} \quad . \tag{2.3.62}$$

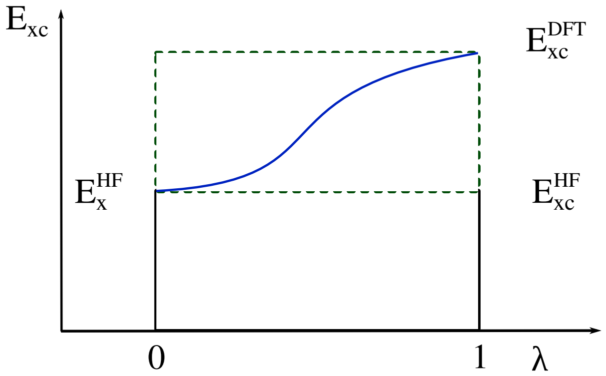

Figure 2.3.3: Geometric interpretation of Eq. 2.3.60. The integral is equal to the the exact HF exchange-correlation functional plus a fraction, z, of the difference between the big box (black plus green) and the one on the bottom (black). [5]

In the simplest approximation, $a = 0.5$. If the E_{xc}^{LDA} is used, Eq. 2.3.62 is the so-called *half-and-half (HH)* functional derived by Becke in the 1993. [68] Despite the crude approximation, the HH functional has an error of about 6 kcal/mol, which is relatively low for many chemical purposes. As such, one might wonder whether the addition of further parameters can lead to better results. These motivations lead to the development of a plethora of empirical exchange-correlation functionals during the 90's and early 2000's. Here, we just mention the B3LYP, [68] which has become by far the most popular exchange-correlation functional in quantum chemistry. In the B3LYP, the first letter refers to the use of B88 exchange-functional, [68] while the three stands for the number of parameters to be fitted. The LYP part instead indicates that the LYP correlation functional is employed. [69] Its full expression is defined as

$$E_{xc}^{B3LYP} = (1-a)E_x^{LSDA} + aE_x^{HF} + b\Delta E_x^{B88} + cE_c^{LYP} + (1-c)E_c^{LSDA} \quad (2.3.63)$$

The large popularity of the B3LYP is due to the fact that its absolute error is reduced to only 2-3 kcal/mol ($a = 0.2$) when computing many properties. [5, 68] Other authors developed hydrid functionals that are not "dependent" on empirical parameters, and the fraction of E_{xc}^{HF} is chosen on the basis of purely theoretical arguments. One example is given by PBE0, [70] which accounts for $a = 25\%$ of E_x^{HF} (despite a is not optimized, it still enters as parameter in the formulation of the hybrid functional)

$$E_{xc}^{PBE0} = E_x^{GGA} + 0.25(E_x^{HF} - E_x^{GGA}) \quad (2.3.64)$$

It is worth noting that the $a = 20\text{-}25\%$ of HF exchange-correlation functional seems to be the panacea for hybrid exchange-correlation functionals in many applications.

In constrast to GGAs, hybdrid-GGAs tend to localise more electron density because of exact HF exchange. This also applies to POMs. For example, Aparicio *et al.* showed that B3LYP is the best functional to compute electron (de)localization and redox potentials of mono-substituted P_2MW_{17} compounds. [45] Better performances of B3LYP over the PBE were also observed for redox potentials of Keggin ions in solution. [47]

On the basis of the comments from the previous section, and the above arguments, it is clear that different levels of accuracy are given by different functionals depending on the property under investigation. Therefore, we decided to use both pure GGA and hybrid-GGA functionals throughout this work. Specifically, we employed both types of functionals whenever an accurate description of electron density, and its related properties (like redox potentials), was needed. For instance, this is the case for all static DFT calculations reported in the next chapters. On the other hand, we only employed PBE when performing QM/MM studies in solution. This choice is motivated by the low computational cost of PBE compared to hybrid-GGAs, which become almost prohibitive for large systems like POMs in solution. [39,48]

2.3.10 Self-Interaction Error

As shown so far, the main challenge in DFT is the computation of the exchange-correlation functional. As such, different exchange-correlation functionals can lead to different answers for a same physical problem. In addition to this, the theory presents another substantial issue, i.e., the so-called *sel-interaction error (SIE)*. If we take the hydrogen atom as example, which contains one electron, we can clearly see the flaws of DFT approaches due to the SIE. The KS energy is

$$E[\rho] = F[\rho] + V_{ne}[\rho] = T_s[\rho] + J[\rho] + E_{xc}[\rho] + V_{ne}[\rho] \quad . \tag{2.3.65}$$

For one-electron system in the HF approach, the Coulomb term $J[\rho]$ cancels out with the exchange integral so that there is not any unphysical self interaction. This is no longer true within the KS-DFT approach, since the exchange-correlation functional is only approximated, and therefore, the difference between $J[\rho]$ and $E_{xc}[\rho]$ will not vanish. The necessary requirement to exclude the self-interaction is obtained by enforcing the condition that the electron-electron term in the Hamiltonian must be zero for a single electron

$$V_{ee}[\rho] = J[\rho] + E_{xc}[\rho] = 0 \quad . \tag{2.3.66}$$

This idea was firstly applied by Perdew and Zunger, [71], who proposed a correction to the SIE in their *self-interaction corrected DFT (SIC-DFT)* approach. Within this approach the resulting external potential is dependent on the molecular orbitals, which leads to non-orthogonal orbitals. The orbital-dependence of the external potential is hardly implemented in quantum chemistry codes, and this is the reason why SIC-DFT theories did not take off in modern quantum chemistry codes. In addition, SIC-DFT functionals often perform worse than the common functionals for the standard tests, like thermochemistry and geometries.

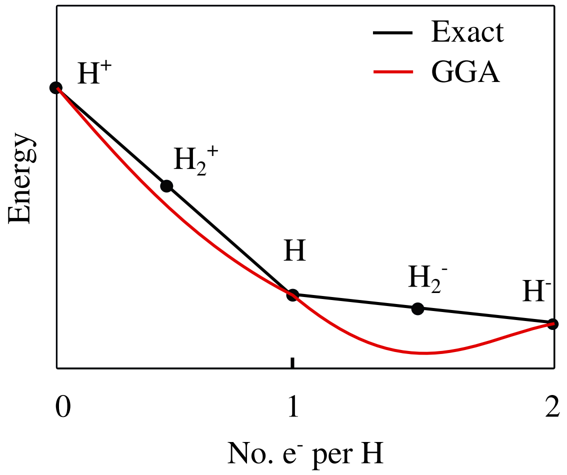

Figure 2.3.4: Schematic representation of energy vs number of electrons per H atom, including also the stretched molecules H_2^+ and H_2^-.

The SIE specifically refers to a one-electron problem. In the case of a many-electron system, it is better replacing the SIE idea with the *delocalization error (DE)*. The DE concept comes from the fractional charge approach developed by Perdew *et al.*, who showed that the energy of system with N electrons varies linearly with fractional electron charge δq, but it has derivative discontinuity at integers values(Fig. 2.3.4). [62] Unfortunately, common DFT functionals have continuous derivatives, and two situations can occur. If the approximate functional has a convex behaviour, it will give too low energies, and/or tend to delocalise charge distribution over integers (delocalised error). For this reason, the DE can be defined as the negative deviation of the E(N) curve from the exact linearity condition for fractional charges. Vice versa, functionals with concave energy, like HF, will give higher energy, and predict too localized charge distribution (localized error).

Large DE deviations are already obtained for small systems. For example, for stretched H_2^+ (one electron) both LDA and GGA functionals give more negative binding energy with large error of 50-60 kcal/mol. [72] The origin of such strong SIE is due to the incapability of approximate functionals to correctly delocalise the exchange-correlation hole as the molecule stretches, and therefore, half an electron is localized over each proton.

Furthermore, if a third proton is added far way to the largely stretched H_2^+. From a chemical point of view, we should have one hydrogen atom and two protons, however, functionals, like the GGAs, take into consideration the possibility to put a third of an electron on each proton. This will further drop the energy, and give rise to a too delocalised electron density.

Early DFT computations on POMs were carried by not neutralising their charge, and therefore, a strong SIE (or DE) is to be expected for these calculations. [20, 45, 49] One easy solution is to add as many counter ions as the total charge of POM. In this regard, Kremleva *et al.* showed that the distribution of a relatively small number of counter ions does not influence the electronic structure and relative energies of POMs. [46, 47] Therefore, we decided to carry out our simulations by neutralising the POM charge with a sufficient number of counter ions. This was not possible for the redox potentials in solution (Chapter 3) because of the formalism of free energy sampling techniques.

2.4 Basis Sets

One of the approximations made in any quantum chemistry method is the use of a basis set (BS). A BS refers to a set of functions used to approximate any wavefunction in quantum chemistry methods like HF or DFT. It is worth noting that the expansion of wavefunction with a BS would not be an approximation, if the BS is complete, i.e., it contains an infinite number of functions. However, this is impossible in actual calculations, and the electronic wavefunction is approximated by a finite number of functions constituting BS. The accuracy of a BS depends on several factors, for instance, the smaller is the BS, the poorer is the representation. The type of basis functions also influences its performance. These factors are extremely important due to their role into the computation of integrals, and therefore into the speed of computation.

The most commonly used types of BS are two: the Slater Type Orbitals (STOs) and Gaussian Type Orbitals (GTOs). STOs can be expressed in terms of polar coordinates as

$$\chi_{z,n,l,m}(r,\theta,\phi) = NY_{l,m}r^{n-1}exp(-\zeta r), \quad , \tag{2.4.1}$$

where N is a normalization constant, $Y_{l,m}$ are the spherical harmonics, and r^{n-1} is the radial part. The exponential dependence on the distance between the nucleus and electron stems from the exact solution of the hydrogen atom. GTO has a similar expression,

$$\chi_{z,n,l,m}(r,\theta,\phi) = NY_{l,m}r^{2n-2-l}exp(-\zeta r^2) \quad . \tag{2.4.2}$$

The gaussian shape of Eq. 2.4.2 makes GTOs less accurate than STO. At nucleus GTO has zero slope, in contrast to STO which has a discontinuous derivative (cusp), and GTOs consequently have problems representing the proper behaviour near the nucleus. Another problem is that GTOs fall off too rapidly far from the nucleus with respect to STOs, and the ends of the wavefunction are then poorly represented. In general, a high number of GTOs need to reach the same accuracy of STO representation. Despite these differences, GTOs are mainly used in modern calculations, since they offer a fast computation of one- and two-elctron integrals over STOs. Therefore, to better represent the cusp in the electron density of at nuclei, and at the same time have fast computations, the current GTOs are constructed from a fixed linear-combinations of Gaussian functions, contracted GTOs (CGTO).

As mentioned above, the number of functions used determines the accuracy of BS. The smallest number of functions possible is referred to as *minimum basis set*. This employs only the functions corresponding to all electrons of a neutral atom. For example, for the hydrogen this means a single s function, whereas for the first row elements it is two s-functions (1s and 2s) plus p functions (2p$_x$, 2p$_y$, 2p$_z$). The minimum basis set is in most cases not sufficient. A further improvement is obtained by doubling the minimum basis functions, producing a Double Zeta (DZ) basis set. A DZ consists of two s-functions for hydrogen, four s-function plus two sets o p-functions for the first row elements, and six s-function plus four sets of p-functions for second row elements. A higher number of functions can be added producing the Triple Zeta (TZ), or even the Quadruple Zeta (QZ) basis set, containing respectively three and four times as many functions as the minimum basis. Usually, the addition of core orbitals would rarely be considered, and in this case only the terms of valence orbitals are increased, turning DZ, TZ, and QZ into the so-called split valence basis (VDZ, VTZ, and VQZ). Additional improvements can be obtained by adding *polarizing* functions, which are extremely important into the description of the chemical bonding. Examples are the additions of p orbitals to the hydrogen, and d-orbitals to p functions. [5] A single set single set of polarization functions to the DZ gives the Double Zeta plus Polarization (DZP) type basis, while if two sets of polarization functions are added to a TZ basis, a Triple Zeta plus Double Polarization (TZ2P) type basis is generated.

Different family of BS exists, the Pople family is probably the most famous one. This is indicated as k-nlmG basis set, with k indicating how many GTOs are used for the core orbitals, while the nml indexes give how many functions the valence orbitals are split into, and how many GTOs are used for their representation. For example, for 6-31G the core orbitals are a contraction of six GTOs, the inner part of the valence orbitals is a contraction of three GTOs and the outer part of the valence is represented by one GTO.

Throughout this work, we employed the R. Ahlrich basis set, namely, the def2-SVP (double zeta) and def2-TZVP (triple zeta) basis sets. [73] These are contracted split valence basis sets containing polarization functions for both s- p- and d-orbitals. These basis sets are more reliable than the split-valence Pople basis sets for DFT calculations as shown in Ref. [73] Lopez *et al.* showed that a double zeta BS is sufficient to reproduce accurate electronic and molecular structures of different POM types, however, a triple zeta is needed to accurately describe specific properties such as NMR shifts. [14] On the other hand, Bonchio *et al.* found that there is a little difference in energy between the two basis sets when studying a substituted W-based Keggin ion. [74] These discrepancies in the literature, and the high computational cost associated with the use of larger basis sets makes the identification of the fastest and most accurate BS for POM applications difficult, and therefore, it is recommended to test different BSs for each POM type.

The above BSs work for many purposes, however, the number of core electrons of heavy elements can be quite high, and so will be the relative computational cost. Besides the number of core electrons, the inclusion of relativistic effects further increase the computational time. An easy solution is offered by the *Effective Core Potentials (ECP)* (or Pseudopotential). The construction of ECP is quite laborious, however, the key idea is to compute the all-electron wafunction for an atom from the Dirac-Fock equation, [75] and then replace the core potential by a potential parameterized which is expanded into a suitable set of analytical functions (spherical Bessel or Gaussian functions). The parameters of the approximated wavefunction are then fitted such that it matches the original all-electron wavefunction. For transition metals, the (n + 1)s-, (n + 1)p- and (n)d-orbitals usually constitute the valence orbitals, while all other remaining orbitals are treated by ECP. This approximation gives reasonable results, however, a larger (lower) number of electrons can be added (subtracted) to this set. Returning to POMs, since these molecules contain many heavy transition metals, it is clear that the use of ECP would help to speed the calculations. Therefore, as outlined in the next sections, we employed the family of ECPs alongside the Ahlrich basis set to describe the innermost and valence electrons of POMs. [73,75]

2.5 Molecular Dynamics in a Nutshell

In this section, we give a brief introduction to the broad topic of classical molecular dynamics (MD). MD successfully describes complex systems by extracting their macroscopic information from the dynamics of their microscopic components (atoms and molecules). In contrast to the quantum mechanical methods, classical MD neglects the electronic motion, and treats any atom (electron plus nucleus) as hard spheres obeying the Newton equation of motion. Specifically, the electronic features are implicitly taken into account by assigning structural parameters, atomic charges, or even dipoles to atoms and bonds so that it is possible to distinguish atoms in different chemical environments.

These assumptions allow the study of large systems (over ten thousands of atoms) over long time scales (normally up to microseconds), and thus, macroscopic observables can be obtained as statistical average of their value along the simulation. In the next sections, we will discuss the principles of MD, and illustrate how these simulations can be used to theoretically investigate the properties of POMs.

2.5.1 Classical Statistical Mechanics

From quantum mechanics, we know that any observable O can be obtained as $\langle O \rangle = \langle \psi | \hat{O} | \psi \rangle$. In classical mechanics, the analogous quantity can be obtained by averaging O over all phase space. In the microcanonical ensemble (also called NVE ensemble), where the constraints, that the number of particles, N, the volume V, and the energy of the system E, are constant, this average is expressed as

$$\begin{aligned}\langle O\rangle &= \frac{\int O(q,p)e^{-E/k_BT}dq^N dp^N}{\int e^{-E/k_BT}dq^N dp^N} \quad , \\ Q &= \int e^{-E/k_BT}dq^N dp^N\end{aligned} \tag{2.5.1}$$

where q and p are respectively the coordinates and the momentum of a N-particle system, k$_B$ is the Boltzman constant, and Q is the partition function. The integration of Eq. 2.5.1 is performed over $dq^N dp^N$, which is called phase space and it represents all possible configurations that can be taken by a molecular system. Note that we will focus only on the NVE ensemble, however, the same arguments are valid for other ensembles.

Eq. 2.5.1 is the main tool to connect the microscopic behaviour of a system to its macroscopic response. More correctly, the exponent of the partition function should be replaced by its Hamiltoninan (H = T + V), however, the kinetic and the potential energy can be separated. For non-interacting particles the Hamiltonian is purely kinetic, and system is considered as an ideal gas. Therefore, the interesting component is the potential part, whose form is approximated by force field types as described in the Section 2.5.4. All other thermodynamic functions can be computed from Q, for example, the internal energy U and Helmholtz free energy (A = U - TS) are expressed as

$$\begin{aligned}U &= k_BT^2\left(\frac{\delta Q}{\delta T}\right)_V \quad , \\ A &= -k_BTlnQ \quad .\end{aligned} \tag{2.5.2}$$

Other macroscopic observables, such as enthalpy H, entropy S, pressure P and heat capacity at constant volume may be calculated as derivatives of the thermodynamic functions in Eq. 2.5.2. In practice, Eq. 2.5.1 is unusable because all possible microstates should be known. However, the *ergodicity principle* states that the average value of a function of coordinates and momenta of a many-body system can be either computed by time averaging or ensemble averaging

$$\langle O\rangle = \lim_{t\to\infty}\frac{1}{t}\int_0^t Odt = \lim_{N\to\infty}\frac{1}{N}\sum_i^N O_i \quad . \tag{2.5.3}$$

This has an important practical consequence, that is, in the limit of sufficiently long dynamics, the integral can be replaced by a sum, and the observable O can be simply computed by summing its value at each time (a frame of the MD), and then divided by the length of the simulation. This is what is actually done by any common MD program. As result of this, for instance, the Helmholtz free energy can be now calculated as an average over a corresponding microscopic quantity

$$A = k_B T ln \left(\frac{1}{N} \sum_{i}^{N} e^{-E/k_B T} \right) = k_B T ln \langle e^{-E/k_B T} \rangle_N \quad . \tag{2.5.4}$$

Each average value has its relative statistical uncertainty, which is the square root of the variance σ^2:

$$\sigma(O) = \sqrt{\frac{1}{N} \sum_{i}^{N} (O_i - \langle O \rangle)^2} \quad . \tag{2.5.5}$$

From Eq. 2.5.5 one can see that increasing the sample size reduces the standard deviation, however, the calculated average might be affected by strong systematic errors if the configuration is not close to the true system. Provided the initial configuration is reasonable, Eq. 2.5.5 is also a measure of how well a MD simulation converges to the desired results, i.e. if its value is small enough the dynamics has reached the equilibrium. The ergodic hypothesis makes MD simulations an actual powerful tool that connect the microscopic behaviour to macroscopic results, however, it hides two major issues. The simulations have a finite time length, which is dictated by the real computational resources, and secondly, the potential energy used to describe any physical system is only approximated. The first problem is strictly related to the computational resources at disposal. In this regard, the current CPUs (central processing units) usage might be the rate-determining step for long simulations, and therefore, new technologies are needed. One example is given by running long MD runs on graphics processing units (GPUs), which perform better than common CPUs. [76] Another intuitive consequence of the ergodic principle is as follow. If we run two sufficiently long simulations of the same system but with different initial structural configurations, it turns out that the final states of these two runs lead to different final structures but this is in contrast with what Eq. 2.5.3 says. This is normally called phase-space sampling (equilibration) issue, where the simulated potential energy profile is limited only to certain region of the phase-space close to its initial structure.

The sampling problem is currently one of the major challenge in MD simulations. For example, its effect is significant for biomolecules, like proteins, which often possess intricate energy profiles with deep local minima that limit the exploration of the full energy landscape. [7] Several solutions have been proposed, and they can all be grouped in the so-called *enhanced sampling techniques*. Further description of these latter can be found in Ref. [7] Electronic structure calculations have shown that POM structures are not affected by redox reductions unless in super-reduced states. [37, 48] This behaviour and the rigidity associated with their molecular shapes allow POMs to preserve their initial conformation. [14, 53, 77] From a theoretical prospective, this means that, unlike proteins, there might be just few or even one energy minima when modelling a single POM, and therefore, the use of enhanced samplings is not necessary. In contrast, this might become important when dealing with more POMs in solution, like when studying their aggregation process. For example, in Chapter 5, we discuss the agglomeration of Wells-Dawson POMs, and we expect that these methods can give us more insights into the understanding of the key factors controlling their agglomeration.

Besides the enhanced sampling algorithms, another alternative is represented by using quantum mechanical MD. Essentially, two main techniques exist: the QM/MM methods (see next section), and full *ab initio* MD. These methods solve only half of the sampling issue. Indeed, their advantage is to correctly describe potential energy surfaces, since the interatomic interactions are computed directly from the electronic structure "on the fly", thereby allowing chemical bonding breaking and forming events. However, the time length of the simulations is significantly limited (up to pico seconds) due to the incredible computational cost required by the current resources. Returning to POMs, we made use of one of these methods, i.e. QM/MM, to accurately follow the change of their electronic and molecular structure as explained in Section 2.6. This has a great advantage over a full AIMD, since it allows the explicit treatment of a sufficiently large number of solvent molecules.

2.5.2 Canonical and Isothermal-Isobaric Ensemble

The above arguments have been discussed for a microcanonical ensemble (NVE), whose number of particles N, volume V, and total energy E are conserved. Although MD simulations can reproduce a microcanonical ensemble, the evolution of any real physical system often occurs at a certain constant temperature or pressure, and therefore, it is recommended to reproduce MD simulations that respect such conditions.

In the NVE ensemble, the instant value of the temperature is given by the average of the kinetic energy as

$$\langle T_{kin} \rangle = \frac{1}{2}(3_{atoms} - N_{constraints})k_B T \quad . \tag{2.5.6}$$

Since the kinetic energy is the difference between the total energy (almost constant) and the potential energy, which depends on the positions of atoms, the kinetic energy will vary significantly, and so will the temperature. In contrast, the canonical ensemble (NVT) allows to perform MD simulations by keeping the temperature fixed. One way to do this is to scale the atomic velocities by a certain factor such that the temperature corresponds to the desired value (*v-scaling*). This approach, however, might lead to instabilities, and the simulations might not longer correspond to a canonical ensemble. Alternatively, the system may be coupled to a "thermal bath", which gradually adds (removes) energy to (from) the system with a suitable time constant, often called a thermostat (*Berendsen thermostat*). [78] However, despite it simplicity and efficiency with which it relaxes a system to some target temperature, it does not generate a correct canonical ensemble. For this reason, most NVT simulations are performed with the Nosé-Hoover method which correctly produces a canonical ensemble. [79] Throughout this work, we used this last method to keep the temperature fixed. More specifically, we performed NVT simulations by heating any system up to 1000 K, followed by a slow temperature decrease down to 300 K. This approach helps the system to relax, and thus reach the equilibrium. Another important ensemble is the isothermal-isobaric ensemble (NPT), within which both temperature and pressure are kept fixed. The above arguments for keeping the temperature constant are also valid for the pressure. In practice, the Nosé-Hoover method can be used to reach a desired pressure. [79] The trajectory from the NPT ensemble is often used as final product for the computations of all relative properties. The reason is that it corresponds most closely to experimental conditions, which are subject to constant temperature and pressure. The NPT ensemble has been used as final product for all MD simulations presented later on.

2.5.3 The MD Engine

The momentum p_i and the position r_i of a particle of mass m$_i$ are classically described by the Newton equation

$$F_i = m_i \ddot{r}_i \tag{2.5.7}$$

or can equally be expressed by the Hamiltonian equations of motion (EOM)

$$\begin{cases} \dot{r}_i = p_i/m_i \\ p_i = -\nabla U = f_i \end{cases} \tag{2.5.8}$$

In MD, these 3N equations (or equivalently 6N) are numerically solved for each particle at each time step. Before discussing the common algorithms to solve the equation of motions, it is worth discussing the requirements for an ideal algorithm. Firstly, the EOM are reversible in time, therefore, once solved the trajectory of a system by changing the sign of position and momentum, we should be able to trace back their dynamics. Secondly, the motion of particles in Eq. 2.5.8 depends upon the spatial derivative of the potential. This might be appear as an obvious statement but, since in MD simulations the potentials are approximated in different ways (see next section), it means that trajectories of a same system treated by two different potentials might differ from each other. Therefore, care must be taken in the choice of the potential form. For example, the potential energy must be a continuous function of particle position, and this latter does not have to vary too drastically with time. Another important criterion is that the algorithm must be symplectic, i.e., it must preserve the energy (Hamiltonian) of the system throughout the simulation. For example, many high order numerical approaches such as the Runge-Kutta methods are not symplectic and therefore generate large energy deviation from one step to the successive one. [7] On the other hand, lower order methods, like the Verlet and the Leapfrog algorithms, respect the aforementioned requirements, and they are the common choice for many modern MD programs.

In practice, the user chooses a sufficiently small time step δt (normally $\delta t \leq 0.4$ fs) and specific boundary conditions, and the algorithm returns the position and the velocities at each successive time $(t + \delta t)$. Let us now take a closer look at the Verlet algorithm. The addition of the Taylor series of the position time-stepped forward $r(t+\delta t)$ and backward of $r(t-\delta t)$

$$\begin{aligned} r(t+\delta t) &= r(t) + \delta v(t) + \frac{1}{2}\frac{f(t)}{m}\delta t^2 + O(\delta^3) \\ r(t-\delta t) &= r(t) - \delta v(t) + \frac{1}{2}\frac{f(t)}{m}\delta t^2 + O(\delta^3) \quad , \end{aligned} \tag{2.5.9}$$

gives the final expression of the Verlet algorithm [80]

$$r(t+\delta t) = 2r(t) - r(t-\delta t) + \frac{f(t)}{m}\delta t^2 \quad . \tag{2.5.10}$$

Note that the current and previous position of particle must be computed to calculate the new position. In practice, these early positions are computed only for the first step by a simpler algorithm like the Euler's one, after which the Verlet algorithm is triggered. The algorithm in Eq. 2.5.10 does not use the velocities to compute the trajectory of the particle, however, these can be computed after calculating the new position in the following way

$$v(t) = \frac{r(t+\delta t) - r(t+\delta t)}{2\delta t} \quad . \tag{2.5.11}$$

It must be noted that, while high accuracy is achieved on the position (the error goes like $O(\delta t^4)$), the velocity value is less precise ($O(\delta t^2)$). Another version of this algorithm, the velocity Verlet, is also commonly used, however, the two algorithms have the identical stability.

In practice, once some boundary conditions are sets, the MD is triggered by time-stepping forward the position, and Eq. 2.5.10 and 2.5.11 are solved at each step. These new position and momentum are then used to compute any thermodynamic property of interest.

To complete the discussion on practical implementation of common MD simulations, it is worth mentioning the *Lyapunov instability* effect. For any approximated algorithm, two classical trajectories which are initially very close will diverge from one another exponentially with the time. This means that sufficiently long simulation are needed so that the two MD simulations converge to the "true" trajectory. This aligns with the ergodic hypothesis that states that the longer is the dynamics, the more accurate are its results.

2.5.4 The Potential Energy Formulations

From Eq. 2.5.8 one can see that the forces depends on the form of the potential used to describe the system. Unfortunately, the classical approximation of molecules prevents us to know the real forces, and thus, we do use approximated formulae to describe the intra- and inter-molecular potentials. These potential models take the name of *force field (FF)*. The first FFs were developed more than 40 years ago but they are constantly being updated or improved for several specific physical problems. A FF is made up of functions and parameters which are normally derived from quantum mechanical simulation and experimental data. There exist several types of FFs, we just mention some of the most famous, like CHARMM, [81] developed by Karplus *et. al*, or AMBER, [82] both designed to model proteins. Other ones are the OPLS [83] for drugs, and AMOEBA [84] which accounts for polarization effects. Throughout this work, we employed the AMBER force field. Sometimes the name of the FF is also attributed to the MD package that implements it, like for CHARMM and AMBER. A typical FF can be expressed as

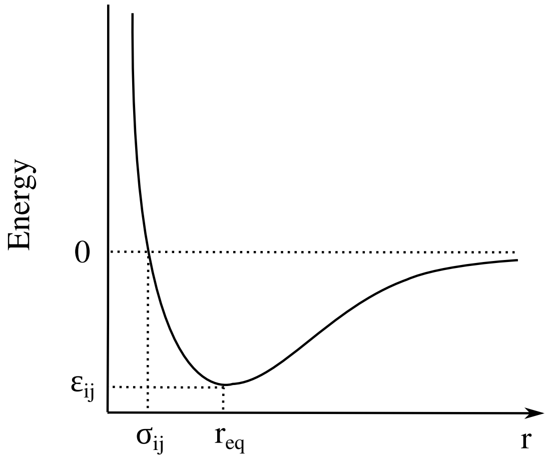

Figure 2.5.1: Lennard-Jones potential for a distance r between two atoms.

$$\begin{aligned} U(r) = &\sum_{bonds} k_r(r_{ij} - r_0)^2 + \sum_{angles} k_\theta(\theta_{ijk} - \theta_0)^2 \\ &+ \sum_{dihedrals} \sum_{n} \frac{k_\phi}{2}(1 + cos[n\phi_{ijkl} - \delta]) \\ &+ \sum_{nonbij} \left[4\varepsilon_{ij} \left(\frac{\sigma_{ij}^{12}}{r_{ij}^{12}} - \frac{\sigma_{ij}^{6}}{r_{ij}^{6}} \right) + \frac{q_i q_j}{r_{ij}} \right] \end{aligned} \tag{2.5.12}$$

The first term in Eq. 2.5.12 is the sum over bonds, with r_0 the equilibrium bond length. This harmonic expression can be replaced by more realistic forms, like the Morse potential, or higher correction terms can be added. The second term is the sum over all bond angles. This is usually only harmonic, and it is computed for each set of three connected atoms. The third term accounts for the torsional energy involving four atoms. Its trigonometric expansion involves different values of n, however, $n = 3$ is commonly used in many cases. This term can also include improper torsion angles, where the four atoms are not all connected by bonds. The type of FFs in Eq. 2.5.12 are called force field of class I. Additional anharmonic corrections to the stretching and bending terms can be added to FFs of class I, and these take the name of FFs of class II.

The last two terms account for the non-bonded interactions, namely, the Van der Waals and the Coulombic forces. For the dispersion forces, a Lennard-Jones type of potential is commonly used. The σ_{ij} constant is the distance at which the repulsive and attractive forces balance, and thus the potential is zero, while the ε_{ij} is the Lennard-Jones well depth (Fig. 2.5.1). The values of these parameters are often obtained by using the Lorentz-Berthelot combining rules, i.e., for an atom i and j their parameters are combined as: $\sigma_{ij} = (\sigma_i + \sigma_j)/2$, and $\varepsilon_{ij} = \sqrt{\varepsilon_i \varepsilon_j}$. As outlined in the introduction, since the absence of general FFs for inorganic compounds, and more specifically for POMs, the best choice to classically model POMs is to derive an ad hoc FF for each type. In this regard, we computed all bonded terms in Eq. 2.5.12 from frequency calculations as described in the modified-Seminario method, [85] while the Lennard-Jones terms for all atoms were taken from the Universal Force Field (UFF) with the use of Lorentz-Berthelot combining rules. [86]

The electric charge on atoms in molecules is distributed according to their affinity towards the electron, i.e., their electronegativity. The expression of the electrostatic potential in Eq. 2.5.12 assign a partial charge to each atom so that different chemical environments are taken into account. These partial atomic charges are normally derived from first principles calculations. For example, typical DFT or wavefunction simulations give the respective atomic charges, and the electrostatic potential maps. Within this model the atomic charges are static, i.e., they do not change during the simulations, and therefore, large energy deviations can occur because the contribution of the electrostatic potential to the total energy is normally larger than the other bonded terms. The point-charge model works well for many physical systems, however, deviations might occur for specific systems (for example ionic liquids), due to the fact that the model does not account for any polarization effects generated by dipoles or even higher order multipole interactions. To this end, several polarizable FFs have been developed (class III), for example, the AMOEBA force field includes distributed multipoles and atom polarizabilities. Returning to POMs, we model the Coulomb potential in Eq. 2.5.12

by computing the atomic charges with the CHELPG method as implemented in ORCA, [87] without adding any dipole corrections to our FF. This choice is justified by symmetrical structure of POMs, which do not possess any net dipole moment.

2.5.5 Ewald sum for long-range forces

The Lennard-Jones potential belongs to the the family of short-range forces, which decay fast at long interatomic distances. This means that their interactions are weak and they usually fall within the dimensionality of the system. In contrast, the Couloumb potential in Eq. 2.5.12 is associated with a long-range force (r^{-1}). A long-range force can be defined as one in which the spatial interaction falls off no faster than r^{-d} where d is the dimensionality of the system, for instance, the length of the simulation box used for the MD sampling. Another example of long-range forces are the dipole-dipole interactions between molecules, whose potential falls off as r^{-3}. These forces are the most difficult part to handle in any MD program, since their range of action is greater than half the length of simulation box in many cases. One possible solution would be to increase the box size to hundreds of nanometres so that the screening by neighbours would diminish the effective range of the potentials. However, this solution is not feasible since it is computationally prohibitive. An elegant way to this problem is the Ewald sum which accounts for the interaction of an ion or molecule with all its periodic images. [88]

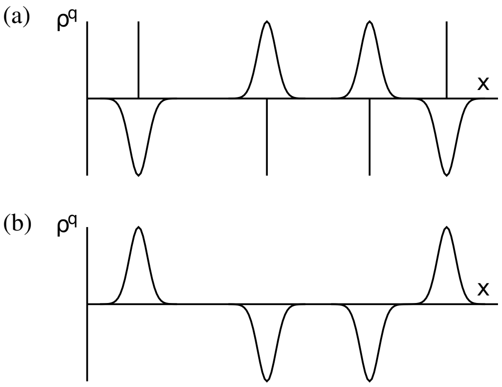

Figure 2.5.2: **(a)** Schematic representation of atomic charges plus their charge distribution in one-dimension Ewald sum. **(b)** Cancelling distribution. This image was taken from Ref. [6]

Let us consider the interaction of an ion with all other ions in the central simulation box and with all other ions in all its periodic images. For this system, the Ewald sum can be expressed as:

$$U_{elec} = \frac{1}{2}\sum_{m}\left(\sum_{j}^{N}\sum_{i}^{N} q_i q_j |r_{ij} + mL|^{-1}\right) \quad , \tag{2.5.13}$$

where q_i and q_j are the atomic charges, while L is the box length. Note that the $4\pi\varepsilon$ factor is omitted. The sum over m = (m$_x$, m$_y$, m$_z$) is over all triplets of integers and the self-interaction of each charge is excluded. This sum is conditionally convergent, and its values depends on the order in which we add up the terms. A common solution to get an absolutely convergent potential is to add an uniform background charge density. Within this approach, each point charge is surrounded by a charge distribution of equal magnitude and opposite sign, which spreads out radially from the charge. This distribution is usually taken to be Gaussian,

$$\rho_i(r) = q_i k \cdot exp(-k^2 r^2)/\pi^{\frac{3}{2}} \quad , \tag{2.5.14}$$

however, other distribution types can be equally used. Here, k is an arbitrary parameter that determines the width of the distribution, and r is the position relative to the centre of the distribution (Figure 2.5.2a). This distribution screens the interaction between neighbouring charges, and the total screened potential is computed by summing over all atoms in the central box and all their images in the real-space. A second charge distribution with same original charge and shape of the previous distribution q$_i$ is added to each atom (Figure 2.5.2b). This cancelling distribution reduces the overall potential to that due to the original set of charges, and is summed in reciprocal space. In practice, the cancelling distribution is Fourier transformed in the k-space, and the total is then transformed back into r-space. The final potential can be then expressed as

$$\begin{aligned} U_{elec} =& \frac{1}{2}\sum_{j}^{N}\sum_{i}^{N} q_i q_j \left(\sum_{|m|}^{\infty} \frac{erfc(k|r_{ij} + mL|}{|r_{ij} + mL|}\right. \\ & + (1/\pi L^3)\sum_{k=1}(4\pi/k^2)exp(-k^2/4k^2)exp(-ik \cdot r_{ij}) \\ & \left. - (k/\pi^{1/2})\sum_{i}^{N} q_i^2\right) \quad . \end{aligned} \tag{2.5.15}$$

The first term of Eq. 2.5.15 accounts for the sum in r-space, and the erfc(x) is the error function which falls to zero with increasing x. The last term is a correction due to the interaction of the cancelling distribution with itself, and thus it must be subtracted from the total. The second term indicates the sum over the k-space, and it must be noted that for a sufficiently large k value, the only term which contributes to the sum in real space is that with m = 0, and so, the first term reduces to the normal minimum image convention.

Throughout the simulations, a further improvement of the Ewald method has been employed, i.e. the particle-mesh Ewald (PME) algorithm Darden et al. [89] As for the Ewald sum, PME splits the electrostatic potential into a direct and a reciprocal part, but the reciprocal part is computed on a mesh. Usually, a cutoff of 8-10 Å is chosen for the sum in the r-space. A cutoff of 8 Å has been used for all MD simulations presented in the next sections. The reciprocal part of the potential is determined by solving Poisson's equation of a smooth charge distribution on a grid. This can be done via fast Fourier transform (FFT) under periodic boundary conditions (PBC). This method was originally developed for an implicit solvation, however, it equally works for simulations with an explicit solvent.

2.6 QM/MM Methods

The Quantum Mechanical/Molecular Mechanics (QM/MM) method consists of treating a part of a system, normally the most interesting region, at quantum mechanical (QM) level of theory, for example using wavefunctions or DFT methods, while the remainder is described by the classical molecular mechanics. [90–92] The full energy associated of QM/MM Hamiltonian is then expressed as:

$$\begin{aligned} E &= E_{QM} + E_{MM} + E_{QM/MM} \\ &= \langle\psi|\hat{H}_{QM} + \hat{H}_{MM} + \hat{H}_{QM/MM}|\psi\rangle \end{aligned} \tag{2.6.1}$$

where the first term accounts for the energy from the QM part, the second term represents the energy from the classical MM region, while the third one is the energy due to the interaction between the QM and MM particles. In a QM/MM scheme, the energy of QM region is extracted from any quantum mechanical theory, like HF, semi-empirical, MCSFC, or DFT method, while the energy of MM region is followed by the chosen force field. The new element in this theory is then the last term of Eq. 2.6.1 and its evaluation gives rise to the so-called different *embedding* schemes, which are currently the

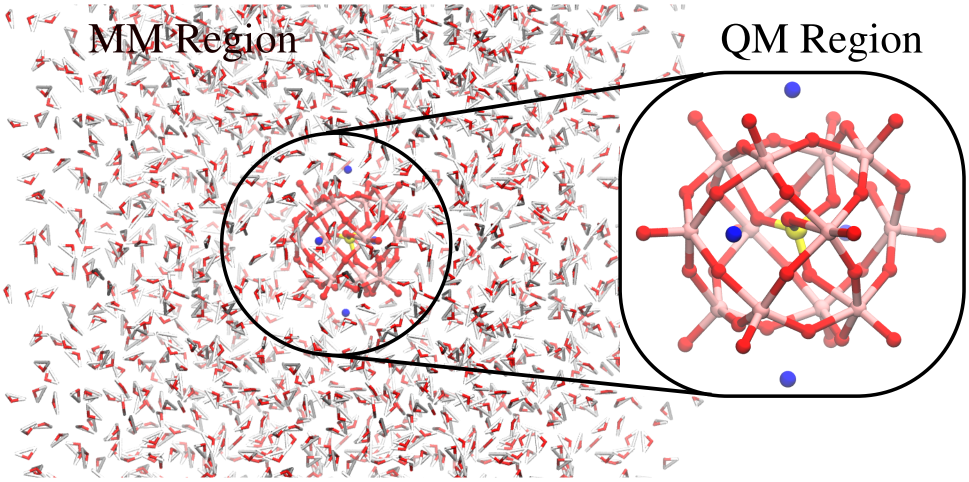

Figure 2.6.1: Illustration of the QM/MM concept. A small region (for example a POM), in which a chemical reaction occurs, and therefore cannot be described with a force field, is treated at a sufficiently high level of QM theory. The remainder of the system (solvent) is modelled at the MM level.

main challenge relative to the QM/MM field. Many different QM/MM embedding schemes exist, however, only three types are mostly implemented in quantum chemistry programs: the mechanical, electrostatic, and polarization embedding. The literature about QM/MM methods used for studying POMs is very limited. Some of these works focused on studying the interactions between POMs and proteins, and given the POM size and its relative computational cost, a mechanical embedding has been mainly used. [93,94] However, as explained below, this approach suffers from an inaccurate description of the interaction between the MM and QM regions. In contrast, the electrostatic embedding accounts for a more realistic interaction providing thus more accurate results. For example, in Chapter 3 we computed the redox potentials of POMs in solutions by using an electrostatic embedding. Since the redox potentials of POMs are connected to their electron density, which in turns depends on solvent polarization, a mechanical embedding would not take into account this polarization, and therefore fail to describe POM electron density.

2.6.1 Embedding Schemes

The most basic approach is the mechanical embedding, where all the interactions between the QM and MM regions are handled classically. In this scheme, all the interactions across the QM/MM boundary are modelled by the classical force field, whose energy is due to bonded and non-bonded terms (see Eq. 2.5.12). In absence of capping atoms, which are explained below, the interaction between the two regions is only determined by the Van der Waals and Coulomb forces, and an interacting Hamiltonian operator can be expressed as

$$\hat{H}_{QM/MM} = \sum_{i}^{solute} \sum_{j}^{solvent} \left[\frac{q_i q_j}{r_{ij}} + 4\epsilon_{ij} \left(\frac{\sigma_{ij}^{12}}{r_{ij}^{12}} - \frac{\sigma_{ij}^{6}}{r_{ij}^{6}} \right) \right] \quad . \tag{2.6.2}$$

The atomic charges are normally taken from previous QM calculations: these could be Mulliken, NBO (Natural Bond Orbital), CHELPG (CHarges from ELectrostatic Potentials using a Grid-based method) and etc. While the charges of the MM atoms are kept fixed, the charges of the QM atoms can be either fixed or can be re-computed at each iteration step. The Lennard-Jones parameters are normally not updated, and there is no harm in this, since the Lennard-Jones forces are short-range functions, and their relative uncertainty due to keeping the fixed parameters is not particularly high.

A better description of the forces acting across the QM/MM boundary is given by the electrostatic embedding. The idea is similar to Eq. 2.6.2, except that in this approach the Coulomb forces between the QM electrons and the MM atoms enters into QM Hamiltonian

$$\hat{H}_{QM/MM} = \sum_{i}^{solute} \sum_{m}^{solvent} \frac{q_m}{r_{im}} + \sum_{k}^{solute} \sum_{j}^{solvent} \left[\frac{Z_k q_m}{r_{km}} + 4\epsilon_{ij} \left(\frac{\sigma_{ij}^{12}}{r_{ij}^{12}} - \frac{\sigma_{ij}^{6}}{r_{ij}^{6}} \right) \right] \quad . \tag{2.6.3}$$

The substitution of Eq. 2.6.3 in 2.6.1 gives the expectation value of the full Hamiltonian, which would be

$$\begin{aligned} \langle \psi | H_{full} | \psi \rangle = & \\ & \left\langle \psi \middle| -\sum_{i}^{N} \frac{1}{2} \nabla^2 - \sum_{i}^{N} \sum_{k}^{K} \frac{Z_k}{r_{ik}} + \sum_{i<j} \frac{1}{r_{ij}} + \sum_{k<l} \frac{Z_k Z_l}{r_{kl}} \middle| \psi \right\rangle \\ & + \langle \psi | \psi \rangle H_{MM} \\ & + \left\langle \psi \middle| \sum_{i}^{N} \sum_{m}^{M} \frac{q_m}{r_{im}} \middle| \psi \right\rangle + \langle \psi | \psi \rangle \sum_{k}^{K} \sum_{m}^{M} \left[\frac{Z_k q_m}{r_{km}} + 4\epsilon_{ij} \left(\frac{\sigma_{ij}^{12}}{r_{ij}^{12}} - \frac{\sigma_{ij}^{6}}{r_{ij}^{6}} \right) \right] \end{aligned} \tag{2.6.4}$$

where i and j run over the electrons of the QM atoms, k and l over the QM nuclei, while m runs over the atoms in MM region. The first term is the Hamiltonian due only to the QM atoms, while the second and last term, which do not depend on the electronic coordinates, are simply constant, provided that the wavefunction is normalized. In contrast to the mechanical embedding, one can now see that the third term needs to be evaluated at each QM iteration, since this represents the direct interaction of the QM electrons with the partial atomic charges of the MM atoms. Therefore, this term behaves like an one-electron operator, and it enters in the Fock (or similarly KS) operator of Eq. 2.2.8 as additional term

$$\hat{f}_{HF}{}^{QM/MM} = -\frac{1}{2}\nabla^2 - \sum_{k}^{nuclei} \frac{Z_k}{r_{ik}} + \sum_{m}^{solvent} \frac{q_m}{r_{im}} + V_{HF} \quad . \tag{2.6.5}$$

Since the presence of this additional element (third term in Eq. 2.6.5), quantum chemistry codes needed to be modified to include the QM/MM part. The bottleneck of SCF procedures is usually due to the two-electron integral evaluation and the diagonalization, while the computational cost of evaluating the one-electron QM/MM term can be relatively low. Note that within the electrostatic approach, the QM/MM term must be evaluated every time that either a QM or MM atom moves, which is in contrast to the mechanical embedding, in which case it is evaluated when QM atoms move.

One of the flaw of the electrostatic embedding is that the QM region can be over-polarized near the QM/MM boundary by the atomic MM charges. Essentially, the atomic point charges may attract or repel the electrons, resulting in a spill-out of the QM electron density into the MM region (density leakage). A remedy is given by using smeared charges rather than point charges. [95]. Within this approach the atomic charges are approximated by gaussian-like functions, and the one-electron operator represents the Coulombic interaction between the wave function and the Gaussian distribution of the MM atoms. This approach avoids the evolution of unphysical attraction (or repulsion) near the boundary.

A further improvement is achieved by allowing the MM atoms to be polarized by the QM region. One way of accounting for the polarizability of MM atoms is to assign to each MM atom a polarizability tensor α, and the energy resulting from the interactions between the induced dipole moments and atomic charges, as well as the dipole-dipole are added into the H_{MM} term. In addition, the interaction between the induced dipoles and the electronic wave function is accounted by including an additional one-electron operator in the Fock operator. All these terms are evaluated in an iterative manner, which thus adds an additional computational expense to the QM/MM procedure. Despite the polarization embedding reflects the most realistic picture of the forces across the boundary, it does not find many applications due to the limits of the current polarizable FFs for both organic and inorganic compounds.

Indeed, the development of polarizable classical force field is currently one of the major challenge in the classical MD simulations, and in most cases the electrostatic embedding approximation is the best compromise between accuracy and computational cost. This is is particularly true for biomolecular systems, like drug-like compounds, and proteins. For instance, Shi *et al.* used the the AMOEBA FF to calculate the components of the gas phase dipole moments of multiple conformations of each amino acid dipeptides. [96] In that work, a direct comparison with high-level QM results gives a correlation coefficient close to 1, which would not be possible with a FF of class I or II. [96] However, there are still a number of issues that remain to be overcome with these force fields: firstly, the weakness in current parameters of FFs that might lead to undesired results; and the relative slowness of simulations employing polarizable force fields remains an issue. [96]

2.6.2 Bonds across the QM/MM Boundary

The embedding approaches are the general procedure to account for the non-bonded interactions between the QM and MM regions. However, cutting bonds across the QM/MM boundary generates one or more unpaired electron, and further additional corrections must be implemented in the QM/MM approach to preserve the electronic valence of the atoms near the boundary. Different methods have been proposed as solution to such boundary problem but the most commonly implemented methods in QM/MM packages are the link atoms and the frozen localized orbitals.

In the link approach the missing MM atom is replaced by a link atom (or

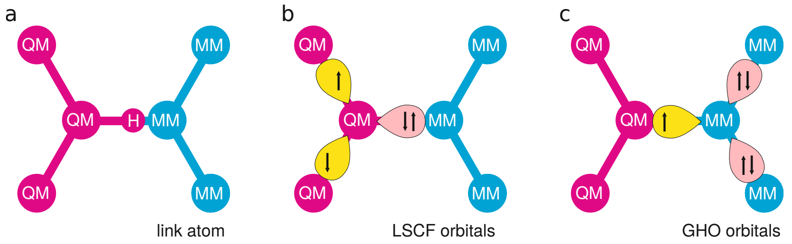

Figure 2.6.2: Illustration of the approaches to cap QM atoms: link atom **(a)** and frozen orbitals **(b,c)**. This image was taken from Ref. [7]

capping atom), which is physically connected to both QM and MM atoms involved in the cut bond (Figure 2.6.2). The hydrogen atom is usually chosen as capping atom because of its simplicity. The choice is motivated by the fact that when a bond is cut through the boundary, the use of a hydrogen atom will reproduce the physically separation of an electron pair into two single electrons, namely, one on the QM and the other on the MM atom. Furthermore, C and H have similar electronegativity, which then fairly imitates the valence of the carbon atom. The only energy correction added to the $H_{QM/MM}$ is due to the interactions between the QM and link atoms, since the link atoms do not interact in any way with the MM atoms. The $H_{QM/MM}$ can be defined similarly to the one in Eq. 2.6.3, however, the interactions are only treated classically, and further energy terms due to QM link-atom interactions are added to it. Namely, the energies due to the bond stretching, angle bending, torsion angles, and dispersion terms are computed by using a classical force field formulation. Despite its popularity, the link-atom approach might lead to strong overpolarization errors. Indeed, the closer is the link atom to the boundary, the more important becomes the effect of the overpolarization.

An alternative comes from the frozen localized orbital approach. The mathematical description is somewhat laborious, however, its basic idea is to replace the cut bonds with one electron or a single electron pair, whose orbitals are kept frozen throughout the dynamics so that they are not optimized in SCF iteration. The first approach is the localized self-consistent-field (LSCF) method [97,98], which consists of a frozen orbital containing two electrons along the QM-MM bond. This bond can be idealized as an electron lone pair along the boundary (Figure 2.6.2b). Further modification of the LSCF involves the inclusion of hybrid singly-occupied orbitals along the bonds between the QM boundary atom and its neighbouring QM atoms (Figure 2.6.2b). In this case, while the doubly-occupied orbitals are kept frozen, the singly-occupied orbitals are mixed with orbitals of QM boundary atoms and included in the SCF procedure. Another approach is the generalized hybrid orbital method (GHO) of Gao et al. (Figure 2.6.2c), within which both hybrid and localized orbitals are now located on MM atoms. Specifically, the hybrid orbital on the MM boundary atom is included in the SCF iteration, while the remaining doubly-occupied orbitals on the closest MM atoms are kept frozen.

2.7 Computation of Redox Potentials

In this section, we will provide an overview of a number of fundamental techniques widely used in computational chemistry to compute the redox potentials of compounds in solution. In particular, we group these methods in two types: (i) implicit solvation model and (ii) explicit solvation.

In the first type of solvation a quantum mechanical treatment of the solute is combined with an approximation of the solvent as a dielectric continuum model. Within this approach, the standard reduction potential of a redox couple can be computed by using a thermodynamic cycle that permits the estimation of the standard Gibbs free energy of the reduction of the couple.

The second method involves the computation of redox potentials from the free energy obtained by sampling each individual redox state in the reaction by means of MD. Here, we will only focus on the MD approach. In this case, the solute is explicitly immersed in a box with solvent molecules, and the dynamics is processed afterwards to compute the free energy. The classical MD is the simplest way to compute the free energy from the sampling, however, AIMD or even QM/MM dynamics can be equally used. These latter are undoubtedly more accurate, however, their computational cost can be quite high, and therefore, the choice of the sampling method must be a good compromise between accuracy and computer resources.

A classical MD approach depends on careful choices of parameters and initial configurations set by users. For example, if one is studying the free energy due to the transformation of a phenol in toluene in solution, the OH moiety must disappear, and the methyl must appear. This approach consists of turning off the OH charges, while the CH_3 charges are trigged on. Additionally, despite having less influence, the other bonded and non-bonded parameters need not to be changed too abruptly. Therefore, the atomic charges, and more generally FFs, must be sufficiently accurate to give quantitative results. [7] As explained in section 2.5, the development of FFs for POMs is still in progress, and the best choice is to make an ad hoc FF for each POM type. However, the employment of a classical MD approach for computing the free energies of POMs would mean to carry out a detailed investigation of the aforementioned factors, which will require an effort that cannot be addressed in a single work. For this reason, we chose to employ a QM/MM approach, which offers a more robust description of the electron density of the redox states, since this latter is computed by DFT.

Let us now introduce the general electrochemical concepts that are at basis of the computation of reduction potentials. The following half-reaction represents the reduction of the Ox compound to Red

$$Ox_{(s)} + n \cdot e^-_{(g)} \rightarrow Red_{(s)} \tag{2.7.1}$$

where "g" and "s" refer respectively to the gas and solution phase, while n is the number of electron taking part in the reaction. The free energy of the reaction at any temperature, T, is obtained as

$$\Delta_r G(Ox|Red) = \Delta_r G^o(Ox|Red) + RT \cdot ln \frac{a_{Ox}}{a_{Red}} \tag{2.7.2}$$

where R is the ideal gas constant, $\Delta_r G^o(Ox|Red)$ is the Gibbs free energy of the reaction at standard condition, and a_X is the activity of X (Ox, or Red) that depends on bulk, c_X, and standard concentrations, c^o, as

$$a_X = \gamma_X \frac{c_X}{c^o} \tag{2.7.3}$$

where γ_X is the activity coefficient. The absolute redox potential of Eq. 2.7.1 is thermodynamically related to the Gibbs free energy in solution from the Nerst equation

$$E_{abs}(Ox|Red) = -\frac{\Delta_r G(Ox|Red)}{nF} = E^o_{abs}(Ox|Red) + \frac{RT}{nF} \cdot ln \frac{a_{Ox}}{a_{Red}} \tag{2.7.4}$$

where F is the Faraday constant, and $E^o_{abs}(Ox|Red)$ the standard redox potential

$$\Delta^o_r G(Ox|Red) = -nFE^o_{abs}(Ox|Red) \quad . \tag{2.7.5}$$

Eq. 2.7.4 allows the computation of the absolute redox potential as function of concentrations and the temperature. However, the redox potentials are measured with respect to a reference half-reaction, whose potential is set to a certain value by definition. Different types of reference electrodes exist but the most commonly used is the standard hydrogen electrode (SHE). The SHE electrode refers to the hydrogen production occuring at Pt electrode in standard condition (1 atm at 298.15 K)

$$H^+_{(aq)} + e^-_{(g)} \rightarrow H_{2(g)} \tag{2.7.6}$$

and its redox potential is set to zero by definition. The redox potentials of redox reactions, like Eq. 2.7.6, are then measured relative to the SHE. Since the computation of Eq. 2.7.5 returns absolute redox potential, a comparison relative to the absolute SHE value is needed

$$E^o_{rel}(Ox|Red) = E^o_{abs}(Ox|Red) - E^o_{SHE}(Ox|Red) \quad , \tag{2.7.7}$$

$$E^o_{rel}(Ox|Red) = -\frac{\Delta^o_r G(Ox|Red)}{nF} - E^o_{SHE}(Ox|Red) \quad . \tag{2.7.8}$$

Despite a large number of studies have been performed to determine $E^o_{SHE}(Ox|Red)$, its exact value is still in discussion. Some of these suggested values ranging between 4.05 V to 4.44 V, [99, 100] where this latter is recommended by the IUPAC. [101] More often redox potentials are measured at non-standard conditions, and the so-called formal potential $E^{o'}$ is used

$$E(Ox|Red) = E^{o'}(Ox|Red) + \frac{RT}{nF} \cdot ln\frac{c_{Ox}}{c_{Red}} \tag{2.7.9}$$

$$E^{o'}(Ox|Red) = E^o_{abs}(Ox|Red) + \frac{RT}{nF} \cdot ln\frac{\gamma_{Ox}}{\gamma_{Red}} \tag{2.7.10}$$

This expression is useful because it allows the contribution of different effects, like concentrations and ionic strength, to the potential. The normal hydrogen electrode (NHE) is an example of formal electrode, whose redox potential is estimated to differ from the SHE of 6 mV. [102] Due to the very small difference between NHE and SHE, there is no harm in computing redox potentials relative to one or another electrode.

In many single or multiple electron reduction the use of Eq. 2.7.5 is sufficient to determine the potential of the redox couples, however, when additional chemical processes occur, further corrections are needed, and Eq. 2.7.4 has to be employed. This is the case, for example, when Ox and Red can be equally protonated, and their concentration, plus the pH, can affect the final potential.

These corrections are often taken into account by computing the so-called Pourbaix diagrams, [103] which show how each redox state is dependent on the pH and concentration. For instance, Truhlar *et al.* showed that the deviations of redox potentials for a ruthenium-based water oxidation catalyst are about 0.1 V, which is very low for an implicit solvation model. [104] However, when multiple reductions occur for transition metal complexes, the computation of the Pourbaix diagram becomes a complex task. [103] The scenario becomes even more complex for POMs due to the many metals composing their structure. For this reason, we did not take into account the effect of the pH on all possible intermediates of POM reductions in the next chapters.

2.7.1 Implicit Solvent Model

We showed that the redox potential of a reaction or half-reaction can be computed from its reaction free energy, however, since most reduction processes occur in solution, it is necessary to include the effect of the environment in order to predict redox potentials with accuracy. One approach is the so-called implicit solvent model (ISM), where the solvent effect is taken into account by simulating a dieletric continuum medium around the solute.

The reaction free energy is calculated as the energy difference between of the free energy of each component of the product and reagent, where the free energy of a given species is expressed as

$$G^o_s(X) = G^o_g(X) - \Delta G^o_S(X) \quad . \tag{2.7.11}$$

The first term is the gas-phase free energy, while the second term is the solvation free energy, i.e., the energy needed to transfer the solute from gas-phase to the solution. The gas-phase free energy is computed as follows

$$G^o_g(X) = E_{ele}(X) - E_{ZPE}(X) - RTlnQ - TS(X) \tag{2.7.12}$$

where the first term is the electronic energy at fixed configuration, the second the zero point vibrational energy, the third represents the thermal contribution obtained by calculating the total partition function, while the last term is the entropy contribution. Once the quantities in Eq. 2.7.12 are computed for each species, the standard free energy of the reaction in solution can be obtained by using the *thermodynamic cyle* (also called Born-Haber). In the following we are referring to standard free energies unless specified otherwise. In this scheme, shown in Fig. 2.7.1, the liquid-phase free energy can be expressed as

$$\Delta_r G^o_s(Ox_i|Red_i) = \Delta_r G^o_g(Ox_i|Red_i) + \Delta\Delta G^o_S \tag{2.7.13}$$

where $\Delta\Delta G^o_S$ is difference between the solvation energies of products and reagents, while $\Delta_r G^o_g(Ox_i|Red_i)$ is the gas-phase free energy of the reaction

$$\begin{aligned} \Delta_r G^o_g(Ox_i|Red_i) &= \sum_i G^o_g(Ox_i) - \sum_i G^o_g(Red_i) \\ \Delta\Delta G^o_S &= \sum_i \Delta G^o_S(Ox_i) - \sum_i \Delta G^o_S(Red_i) \quad . \end{aligned}$$

The resulting reaction free energy in solution is then inserted in Eq. 2.7.8 to

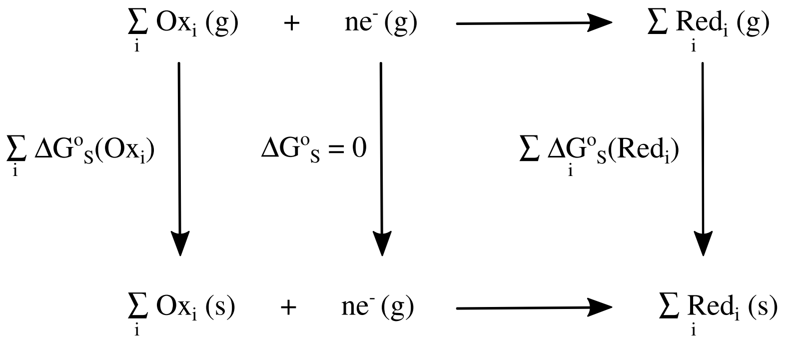

Figure 2.7.1: Thermochemical cycle relating the standard free energy of the redox reaction in solution, $\Delta_r G^o_s(Ox_i|Red_i)$, to the standard free energy of the gas-phase reaction, $\Delta_r G^o_g(Ox_i|Red_i)$, using the solvation free energies of the reactants Ox and products Red. The symbol g denotes gas-phase processes, while the symbol s indicates the liquid-phase reduction. The upper-case subscript S refers to the free energy of solvation. Note that the solvation energy of electron is zero.

obtain the standard redox potential relative to SHE.

The standard free energy of solvation of a compound can be written as

$$\Delta G^o_S = \Delta G_{BE} + \Delta G_{NB} + \Delta G_N \tag{2.7.14}$$

where the first term accounts for the bulk-electrostatic (BE) interaction between the solute and polarizable solvent, the second term represents the non-bulk effect (NB), and the last term is the energy due to the solute geometry change between the solution and gas-phase, provided the gas-phase geometry is used for calculating the first two terms. The gas-phase and solute geometries do not usually differ significantly from each other, this results in a small ΔG_N, which can be safely neglected in many cases. [105]

The first term of Eq. 2.7.14 can be expressed as

$$\Delta G_{BE} = \Delta E + G_p \quad , \tag{2.7.15}$$

$$\Delta E = \langle \psi_s | H | \psi_s \rangle - \langle \psi_g | H | \psi_g \rangle \tag{2.7.16}$$

$$G_p = -\frac{1}{2} \int \rho(r)\ \phi(r)\ dr \tag{2.7.17}$$

where the ψ_g and ψ_s are respectively the electronic wave function from the gas-phase and solution computations. The ρ is the charge density, when classical atomic charges are used, or the electronic density obtained from the wave function, while ϕ is the electrostatic potential at the distance r. The ΔE term is the energy difference required to transfer the solute from the gas phase to the solution, while G_p is the energy due to the mutual polarization of the solvent and solute.

From Eq. 2.7.17 one can see that the value of ϕ needs to be known at each fixed geometry, and this normally means solving the nonhomogeneous-dieletric Poisson equation (NPE)

$$\nabla \cdot (\epsilon \nabla \phi) = -4\pi\rho(r) \tag{2.7.18}$$

where ϵ is the dieletric constant of the medium. The electronic density of the solute is put inside a cavity that has a dieletric constant equal to one, whereas it is equal to the bulk dieletric constant outside the cavity. Once the electronic wave function is obtained by any electronic structure method, such as HF, semi-empirical, DFT and etc, the NPE must be solved to account for the solvent-solute interactions. The NPE solution is usually solved in an iterative manner, and the full procedure is often referred to as *Self-Consistent Reaction Field* (SRCF).

Alternative approaches to the NPE exist, for instance, the simplest method is the *Born model*. [106] In this approach, the term G_p for a net charge q in a cavity of radius a, in a medium with dieletric constant ϵ is given by [106]

$$G_p = -\left(1 - \frac{1}{\epsilon}\right)\frac{q^2}{2a} \quad . \tag{2.7.19}$$

In this expression the effect of neighbouring atoms is not accounted. This description can be ameliorated by the so-called *Generalized Born* (GB) model, where the solute is approximated as set of partial atomic charges centred at nuclear positions. This approach is commonly implemented in classical MD programs, where it is combined with the force field of the systems. A similar approach is the Kirkwood-Onsager equation, where the atomic charge is replaced by the electric dipole moment μ. Despite these methods possess a simple analytical form, and therefore, are very cheap from a computational prospective, their implementation can only be considered as a rough estimate of the solvation effect. Indeed, the Born model gives similar solvation energy for positive and negative ions of same size, while the Onsager model only gives acceptable estimation for small molecules, and it fails to describe symmetric molecules with no net dipole moment.

The non-bulk effects of the solvent are due to the energy required to form the cavity which hosts the solute, and the dispersion energy due to the Van der Waals interactions between the solvent and solute. As for the electrostatic interaction, different ISMs treat these effects in a different way. One common approach is to estimate the ΔG_{NB} from the computation of the *solvent-accessible surface area* (SASA). The SASA can be thought of as the surface generated by a spherical solvent molecule that rolls over the Van der Waals surface of the solute, which is equivalent to the surface generated by the sum of the solute and solvent Van der Waals surfaces. A linear empirical relationship between the ΔG_{NB} and the SASA can be expressed as

$$\Delta G_{NB} = \sum_i \sigma_i A_i \tag{2.7.20}$$

where the index i runs over the atoms or group of atoms, σ is a parametrized constant, and A is the SASA of atom i. The method accounts for cavity, dispersion, and repulsions effects but it is highly dependent upon the parametrization of the solvent probe and solute Van der Waals surface. Indeed, these two are built from choosing a fixed solvent and solute radius. Another sensible aspect is that in realistic solute-solvent boundary the dieletric constant does not suddenly change to the bulk constant, and therefore, the description of ΔG_{NB} term might no be sufficient. [107] The implicit solvent model has been used in next chapters to compute the solvation energies of POMs and thus their redox potentials. Specifically, we employed the conductor-like polarizable continuum model (CPCM) to compute the terms in Eq. 2.7.14.

2.7.2 Free Energy Sampling Methods

The standard redox potentials in solution can be computed from simulations employing the free energies methodologies. There exists a large class of methods to compute the free energy of a process in solution, in the following we only discuss about some of most commonly used approaches. The main idea of each of these methods is to sample the energy of the state involved in the reduction by means of MD or MC simulations, and extract from these the difference in energy between the initial and final states. When explicit solvation models are employed, several aspects must be taken into account to avoid spurious energy changes. For instance, if periodic boundary conditions (PBC) are employed, simulations at different unit cells might need to be performed in order to investigate the influence of the closest images on the reduction process.

Another aspect of liquid-phase simulations is the choice of the statistical ensemble. A common practice is based on the execution of NPT simulation to equilibrate the density of the system, followed by NVT simulations which give the final trajectories for any other use. It must also be noted that free energies from simulations in solution are proper Helmholtz free energy (A). However, the difference between Gibbs, ΔG, and Helmholtz, ΔA, free energy for reactions in solution under ambient conditions is expected to be negligible because the volume change is small for such reactions, and therefore, there is no harm to talk about Gibbs free energies. [103, 108]

As outlined in section 5.3, the free energy change Δ_rG depends on the activities of Ox and Red, and thus these should in principle be accounted for the computation of correct free energies. However, if the MD simulations for Ox and Red states are carried out with the same box size and similar number of solvent molecules, one can assume that Ox and Red activities are the same, provided that the activity coefficients are also similar. The Δ_rG is then equal to the $\Delta_r G^o$, which can easily be related to the standard redox potential of the reduction through Eq. 2.7.8.

Free Energy Perturbation

Historically, the well-know idea of computing free energies from MD simulations dates back to the Zwanzig relationship, [109] and it is sometimes called *free energy perturbation* (FEP) (or *exponential averaging*). Assuming that two end states are described respectively by $U_0(q)$ and $U_1(q)$ potentials, with reaction coordinate q, the free energy can be expressed as

$$\Delta_r G^o = -\beta^{-1} ln \left\langle e^{-\beta(U_1 - U_0)} \right\rangle_X = -\beta^{-1} ln \left\langle e^{-\beta \Delta U} \right\rangle_X \qquad (2.7.21)$$

where the subscript X is used to indicate each state (X = Ox or Red), and the term in the bracket is

$$\left\langle e^{-\beta(U_1 - U_0)} \right\rangle_X = \frac{1}{Z_X} \sum_k e^{-\beta(U_1(q_k) - U_0(q_k))} \qquad (2.7.22)$$

with Z_X the partition function. In this way the free energy is simply obtained by the exponential average of the potential difference. In practice, the exponential average of the difference e$^{U_1 - U_0}$ (forward integration) and e$^{U_0 - U_1}$ (backward integration) are computed, and if their difference is small enough, the free energy can then be expected to be accurate. This is not the case for many chemical processes, such as Eq. 2.7.1, which normally undergo relaxation effects that lead to very different equilibrium configurations. Therefore, it does not find any practical use in computer simulations, unless in very specific cases. For example, if one is interested in the effect of more accurate potentials, it can be used to compute the free energy due to the different FFs. [110]

Thermodynamic Integration

A further improvement to the FEP can be obtained by introducing a potential energy function U that depends linearly on a coupling parameter λ such that, for λ = 0, U refers to the potential energy of the initial state Ox, while for λ = 1, it is the potential energy of the final state Red. This method is called *thermodynamic integration* (TI), and $U(r, \lambda)$ can be expressed as

$$U(r, \lambda) = \lambda U_{Red} + (1 - \lambda) U_{Ox} \tag{2.7.23}$$

where $0 \leq \lambda \leq 1$. Since the potential, U now depends on λ, so does the partition function leading to the free energy, $\Delta G(\lambda) = -\beta^{-1} lnZ(\lambda)$ (here A is replaced by G). We can now write the derivative of free energy with respect to λ as

$$\begin{aligned} \frac{\partial G}{\partial \lambda} &= -\beta^{-1}\frac{\partial Z}{\partial \lambda} = -\beta^{-1}\frac{\partial}{\partial \lambda}\int dr^N e^{-\beta U(\lambda)} \\ &= \beta^{-1}\int dr^N \left(\frac{\partial U}{\partial \lambda}\right) e^{-\beta E(\lambda)} \quad . \end{aligned}$$

This leads to the following expression for the free energy corresponding to $U(r, \lambda)$

$$\Delta G = -\int_0^1 d\lambda \left(\frac{\partial G}{\partial \lambda}\right) = -\int_0^1 d\lambda \left\langle \frac{\partial U}{\partial \lambda} \right\rangle \tag{2.7.24}$$

where is $\langle ... \rangle_\lambda$ denotes the average at fixed values of λ. It must be noted that only the final states $U(r, 0) = U_{Ox}$ and $U(r, 1) = U_{Red}$ have a physical sense, while other values of λ represent imaginary states. In practice, modern classical MD packages normally have built-in tool that returns the $\partial U / \partial \lambda$ for simulation at different λ values, and the integration in Eq. 2.7.24 can be then carried out numerically by Gaussian quadrature. Occasionally, it turns out that the linear parameterization as shown in Eq. 2.7.23 is not sufficient, and other non-linear expressions must be adopted.

Other the other hand, quantum chemistry packages are often not programmed to return the potential derivative in an easy way. An alternative approach is to compute the vertical energy gap (VEG). With the use of Eq. 2.7.23, the $\partial U/\partial\lambda$ can be expressed as

$$\frac{\partial U(r,\lambda)}{\partial\lambda} = \langle U_{Ox} - U_{Red}\rangle_\lambda = \Delta U(r) \tag{2.7.25}$$

where $\Delta U(r)$ is the VEG: the analogue of the vertical excitation energy controlled by the Franck-Condon principle. [111] The free energy can then be computed as

$$\Delta G = \int_0^1 d\lambda \, \langle U_{Ox} - U_{Red}\rangle_\lambda \quad . \tag{2.7.26}$$

Practically, TI involves evaluating the $\langle U_{Ox} - U_{Red}\rangle_\lambda$ for a set of λ values which are then inserted into Eq. 2.7.26 in order to calculate the redox free energy.

Despite its theoretical simplicity, once again quantum chemistry packages can not often be used to retrieve $\Delta U(r)$ at intermediate values of λ. To this end, a helpful solution comes from the linear response (LR) approximation. In the LR approximation the free energy derivative $\partial G/\partial\lambda$ is assumed to be linear with respect to λ, and within this regime, Eq. 2.7.26 only needs to be evaluated at the end points, i.e. $\lambda = 0$, and 1

$$\begin{aligned} \Delta G_{Ox/Red} &= \frac{1}{2}(\langle U_{Ox} - U_{Red}\rangle_{Ox} + \langle U_{Ox} - U_{Red}\rangle_{Red}) \\ &= \frac{1}{2}(\langle \Delta U\rangle_{Ox} + \langle \Delta U\rangle_{Red}) \quad . \end{aligned} \tag{2.7.27}$$

Here $\langle\Delta \mathrm{E}\rangle_{Ox}$ is obtained by the ionisation potential (IP) of the oxidised species, and $\langle\Delta \mathrm{E}\rangle_{red}$ from the electronic affinity (EA) of reduced species. In this way one only needs to compute the VEG for each independent state, i.e., Ox and Red. Eq. 2.7.27 has shown to give good results for many half-reactions, [112] however, if the solvent response is not linear with energy change, it might suffer of large uncertainties for other type of reactions, like proton coupled electron transfers.

The TI method is strictly related to the Marcus theory of electron transfer in solution. In Marcus theory the free energy surface of each redox state is described as a diabatic curve which is a function of a proper reaction coordinate q, and these curves are assumed to be quadratic with respect to q and with equal curvature. The q is normally taken as the solvent polarization, [113] since this quantity is sensitive to the actual electron change as the reaction proceeds. The diabatic state G_X(q) is the analogue of the gas-phase potential energy but in solution, and it uniquely defines the reorganization free energy of each state, i.e. λ, which is the energy that the reaction needs to overcome

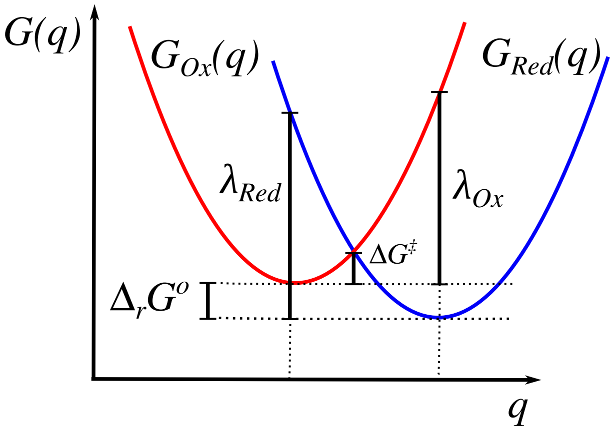

Figure 2.7.2: Schematic representation of diabatic profiles of half-reaction in Eq. 2.7.1 within the Marcus theory.

such that the solvent configuration is favourable to the process.

From Figure 2.7.2 one can see that the $\Delta_r G^o$ can be related to the VEG and the reorganization energy as follows

$$\Delta_r G^o = \Delta G(q_{Ox}) + \lambda \tag{2.7.28}$$

where $\Delta G(q_{Ox}) = G_{Ox} - G_{Red}$ computed at $q = q_{Ox}$. A similar expression can be written for the Red state

$$\Delta_r G^o = \Delta G(q_{Red}) + \lambda \tag{2.7.29}$$

with $\Delta G(q_{Red}) = G_{Ox} - G_{Red}$ computed this time at $q = q_{Red}$. Combining Eq. 2.7.28 and 2.7.29, one obtains

$$\Delta_r G^o = \frac{1}{2}\Big[\Delta G(q_{Ox}) + \Delta G(q_{Red})\Big] \tag{2.7.30}$$

Eq. 2.7.30 is equal to Eq. 2.7.27, provided that the $\Delta G(q_X) = \langle \Delta U \rangle_X$

Assessing the limits of the LR approximation, and therefore, the validity of the calculations can be achieved by exploiting the reorganisation energy (indicated by λ symbol) of the process under study. Although the total reorganisation energy is the sum of the inner-sphere (λ_i) and outer-sphere (λ_o) energies, i.e. $\lambda_{tot} = \lambda_i + \lambda_o$, the main contribution derives from the λ_o, and we only focus upon this. Within the limit of LR approximation, λ_o can be calculated as

$$\lambda_o = \frac{\langle \Delta U \rangle_{Ox} - \langle \Delta U \rangle_{Red}}{2} \tag{2.7.31}$$

provided that the fluctuations of each energy gap, $\langle \Delta E \rangle$, is Gaussian. In this case, it is possible to write the root-mean square deviations of the energy gap as $\sigma_X = \langle \delta \Delta U \rangle_X^{1/2}$ (X = Ox or Red), and define the outer-sphere reorganisation energy as

$$\lambda_o^{'} = \frac{\sigma_{Ox}^2 + \sigma_{Red}^2}{4k_BT} \tag{2.7.32}$$

When the LR approximation is valid, Equation 2.7.31 is equivalent to Equation 2.7.32, and therefore, a comparison of λ_o and $\lambda_o^{'}$ gives an estimate of the deviation from the LR approximation in each redox process [108].

As shown in Chapter 3, for the ET reductions occurring to W-based Keggin ion, λ_o and $\lambda_o^{'}$ differ by each other by about 2 kcal/mol, and the computed redox potentials deviate from the experiment by less than 0.1 V. This means that the LR approximation is respected for this system. In contrast, we found larger deviations of reorganisation energy and redox potentials for PCETs of V-based Keggin ion, suggesting that the solvent response is not linear. The deviations are due to the two main factors: (i) the limited size of the cluster model, and (ii) a strong SIE. For a more detailed discussion, see Chapter 3.

2.8 X-ray Absorption Spectroscopy

X-ray spectroscopy represents one of the most commonly used techniques to probe the properties of materials in both condensed and gas form. In particular, the X-ray Absorption spectroscopy (XAS) is widely used to describe the physical state of specific target and its surrounding. In an XAS experiment, after an atom has absorbed a x-ray photon, there is a transition of its core electrons (photoelectron) to virtual level of energy (or continuous states). Besides depending on the atom type, this phenomenon depends also on the environment around the absorbing atom, and therefore, this gives information about the physical or chemical state of a specific element. In a typical XAS spectra, the absorption probability suddenly increases at the resonant energy giving rise to a so-called edge profile. The edge position depends on the atomic number and on the element type. Other factors, like the coordination number and the oxidation states of the elements, influences the position and the intensity of the edge peak. For example, as the oxidation state increases, the edge tends to shift towards higher energy. This is often used to distinguish the different valence states of the same element in different molecular environments. The edges are named by which core electron is excited, namely n = 1, 2, 3, correspond to K, L, and M-edges respectively. For each edge there is

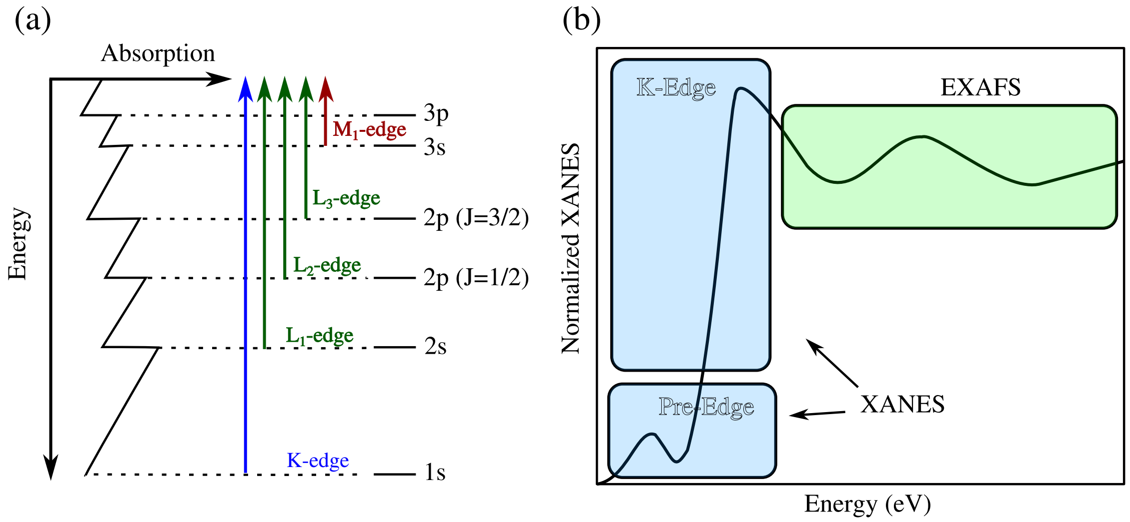

Figure 2.8.1: Schematic representation of **(a)** core-to-virtual electron transition, and **(b)** XANES spectra.

a corresponding index that refers to the angular momentum number l. This index is 1 for l = 0, 2 and 3 for l = 1, and 4 and 5 for l = 2.

In addition to the edge, a pre-edge region might exist. This is commonly due to symmetry forbidden transitions occurring between s and d orbitals. The pre-edge and the edge region together constitutes what is called X-ray Absorption Near-Edge Structure (XANES). In a XAS spectra after the edge peak, we find the region where the scattering of the photoelectron with neighbouring atoms produces constructive or destructive interference profiles. This region is called Extended X-ray Absorption Fine Structure (EXAFS). A schematic illustration of XAS spectra and its specific region is given in Figure 2.8.1.

The treatment of excited states is a very broad topic, in the following section, we briefly introduce the basic concepts behind the electronic transition from two states, and discuss the elements governing the spectra profiles. For a more detailed discussion about the x-ray interaction with matter, the reader is referred to different textbooks or articles. [114,115]

There exists a broad literature on the simulation of XANES and EXAFS, here, we only mention few recent works to highlight the contribution of these methods to the understanding of material behaviours. Joly *et al.* illustrated that simulated XANES spectra can be employed to accurately determine the shape and chemical shift of a short-lived triplet state of the tris(bipyridine)-iron(II) complex, which has only recently been indicated by theoretical simulations and X-ray emission experiments. [116] They also showed that useful insights into the structure of molecular organic frameworks (MOFs) can be grasped from XANES and EXAFS simulations. [116] This last work is particularly interesting, since similarities exist between POMs and MOFs. Despite the large literature about theoretical XAS studies, there has been a surprisingly limited number of examples in which XAS has been used for the quantitative structural analysis of POMs during electrochemical reactions, and fewer still employing the XANES region of the spectrum. In this regard, besides the contribution to POM community, our theoretical study in Chapter 4 reveals the factors controlling the XAS observables so as to provide perspectives for future experimental and theoretical studies into the redox properties of POMs.

2.8.1 Absorption Cross-Section

The absorption process deals with the transition of a single electron from a core state to an excited state (absorption). In this case, the non-relativistic Hamiltonian of a charged particle in an electromagnetic field is $H = H^0 + H^{'}$, where H^0 is the Hamiltonian for the unperturbed system, whereas $H^{'}$ represents the matter-field interaction term. This latter is classically expressed as

$$H^{'} = \frac{e}{m}p \cdot A + \frac{e}{m}\phi \cdot B + \frac{e^2}{2m}A^2 \tag{2.8.1}$$

where ϕ and A are respectively the scalar and the vector potential related to the Maxwell equations. In the absorption case, it is possible to disregard the last term of Eq. 2.8.1, and the transition operator is only due to the first two terms. The transition occurs from an initial state $|i\rangle = |\psi_i, k\rangle$, where ψ is the one particle core electron state and k represents the incoming photon. The energy of full initial state (electron plus photon) is sum of the unperturbed electron ε_i and photon energy $\hbar w$. Whereas the final state can be represented by $f\rangle = |\psi_f, 0\rangle$, where we set the photon state equal to 0, since the final state energy depends only on photoelectron ε_f. The transition rate is then given by the Fermi Golden Rule:

$$R_{if} = \frac{2\pi}{\hbar}|\langle f|H^{'}|i\rangle|^2 \delta(\varepsilon_f - \varepsilon_i - \hbar w) \tag{2.8.2}$$

where δ is the Kronecker symbol, and indicates that the probability of transition is 1 or 0. By recalling the relationships existing between the vector potential and electric and magnetic field, one obtains a final expression that relates the cross section to the transition rate (with finite structure constant

$\alpha = e^2/2hc\epsilon_0)$

$$\sigma_{if} = 4\pi^2 \alpha \hbar w |\langle \psi_f | \hat{o} | \psi_i \rangle|^2 \delta(\varepsilon_f - \varepsilon_i - \hbar w) \quad . \tag{2.8.3}$$

The operator $\hat{o}$ can be expressed as the sum of different contributions: $\hat{o} = \hat{o}_{E1} + \hat{o}_{E2} + \hat{o}_{E3} + \hat{o}_{M1} + \cdots$. the terms E1, E2, and E3 are respectively the electric dipole, quadrupole, and octupole

$$\begin{aligned}
E1 \qquad & \hat{o}_{E1} = \epsilon \cdot r \quad , \\
E2 \qquad & \hat{o}_{E2} = \frac{i}{2}(\epsilon \cdot r)(k \cdot r) \quad , \\
E3 \qquad & \hat{o}_{E3} = -\frac{1}{6}(\epsilon \cdot r)(k \cdot r)^2 \quad , \\
M1 \qquad & \hat{o}_{M1} = c_m(\epsilon \times r) \cdot (L + 2S) \quad ,
\end{aligned} \tag{2.8.4}$$

whereas M1 is the magnetic dipole. Here, $c_m = \hbar/2m(\varepsilon_f - \varepsilon_i)$, while ϵ and k are respectively the polarization and wave number of the vector potential A. Normally, E1 is the predominant term, however, E2 and M1 terms may contribute significantly to the edge energy for heavy elements. For example, the weight of E2 is usually significant from 4500 eV onwards. These transitions are governed by the sum rules, namely, for dipole and quadrupole the angular momentum must vary respectively as $\Delta l = \pm 1$, and $\Delta l = 0, \pm 2$.

Although the mono-electronic theory may give good results, its validity is limited by many physical phenomena, like the *relaxation time of the core-hole* and *the time associated with kinetic energy of the photoelectron*. Both phenomena occur within the same timescale 10^{-15} - 10^{-16} s^{-1}, which means that to properly describe the physical evolution of the system after the absorption, one must take into account both events in the theoretical method. For this reason, normally a multi-electronic process approach is used, where all the possible transitions from core to the valence states are considered. This basically translates into inserting a sum over the all transition states in the cross section formula (Eq. 2.8.3).

A common approximation is to use a spherical potential around the absorbing atom such that spherical SE must be solved in order to evaluate the matrix elements $\langle \psi_f | \hat{o} | \psi_i \rangle$ within such volume. Among different approaches the finite-difference method (FDM) has been recently shown to be very efficient to calculating XANES and EXAFS spectra. [117, 118] Within the FDM approach one solves the SE by discretizing the coordinate space over a grid of points in the whole volume where the approximations are taken. The SE is then turned into a set of linear equations that are solved by using classical algebra solvers: for more details the readers are referred to [117, 119].

The potential expression is given by DFT methods, more specifically, the LSDA exchange-correlation functional is commonly used. The surrounding area of the electron is taken into account by the exchange-correlation potential which depends only on the density of the electron. For instance, Gaudry *et al.* showed that the LSDA functional reproduces satisfactorily the experimental features of Fe and Ti k-edge as well as the electronic transitions involved in the pre-edge region. [120] Although small in amplitude, the pre-edge signal carries valuable information regarding the coordination environment of the absorber atom. In this regard, we found that the intensity of the pre-edge peak of POMs, which is allowed by the hybridization between the d (Mo) and p (O) orbitals, progressively decreases as the POM is reduced. This is due to the evolution of a noncentrosymmetric environments to centrosymmetric one (Chapter 4).The LSDA potential is currently implemented in FDMNES program, [117] which has been used throughout this work to compute the Mo K-edge XANES spectra of POMs (see Chapter 4). DFT often fails to describe the absorption spectra when the probed electronic states are localized, as in the case of $L_{2,3}$ edges of d elements in different compounds. [121] An alternative option is the use of *time-dependent density functional theory (TDDFT)), which takes into account a part of the interaction between the core-hole and the photoelectron states. The application of TDDFT is normally restrained to the linear response (LR) regime. For instance, Joly et al. have shown that TDDFT calculations yield an improvement over the corresponding LSDA method within the muffin-tin (MT) approximation. [121] In contrast to the FDM approach, the MT approximation assumes that the potential has spherical symmetry within the MT spheres centered on the atoms, and is constant between spheres. This crude approximation fails to describe non-spherical effects which are often significant for many real systems, therefore, it has not been used in this work.*

Chapter 3

Redox Potentials of Polyoxometalates

3.1 Introduction

This chapter refers to the results of the first article listed in Section List of Publications at start of this manuscript, which was published in *J. Phys. Chem C* 2020, 124, 28, 15045-15056. The relationship between the authors and their contribution to the presented work are outlined in that section.

Our energy systems are rapidly evolving, driven by the challenges associated with decarbonisation and shifts in societal expectations. This requires a rethink in how we supply, manage and consume energy. As outlined in Chapter 1, the major challenge of renewable energy sources, like wind and solar, is their intermittent nature, and therefore an increasing interest in EESs was recently gained to manage the peaks and troughs in demand [122].

Amongst a wide variety of solutions based upon electrochemical storage [1], RFBs have recently attracted a significant amount of research interest as a safe and cost-effective energy storage technology for power grid applications [123]. Importantly, by storing the electro-active material in external tanks, RFBs are the only type of battery for which energy and power output can be scaled independently, making them highly flexible approaches to energy storage. Despite offering clear advantages, the current technology based upon the all-vanadium RFB [124], still suffers from distinct problems. Indeed, the main drawbacks are the slow kinetics and low number of electrons taking part in the redox reactions, which reduces the energy and power density of the battery. [2, 9]

To overcome this, there has been a significant research effort into developing high performing redox couples, which has focused upon transition metal ions [2, 125–127] or organic redox active materials [128–130]. For the former Polyoxometalates (POMs) have gained increasing attention because this class of discrete transition metal-oxide nanoclusters shows significant promise owing to their ability to store multiple electrons in a reversible manner. [131, 132] As outlined in Chapter 1, recently Friedl *et al.* [9] developed an asymmetric RFB based on $[SiW_{12}O_{40}]^{4-}$ (**SiW**$_{12}$) and $[PV_{14}O_{42}]^{9-}$ (**PV**$_{14}$) as anolyte and catholyte, respectively. They demonstrated that these POMs could exhibit fast redox kinetics alongside multiple electron transfers which enables the simultaneous high power density and capacity (10.7 A h L^{-1}).

The high energy density is related to the high number of electrons involved during the reduction of POMs, namely, four electrons for both **PV**$_{14}$ and **SiW**$_{12}$. However, only two one-electron reductions of **SiW**$_{12}$ are exploited, since the third redox wave, which is a two-electron reduction, irreversibly modifies the electrode leading to its decomposition and catalysis of the hydrogen evolution reaction. The electrochemistry of **SiW**$_{12}$ has been largely studied, [14] since this compound is the progenitor of several substituted POMs, which are commonly synthesized in laboratory. [9, 14] On the other hand, this is the first time that the **PV**$_{14}$ ion is produced, therefore, its structural and redox behaviour have been investigated only in this reference. [9] The ^{51}V NMR measurements revealed that 6 electrons are transferred to **PV**$_{14}$ during the reduction, whereas the oxidation was fully completed after removing 4 electrons from the polyoxoanion. The reason of this imbalance is believed to be the absence of a separator in the NMR tube during the analysis. As a consequence of this, reduced species diffuse out of the working electrode volume and go into the supernatant region, where these are replaced by fully oxidised **PV**$_{14}$. Similarly, during the oxidation, less **PV**$_{14}$ can be re-oxidised, because some of the reduced species is able to diffuse away from the working electrode. [9] In conclusion, by taking into account these effects, the authors estimate that the exact number of electrons reducing the POM is given by the average of reduction and oxidation processes, i.e. 4 electrons. Despite the uncertainties relative to the diffusion, it is worth noting that such a number of electrons is high compared to the VRFB, where the reduction of the redox couple V^{2+}/V^{3+} involves just one electron. [9]

The POM-based RFB proposed by Jochen *et al.*, is one of the most performing battery ever made, [9] and it represents a valid alternative to the commercial VRFB. However, on the basis of the above discussion, the mechanism behind the POM electrochemistry, in particular, the number of electrons reducing each POM type is not completely clear, and further analysis would definitely help to shed light on this aspect. Furthermore, how **PV**$_{14}$ and **SiW**$_{12}$ structures change after the reductions is not discussed in their work. [9] This aspect is extremely important, indeed, previous theoretical and experimental studies showed that the POM structure is strongly affected at high charge states. [8]

In addition to the asymmetric RFB of Friedl *et al.*, it is worth mentioning a new type of POM-based RFB recently proposed by Cronin *et al.* [27] They demonstrated that the polyoxoanion, $[P_2W_{18}O_{62}]^{6-}$, could act simultaneously as a high-performance redox flow battery electrolyte or as an electrolytic cell for the generation of hydrogen. This work is the subject of Chapter 5, and for more details, the reader can refer to this chapter.

Generally, the relationship between a POMs structure and its redox properties remains unclear and improving its understanding is crucial to design high-performing POM-based RFBs. Here, computational and theoretical chemistry can play a key role, yet predicting the redox behaviour of such systems remains a challenge. Due to their sizes, simulations are performed within the framework of density functional theory (DFT) in most cases. However, for anions exhibiting large charges this can be problematic owing to *self interaction error* (SIE) of DFT. Besides the SIE, the high charge state of some POMs means that careful consideration of the counter ions and the environment is needed. Indeed, in ref. [9], the authors reported that the hydrodynamic radius of $\mathbf{SiW}_{12}$ was ∼2 nm, much greater than the crystallographic radius (∼0.5 nm), which was attributed to the hydration shell of the anionic POM [133].

Early computational works simulating the stability and frontier orbitals of POMs considered only their structure without accounting for the electrolyte environment as well as the counter ions. In this regard, Poblet *et al.* showed that the relative stability as well as for the structure of α/β Keggin ions are not properly predicted by gas phase calculations, and the introduction of solvent effects by means of a continuum model is necessary. This was also demonstrated by Zhang *et al.*, who showed that the solvent effect is very important for $[XW_{12}O_{40}]^{n-}$ (X = Fe(II), Co(III), Zn(II)) ions at high charge states. [134] In addition, in their work these authors suggested that the DFT functional also plays an important role, for instance, after testing several GGAs, their results show that BP86 and PBE give the best comparison with experimental data. [134] However, as mentioned in the introduction, Poblet *et al.* showed that GGAs suffer from a poor description of the electron delocalization for singly-substituted Wells-Dawson ion, [45] and therefore, the inclusion of a certain amount of exact exchange gives results in better agreement with the experiment.

Therefore, it is clear that both elements, i.e. the choice of xc-functional and the incorporation of the solvent in the calculations, are fundamental to accurately describe POM structures.

As with structure calculations, theoretical works on the redox potentials of POMs [135,136] only focused on barely charged POMs, describing the solvent by a polarisable continuum model [137,138]. For instance, Aparicio *et al.* computed the redox potentials of singly-substituted Keggin ions, without adding counter ions to the POM. In that work, the solvent effect was included by the continuum COSMO model. [135] This simplification leads to strong uncertainties in the absolute reduction potential. However, shifts of the reduction potentials, relative to the unsubstituted Keggin ion, successfully reproduced the corresponding experimental data. [135] A similar approach was used by Poblet *et al.* to study the redox potentials of singly-substituted Wells-Dawson POMs. [45]. Their result showed that the reduction potentials obtained with DFT are less exothermic than they should. The authors highlight that the origin of these discrepancies with the experiment is due to the oversimplification of the real environment of POMs, namely an approximate treatment of the solvent effects, and the absence of explicit counter ions.

Large errors are likely due to the large negative charges which both exacerbate the SIE problem and are problematic for continuum solvent models [139]. Recently, Kremleva *et al.* [46] adopted a similar approach, but also included counter ions absorbed onto the surface of POM to neutralise the overall system. For a tri-Mn-substituted W-based Keggin ion, they tested a pure GGA (PBE) and several hybrid-GGA functionals, and found that the main structural parameters of POMs were not affected by the Li arrangement nor the xc-functional. Furthermore, they found redox potentials which were in good agreement with experiment, and were not sensitive to the Li arrangement, but they were rather dependent on the DFT functional used. [46] Specifically, the three hybrid functionals tested, TPSSh, B3LYP, and PBE0, yield reduction potentials which increase with the contribution of exact exchange in the hybrid functional. The best agreement for electron transfer (ET) reductions was given by the GGA functional PBE which underestimates the redox potential by 0.3 V, whereas the B3LYP was the best hybrid-GGA, with an overestimation of 0.5 V. [46] For proton-coupled electron transfer (PCET) reductions, the authors included the contribution of dissociation constants of the protonated POMs into the Nernst equation to reproduce the experimental pH dependence. But even in this case, the best agreement with the experiment was given by PBE, while the redox potentials from hybrid-GGAs show large deviations of about 0.6-1 eV. [46] The authors noted that the good performance of the pure GGA-PBE compared to hybrid methods was due to a fortuitous error cancellation. [140] Once again, another source of error is the approximate description of the solvent effects.

Motivated by their previous findings, the same authors [47] extended their initial work to include explicit solvent molecules (water) extracted from first principle molecular dynamics (FPMD) simulations. The POMs structures from the snapshots extracted from the FPMD were subsequently optimised while keeping the environment fixed. Two different type of reactions were taken into account, namely, an ET and PCET. The authors showed that inclusion of the solvent significantly improved the simulated redox potentials, but not quite as much as the effect of the exchange and correlation functional as shown by the better agreement of simulated redox potentials with experiment obtained using B3LYP compared to PBE. [47] For example, for the reduction of Mn from Mn^{4+} to Mn^{3+}, the deviation of the redox potentials obtained with PBE is 0.7 eV, while B3LYP yealds a deviations of about 0.1 eV. Similarly, PBE underestimates the redox potential of the redox couple Mn^{3+}/Mn^{2+} of about 0.6 eV, while the B3LYP results are more consistent showing the same amount of uncertainty. [47]

This approach has shown that a reasonable description of solvated counterions and the explicit treatment of the solvent are fundamental to compute accurate redox potentials. However, the strong discrepancy between PBE and B3LYP might hint at a potential weakness of this procedure, as only a small layer of solvating molecules was tested. Indeed, it was shown that larger solvation shells, and thus a high number of solvent molecules, are required to obtained converged dynamics. [7] Currently, FPMD represents still a challenge for large systems like POMs, and therefore a valid alternative is the use of a QM/MM approach, which can be adapted to much larger molecular systems (see Section 2.6).

Motivated by Jochen's work, [9] and by the challenge associated with the computation of redox potentials of POMs, in this work we decided to perform a theoretical investigation of $\mathbf{SiW}_{12}$ and $\mathbf{PV}_{14}$ POMs in order to understand the relationship between their structure and redox potentials. Besides gaining insights into their electrochemistry, from this work, we expect to provide a general procedure to predict accurate redox potentials of POMs.

Different theoretical methods were used to calculate the redox potentials of $\mathbf{SiW}_{12}$ and $\mathbf{PV}_{14}$. In the first case we adopt a thermodynamic cycle and use an implicit solvent model incorporating the counter ions to neutralise the overall system to calculate the free energies required for this cycle. In the second case we apply quantum mechanic/molecular mechanic (QM/MM) molecular dynamics (MD) simulations, where the solvent is treated explicitly, to study the evolution of POMs electronic structures and interactions with its environment as well as electrochemical behaviour. In this case the redox potentials are calculated using the thermodynamic integration (TI) and fractional number of electron (FNE) [92] approaches, both within the linear response (LR) approximation. We demonstrate that these methods are able to improve the description of the redox potentials for $\mathbf{SiW}_{12}$. However, owing to the larger structural changes upon reduction, the LR approximation breaks down for $\mathbf{PV}_{14}$. Our present results provides new perspectives for simulating the redox potentials of POMs, but also highlights remaining challenges.

3.2 Theory and Computational Details

In the following subsections the theoretical and computational details used throughout this work are outlined. Initially, the approach for describing the redox potential using an implicit solvent model is outlined and subsequently the two methodologies exploiting explicit solvation are discussed. More details of theory is given in Chapter 2.

3.2.1 Implicit Solvent Model

In this work the redox potentials have been calculated using a thermodynamic cycle as shown in Figure 2.7.1. Within this model the standard free energy of a reaction in solution is related to its standard free energy of reaction in gas-phase through Eq. 2.7.13. Here the Gibbs free energy has been calculated in two ways. In the first, we have neglected zero-point and entropic contributions to free energy of the reaction, often considered a small contribution. [46] Therefore the enthalpic component is equal to the free energy (i.e. $\Delta_r G^o_g(A_i|B_i) = \Delta H_g(A_i|B_i)$). In the second approach, the zero-point and entropic contributions have been included as

$$\Delta_r G^o_g(A_i|B_i) = \Delta H_g(A_i|B_i) + \Delta_{ZPE} - T \cdot \Delta S \tag{3.2.1}$$

The ZPE term has been computed by performing vibrational frequency calculations on the optimized gas-phase structures with an analytical solver for all the exchange and correlation functionals except TPSSh, [87] where a numerical solver was chosen. The thermochemistry calculations were performed at 298.15 K, and the entropic correction includes the vibrational, rotational, and translational contribution.

The standard redox potential of the reduction, U^o_{red}, is then related to the free energy of reaction in solution by the Eq. 2.7.8. Here, the Faraday constant is equal to 23.061 kcal mol^{-1} V^{-1}. Throughout we set $U^o_{abs}(NHE)$ = 4.24 eV [141].

For this part, all calculations have been performed using density functional theory as implemented within the ORCA quantum chemistry package [87]. Four different *x-c* functionals have been used, namely PBE [4], TPSSh [142], B3LYP [68] and PBE0 [70]. These functionals contain respectively (in that order) 0 %, 10 %, 20 %, and 25 % of HF exact exchange. As result of this, we expect to rationalize the effect of the energies and redox potentials as function of the amount of HF exact exchange present.

To assess the effect of the basis set, all structures were optimised by using either def2-SVP or def2-TZVP basis set [73] and a def2-ECP pseudopotential [75] for the heavier elements [46,135]. Unrestricted Kohn-Sham (UKS) theory was employed for all open-shell systems, while close-shell ones were treated by RKS. During the geometry optimisations, the total SCF energy was set to converge within 10^{-6} a.u., while the gradient converged to 10^{-4} a.u.

In each case to ameliorate challenges associated with the self-interaction error [143], all POMs have been neutralised using counter-ions, which were included in the geometry optimisations. The free energy of solvation, $\Delta G_S(X_i)$, of each component of the cycle was determined by using a CPCM approach as implemented in ORCA [87] using the dielectric constant and refractive index of water. The enthalpies of solvation of the proton and Na^+ were set to -264 kcal/mol and -97.74 kcal/mol, respectively. [144]

3.2.2 Explicit Solvent Model

The highly anionic nature of the POMs means that an explicit description of the solvent environment around the POMs is likely to be important. In this section we describe the methods used for explicitly describing the solvent molecules in a computationally efficient manner and the approaches used to exploit these simulations to simulate the redox potential.

3.2.3 QM/MM Molecular Dynamics

The explicit description of the solvent around the POM has been achieved using QM/MM MD. Throughout, all molecular dynamics simulations were performed by using the AMBER package. [82] The initial setup and equilibration of the system was achieved using classical molecular dynamics. Recently, several authors have proposed general force fields for POMs, [54–56] however, this remains elusive. Consequently, our force field consists of bonded terms derives from the potential energy from frequency calculations as described in the modified-Seminario method. [85] The non-bonded terms for all atoms were taken from the Universal Force Field (UFF). [86] Atomic charges have been calculated using the CHELPG method as implemented in ORCA. [87]

The initial setup from the classical MD was generated by solvating the optimised POM and counterions ions in a box of ≈ 3000 TIP3P water molecules. [145] The systems were subsequently equilibrated at a temperature of 300 K and room pressure using periodic boundary condition (PBC). These equilibrated systems were used as a starting point for the QM/MM MD of $\mathbf{SiW}_{12}$ and $\mathbf{PV}_{14}$. The QM region contains the POM plus the counterions, namely $\mathbf{SiW}_{12}$ and Na^+ ions in one case and the protonated $\mathbf{PV}_{14}$ in the other, while the remaining MM region is composed entirely of solvent molecules.

All QM/MM calculations were performed by interfacing ORCA [87] to AMBER. [82, 146] An electrostatic embedding approach was used to connect the QM and MM region. The QM region was described using density functional theory within the approximation of the PBE functional [4] with def2-SVP basis set [73] and def2-ECP pseudopotential. [75] Non-periodic boundary condition (NPBC) were used within the QM region, which sees only the periodic images of the MM region. PBC were applied to the MM region with a cutoff of 8 Å for long-range MM interactions, which have been treated by the particle-mesh Ewald summation. SHAKE has been applied to all bonds involving hydrogen atoms. [147] The dynamics were performed within the NPT ensemble with a Langevin thermostat. An initial equilibration of the QM/MM MD was performed for 5 ps. This was followed by an additional 10 ps pf QM/MM dynamics from which all of the properties were calculated.

Thermodynamic Integration

To determine the redox potential of the POMs from the QM/MM MD, we employ the thermodynamic integration (TI) method. Within the TI, the potential energy of the two systems (reduced and oxidised) are coupled through an order parameter, λ_i, such that the final potential is a mix of the two states as expressed in Eq. 2.7.23. It must be noted that only the final states $U(r,0) = U_{Ox}$ and $U(r,1) = U_{Red}$ have a physical sense, while other values of λ represent imaginary states. However, since the potential, U now depends on λ, so does the partition function leading to a free energy given by Eq. 2.7.24.

$$\Delta G = -\int_0^1 d\lambda \Big\langle \frac{\partial U}{\partial \lambda} \Big\rangle \tag{3.2.2}$$

In the LR approximation, used throughout this work, the free energy derivative is assumed to be linear with respect to λ, the free energy is given by Eq. 2.7.27

$$\Delta G_{Ox/Red} = \frac{1}{2}(\langle \Delta U \rangle_{Ox} + \langle \Delta U \rangle_{Red}) \tag{3.2.3}$$

Here $\langle \Delta \mathrm{U} \rangle_{Ox}$ is given by the ionisation potential (IP) of the oxidised species, and $\langle \Delta \mathrm{U} \rangle_{red}$ from the electronic affinity (EA) of reduced species. In this way one only needs to compute the vertical energy gap (VEG) for each state, i.e., Ox and Red (Section 2.7.2).

We assess the validity of the LR approximation by computing the reorganisation energy in two different ways. The total reorganisation energy is the sum of the inner-sphere (λ_i) and outer-sphere (λ_o) energies, i.e. $\lambda_{tot} = \lambda_i + \lambda_o$. However, we only focus on the λ_o, which is normally gives the major contribution to the λ_{tot}.

In the LR regime, the λ_o can be computed from Eq. 2.7.31. Furthermore, provided that the fluctuations of each energy gap, $\langle \Delta U \rangle$ have a Gaussian distributions, it is possible to write the root-mean square deviations of the energy gap as $\langle \delta \Delta U \rangle_M^{1/2} = \sigma_M$, M = Ox or Red, and therefore to define outer-sphere reorganisation energy as given in Eq. 2.7.32. If the reorganisation energy computed from Eq. 2.7.31 and 2.7.32 are similar, the LR approximation is valid, and the redox process results to be in the Marcus regime. Therefore, we compare these two equation to estimate whether deviation from the LR approximations are present in each redox process. [108]

Throughout this work, the VEG, $\langle U_{Ox} - U_{Red} \rangle_{Ox}$ required in Eq. 2.7.27 has been calculated by randomly selecting 60 snapshots from the 10 ps of QM/MM MD. Each snapshot included the POM, counter ions and 6 Å of solvent molecules surrounding it. Single point calculations, without any additional geometry optimisations, were performed on each snapshot by using DFT within the approximation of PBE [4] functional, def2-TZVP basis set [73], def2-ECP [75], and conductor-like polarisable continuum model (CPCM). [87]

Fractional Electron Approach

While the LR-TI approach offers an efficient approach to simulating larger systems, it still requires knowing the energy of oxidised and reduced species at all oxidised and reduced geometries sampled during the molecular dynamics, An alternative approach is the fractional number of electrons (FNE) proposed by Zeng *et al.* [92]. Here, instead of mixing two potential functions, the FNE gradually changes the number of electrons in the system. The physical implications of the fractional electron can be interpreted as the probability of the electronic distribution on the highest occupied molecular orbital (HOMO) of the solute.

The use of FNE is physically justified by the Janak theorem, which states that the energy derivative with respect to the electron occupation state is equal to its HOMO energy

$$\frac{\partial E}{\partial \eta} = -\epsilon_{HOMO} \tag{3.2.4}$$

Here η indicates the fractional number of electron. Thus, the redox free energy can be then computed by the thermodynamic integration of HOMO energies at different η values

$$\Delta A_{Ox/Red} = -\int_0^1 d\eta \left(\frac{\partial A}{\partial \eta}\right) = -\int_0^1 d\eta \langle \epsilon_{HOMO} \rangle_\eta \tag{3.2.5}$$

As shown for LR-TI, assuming the LR approximation for the FNE, Eq. 3.2.5 (λ = 0 and 1) becomes

$$\Delta A_{Ox/Red} = \frac{1}{2}(\langle \epsilon_{HOMO} \rangle_{Ox} + \langle \epsilon_{HOMO} \rangle_{Red}) \tag{3.2.6}$$

Note that in case of linear response $\langle \epsilon_{HOMO} \rangle_M = \langle \Delta U \rangle_M$. The main advantage of Eq. 3.2.6 is that only requires the knowledge of HOMO energies of each state Ox and Red at their own geometries, halving the number of simulations to be performed with respect to the LR-TI approach.

Throughout this work, the $\langle \epsilon_{HOMO} \rangle_M$ required in Equation 3.2.5 was calculated from 60 randomly selecting snapshots from the 10 ps of QM/MM MD. Each snapshot included the POM, counter ions and 6 Å of solvent molecules surrounding. Single point calculations, without any addition geometry optimisations, were performed on each snapshot by using DFT within the approximation of PBE [4] functional, def2-TZVP basis set [73], def2-ECP [75] and conductor-like polarisable continuum model (CPCM) [87].

3.3 Results

In the following sections we present our results for computing the redox potential using implicit and explicit solvation models. The latter, achieved using molecular dynamics also provides insight into the structural, solvent and charge distributions associated with the POMs, which are subsequently discussed.

3.3.1 Redox Potentials using Implicit Solvent Model

Using the thermodynamic cycle outlined in the previous section, we have computed the standard redox potentials (U^o_{red}) for **PV**$_{14}$ and **SiW**$_{12}$. For the former, previous work [9, 148] has identified that reduction is accompanied by protonation, i.e. proton coupled electron transfer (PCET). This is expressed as

$$H_m[PV_{14}O_{42}] + nH^+ + ne^- \rightarrow H_{m+n}[PV_{14}O_{42}] \tag{3.3.1}$$

where m corresponds to the initial number of H$^+$ bound to the PV$_{14}$ to neutralise it, n is the number of protons and electrons transferred. For **SiW**$_{12}$ [9, 133, 149] the reduction is expressed as

$$Na_m[SiW_{12}O_{40}] + ne^- + nNa^+ \rightarrow Na_{n+m}[SiW_{12}O_{40}] \tag{3.3.2}$$

where m is the initial number of Na$^+$ counter ions and n is the number of electrons and cations transferred. Table 3.3.1 shows the standard redox potentials for the reduction of **SiW**$_{12}$, calculated as two sequential one electron processes and a single two electron reduction [9, 133, 149]. This has been calculated for 4 different exchange and correlation functionals with increasing amounts of Hartree-Fock exchange (0 % PBE , 10 % TPSSh, 20 % B3LYP, 25 % PBE0), two types of basis set and also with and without the contributions from ZPE and entropy.

Table 3.3.1: U^{o}_{red}vs NHE (V) values calculated using 4 different DFT *x-c* functionals, 2 basis sets and with or without the effect of zero point energy (ZPE) and entropy. Here (m,n) refers to Eq. 3.3.2.

	(m,n)	Basis Set	PBE	TPSSh	B3LYP	PBE0	Exp. [9]
Redox State[a]							
$Na_{m+n}[SiW_{12}]$	(4,1)	def2-SVP	0.517	0.528	0.544	0.588	
		def2-TZVP	0.176	0.077	0.172	0.150	0.01
	(5,1)	def2-SVP	0.129	0.002	-0.014	-0.048	
		def2-TZVP	-0.115	-0.277	-0.257	-0.299	-0.21
$Na_6H_2[SiW_{12}]$		def2-SVP	-0.635	-0.641	-0.689	-0.713	
		def2-TZVP	-0.699	-0.473	-0.763	-0.802	-0.37
Redox State[b]							
$Na_{m+n}[SiW_{12}]$	(4,1)	def2-SVP	0.358	0.359	0.399	0.430	0.01
	(5,1)	def2-SVP	-0.042	-0.157	-0.265	-0.203	-0.21
$Na_6H_2[SiW_{12}]$		def2-SVP	-0.670	-0.731	-0.721	-0.778	-0.37

[a] Without ZPE and Entropy
[b] Including ZPE and Entropy

The results show an effect of the exchange-correlation functional which is typically between 0.1-0.2 V, which is not as strong as previously reported [46]. In contrast, the effect of the basis set is much larger, in line with previous work [46, 135]. Indeed, for this implicit solvation model, changing a def2-SVP basis to a def2-TZVP basis causes changes as large as 0.35 V for the first reduction of $\mathbf{SiW}_{12}$. In all cases, the larger basis set reduces the reduction potential and therefore the first two one electron reductions of $\mathbf{SiW}_{12}$ become in much better agreement with experimental values. However, the final two electron reduction become slightly further away. The addition of ZPE and entropy effects, only possible at def2-SVP level in the present case, decreases the U^{o}_{red} by $\leq$0.15 V.

The deviation between experiment and theory is consistent with previous recent work by Kremleva *et al.* [46], indicating that the observed uncertainties are within the limits of the implicit solvation model. We now turn our attention to $\mathbf{PV}_{14}$, whose electrochemistry has been significantly less studied. Recently, Friedl *et al.* [9] reported a U^{o}_{red} = 0.6 V. However, as the redox waves were multi-electron transitions, the overlap of many redox reactions made

Table 3.3.2: U^{o}_{red}vs NHE (eV) values calculated for the reaction 3.3.1 with 4 DFT *x-c* functionals, 2 basis sets with or without the effect of zero point energy (ZPE) and entropy. Their values are compared to experimental data. [9].

	(m,n)	Basis Set	PBE	TPSSh	B3LYP	PBE0	Exp. [9]
Redox State[a]							
$H_{m+n}[PV_{14}]$	(9,1)	def2-SVP	1.609	1.934	2.101	2.327	
		def2-TZVP	1.718	2.202	1.855	2.022	
	(9,2)	def2-SVP	0.839	1.208	1.093	1.161	
		def2-TZVP	0.923	1.120	0.951	0.802	
	(9,3)	def2-SVP	0.845	1.754	1.211	1.082	
		def2-TZVP	0.902	1.261	1.199	1.355	
	(9,4)	def2-SVP	0.392	0.493	0.412	0.397	
		def2-TZVP	0.516	0.552	0.705	0.575	0.60
Redox State[b]							
$H_{m+n}[PV_{14}]$	(9,1)	def2-SVP	1.615	1.968	2.093	2.313	
	(9,2)	def2-SVP	0.856	1.247	1.365	1.301	
	(9,3)	def2-SVP	0.822	1.065	1.168	1.033	
	(9,4)	def2-SVP	0.362	0.461	0.685	0.508	0.60

[a] Without ZPE and Entropy
[b] Including ZPE and Entropy

it difficult to determine exact potentials and determine exactly how many electrons were transferred. The authors estimated that $\mathbf{PV}_{14}$ can be reduced by approximately four electrons, although this could increase to as many as seven electrons upon increasing the acidity of the solution. [9] Table 3.3.2 shows the reduction potentials calculated for $\mathbf{PV}_{14}$ for a single PCET, two (9,2), three (9,3), and four (9,4) simultaneous PCETs, both with and without ZPE and entropic contributions.

In contrast to $\mathbf{SiW}_{12}$ a larger effect of the *x-c* functional is observed. This is strongest for a comparison between the PBE and PBE0 functionals in all reactions, and is consistent with previous work. [46] A difference of ∼0.4-0.5 V is observed between these two functionals for the (9,1) and (9,2) reductions and the origin of this difference is expected to be the fraction of Hartree-Fock exchange. A smaller deviation of 0.1 V is observed for both (9,3) and (9,4), which is important for the QM/MM MD simulations presented later.

The effect of the basis set is reduced compared to **SiW**$_{12}$ and its influence is comparable to the *x-c* functional with a typical change between 0.1-0.2 V observed. This is due to different transition metal elements constituting the POM. In fact, the valence electronic configuration of the vanadium does not contain f functions, and a small basis set like the def2-SVP can provide good results. Conversely, for third-row transition metals like the tungsten, the def2-SVP does not suffice to describe its electronic valence, and a bigger basis is needed.

From Table 3.3.2, one can see that the best agreement with experiment is provided by the (9,4) reaction, where a small deviation of $<$0.1 V is observed from the B3LYP and PBE0 values and 0.24 V from the PBE value. The PBE functional also returns U^o_{red} values for (9,2) and (9,3) relatively close to the experimental redox potential. However, Batista *et al.* showed that pure GGA functionals, like the PBE, tend to underestimate the computed redox potentials compared to the hybrid-GGA functionals. [140]. Thus, since the PBE gives lower U^o_{red} values than the other functionals for all the reactions, it means that the closeness of PBE U^o_{red} values for (9,2) and (9,3) is the result of such underestimation, and not of the accuracy of predicting the correct reaction. This is confirmed by the larger deviation from experiment observed for the hybrid functionals.

Finally, it is worth noting that the reduction of **PV**$_{14}$ is pH-dependent, since it occurs through PCETs. Further insights into possible reaction pathways can be obtained by combining the electron transfers (ETs) and proton transfers (PTs) occurring for each individual redox intermediate. This analysis leads to the construction of Pourbaix diagrams, which depicts all possible species for a given potential and pH. Such an approach has previously been shown to provide good results for POMs, where only one PCET was studied [46]. Generally, the use of Pourbaix diagrams has been shown to predict redox potentials within an error of 0.1 V. [103] However, it becomes extremely computationally expensive when multiple intermediates need to be accounted as in the **PV**$_{14}$ case. Besides, the uncertainty of 0.1 V obtained from the computed U^o_{red} values of (9,4) is already a good result, and thus we do not discuss it in this work.

3.3.2 Redox Potentials using Explicit Solvation

In the previous section an implicit solvent model was used to calculate the redox potentials. However, an explicit description of the solvation environment of the POMs is expected to play crucial role. Indeed, the diffusion coefficients of many POMs consider a hydrodynamic radius larger than crystallographic radius of the POM structure due to the strong binding of the first hydration shells to these charged species. [133] Consequently, in this section we perform QM/MM MD to provide further insight into the redox potential of these species in the presence of explicit solvation. It is worth noting that throughout this section a def2-TZVP basis set has been used, however, the influence of the basis set is much reduced compared to the results discussed for the implicit solvent models.

Table 5.3.1 shows the redox potentials for the first two one electron reductions of **SiW**$_{12}$ calculated using the LR-FNE and LR-TI methods outlined above. This shows that both approaches yield redox potential which are in good agreement with one another and are closer to the to experiment than the implicit solvent model approach. Furthermore, the values of λ' and λ calculated for the LR-TI method differ only of about 2 kcal/mol and such a small deviation [38, 108] is consistent with the validity of the LR approximation. This illustrates the importance of explicit description of the solvation shell in predicting the redox properties of POMs. Table 3.3.4 shows the energetics, redox potentials and reorganisation energies for the simultaneous

Table 3.3.3: Calculated electron transfer energies, redox potentials U^o_{red}, and reorganization energies for the **SiW**$_{12}$ by using the LR-FNE and LR-TI approaches from the QM/MM dynamics[a]

		LR-FNE		LR-TI	
$Na_{m+n}[SiW_{12}]$		(4,1)	(5,1)	(4,1)	(5,1)
	$\langle\Delta\mathbf{E}\rangle_{ox}$	-118.25	-96.28	-91.65	-84.85
	$\langle\Delta\mathbf{E}\rangle_{red}$	-78.56	-84.19	-104.95	-103.22
	λ	-	-	6.64	9.18
	λ'	-	-	7.06	7.98
	$\mathbf{U}^o_{red}$	0.027	-0.229	0.022	-0.162

[a] All energies are in kcal/mol, whereas the redox potentials in V.

multiple electron reduction of $\mathbf{PV}_{14}$. In contrast to $\mathbf{SiW}_{12}$, the redox potentials show significant difference between each other and the experiment. Indeed, for the LR-TI approach, a deviation from experiment of 0.8 V is found, much larger than for the implicit solvent model. However, the reason for this deviation becomes clear when comparing the calculated reorganisation energy, as λ' deviates by ~75 kcal/mol from λ, indicating the breakdown of the LR approximation. This is due to the larger structural change observed in $\mathbf{PV}_{14}$ upon reduction compared to $\mathbf{SiW}_{12}$. Besides the breakdown of the LR approximation, there still remains large deviations between the TI and FNE approaches. This is because the energy of the HOMO orbital is destabilised (-110 kcal/mol) compared to what it should be, ~ -500 kcal/mol to retrieve the correct redox potential. This error can be traced back to the decreasing HOMO-LUMO gap which arises from the edge waters that are unsaturated and robbed of their hydrogen bonding partner [150] in setting up the cluster model. Importantly, in contrast, the total energy used in the LR-TI method is less affected by this. This limitation can be overcome, as proposed in ref. [150] by adopting a large system with periodic boundary conditions and Hartree-Fock exchange in the functional. However, due to the size of the present system, this has not been possible.

Table 3.3.4: Calculated electron transfer energies, redox potentials U^{o}_{red}, and reorganisation energies for the PV_{14} by using the LR-FNE and LR-TI approaches from the QM/MM dynamics[a]

		LR-FNE	**LR-TI**
$H_{m+n}[PV_{14}]$		(9,4)	(9,4)
	$\langle \Delta \mathbf{E} \rangle_{ox}$	-120.90	-442.81
	$\langle \Delta \mathbf{E} \rangle_{red}$	-140.24	-595.63
	λ	-	76.41
	λ'	-	2.79
	$\mathbf{U}^{o}_{red}$	-2.82	1.38

[a] All energies are in kcal/mol, whereas the redox potentials in V.

In addition to the edge waters issue, a common characteristic of the many DFT functionals, such as PBE, is that for charged systems or molecules with the excess of electrons on localized or strong donor sites, such as can be the terminal and bridging oxygens of POMs, can lead to a wrong evaluation of HOMO and LUMO orbitals due to a strong SIE. [43, 44] As outlined in Chapter 1, a large SIE is due to the incorrect behaviour of almost all E_{xc} functionals far from a nucleus, indeed, these decay exponentially rather than asymptotically. [43] Crucially, these two aspects do highlight the limitations of the LR-FNE approach for systems with this size. One possible solution would be to use range-separated (RS) hybrid xc functionals, which return accurate energies and redox potentials for a large class of compounds. [112,151] For instance, Mikkelsen *et al.* calculated the the one-electron reduction and oxidation potentials of azulene-1-carbonitriles by using the RS CAM-B3LYP functional. [152] Importantly, the data were extracted directly from implicit solvation calculations, avoiding thus the use of the thermodynamic cycle. In that work, they found that CAM-B3LYP gives redxo potentials with a mean absolute error of 0.02 V, while the hybrid Minnesota M06-2X functional returns deviations in the range of 0.2-0.3 V. [152] Recently, Kar *et al.* have studied the performance of RS functionals in reproducing the vertical oxidation energy, reduction energy, and the frontier orbital energies of 113 molecules taken from the IP131 database. [153] Their results showed that the oxidation (reduction) energy computed by RS functionals, like LC-BLYP and LC-wPBE, return deviations of about 3 eV (2eV) in an implicit environment, whereas the RS hybrid CAM-B3LYP shows a deviation of 0.5 eV. [153] However, the authors claim that the good performance of CAM-B3LYP might due to error cancellations originating from DFT and implicit solvent methods.

3.3.3 Solvent and Structural POMs Distributions from QM/MM MD

Besides enabling the calculation of redox potentials, the QM/MM MD of $\mathbf{SiW}_{12}$ and $\mathbf{PV}_{14}$ are able to provide detailed insight into the structural dynamics of the POM, the solvent environment and its interactions with the counter ions and the charge distribution within the POM upon reduction.

3.3.4 The Effect of Reduction on Geometry

For the geometric structure of the POM upon reduction, we focus on the metal-metal, metal-oxygen distances, which are the key features that underline the change in the POMs structure. Figure 3.3.1 shows the structural distribution extracted from the QM/MM MD simulations for $\mathbf{SiW}_{12}$ (left) and $\mathbf{PV}_{14}$ (right). It is usually observed that the structure of the POM is not strongly affected by redox states when only few electrons are involved [14].

This is consistent for **SiW_{12}** for which only a very small change in the geometry of the metal-metal (M-M), metal terminal-oxygen (M-O_t), and metal bridging-oxygen (M-O_1) distances are observed for all three charge states, as shown by the strong overlap between the distributions of each structural parameter. The average M-M distance is ∼3.6 Å, the average M-O_1 distance is ∼1.97 Å and M-O_t is 1.73 Å. These are all in excellent agreement with the structure found using X-ray crystallography [154], confirming the validity of the QM/MM MD simulations. A larger variation in the structures is observed for **PV_{14}** and this is a strong contributing factor to the breakdown of the LR approximation discussed in the previous section. The average V-V_c distance decreases by ∼0.1 Å. This is accompanied by the opposite trend for the V-O_t and V-O_1 distances where an increase of ∼0.07 and ∼0.05 Å, respectively is observed. This trend is consistent with other transition metal oxo complexes, where double bonds between the metal and terminal oxygen becomes single bonds when the oxygen is protonated. [18] These results suggest that the synergistic combination of M-M shortening and M-O extension is a key factor that permits the **PV_{14}** to undergo multiple reductions.

3.3.5 Electron Delocalisation upon Reduction

Besides the geometric structure, the electronic structure of the POM upon reduction plays a crucial role [155] and has been proposed to facilitate fast electron transfer [156]. Recently Friedl *et al.* [9] used NMR to observe that upon reduction of **PV_{14}**, the diamagnetic V(V) peaks are simultaneously transformed to paramagnetic V(IV), indicating that the added electrons are delocalised.

To rationalise this NMR data, we investigated the HOMO orbitals obtained from representative QM/MM snapshots by performing single-point calculations with PBE and PBE0 functionals. Previous studies showed that hybrid-GGAs best describe the HOMO delocalisation in substituted POMs, [14, 135] with over delocalisation occurring in GGA functional due to the SIE. Figure 3.3.2 shows the HOMO orbitals obtained from representative QM/MM snapshots for Na_5SiW_{12} (Na_5), Na_6SiW_{12} (Na_6), and $H_{13}PV_{14}$ (H_{13}) calculated using PBE and PBE0. Regardless of the functional, we observe that in all 3 cases the HOMO is composed of a mix of d (W or V) and non-bonding p (O) atomic orbitals, which is a common element of Keggin-ion POMs, where the metal centres are not entirely in a perfect octahedral geometry. [14, 37, 65] Regarding the extent of delocalisation, Figure 3.3.2a shows

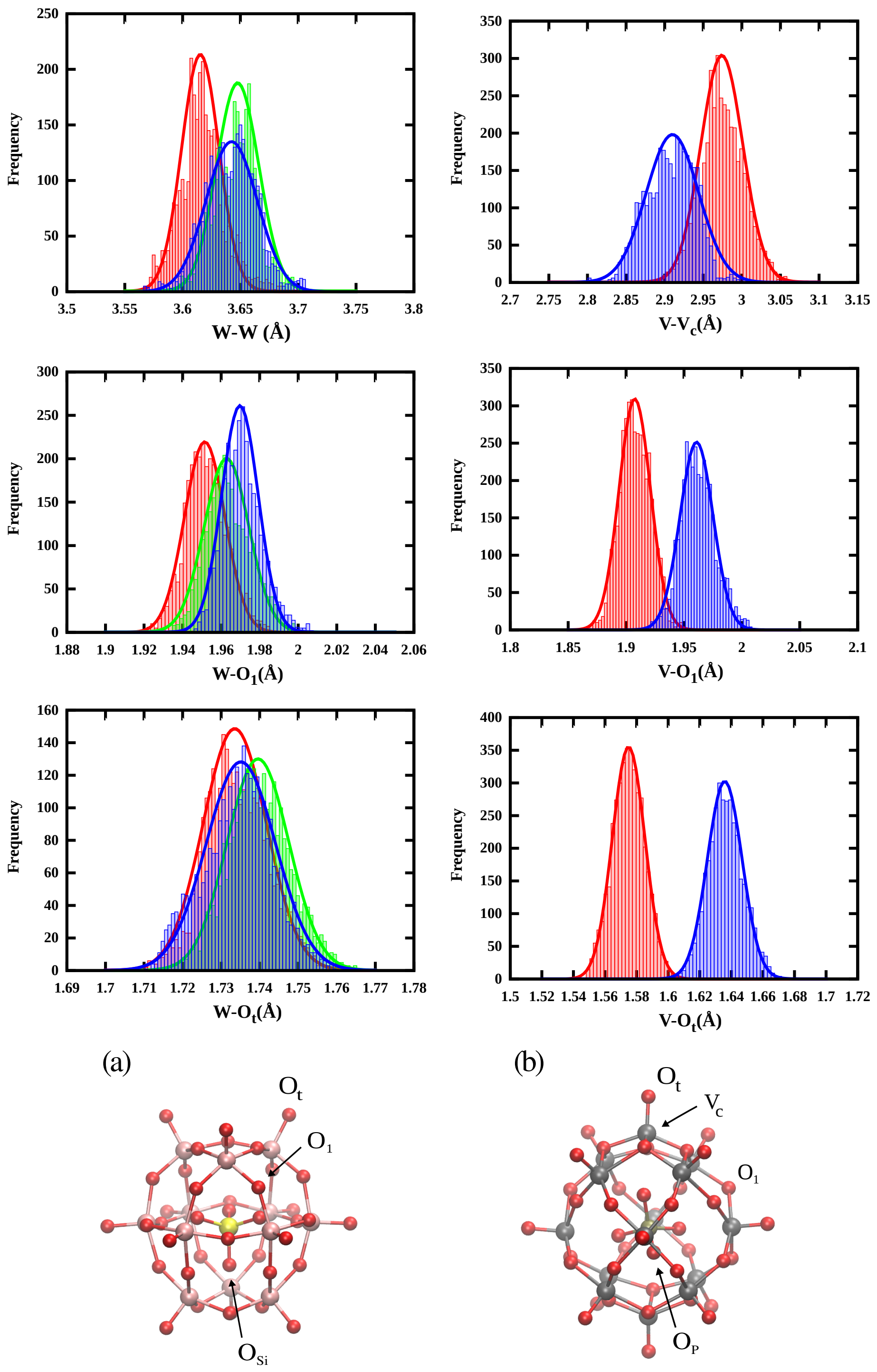

Figure 3.3.1: Distributions of W-W, W-O_{si}, W-O_t, and W-O_1 along 10 ps QM/MM dynamics of Na_xSiW_{12}, x = 4 (red), 5 (green), and 6 (blue). **(b)** Distributions of V-V_c, V-O_p, V-O_t, and V-O_1 along 10 ps QM/MM dynamics of H_9PV_{14} (red) and $H_{13}PV_{14}$ (blue). All distributions have been fit with a Gaussian function. **(a)** Structural parameters of **SiW**$_{12}$ and **(b)** of **PV**$_{14}$.

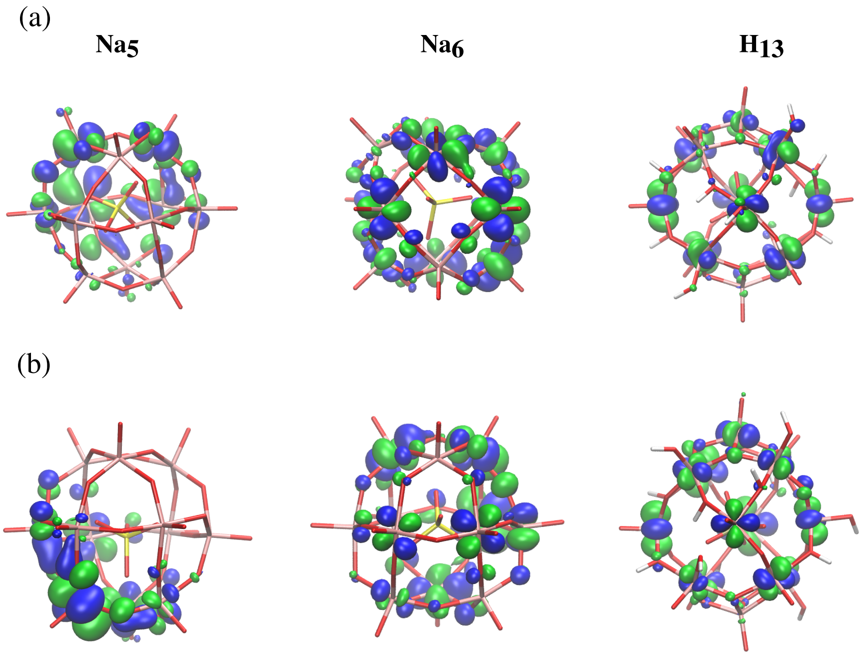

Figure 3.3.2: **(a)** HOMO calculated from a single QM/MM snapshot at PBE and **(b)** PBE0 level of theory. Water and sodium atoms are not shown for clarity.

that for Na_5SiW_{12}, the electron is partially localised only on nine out of the twelve W atoms. Such localisation is even stronger in the HOMO from the PBE0 results, where the electron is delocalised over six W atoms.

However, in contrast, the HOMO of Na_6SiW_{12} and $H_{13}PV_{14}$ is delocalised over the whole POM in both PBE and PBE0 case. This result suggests that, with the exception of the first single electron reduction, all metals atoms are involved during the reduction of $\mathbf{SiW}_{12}$ and $\mathbf{PV}_{14}$, consistent with previous work [9].

This delocalisation increases the overlap with the wavefunction on neighbouring molecules facilitating thus the electron transfer to the POMs.

3.3.6 POM Counter Ion Interaction

Figure 3.3.3 shows the radial distribution function (RDF) of Na^+ to the oxygen atoms in $\mathbf{SiW}_{12}$. Leroy *et al.* computed the diffusion coefficients of $\mathbf{SiW}_{12}$ as function of the hydrodynamic radius created with K^+, Na^+, and Li^+ ions. [52] In that work, they found that the diffusion coefficients increase as follow: $K^+ \approx Na^+ > Li^+$. This is due to the formation of closed ion pairs between larger cations, like K^+ and Na^+, with the POM, while the small Li^+ ions form semi-closed ion pairs, whose hydrodynamic radius depends on the number of water molecules solvating both ions. [52]. In contrast to **SiW**$_{12}$, their results showed that for POM with higher charge states, like $[AlW_{12}O_{40}]^{5-}$, the trend is inverted. [52] This last case suggests that the scenario might change for **SiW**$_{12}$ at high charge states. For instance, in Chapter 4 one can see that solvating **PMo**$_{12}$ by a high number of Li^+ ions lead to the formation of two type of ions pairs: a closed- and semi-closed ion pairs. In this work we took into account only the Na^+ ions, since these give higher diffusion coefficients, which means higher power density for the battery. In addition, in contrast to Leroy's work, [52] our QM/MM simulations have a high computational cost compared to classical MD, and therefore, a detailed investigation of the role of different cations, like Li^+ and even the proton, is beyond the scope of this work.

A similar analysis is not performed for **PV**$_{14}$, as the counter ions are bound to the POM. This RDF exhibits a first peak at 2.2 Å for all three oxidation states, and this corresponds to the closed ion pair interaction between the Na^+ and both the bridging and terminal oxygens in the POM. Such behaviour can be simply understood in terms of classical Coulomb interactions, i.e. rather than interacting with only one oxygen atom, a single Na^+ cation more likely occupies the center of both 3-fold and 4-fold hollow sites because of the higher attraction generated by these sites. There is very little exchange between interaction of the POM and bulk solvation observed through the QM/MM dynamics as indicated by the strength of the peak, which is almost completely separated from the other bands in the RDF. For $Na_4[SiW_{12}]$, the second peak is observed at just under 6.0 Å and this corresponds to a solvation shell of the Na ion interacting only with the bridging oxygens. For $Na_6[SiW_{12}]$, this peak becomes weaker but a large peak at 4.0 Å emerges, which corresponds to the interaction of counter ions with the terminal oxygen. These are weaker interactions and therefore exchange between the two solvation sites is observed during the QM/MM dynamics. The preference for the interactions with the terminal oxygen for high charge states is consistent with the increased negative change on these sites upon reduction. All of these interactions are also closed ion pairs.

3.3.7 Solute-Solvent Interactions

Figure 3.3.4 shows the RDFs for the terminal oxygens and the hydrogen and oxygen atoms in the water for **SiW**$_{12}$ and **PV**$_{14}$. As expected, in all cases, the

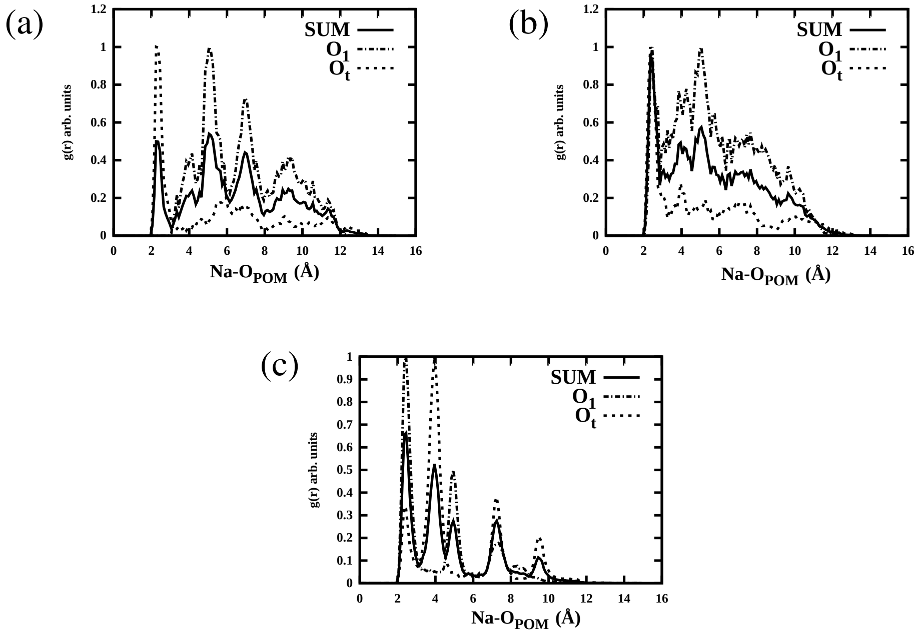

Figure 3.3.3: RDFs of terminal oxygen (O_t)-Na, bridging oxygen (O_1)-Na distance and their sum for Na_4SiW_{12} (a), Na_5SiW_{12} (b) and Na_6SiW_{12} (c).

RDF to the hydrogens begins at shorter distances that the oxygens, indicating an orientation driven by partial charges on each site required to solvate the POM. For $\mathbf{SiW}_{12}$, the solvent structure of Na_4 and Na_5 shows very little variation. However, for Na_6 a significant increase in the distance between the POM and the solvent occurs leading to weaker solute-solvent interactions and solvent structure. This is because the larger charge of the POM increases the interaction between the counter ion and the POMs expelling the nearby solvent molecules. This reflects a desolvation of the POM at higher charge states, as it prefers to interact with the counter ion rather than the solvent.

Further insights into the effect of the POM solvation environment can be obtained from their hydrodynamics radius r_{hydro}, representing the radius the POM and surrounding solvent environment which influences the diffusion rate. This is estimated by inserting the diffusion coefficient for $\mathbf{SiW}_{12}$ into the Stokes-Einstein equation, $D_{coeff} = k_BT/6\pi\eta r_{hydro}$, where $\eta = 8.91 \times 10^{-4}$ kg m^{-1} s^{-1} (water viscosity). The Stokes-Einstein equation can be also expressed as $D_{coeff} = \lim_{t\to\infty} \partial < MSD > /\partial t$, in which $< MSD >$ is the averaged mean square displacement. In order to calculate D_{coeff}, we extracted the averaged MSD over the time, and compute the slope of the graph, which gives the average $< MSD >$. This is then inserted into the Stokes-Einstein to return the diffusion coefficient. The calculated D_{coeff} values for each POM is $\sim 2 \times 10^{-5}$ cm^2s^{-1} which yields a r_{hydro} of $\sim$2.0 nm in each case. This is in excellent agreement with the experimental data of ref. [9], which estimate a

$r_{hydro} \geq 2$ nm. This is also in agreement with the RDFs shown in Figure 3.3.4, which show a first solvation shell ∼0.6 nm, which when added to the POM radius of 1.1 nm gives an estimated r_{hydro} of just under 2 nm.

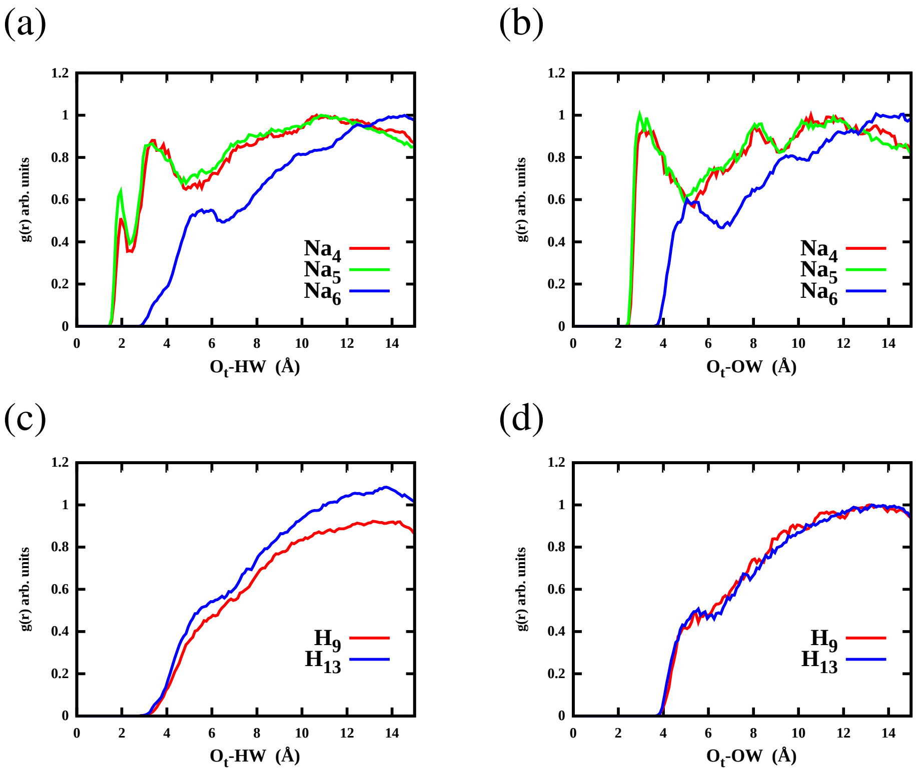

Figure 3.3.4: RDFs between the terminal oxygens of the **SiW**$_{12}$ with the hydrogen (a) and oxygens (b) on the water. RDFs between the terminal oxygens of **PV**$_{14}$ with the hydrogen (c) and oxygens (d) on the water

Previous molecular dynamics simulations of the $PW_{12}O_{40}^{3-}$ Keggin POM [50] using an entirely classical force field, has proposed that hydrogen bonds with a distance of about 2.5 Å could form between the terminal oxygens (O_t) and the hydrogens atoms of water molecules. However, in this case the counter ions were Na^+ which do not bind to the POMs as strongly as the H^+ used in the present case. Thus, the peaks at 2-3 Å (Figure 3.3.4a for **SiW**$_{12}$) represent the POM-water interaction through the formation of hydrogen bonds. For our present work using QM/MM, the picture obtained from **PV**$_{14}$ is somewhat different. The RDFs (Figure 3.3.4c and d) show, in contrast to **SiW**$_{12}$ and other simulations [50], a rather structureless solvation. This is because the solvent molecules are further away from the terminal oxygens, meaning the interaction between the POM and the solvent is weaker. In this case, hydrogen bond interactions between a water molecule and POM have been calculated to be ∼8 kcalmol^{-1}, as this is weaker than hydrogen bonding in water it is more energetically favourable for the surrounding water molecules to interact with themselves rather than the POM. Similar situations have previously been reported for the solvation of small ions in water [157].

3.4 Conclusions

In this present work we have computationally studied two POMs, namely $\mathbf{SiW}_{12}$ and $\mathbf{PV}_{14}$, which have recently been used to achieve high performance in redox flow batteries (RFBs) [9] offering a flexible solution to electrochemical energy storage. Our aim has been to explore the factors most strongly affecting the ability to calculate the redox potentials of these systems, but also to provide atomistic insight in the electronic and geometric factors controlling it.

Using DFT calculations combined with a thermodynamic cycle, we have calculated the redox properties using an implicit solvent model. Throughout this part we have reduced the influence of the self-interaction error in DFT by neutralising the highly charged species by including counter ions into our model systems. The results, especially for the larger def2-TZVP basis show a good agreement between theory and experiment, with uncertainties within 0.1 V for the $\mathbf{PV}_{14}$ reaction and the second reduction of $\mathbf{SiW}_{12}$. However, higher deviations of 0.3 V are observed for the remaining $\mathbf{SiW}_{12}$ redox potentials. This highlights that the efficiency of using an implicit solvent model depends on the nature of the charged POM, and the highly charged nature of these species means that a strong interaction with the surround solvent can be expected and should be included to achieve accurate simulations.

In order to further reduce the uncertainties in the redox potentials, we have also performed QM/MM MD simulations combined with thermodynamic integration (TI) and fractional number of electrons (FNE) method, both within the linear response (LR) approximation. We demonstrate that explicitly including the solvent environment can significantly improve the calculated redox potentials, which is especially evident for $\mathbf{SiW}_{12}$. However, for $\mathbf{PV}_{14}$, the large structural change associated with the addition of four electrons leads to a breakdown of the LR approximation made throughout this present work. Indeed, the LR response approach has been achieved by only the samplings from the final states of a reaction. [38,112,158,159] Recently this has been shown to be a good approximation for many reactions [112], however, for reactions such as proton-coupled electron transfer, redox potentials at several intermediates may need to be calculated, since the solvent response is not linear. [159] This is a significant contributing factor to the breakdown of the LR approximation for **PV**$_{14}$. In this regard, Sprik *et al.* studied PCETs of several quinone systems by means of full TI approach, accounting also for the intermediate steps of the coupling parameter in Eq. 3.2.2. [159] In that work, the authors found deviations from LR approximation for the reduction (oxidation) of $HQ^- + H^+ \rightarrow HQ_2$ (Q = quinone). They estimated that the possible reason of this deviation is the shortening from 1.9 Å to 1.7 Å of the bond length of oxygen of the quinone with the hydrogen of the water (solvent). Indeed, this structural change leads to an increase of the coordination number of the oxygen of the quinone, which in turn will dramatically reduce the available space for a further H insertion (from the solvent or another source). In contrast to this, the electron reduction of a quinone Q to Q^-, which does not lead to substantial structural changes, respects the linear response approximation, showing small deviations (0.1 eV) of redox potentials. [159] In conclusion, they propose that the deviations from the LR approximation seems to be correlated with reorganization of the first solvation shell. In particular, when the change in the structure of the redox couple is not large, deviations are due to the reorganization of the solvent, i.e. the dielectric response of the solvent polarization. In contrast, for deprotonation/dehydrogenation reactions, the H insertion process is rather sensitive to the changes in solvation structure, in particular the amount of the space available to accommodate the inserted H atom. Thus, the larger the coordination number and the shorter the hydrogen bond are, the more nonlinear is the response. [159]

These results [159] support our findings, which show that multiple structural changes of **PV**$_{14}$ are related to the large deviation from the LR approximation. In addition to this, the VEG was computed on a cluster model extracted from the QM/MM MD, and therefore, deviations might also arise from an insufficient number of water molecules in the cluster.

In addition, while the LR-FNE approach is more computationally efficient, the closing of the HOMO-LUMO gap associated with edge effects of the cluster calculated using DFT, means that it is more susceptible to errors than the LR-TI method. This is also most strongly observed for **PV**$_{14}$.

Besides calculating the redox potentials, our QM/MM MD simulations also permit insight into the structural dynamics of the POM, the solvent environment, counter ion interactions and the charge distribution of the POM. The highly charged nature of the POMs means that there is often a strong interaction between the POM and the surrounding counter ions and solvent. For **SiW**$_{12}$, as the charge state is increased by reduction, the interactions with the counter ions get stronger reducing the interaction with the solvent leading to an expansion of the first solvation shell. The smaller counter ions used for $\mathbf{PV}_{14}$ bind directly to the POM, reducing the interaction with the solvent in all cases. Consequently, the relative contribution of each component depends on the type of counter ion, charge state and solvent. Importantly, the effect of this can be clearly seen in the diffusion coefficient of POM, which yields a hydrodynamic radius consistent with the radius of POM and first solvation shell.

In summary, it is now possible to adopt a range of computationally approaches to develop a detailed understanding of the functional properties of POMs. While the size of these systems still makes these simulations challenging and errors can still arise, it represents an excellent starting point to develop a more detailed understanding of the structure-property relationships of POMs.

Chapter 4

On the Analysis of X-ray Absorption Spectra for Polyoxometalates

4.1 Introduction

As outlined in Chapter 1, LIBs have earned the record of being the most commonly used batteries in several fields, like portable electronic devices and electric vehicles, due to their high energy density. However, the common Li-based cathode materials, like LCO and LNO, suffer of instabilities due to the addition and removal of Li ions, which also leads to slow kinetics during the charging/discharging process. [160]

For this reason, much effort has been put in discovering new storage materials to overcome the current LIBs limitations. In this regard, POMs have been employed in molecular cluster batteries (MCBs) as alternative to the Li-based cathodes due to their ability to undergo multiple redox reductions in a reversible fashion . [8, 16, 35, 36, 161–164] In the introduction, we talked about one of the most performing POM-based LIB, which was proposed by Yoshikawa *et al.* [8] In that work, the discharging process of Keggin $X_3[PMo_{12}O_{40}]$ (X = TBA) type occurs through the transfer of up to 24 e^- to POMs, resulting in a high theoretical capacity (270 mA h g^{-1}) in a voltage range between V = 4.0 V - 1.5 V. [8] This capacity is comparable to that one of commercial LCO and LNO cathod materials, whose capacity ranges between 150-300 mA h g^{-1}. [1]

The XANES and EXAFS analysis revealed that the molecular structure of $[PMo_{12}O_{40}]^{27-}$ (**PMo**$_{12}{}^{27-}$) varies compared to the fully oxidized $[PMo_{12}O_{40}]^{3-}$ (**PMo**$_{12}{}^{3-}$) owing to the formation of Mo-Mo bonds within Mo_3O_9 triads. A recent theoretical investigation by Irle *et al.* showed that the formation of metal-metal bonds is responsible for accepting so many electrons, and an almost linear relationship has been found between the number of Mo-Mo bonds and the excess of charge on the cluster. [37] However, more than 27 Li^+ ions needs to be added to the POM to formally observe twelve Mo-Mo bonds, which underlines the limits of the current DFT theories to properly describe highly charged species like POMs. [37] In addition, their ab initio MD simulations showed that fully reduced POMs can undergo a breakup of their molecular structure. [37] This was also experimentally observed by Yoshikawa *et al.*, who highlighted the poor capacity retention due to the structural instabilities of the fully reduced $[PMo_{12}O_{40}]^{27-}$ during the operating time of the battery. [8]

In this work we present a theoretical study that focuses on the different charge states of $\mathbf{PMo}_{12}{}^{3-}$ ($\mathbf{PMo}_{12}$) in order to understand how many electrons can actually be transferred to the POM without decomposition . Furthermore, we aim to unveil the role of the metal-metal bonds in the formation of super-reduced states.

In the first part we employed static DFT calculations to model the POM reduction by using hybdrid-GGA *x-c* functionals. The structural changes from the DFT calculations are in agreement with experimental data, however, our results do not show any linear relationship between the number of metal-metal bonds and the POM charge. The frontier molecular orbitals (FMOs) analysis illustrates that the electrons are delocalized over the whole POM for the intermediate redox states, while the presence of metal-metal bonds, due to the overlap between bonding d orbitals, occur only on a small number of metallic centers. Irle *et al.* also observed that all Mo atoms participate in the composition of HOMO and LUMO orbitals at both low and high charge states. [37] However, in contrast to our results, they observed that the LUMO of fully reduced $[PMo_{12}O_{40}]^{27-}$ is mainly composed by Rydberg 3p orbitals on oxygen atoms, indicating that it is impossible to further reduce the POM beyond the addition of 24 electrons. [37] It must be mentioned that in their work they constrained the $[PMo_{12}O_{40}]^{27-}$ to T_d symmetry, which already consists of the presence of 12 Mo-Mo bonds by construction of the model. [37] As results of this symmetry adapted model, the overlap between bonding d orbitals are observed for all Mo atoms. This analysis might be too biased toward a realistic behaviour of the fully reduced POM, and therefore, an unconstrained research is fundamental.

Furthermore, we carried out XANES and EXAFS simulations on the DFT-optimized geometries of POMs to assess all the intermediates present during the reduction. This analysis also offers us the possibility to connect the geometrical variations to the experimentally observed spectra, and it gives the guidelines to model POMs through x-ray simulations.

To investigate the role of an explicit solvation on the POM molecular structure, we carried out quantum mechanic/molecular mechanic (QM/MM) molecular dynamics (MD) simulations on $\mathbf{PMo}_{12}$ intermediates of the charging process. In this regard, we use an in-house Deep Neural Network (DNN) approach to compute the XANES spectra of POM states from their MD trajectories. [165] The DNN results provide quantitative analysis of the XANES spectra and subtle changes upon the initial reduction phase.

4.2 Computational Details

4.2.1 DFT simulations

Optimizations were carried out with PBE [4] and PBE0 [70] functionals as implemented in the software ORCA [87]. Since the large number of heavy metals, the effective core potential def2-ECP [166] approximation was used for the Mo atoms alongside the def2-TZVP basis set. [73] In order to speed up the calculations the RI-J and COSX (RIJCOSX) were used respectively for Coulomb integrals and numerical integration for HF exchange. The restricted Kohn-Sham (RKS) theory was applied to all closed-shell systems, whereas an unrestricted Kohn-Sham (UKS) formalism was employed when necessary for the open-shell ones. The energy threshold of 10^{-8} au was set for self-consistent convergence. The energy gradient for the optimization was required to converge within 4^{-3} au.

CPCM for all optimizations and single-point energy calculations was used to correctly describe the POM electronic structure. [87, 138] Previous studies have used a value of dieletric constant $\epsilon = 46.3$, [37] we decided to employ the same value in order to make our results comparable with these ones. [37]

4.2.2 XANES and EXAFS Simulations

The EXAFS spectra were calculated using the DFT(PBE0) optimised geometries using the FEFF9 package. [167] A maximum path length of 6.0 Å with up to 4 scattering legs (1 leg would be scattering from the absorbing atom to a neighbour and back again) were used. The amplitude reduction factor, which accounts for many-body interactions, was 1.0 at all times. To support the interpretation of the EXAFS spectra a wavelet transform (WT) is reported. In contrast to the Fourier transform method used to translate k-space into R for EXAFS, the WT goes beyond this 1D picture, yielding a 2D-correlation plot which deconvolutes the scattering pathways in both R- and k-space, providing additional information about the different contributions to the EXAFS spectrum. The details of the method are described in refs. [168,169] and throughout the shape of the wavelet is described by the parameters: $\eta = 10.5$ and $\sigma = 1.5$. The finite difference method as implemented in the FDMNES program [117] has been employed to calculate the Mo K-edge XANES spectra for all DFT-optimized POM structures. The code solves the radial SE by discretising it over a finite grid of points around the absorbing atom. The wave functions are superpositions of harmonic waves and their size depends on the volume of the grid used. Unless specified otherwise, the XANES spectra were calculated for an atomic cluster with radius of 6 Å around the absorbing atom. The energy of the photoelectron relative to the Fermi level was set to go from -10 eV to 70 eV with an energy step of 0.1 eV. The raw spectra were then convoluted by Lorentzian to obtain the XANES spectra within the energy range.

4.2.3 Deep Neural Network (DNN)

The DNN program for XAS analysis was developed by C. Rankine, and more details can be found in ref. [165] The contribution of each author is described in Section List of Publications at start of this manuscript.

The architecture of our DNN has been previously described in refs [165, 170]. Briefly, it is based on the multilayer perceptron (MLP) model, and comprises an input layer, three hidden layers, and an output layer. All layers are dense, i.e. fully connected. The first hidden layer comprises 640 neurons and every subsequent layer is reduced in size by 50% relative to the size of the preceding hidden layer. Featurisation of the inputs, which are X-ray absorption sites (i.e. the local environments around absorbing atoms), is achieved using the weighted atom-centered symmetry functions (wACSF). [171] The performance of our DNN is assessed via K -fold cross validation [172] with five folds, i.e. an 80:20 'in-sample'/'out-of-sample' split, and 50 repeats as described in Refs. [165,170]. Our dataset comprises Mo X-ray absorption site geometries derived from 3650 Mo-containing structures harvested from the Materials Project Library via the Materials Project API. Mo K-edge XANES spectra were calculated using multiple scattering theory as implemented in the FDMNES package [117]. A self-consistent muffin-tin-type potential of radius 6.0 Å around the X-ray absorbing site was used and the interaction with the X-ray field was described using the electric quadrupole approximation. To transform the computed cross-sections into XANES spectra that can be compared to experiment, the cross-sections need to be convoluted with a function that accounts for the core-hole-lifetime broadening, instrument response, and many-body effects, e.g. inelastic losses. Throughout this work, this convolution has been performed using an energy-dependent arctangent function via an empirical model close to the Seah-Dench formalism. The arctangent convolution is only applied as a post-processing step on cross-sections estimated by our DNN; our dataset comprises only unconvoluted cross-sections, and our DNN learns from these unconvoluted cross-sections, as in Ref. [165] The performance of this approach is discussed in the next sections of the chapter.

4.2.4 QM/MM simulations

Molecular dynamics simulations were performed by using AMBER. [82] Recently, several authors have attempted to define a general force field (FF) for POMs, [54–56] however, a general guideline has not yet been found, and adhoc FF still remains the first valid option to simulate their dynamics.

To this end, we made use of a mix approach to describe the POM FFs, namely we calculated the bonded terms of the potential energy from frequency calculations as described in the modified Seminario-method [85]. Whereas the dispersive terms for all atoms were taken from the Universal Force Field (UFF). [86] Additionally, we computed the CHELPG atomic charges, as implemented in ORCA, [87] from single point calculations, run on the optimized structures. In the POM-based MCB a solution with a ratio 1:1 of ethylene carbonate (EC) and diethyl carbonate (DEC) was used, [8] however, we used acetonitrile as organic solvent for the simulations. This choice is motivated by the fact the acetonitrile dieletric constant is close to the the one given by the mixed solution EC:DEC ($\epsilon = 37.5$). Also, the use of one molecular solvent type reduces the potential uncertainties due to the adequacy of force fields for organic solvents.

We then used the optimized structures to make a cell containing the POM and $\approx$ 1800 acetonitrile molecules. Prior to running QM/MM calculations we relaxed each initial system by running a classical MD. Namely, after a minimization, each system was heated up to 1000 K, and then gradually cooled down to the final temperature of 300 K. This was then followed by 500 ps of equilibration in order to let the density reach convergence. From this last step we took one snapshot that was used as starting point for the QM/MM calculations. In the QM/MM calculations we divided the full system in two parts: the POMs were treated at PBE level, while the rest of the molecules were modelled classically. An electrostatic embedding has been implemented in AMBER [146] to take into account the solute-solvent interactions. During the dynamics the temperature was kept at 300 K. No-periodic boundary condition (NPBC) were used within the QM region, which sees only the periodic images of the MM region. Whereas PBCs were applied to MM region with a cutoff of 8 Å to cut the long-range MM interations, which have been treated by the particle-mesh Ewald summation. SHAKE has been applied to all bonds involving hydrogen atoms. [147]. Dynamics were performed within the NPT ensemble with a Langevin thermostat with a time step of 2fs. An initial equilibration of QM/MM MD was performed for 4 ps. This was followed by an additional 8 ps of QM/MM dynamics from which all of the properties were studied.

4.3 Results and Discussion

4.3.1 Molecular Structure of Neutral PMo_{12}

To understand the structural changes due to the reduction, we optimised geometries of $Li_n[PMo_{12}]$ for n = 3, 15, and 27 using PBE0 functional. Here, we focused on the metal-metal (Mo-Mo), metal terminal-oxygen (Mo-O_t), metal bridging-oxygen (Mo-O_1), and metal phosphorous-oxygen (Mo-O_p) distances. These four distances are the key features that give insight into the structural change (Figure 4.3.1). [14,48] All the results are shown in Table 4.3.1, where a direct comparison with the experimental values is reported.

In the native $Li_3[PMo_{12}]$ (Li_3) state, the average Mo-Mo, Mo-O_t, and Mo-O_1 distances are all in excellent agreement with previous X-ray analysis [8, 173, 174]. A good agreement is also found for the Mo-O_t distance, whose experimental values is ~ 1.7 Å. These distances are consistent with absence of Mo-Mo bonds, and a single and double bond respectively along the Mo-O_1 bonds and with terminal oxygens. After the POM is reduced by 12 e^-, formally one electron per each Mo, the structural parameters do not show any substantial change from the fully oxidized state. Indeed, there is a very

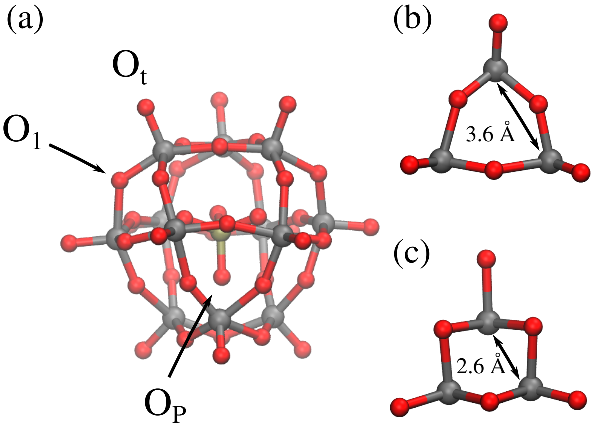

Figure 4.3.1: **(a)** The structure of the Keggin-type POM, $\mathbf{PMo_{12}}^{3-}$. Mo = grey, P = brown and O = red. Specific oxygen used in the main text are labelled. **(b)** shows a triangle of $\mathbf{PMo_{12}}^{3-}$ charge state, while **(c)** of $\mathbf{PMo_{12}}^{27-}$.

Table 4.3.1: Average structural parameters obtained from the DFT(PBE0) optimised structures, QM/MM MD (includes average and standard deviations) and experiments [8] for the different $\mathbf{PMo_{12}}^{x-}$ systems considered in the present work. For the $\mathbf{PMo_{12}}^{27-}$, the parameters are displayed in two rows, indicating the Mo atoms that form Mo-Mo bonds and those which do not. All distances are in Å. The $\mathbf{N}_b$ gives the number of Mo-Mo bonds formed.

x	$\mathbf{N}_b$	**Mo-Mo**	**Mo-O$_p$**	**Mo-O$_t$**	**Mo-O$_1$**
DFT					
3	0	3.41	2.41	1.66	1.93
15	0	3.54	2.48	1.69	1.99
27	0	3.59	2.46	1.74	2.06
	4	2.58	2.22	1.96	2.07
QM/MM MD					
3	0	3.47 ± 0.04	2.50 ± 0.07	1.69 ± 0.01	1.94 ± 0.02
15	0	3.56 ± 0.07	2.54 ± 0.12	1.69 ± 0.02	1.98 ± 0.04
Expt.					
3	0	3.4	2.4	1.7	1.9
27	12	2.6	2.0	1.9	2.0

slight expansion of the Mo-Mo distances followed by a small increase of Mo-O$_t$ bond lengths, which were reported for this oxidation state [174]. This is a common observation for POMs, which do not usually vary upon reduction due to their ability to delocalise a high number of electrons over the all structure such that the electronic repulsion between each metal center is lessened. [14] For instance, this was also the case for the reduction of $\mathbf{SiW}_{12}$, which was studied in Chapter 3. In contrast, for the reduction of $\mathbf{PV}_{14}$ we observed structural changes, which are likely due to the asymmetrical geometry of $\mathbf{PV}_{14}$ as well as the occurring of PCETs rather than simple ETs. However, despite the different structural modifications, the distribution of the frontier orbitals of these POMs and $Li_3[PMo_{12}]$ indicate that all metals take part in the reduction.

A strong asymmetry is present in the $Li_{27}[PMo_{12}]$ ((Li_{27}). On one hand, the structure of 8 Mo atoms out of the twelve remains the same as those in the native POM. On the other hand, the remaining 4 Mo atoms form Mo-Mo bonds. In this case, the shortening of Mo-Mo bond length from $\sim$ 3.6 to $\sim$ 2.5 Å parallels well with experimental findings that assign to the Mo-Mo a bond length of 2.6 Å. The Mo-O_t and Mo-O_1 bond lengths are closer to the experimental Li_{27} values. Whereas the Mo-O_p distances are in between the 2.4-2.0 Å, indicating that the Mo atoms start binding also these internal oxygens. This synergistic combination of shortening of the Mo-Mo, and extension of Mo-O distance has also previously observed, [37, 48], and therefore, it is important to bear in mind when theoretically modelling POMs. [37, 48]

It is worth reflecting on the asymmetry arising from the reduction. Such asymmetry indicates that only four Mo atoms out of twelve are doubly reduced from Mo^{6+} to Mo^{4+}, and thus the remaining 14 e^-, over the total 24 added to the POM, are delocalized over the other metallic centers. This behaviour could be ascribed to the strong delocalization error (DE) which is typical of most common DFT functionals for highly charged system. [72] For instance, *Yang et al.* showed that common DFT functionals, like PBE and PBE0, tend to delocalize too much electron density even at the geometrical equilibrium of large clusters. [175]

This aspect is confirmed by the fact that the Li^+ ions dot not have a purely cationic behaviour but they are instead partially bound to the POM oxygens. This allows further delocalization of electron density over the partial covalent Li-O_{POM} bonds. Li-O_{POM} distances, which are close to $\sim$ 2.0 Å, were also found in previous DFT studies on tri-Mn-substituted W-based Keggin ions, [46] and they are further confirmed by our QM/MM simulations as explained below.

4.3.2 Electronic Structure upon Reduction

The HOMO-LUMO gap acts as key factor to determinate the ability of POMs to undergo multiple reductions. [14] For the present **PMo_{12}**, Figure 4.3.2 shows the HOMO and LUMO orbitals and the relative gap between them for the charge states. The effect of reduction is to reduce the HOMO-LUMO gap, which drops down to 1.2 eV for the Li_{27} state. This value is still high, and therefore, it suggests that super-reduced species are stable in an implicit solvent model.

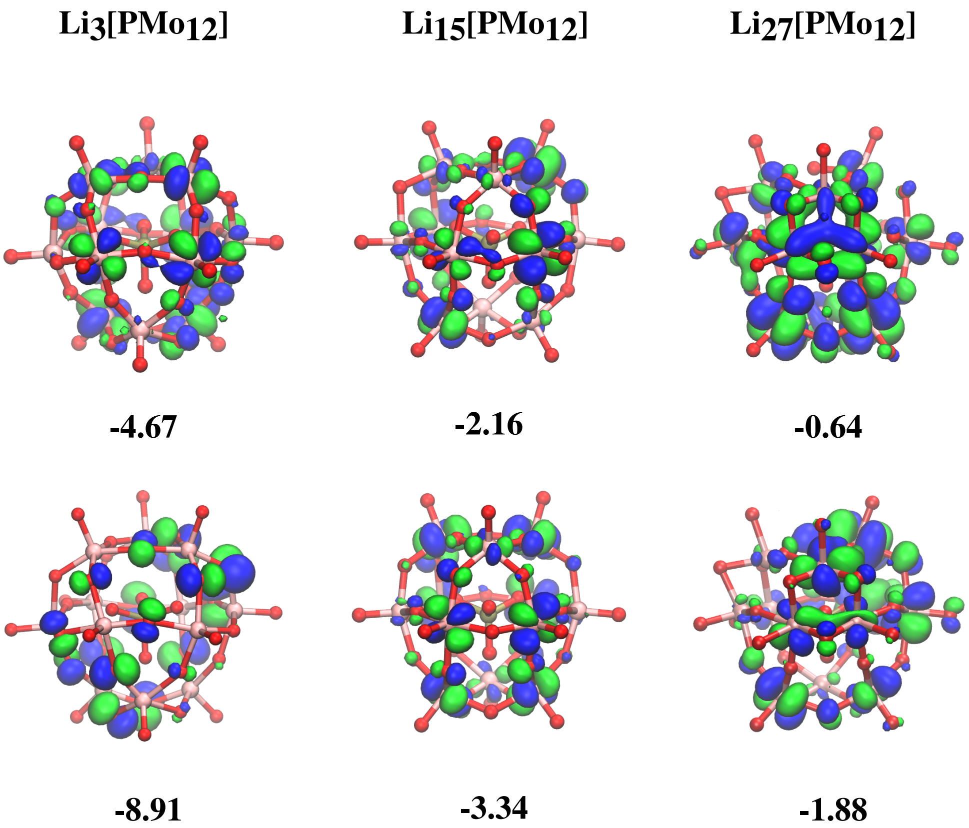

Figure 4.3.2: FMOs plots and their energies (eV) calculated with PBE0 functional for Li_xPMo_{12} redox states (x = 3, 15, and 27). MO isovalue is ± 0.03. The orbitals on the bottom are the HOMOs, while the LUMOs shown on the top row.

For the Li_3, the HOMO is only composed of p oxygen orbitals, whereas the LUMO is a mix of d (Mo) and non-bonding p (O) orbitals. This feature is a common element of Keggin-ion POMs, where the metal centers are not entirely in a perfect octahedral geometry but belong to a different symmetry point group. [14, 37, 48, 65] Both HOMO and LUMO of Li_{15} are delocalised over the whole POM, and therefore, all twelve Mo atoms can formally be reduced from Mo^{6+} to Mo^{5+}.

The FMOs composition of Li_{27} show the formation of d-d bonding orbitals over the 4 Mo atoms involved in Mo-Mo distance lower than 2.6 Å. Particularly, the LUMO displays that a three-center d-d orbitals are formed along the Mo-Mo bonds. This type of bond was also previously found by Irle *et al.*, who suggested that these bonds occur on triangular metal sites as a result of the increasing excess of electrons.

The knowledge of the electron density $\rho(r)$ and the atomic charges allow us to calculate the molecular electrostatic potential (MEP) map, which represents the electrostatic potential at any point in a molecule, and thus its reactivity towards positively or negatively charged reactants. To avoid the complications due to the presence of lithium ions, we discarded the Li^+ from the optimized geometry of each charge state, and run single point calculations on barely charged POMs. MEP surfaces are shown in Figure 4.3.3. The MEP values become more negative as the POM get more charged, and their values are approximately -0.3, -1.2, and -2.7 for respectively **$PMo_{12}{}^{3-}$**, **$PMo_{12}{}^{15-}$**, and **$PMo_{12}{}^{27-}$**. This increment of nucleophilicity aligns well with the HOMO-LUMO trend given by the PBE0 functional, where the HOMO-LUMO gap becomes smaller for any further addition of electrons to the POM.

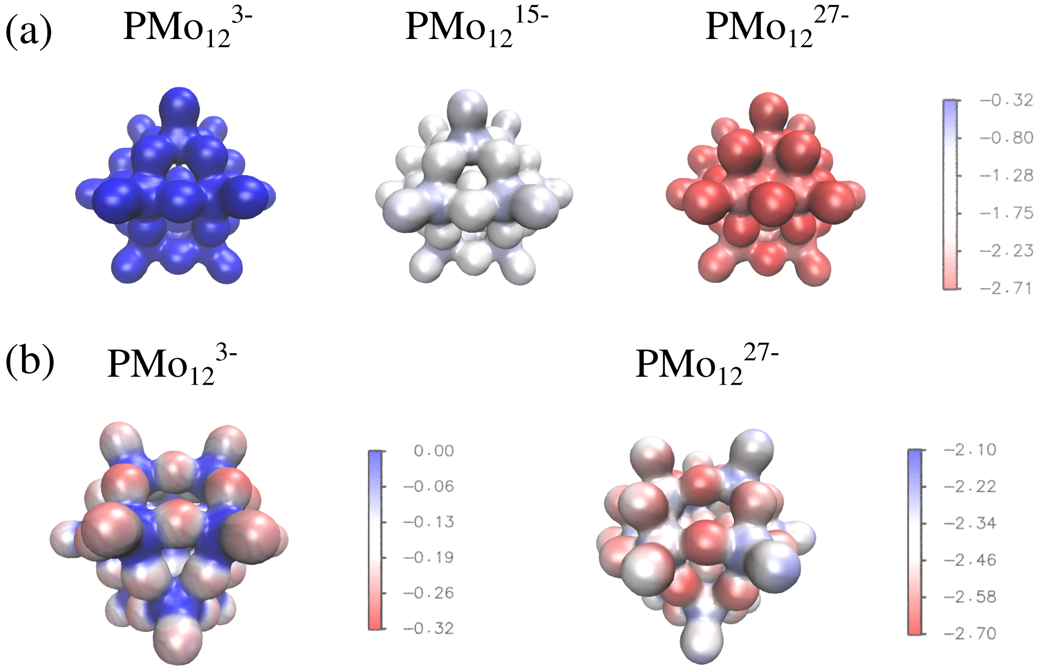

Figure 4.3.3: (a) MEP maps projected onto electron density (isosurface ρ = 0.04), calculated for **(a) $PMo_{12}{}^{3-}$**, **$PMo_{12}{}^{15-}$**, and **$PMo_{12}{}^{27-}$**. **(b)** Scaled MEP surfaces for **$PMo_{12}{}^{3-}$** and **$PMo_{12}{}^{27-}$** to show the different nucleophilic regions. The color coding goes from more positive (blue) to more negative (red) regions of the MEP. Arbitrary units are used.

In Figure 4.3.3b one can see that in both fully oxidized and reduced POM the bridging oxygens (O_1) are more nucleophilic than the terminal ones. Therefore, one would expect these sites to be more solvated than the terminal oxygens. This aspect is also valid in solution, as illustrated by the RDFs from the QM/MM MD calculations (Figure 4.3.10).

4.3.3 Structure Analysis from X-ray Absorption Spectroscopy

The mismatch between structures previously reported and those found in the present work requires further analysis. Owing to its ability to provide direct structure insight, X-ray spectroscopy is a powerful tool for this. Figures 4.3.4a,b show the calculated and experimental EXAFS spectra for respectively the Li_3 and Li_{27}. In addition to the structures in Table 4.3.1, for this latter we computed the EXAFS spectra for constrained POM structure with 8 and 12 Mo-Mo bonds. There is good agreement between the two, especially for the phase and frequency of the oscillations, supporting the optimised structures presented in Table 4.3.1.

Importantly, the EXAFS shows that the difference between all three scenarios is not huge illustrating the importance of achieving a high signal to noise ratio when performing these experiments. Overall, the best agreement is achieved for 8 Mo-Mo bonds (Figure 4.3.4b) and this is determined primarily from the peak around $k = 10$ Å^{-1} . The reason for this weak dependence is highlighted in the Wavelet transform (WT) analysis shown in Figure 4.3.5. In contrast to the Fourier transform, which separates the neighbouring atoms according to their distances from the central atom, WT resolves the centers of the backscattering wave functions in both energy (or wave vector) and distances from the absorbing atom. Therefore, it offers a straightforward way to discriminate different atoms within one atomic shell. In practice, a WT consists of a 3-D plot, which can be projected onto a 2-D plane, where the intensity of the EXAFS signal is reported as function of the wave vector of the scattered wave function and the distance from the central atom, which are respectively reported on the x-axis and y-axis.

For Li_3 (Figure 4.3.5a), we identify 3 main regions. The first peak at ~ 1 Å (distances are not phase corrected and therefore slightly shorter than actual bond length), which contributes throughout k-space, corresponds to a Mo-O_t and Mo-O_1 bond distances. The significant contribution to the EXAFS spectrum is simply due to the number of scatters present. The two other regions correspond to the Mo-O_p and Mo-Mo bond lengths occurring at ~ 2 Å and

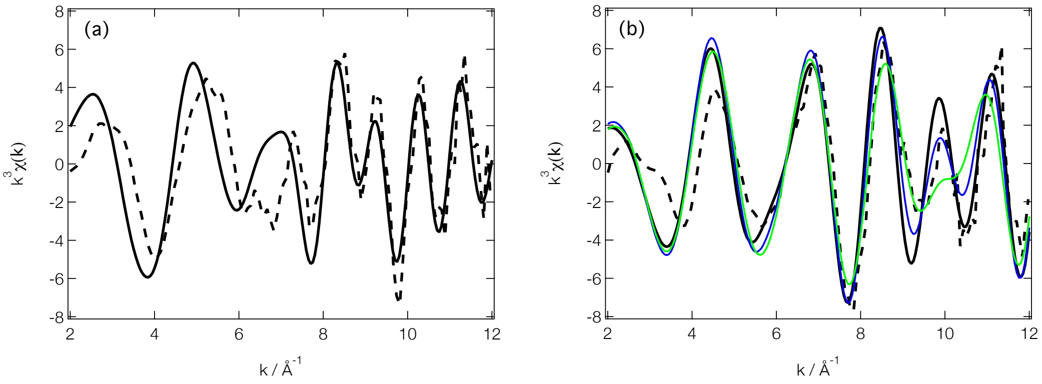

Figure 4.3.4: Calculated (solid) and experimental (dashed) Mo K-edge EXAFS for **(a)** Li_3PMo_{12} and **(b)** $Li_{27}PMo_{12}$. In **(b)** the solid lines corresponds respectively to 4 Mo-Mo bonds (green), 8 Mo-Mo bonds (blue), and 12 Mo-Mo bonds (black).

3 Å, respectively. These slightly overlap in R-space, but the WT transform allows them to be separated in k-space due to the fact that scattering of heavier elements occurs at higher k-values. Indeed, it is worth noting Blackburn *et al.* [176] have shown that to obtain an accurate description of the Cu-Cu distance in cytochrome oxidase, the spectrum needs to be fitted up to 16 Å.

In Figures 4.3.5b, i.e. the fully reduced species, the Mo-O bands merge into one, reflecting the fact that the Mo-O bond lengths all become a lot more similar when fully reduced, consistent with the calculations shown in Table 4.3.1. The Mo-Mo band also reduces by $\sim$ 0.75 Å and merges, at high k, with the Mo-O band, consistent with the formation of Mo-Mo bonds. However, the weak intensity of this band is due to the overlap with Mo-O band, which dominates over the other contributions.

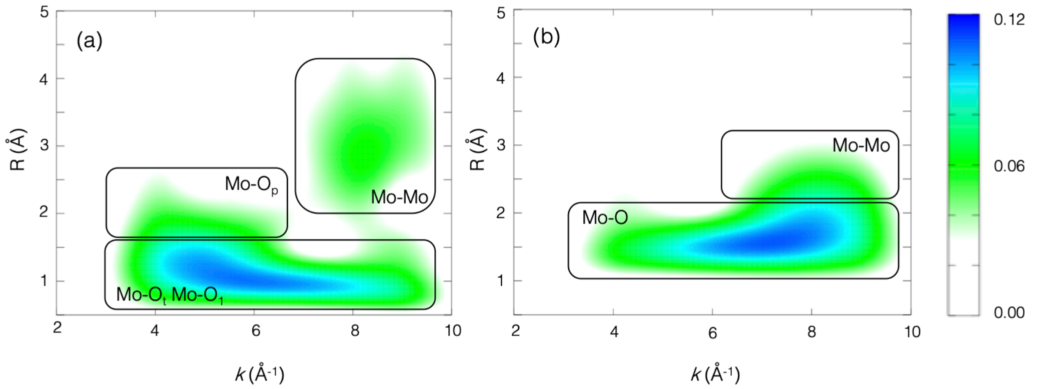

Figure 4.3.5: Calculated (solid) and experimental (dashed) Mo K-edge EXAFS for **(a)** Li_3PMo_{12} and **(b)** $Li_{27}PMo_{12}$. The color in the bar goes from low (white) to high values (blue) of WT.

4.3.4 XANES Analysis: From a Single Structure to an Ensemble

Figure 4.3.6a shows a comparison between the experimental [8] and calculated XANES spectra for Li_3, using the same geometry obtained and discussed in the previous section. This shows a pre-edge peak, which is commonly associated with the dipole-forbidden 1s-4d transition, which gains intensity from mixing with the 4p orbitals [177] due to deviations from an octahedral geometry. Above the edge, there are two ionisation resonances, which are separated by $\sim$14 eV and are associated with multiple scattering resonances reflecting the geometric structure. Figure 4.3.6b shows the calculated spectrum for Li_{27}, using the structure optimised from the EXAFS simulations, i.e. with 8 Mo-Mo bonds. This is compared with the experimental spectrum recorded following discharging and the reduction of POMs. The additional electrons converting the Mo^{6+} to Mo^{4+} [37] causes a reduction in the pre-edge intensity as the structural rearrangements form a closer to octahedral geometry around the Mo, preventing 3d/4p mixing responsible for the pre-edge at lower charge states. Above the absorption edge, there is a clear contraction of the two above ionisation resonances which can be explained in terms of Natoli's rule, as a contraction of the Mo-Mo distances become shorter than 3.6 Å.

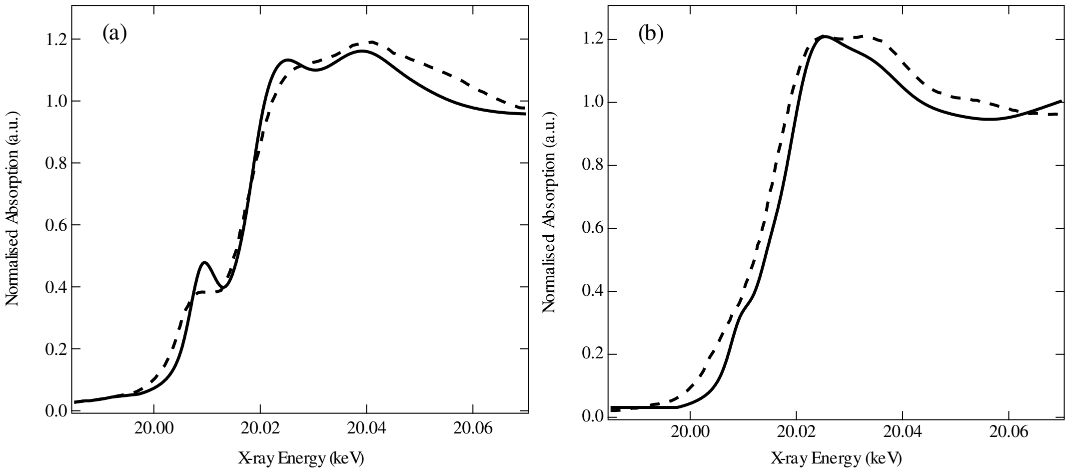

Figure 4.3.6: **(a)** Comparison of the calculated (solid) and experimental (dashed) [8] Mo K-edge XANES spectra for **(a)** Li_3 and **(b)** Li_{27}.

In the previous example, we have studied the two extremes of charge state, namely Li_3 and Li_{27}. However, in previous work [8] the XANES spectra shows significant changes at small potentials, where the first 12 electrons are absorbed with very small structural changes. Being able to follow these smaller structural changes is important for understanding the structural evolution of the POM during reduction. When smaller structural changes are considered, it can become more important to incorporate effect of thermal fluctuations and the interaction between the absorbing atoms and the embedding solvent environment. The latter is likely to be especially more in the context of POMs which have strong solute-solvent interaction. To achieve this we have performed QM/MM MD to provide 10 ps of dynamics at 300 K from which the XANES spectra, including thermal fluctuations and solute-solvent interactions can be included. The XANES spectra are calculated as an average over all spectra from this ensemble, however, given that each snapshot has 12 Mo per POM, this leads to a total of 65,000 spectral calculations for each charge state. To accelerate this step, we have calculated the XANES spectra using our DNN described in previous work. [165, 170] Figure 4.3.7 shows the training and performance of DNN when refit at the Mo K-edge, based on the recent work at the Fe and Co K-edges in Refs. [165, 170] Figure 4.3.7a shows the convergence of DNN as a function of the number of in-sample XANES spectra used in the learning process. DNN converges towards a MSE of 0.07 (evaluated against unseen/*'out-of-sample'* spectra for which the post-edge has been normalised to unity), demonstrating similar performance to that attained in previous work at the Fe K-edge in Refs. [165, 170] Figure 4.3.7b illustrates the improvement in performance of DNN during the learning process; the MSE is given as a function of the number of forward/backward passes through our dataset (*'epochs'*). Convergence of DNN is achieved in ≈100 forward/backward passes. Finally, Figure 4.3.7c shows the average theoretical target XANES spectrum (solid trace) plotted alongside the out-of-sample DNN-predicted XANES spectrum (dashed trace). Figure 4.3.7c indicates the average performance of predictions by the DNN and, as observed, these predictions are almost indistinguishable from the target XANES spectrum. Because of the high excess of electrons, the QM/MM MD of Li_{27} shows that the POM structure falls apart during the simulation, resulting thus in an unstable molecular condition. We then focus only on the dynamics of the Li_3 and Li_{15}.

Figure 4.3.8a shows the experimental spectrum of the charged, $\mathbf{PMo}_{12}{}^{3-}$, system and the XANES spectrum recording during the first discharging with a cell voltage of 2.5 V [8]. The difference between the two spectra is characterised by 4 main effects, firstly a loss in pre-edge intensity associated with a elongation of the Mo-O bond distances, a red shift of the absorption edge,

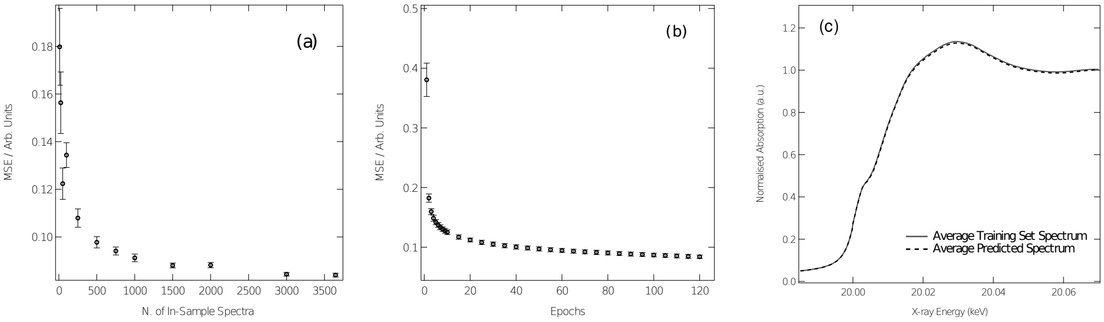

Figure 4.3.7: (a) Evolution of the MSE as a function of the number of in-sample spectra accessible to our DNN during the learning process. **(b)** Evolution of the MSE as a function of real time and the number of forward passes through our data set ('epochs'). In both cases data points are averaged over 100 K-fold cross-validated evaluations; error bars indicate one standard deviation. **(c)** Average theoretical target XANES spectrum (solid trace) plotted alongside the out-of-sample DNN-predicted XANES spectrum (dashed trace).

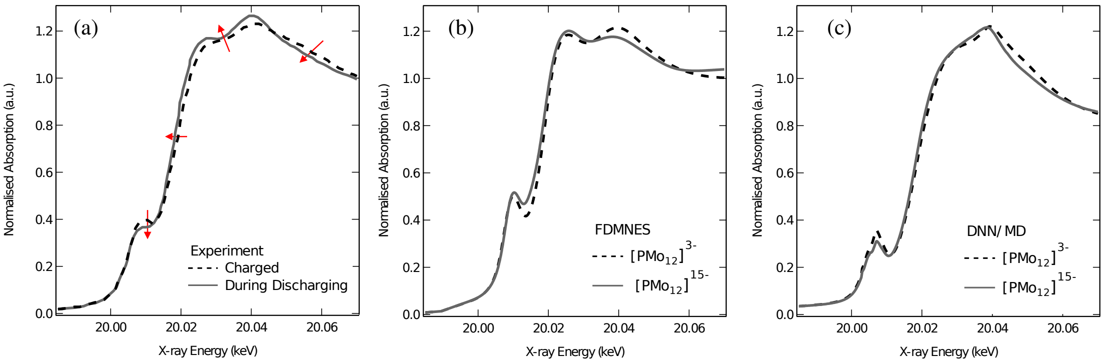

Figure 4.3.8: (a) The experimental Mo K-edge spectrum of the charged (dashed) $\mathbf{PMo}_{12}{}^{3-}$ complex and the Mo K-edge XANES spectrum recording during the first discharging with a cell voltage of 2.5 V (solid) [8]. The red arrows illustrate the key spectral changes between the two spectra. **(b)** FDMNES simulated Mo K-edge spectrum for Li_3 (dashed) and Li_{15} (solid). **(c)** The DNN simulated Mo K-edge spectra for Li_3 (dashed) and Li_{15} (solid) simulated from an ensemble average of 65,000 spectra with snapshots extracted from QM/MM MD simulations.

increase in the white line intensity, and a loss in intensity at 20.06 keV. Figure 4.3.8b shows two spectra simulated using FDMNES from the single point optimised geometries for Li_3 and Li_{15}. This captures the red shift in the absorption edge, but does not replicate the other 4 changes. Figure 4.3.8c shows the spectra simulations from two series of QM/MM MD for Li_3 and Li_{15} and each spectrum is an average of 65,000 absorbing Mo. This reproduces all of the trends observed in the experimental spectra and the average structural parameters and standard deviations are shown in Table 1. In using the

QM/MM MD results to predict the spectra, we have found that the thermal fluctuations and geometry extracted from the QM/MM is most important and despite the strong solute-solvent interaction, the explicit environment, Li^+ and solvents, have no effect on the computed XANES spectra. The red shift is associated with the reduction of the Mo sites leading to a reduction in the binding energy of the core electrons. The pre-edge intensity decreases as the Mo-O bond length changes and the tendency of O_1-Mo-O_t and O_1-Mo-O_2 angles to form closer to a right angle makes the coordination environment around each Mo close of C_{4v} symmetry, this leads to a decrease in 3d/4p mixing and therefore the transition has a stronger quadrupole transition making it weaker. This is better captured by the QM/MM MD, whose accuracy represents the subtle change responsible for the change in the XANES spectra. In addition to speed up the calculations, the DNN/MD approach gives more accurate XANES spectra compared to first-principle calculations on static structures. In order to quantify the improvement, we computed the mean square error (MSE) of theoretical XANES spectrum as a function of the number of snapshots extracted from MD. In Figure 4.3.9, it can be seen that MSE of DNN/MD rapidly drops after 300 snapshots, and then becomes almost constant after 1000 snapshots with a MSE lower than 0.01 a.u. (≈ 0.27 eV). Such a small MSE shows the great advantage of DNN/MD compared to first-principles calculations. Therefore, although we employed more than 5,000 spectra, a good performance of the DNN/MD approach can be reached by using about 1,000 snapshots sampled from MD.

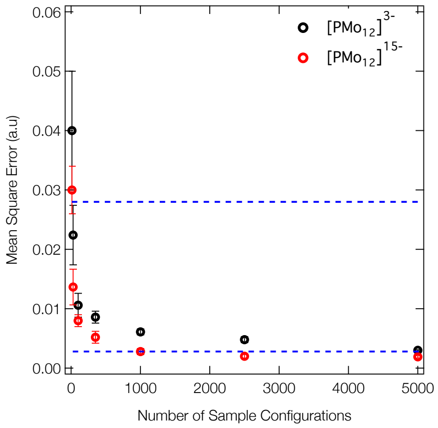

Figure 4.3.9: The MSE between the fully-converged theoretical XANES spectrum, averaged over 65,000 individual theoretical XANES spectra, as a function of the number of snapshots sampled *via* MD. The upper blue dashed line corresponds to the MSE between the two experimental XANES spectra shown in Figure 4.3.8a; the lower blue dashed line represents an improvement by a factor of ×10 over this MSE.

4.3.5 Li^+ Distribution from QM/MM MD

In order to investigate the Li distribution around the POM, and how this is related to its structure during the charging process, we computed the radial distribution functions (RDFs) between the POM and the Li^+ ions. Particularly, we chose the O_p-Li distance to understand whether the Li^+ ions penetrate through the POM, while the RDFs between the couple Li^+ and O_t (O_1) are calculated to address the possible solvation types.

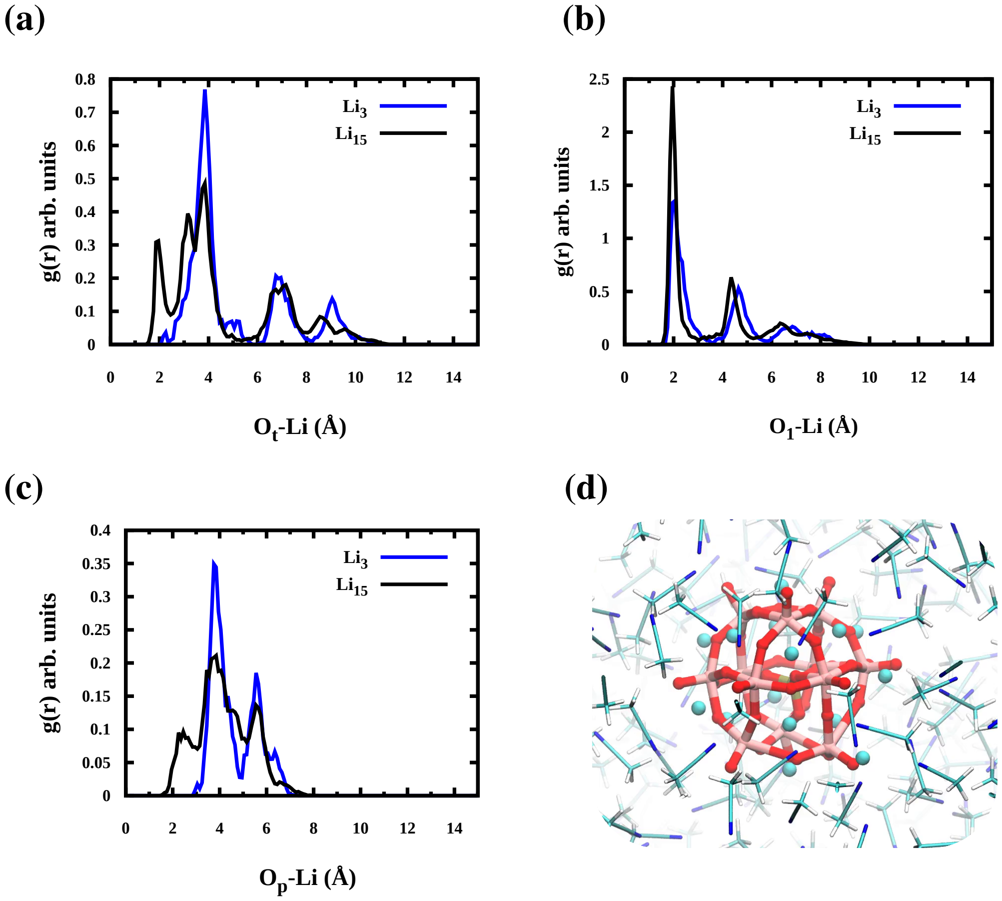

Figure 4.3.10: Calculated RDFs from QM/MM trajectories for **(a)** O_t-Li, **(b)** O_1-Li, **(c)** O_p-Li. **(d)** Snapshot extracted from the QM/MM MD of Li_{15}.

From Figure 4.3.10, the O_t-Li RDFs show that a initial peak at 4 Å for the Li_3. However, as the charge increases this peak becomes less intense, and a stronger peak at about 2 Å occurs for Li_{15}. Similarly, the O_p-Li RDF reflects this same trend, which is due to the fact that the number of Li^+ ions increased, and these can more likely penetrate through the external POM structure. On the other hand, the O_1-Li RDFs have a common shapes with a main peak at 2 Å and a small shoulder at 4 Å. These results suggest that as long as the POM is formally reduced by 15 e^-, the solvation by Li^+ occurs by interacting with most external oxygens, i.e. O_t and O_1.

The presence of relatively pronounced second peak in all charge states makes us think that the two types of solvation exist: POM and Li ions form (i) a closed and (ii) a semi-closed ion pair. The different type of ion pairs is a fundamental aspect that influences the solubility and therefore the agglomeration of POMs in solution. In fact, it has been shown that highly charged POMs interact more strongly with their counter ions, desolvating in this way the nearby solvent molecules [48] and thus facilitating their agglomeration.

This hypothesis has also previously been confirmed by the observation that Li^+ ions form an inner shell that helps to weaken the strong Coulombic repulsions existing in highly reduced POM. [37] This feature is indeed confirmed by O_p-Li RDFs, which shows that the Li^+ ions penetrate through the external oxygens and manage to solvate the internal PO_4^{4-} unit when an excess of electrons is present on the POM.

4.4 Conclusions

In this work we have theoretically studied the molecular and electronic structure of the α-Keggin type **PMo**$_{12}$ in different charge states. Our objective has been to explore how the electronic and geometric parameters of this POM under different oxidation states are translated into changes in the X-ray absorption spectra and how we can simulate them.

In the first part, DFT calcutions, with PBE0 x-c functional, showed that structural parameters of native geometry do not significantly change for the $Li_3[PMo_{12}]$ and $Li_{15}[PMo_{12}]$. Further addition of electrons leads to the formation of metal-metal bonds , followed by the elongation of Mo=O_t bonds that become single bonds Mo-O_t. This behaviour is in agreement with previous theoretical results, which showed that a relationship between Mo-Mo bonds and charge of the POM exists. [8, 37] However, in contrast to this, we found that the number of Mo-Mo bonds are lower, i.e. only four bonds are formed in the fully reduced POM, and therefore, no linear relationship is observed between the number of Mo-Mo bonds and the POM charge.

The molecular orbital analysis showed that HOMO and LUMO are delocalized over the whole POM, and the addition of a high number of electrons is facilitated by the Coulombic repulsion felt by each electron. This excess of electron is utilised to form metal-metal bonds as shown by the presence of d-d bonding orbitals between two or three metallic sites within each subunit. [37] The HOMO-LUMO energy gap decreases as the number of electrons increases and it parallels well with the increasing reactivity of the POM. However, its value, i.e. > 1 eV, for $Li_{27}[PMo_{12}]$ indicates that the POM is still stable when the its embedded in an implicit solvation model.

In the second part, we initially focused upon an analysis of the EXAFS spectra of $\mathbf{PMo}_{12}{}^{3-}$ and $\mathbf{PMo}_{12}{}^{27-}$. In both cases our simulations are in good agreement with experimental observations and this illustrates that in the super-reduced, $\mathbf{PMo}_{12}{}^{27-}$, the structural changes lead to the formation of 8 Mo-Mo bonds. This is less than previously reported [8] but our Wavelet analysis illustrates that the sensitivity of the EXAFS spectra to the Mo-Mo bonds, is not as much as could be expected. Our DFT simulations show that the structural changes do not begin until the addition of over 12 electrons, i.e. each Mo can form an oxidation state of Mo^{5+} with only small structural changes. This EXAFS analysis is supported by XANES simulations. Subsequently from using our newly developed DNN for the rapid simulations of XANES spectra we have shown how QM/MM MD can be used to provide quantitative analysis of the XANES spectra and subtle changes upon the initial reduction phase.

In contrast to an implicit solvation, the QM/MM results illustrates that the $Li_{27}[PMo_{12}]$ structures decomposes when explicitly accounting for the solvent molecules due to the high excess of electrons. In addition, the Li-POM RDFs suggest that the formation of two solvation types, i.e., a closed and semi-closed ion pair are formed, respectively due to the Li-O_1 and Li-O_t interaction. This aspect is extremely important to understand POM-POM interaction, and it needs to be borne in mind when modelling POMs in solution.

Chapter 5

Theoretical Insights into the Self-Assembly Process of Wells-Dawson Polyoxometalates

5.1 Introduction

As outlined in the Chapter 1, RFBs represent a promising technology owing to their safer employment in power-grid applications compared to common alkali-ion batteries. For this reason, significant research effort has been put into discovering new materials that can store as many electrons as possible. In this regard, POMs have shown tremendous efficiency, due to their ability to undergo reversible multi-electron reductions. [131,132]

Currently, one of the most performing battery is the asymmetric RFBs proposed by Jochen *et al.*, which is the subject of Chapter 3. Recently, Cronin *et al.* have demonstrated that the Wells-Dawson polyoxoanion $[P_2W_{18}O_{62}]^{6-}$ ($\mathbf{P_2W_{18}}$) is able to store up to 18 protons and electrons in acidic aqueous solution, permitting the construction of a POM-based RFB with an energy density of 225 Wh l^{-1}. [27] This corresponds to ≈ 9 g of hydrogen stored per litre at room temperature at 0.5 M of POM. Extrapolating to the limits of the solubility of the POM, an effective storage potential of 34.2 g H_2 l^{-1} could be achieved, which compares with that of pure cryogenic liquid hydrogen (71 H_2 l^{-1} at 20 K). [27] They showed that a high number of electrons can be reached by lowering the pH and increasing the POM concentration. While it is a well-known behaviour of POMs that a low pH triggers simultaneous multiple PCETs, the role of POMs agglomeration on their catalytic performance has not yet been explored, and it might be decisive in accepting so many electrons. Furthermore, it has been shown that molecular hydrogen can be obtained by simple dilution of the system, and therefore, the $\mathbf{P_2W_{18}}$ could also be seen as electrocatalyst for on-demand production of hydrogen.

Despite such encouraging prospective, PCETs can lead to a complicated redox scenario when a high number of electrons are transferred to the POM. The main challenge is indeed represented by exactly determining the correspondence between the number of electrons and protons taking part in the reaction and their relative redox potentials. Cronin *et al.* in their work [27] assigned the $\mathbf{P}_2\mathbf{W}_{18}$ redox potentials only to four reduction processes at relatively basic pH, whereas at lower pH the cyclic voltammogram (CV) shows a more complex scenario, where the CV peaks can not easily be assigned to the 18 electrons transferred to the POM.

In this regard, computational chemistry can offer help to predict POMs redox behavior. Because of the size of the POMs, the only effective and practical theoretical approach to study them is DFT. Several works showed that different functionals return essentially the same POM structures, however, large differences between the functionals exist when computing their redox potentials or other properties. For instance, this is the case of $\mathbf{SiW}_{12}$ and $\mathbf{PV}_{14}$ systems studied in Chapter 3. Both pure GGA (PBE) and hybrid-GGAs return similar molecular structures for POMs, whereas different redox potentials are generated. [45, 46, 48] In previous studies and chapters, it has been shown that further difficulties are due to the highly-charged nature of POMs. Indeed, our studies and the previous literature showed the importance of including the external environment to correctly predict both molecular orbitals (MOs) [14] and redox potentials (Chapter 3). [47, 48]

The study of POM in solution is commonly performed by using classical molecular dynamics (MD) simulations. Indeed, the more accurate *ab initio* MD or QM/MM methods are still computationally prohibitive for large systems like POMs. Most of previous MD studies on POMs focused on the Keggin-type ($[XM_{12}O_{42}]^{n-}$) and Lindqvist ($[M_6O_{19}]^{n-}$) ions, while very limited literature exists on the Wells-Dawson ions. Previous studies highlighted that the aggregation of Keggin-type ions generally occurs for low charge density in acidic condition. This means that at a fixed total charge, the bigger is the POM, the higher is its tendency to aggregate. [51] This trend is also respected by Lindqvist ions, except for hexaniobate POMs which shows to be more soluble at lower charge. [178]

The aggregation (solubility) is strongly influenced by both the counter ions and solvent, namely, the solubility is higher for small alkali counter cations, like Li^+ or Na^+. [50]. While, in aqueous condition, H_2O act as a glue that help to stabilize the POM-POM interaction. [51] However, these MD studies focused only on low density charge POMs, namely, only on their native charge state like the $[XM_{12}O_{42}]^{3-}$ Keggin-type.

A detailed study on the effect of the charge of POMs on their self-assembly process has been recently proposed by Poblet *et al.* In that work, they investigated the ability of a mixed-valence host-guest $[I@V^{IV}_{10}V^{V}_{8}O_{42}]^{5-}$ ($\mathbf{V}_{18}$) structure to form agglomerates made of two or more units. [53] They showed that the dynamical behaviour of $\mathbf{V}_{18}$ agglomerates depends on the total charge of the POM, the solvent, and counter ions. [53] In particular, they observed that the agglomeration is mediated by the counter ions; that is, the counter ions act as linkers between $\mathbf{V}_{18}$ units. Furthermore, in aqueous solution, the least hydrophilic $\mathbf{V}_{18}$ units (less negative) agglomerate into a microphase, whereas those with more negative charge interact more strongly with water solvent molecules than with counter ions, reducing both ion pairing and agglomeration. [53]

Almost two decades ago Norskøv *et al.* set the basis for the theoretical description of the efficiency of catalysts towards hydrogen and oxygen evolution reactions (HER and OER) from the water splitting. [179, 180] Their methodology named computational hydrogen electrode (CHE) approach, has since then been applied to several types of electrocatalytic processes. From the thermochemical perspective, they showed that the Gibbs free energy due to hydrogen adsorption, ΔG_H, is an excellent descriptor for the HER: the closer is to zero, the better are the catalyst performances. Several experimental and theoretical works studied POM-based catalysts employed in the reaction of water splitting. In particular, much emphasis has been given to the oxygen evolution reaction (OER), [181, 182] however, to the best of our knowledge, no theoretical studies have been carried out on POMs catalysing the HER.

In this chapter, we present a theoretical study focused on the self-assembly process of $\mathbf{P}_2\mathbf{W}_{18}$, and how this affects the POM redox behaviour and its catalytic performance towards the HER. In the first part, we investigated the POM agglomeration by performing classical molecular dynamics (MD) simulations on both little and highly charged $\mathbf{P}_2\mathbf{W}_{18}$. The MD outcome suggests that the charge of $\mathbf{P}_2\mathbf{W}_{18}$ strongly influences its solubility, and so also the possibility of forming inorganic agglomerates in solution. In addition, we highlight the role of the hydronium ions and water solvents, which play an important role as mediators within the POM-POM interaction.

In the second part, we investigated the effect of the $\mathbf{P}_2\mathbf{W}_{18}$ on their redox potentials and HER efficiency by means of first-principles calculations. In particular, we focus upon single and two $\mathbf{P}_2\mathbf{W}_{18}$ units. This analysis helps us to assess the role of the aggregation, and at the same time, the advantages and limits of current computational approaches.

5.2 Theory and Computational Details

5.2.1 Redox Potentials

Optimizations were carried out with PBE [4] and PBE0 [70] functionals as implemented in the software ORCA [87] for all **P$_2$W$_{18}$** species. While the **(P$_2$W$_{18}$)$_2$** states were only optimized at PBE level, and the PBE0 results for these states comes from single points calculations run onto the PBE optimized geometries. Throughout the optimizations were carried out with the def2-SVP basis set. [73] However, the electronic energies were obtained from single point calculations with def2-TZVP basis set on the optimized structure. [73] Since the large number of heavy metals, the effective core potetial def2-ECP [166] approximation was used for the Mo atoms. In order to speed up the calculations the RI-J and COSX (RIJCOSX) were used respectively for Coulomb integrals and numerical integration for HF exchange. Unrestricted Kohn-Sham (UKS) theory was employed for all open-shell systems, while closed-shell ones were treated by RKS. During the geometry optimisations, the total SCF energy was set to converge within 10^{-6} a.u., while the gradient converged to 10^{-4} a.u.

We computed the redox potentials for the following *electron transfer (ET)*

$$Li_{6+m}[(P_2W_{18})_x] + ne^- \rightarrow Li_{6+m}[(P_2W_{18})_x]^{n-} \quad , \tag{5.2.1}$$

and the following *proton-coupled electron transfer (PCET)*

$$Li_{6+m}[(P_2W_{18})_x]^{2-} + n(H^+ + e^-) \rightarrow Li_{6+m}[H_n(P_2W_{18})_x]^{2-} \quad , \tag{5.2.2}$$

occurring on a single and two POM units. Here, n = 1 and 2 for both ETs and PCETs, m = 0 and 6 are the Li$^+$ ions to neutralise respectively one (x = 1) and two (x = 2) POM units. A thermodynamic cycle was employed to compute the redox potentials. Within this model the standard free energy of each redox state (X = Ox or Red) can be expressed as

$$G_X = E_X^{ele} + \Delta G_X^S \quad , \tag{5.2.3}$$

and the Gibbs free energy of the reaction in solution is then given by Eq. 2.7.13 Where $\Delta_r G_g^o(Ox|Red)$ is the free energy of the reactions in gas phase, while $\Delta\Delta G_S^o$ is the difference between the solvation energies, ΔG_X^S, of the products and reactants. Since the large size of Wells-Dawson POMs, frequency calculations are only possible for def2-SVP basis set, and thus zero-point and entropic contributions from the def2-TZVP simulations have been neglected. This assumption is further justified by previous results which showed that the basis set choice is more sensitive than the contributions to the final free energy of these latter terms, [48] which is normally small. [46] The standard redox potential of the reduction, U_{red}^o, is then related to the free energy of reaction in solution by the thermodynamic law:

$$U_{red}^o = -\frac{\Delta_r G_s^o(A_i|B_i)}{nF} - U_{abs}^o(NHE) \quad . \tag{5.2.4}$$

Here n and F are respectively the number of electrons transferred, and the Faraday constant (23.061 kcal mol^{-1} V^{-1}). Throughout we set $U_{abs}^o(NHE)$ = 4.24 eV [141]. In each case to ameliorate challenges associated with the self-interaction error [143], the $\mathbf{P}_2\mathbf{W}_{18}$ has been neutralised using Li^+ counter-ions, which were included in the geometry optimisations. The free energy of solvation, ΔG_X^S, of each species was determined by using CPCM [138] as implemented in ORCA [87] using the dielectric constant and refractive index of water. The enthalpies of solvation of the proton was set to -264 kcal/mol. [144]

5.2.2 Hydrogen Evolution

Both experimental and theoretical studies have shown that HER in acid media occur through two elemental steps: the adsorption of hydrogen on the catalyst

$$n(H^+ + e^-) + * \rightarrow H_n^* \tag{5.2.5}$$

which is know as Volmer reaction, and the subsequent release of molecular hydrogen H_2 that can either occur through the Tafel reaction (H^* + H^* → H_2) or the Heyrovsky reaction (H^* + H^+ + e^- → H_2). Here, the H^* symbol indicates the catalyst with adsorbed hydrogen, while $*$ the free catalyst. The HER activity of a catalyst can be estimated from the Gibbs free energy of hydrogen adsorption on it. This is can be done by using the CHE approach of Norskøv *et al.* [179, 180] Within the CHE method, the free energy of the hydrogen adsorption (also indicated by H-addition) is

$$\Delta G_H = \frac{1}{n}\Big[G_{H^*} - \Big(G_* + \frac{n}{2}G_{H_2}\Big)\Big] \tag{5.2.6}$$

where G_X is free energy of the each species. We computed the G_X from Eq. 2.7.1.According to the Sabatier principle, an optimal catalyst would not bind neither too strongly or poorly the catalyst, which translates into having a ΔG_H = 0 eV for the HER.

5.2.3 MD simulations

Throughout, all classical molecular dynamic (MD) simulations were performed using the AMBER package. [82] Recently, several authors have derived to define a general force field for POMs, [54–56] however, this remains elusive. Consequently, our force field consists of bonded terms obtained from frequency calculations as described in the modified-Seminario method [85]. The non-bonded terms for all atoms were taken from the Universal Force Field (UFF) [86]. Atomic charges have been calculated using the CHELPG method as implemented in ORCA [87].

We carried out MD simulations for each charge state of $[P_2W_{18}O_{62}]^{q-}$ (q = 6, 10, 14, 18, 24). The initial setup for each classical MD was generated by solvating the optimised POM and counterions ions, from previous DFT calculations, in a box with over 6000 TIP3P water molecules [145]. Within each of MD runs, we studied 12 $\mathbf{P_2W_{18}}$ with H_3O^+ as counter ions. The number of H_3O^+ is equal to the POM charge such that the total system is neutral.

After the minimization, we performed 150 ps of NVT with POM positions restrained in order to allow the relaxation of solvent and counter ions around the solutes. This was followed by further 150 ps of NPT without any restraint. Then, the system was allowed to relax for further 4 ns of NPT, and a further 20 ns of NPT dynamics was used as final production for the subsequent analysis. PBCs were applied with a cutoff of 8 Å for long-range interactions, which have been treated by the particle-mesh Ewald summation. SHAKE has been applied to all bonds involving hydrogen atoms. [147]. A Langevin thermostat was used throughout with a temperature of 300 K and room pressure.

The visualizations of the results were performed with VMD [183]. The POM agglomeration was computed by using the solvent accessible surface area (SASA) algorithm as implemented in AMBER. [82] All types of interactions in solution were investigated by computing their radial distribution functions (RDFs).

5.3 Results

5.3.1 POM-POM Interactions

The effect of the $\mathbf{P_2W_{18}}$ charge on its agglomeration can be appreciated by a direct visualization of the MD trajectories given in Fig 5.3.1, where we focus upon different charge states POM^{q-}, (q = 6, 10, 14, 18, and 24). One can see that monomers (single POM unit) tend to agglomerate and form an inorganic phase in water for POM^{6-} and POM^{10-}. On the other hand, when the charge increases up to q = 14, POMs tend to be more solvated, however, dimers or even trimers can still be observed. The POM^{q-} are then completely solvated when their charge is q = 18 and 24. These results have similarly been reported for Keggin-type polyoxovanadates, which agglomerate to form hydrophobic microphases in water, and their stabilization is strongly dependent on their redox state . [51,53]

One way to quantify the hydrophobic character of a compound in solution is to compute its solvent accessible surface area (SASA). The SASA is a measure of how much area of the solute is exposed to the solvent, and the lower is its value, the less solvated is the solute. We computed the SASA average over the whole simulations of all charge states (Figure 5.3.1). At lowest charge states, q = 6 and 10, the SASA is rather similar, and it then increases with a slow rate when q = 14. These values reflect the poor penetration of water molecules in the hydrophobic agglomerate formed by the POMs even at q = 14 when dimers and trimers species are present. The scenario changes as the POM charge increases, the SASA undergoes a high-rate rise, which is the result of the full solvation of each POM.

We investigated in more detail the POM-POM interaction by calculating their radial distribution function (RDF) with H_3O^+ as the counter ion. Specifically, we computed the RDF between the phosphorus atoms of different POMs, avoiding thus to count the intramolecular P-P distances. Figure 5.3.2a shows multiple peaks that spread over the range of 12-15 Å for q = 6 and 10, which parallels well with the POM agglomeration shown in Figure 5.3.1a,b. In the POM^{14-} case, these peaks become less evident and at the same time they tend to shift toward larger distances. This shift indicates that the

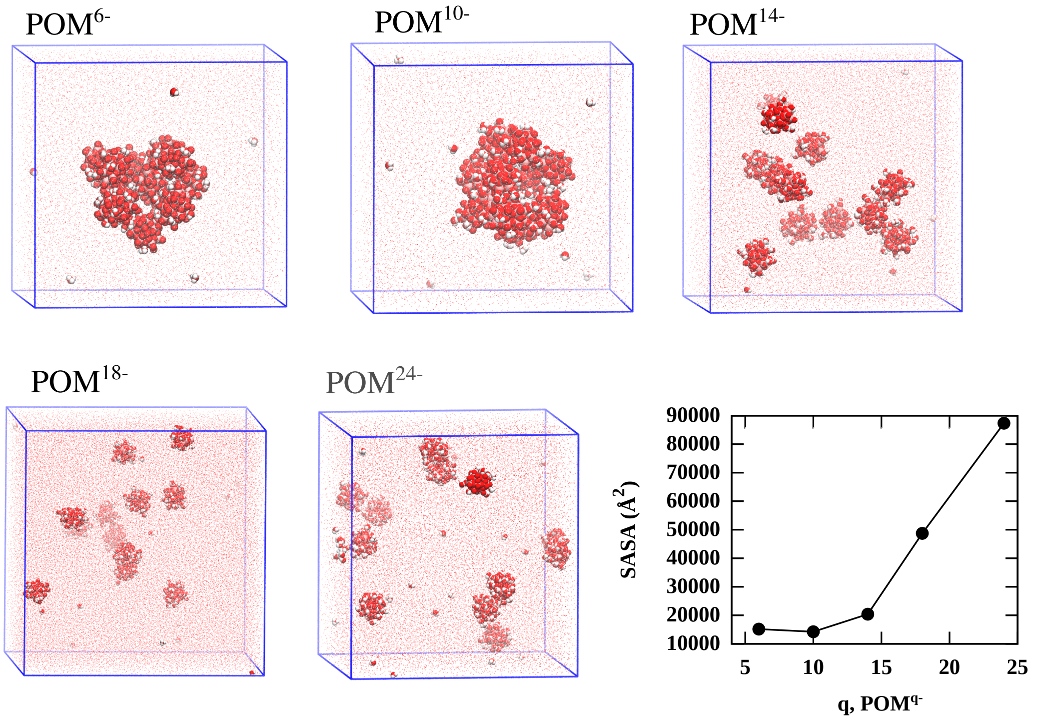

Figure 5.3.1: Evolution of POM^{q-} agglomeration at target charge states at end of 20 ns of MD. The POM and H_3O^+ ions are highlighted with van der Waals suraface, while the water is shown as lines. On the bottom right, the SASA values computed for the respective charge states.

POM-POM distance in dimers and trimers becomes larger than when they form the hydrophobic phase. It then completely disappears in POM^{18-} and POM^{24-}, where there is no longer agglomeration at all.

In addition to the excess of charge, the POM bulky structure does not allow them to enter in direct contact with each other. Instead, their interaction are mediated by the H_3O^+, which plays an important role in the formation of POMs agglomerate as explained below.

5.3.2 POM-H_3O^+ and POM-Water Interactions

To analyse how the POM-H_3O^+ and POM-water interactions evolve during the dynamics for each different POM charge, we computed their RDFs.

In contrast to Keggin-type POMs, Wells-Dawson POMs are less symmetric, and more oxygen sites might differ from each other. For this reason, we investigated the interaction of H_3O^+ ion with each oxygen sites, i.e., terminal O_t, bridging O_b, and belting O_B (Figure 5.3.3). The O_t-H_3O^+ RDFs show that there is a relatively weak peak at about 3.0 Å for POM^{6-}, however, as the

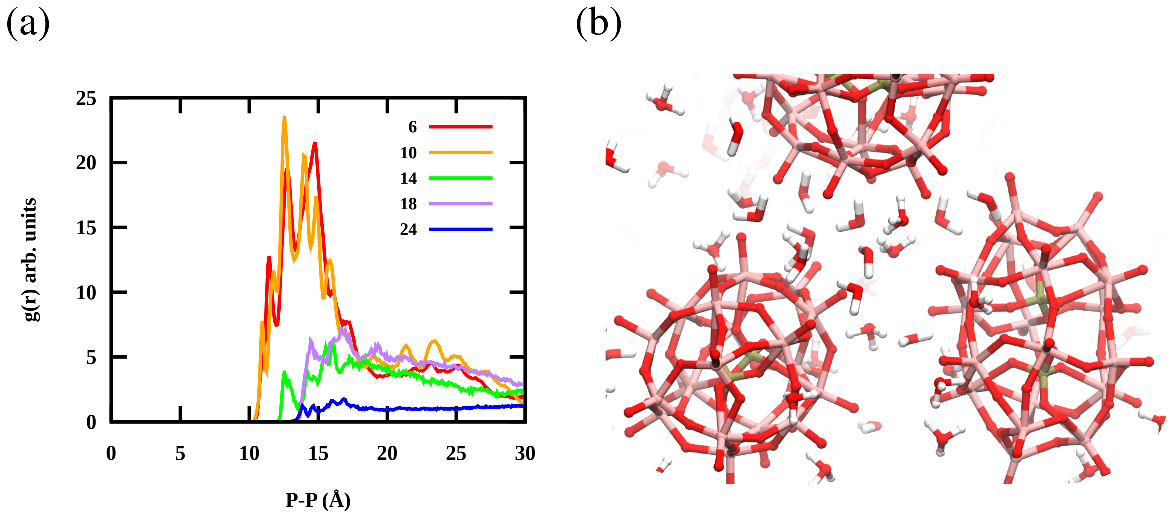

Figure 5.3.2: **(a)** Volume normalized RDFs of intermolecular P-P distances. **(b)** Representative MD snapshot of the POM-POM interactions mediated by H_3O^+ ions. The color-coded legend represents the POM^{q-} charge: q = 6 (red), 10 (orange), 14 (green), 18 (purple), and 24 (blue).

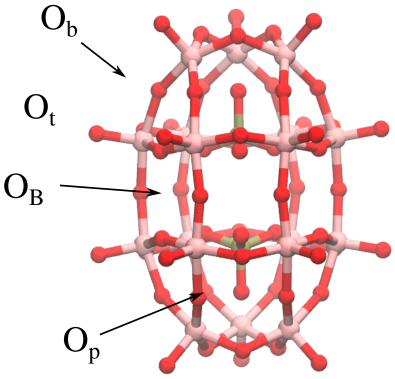

Figure 5.3.3: Molecular Structure of Wells-Dawson $\mathbf{P_2W_{18}}$. Different oxygen types are highlited: terminal O_t, bridging O_b, phosphorus O_p, and belting O_B.

POM charge increases two peaks at respectively 1.4 and 2.6 Å become more evident. Even at lowest charge states, q = 6 and 10, the O_b-H_3O^+ RDFs give two strong peaks, one below 2.0 Å, and another around 2.6 Å. The first peak then shifts towards slightly lower distance when the POM charge increases, indicating a stronger interaction between the two, while the second peak becomes more delocalised over a larger range of distances, despite its intensity increases. In contrast, in the O_B-H_3O^+ case, the RDFs do not possess any prevalent peak when the charge goes from q = 6 up to q = 14, whereas one clear peak below 2.0 Å, and multiple jagged patterns above the 2.0 Å, are found in POM^{18-} and POM^{24-} cases. This means that the H_3O^+ ions are more likely attracted by the bridging and terminal oxygens rather than the belting oxygens.

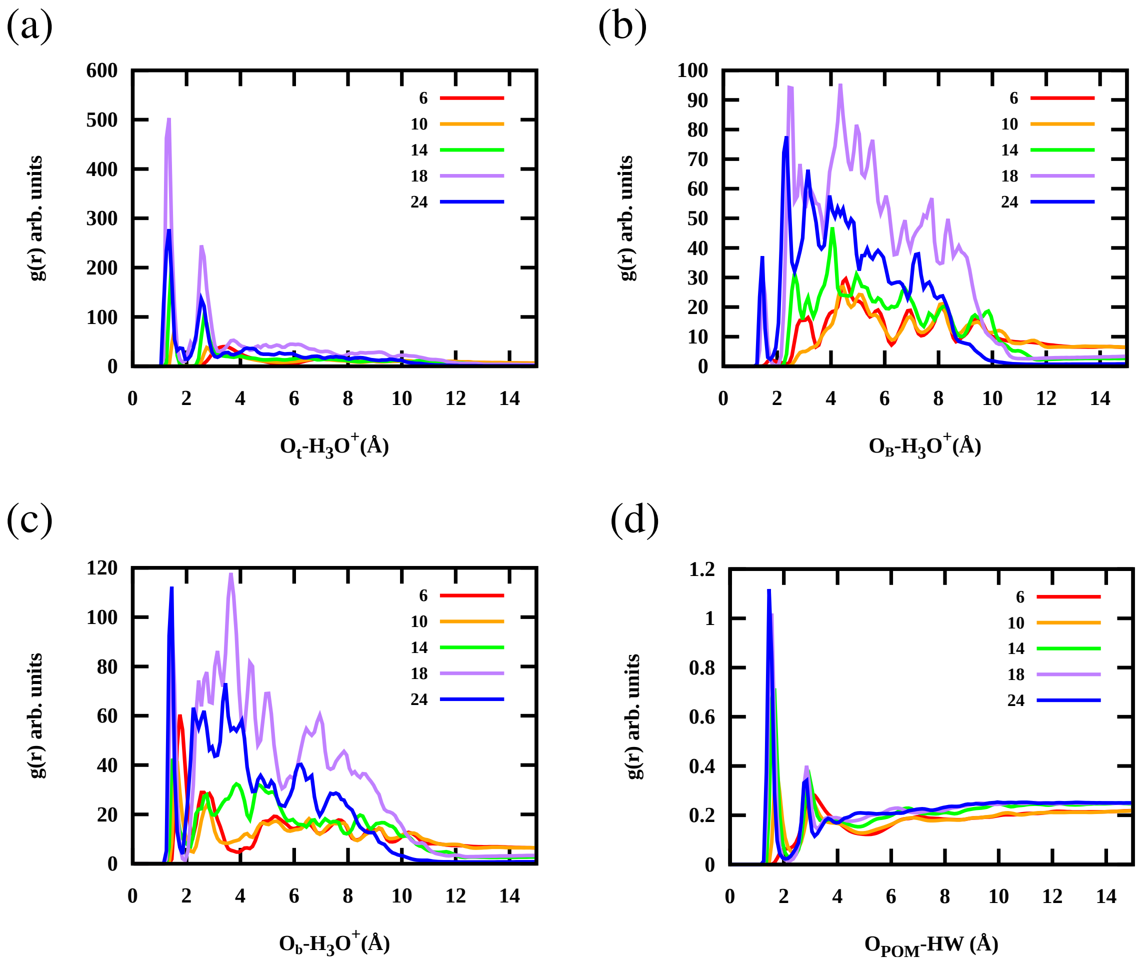

Figure 5.3.4: RDFs of P_2W_{18}-H_3O^+ interaction on different POM sites: **(a)** Ot-H_3O^+, **(b)** O_B-H_3O^+, **(c)** O_b-H_3O^+, and **(d)** HW-O_{POM} sites: HW are the hydrogens of water molecules, and O_{POM} is the most exposed oxygen of the POM (O_t). The color-coded legend represents q = 6 (red), 10 (orange), 14 (green), 18 (purple), and 24 (blue).

Therefore, the RDFs analysis provide the following scenarios: at low charge states the POM agglomeration is followed by a formation of closed or even semi-closed ion POM-H_3O^+ ion pairs, which interact with each other through the most basic sites, namely the O_b oxygens. Importantly, at low charge states the H_3O^+ ions mediate the POM-POM interactions allowing the formation of supramolecular structures. This feature underlines that the cation-mediated self-assembly is the predominant process, whereas direct interaction between POMs is less likely. [184–186] On the other hand, as the charge increases, all POM oxygens become more basic, and therefore, the interaction between

POMs and H_3O^+ ions becomes stronger, stabilizing the strong POM-POM repulsion.

The role of water is shown by its RDF in Figure 5.3.4d. At q = 6 there is no strong peak, while a little peak appears at about 2.0 Å for q = 10. This latter then becomes more marked as the POM charge increases. This means that at low charge the solvent molecules do not enter within the inorganic microphase, however, as the charge increases, each POM becomes more hydrophilic and the inorganic agglomerate falls apart. Therefore, the water molecules do not directly mediate between the POMs as, on the contrary, do the H_3O^+ ions.

5.3.3 Hydrogen-bond Analysis

As emerged from the previous section, the water molecules do not explicitly mediate the POM-POM interaction during the agglomeration. In order to explore the existence of implicit behaviour of water molecules, i.e., the formation of a hydrogen-bond network inside and outside the POM clusters, we carried out a comprehensive analysis of POM-H_3O^+ and water-H_3O^+ distances. Figure 5.3.5 shows the combined distribution functions (CDFs) for O_{POM}-H_3O^+ (d_1) and O_{water}-H_3O^+ (d_2) distances at different POM charges, i.e., the joint distribution that gives the probability of finding these two distances within the range 0-4 Å. In the case of POM^{6-} the CDF shows a relatively large probability when d_1 = 3.0 Å and d_2 = 1.6 Å. The small distances indicate that the water forms hydrogen bonds with the H_3O^+ ions leading to a more likely $H_2O_5^+$ species (Zundel ion). [187] The probability of distance d_2 from our simulations are supported by full quantum chemical simulations, which suggested that a hydrated hydronium ion has an O_{water}-H_3O^+ bond length close to 1.7 Å. [188] The value of d_1 distance indicates that at low charge, the POM-POM interaction is mediated by long H-bonds between POMs. This feature agrees well with the hydrophobic picture in Figure 5.3.1 and the POM-H_3O^+ RDFs of POM^{6-} (Figure 5.3.4), which have significant peaks only in the range of 2-4 Å.

When q = 10, the CDF is split in four regions with d_1 and d_2 values still occurring at $d_2 \approx 1.6$ or ≈ 3.0 Å, where the maxima are also located: d_1 = 1.5 Å and simultaneously d_2 = 1.5 or 2.8 Å. This pattern has also been found for the other higher charge states, where one or two maxima are present in similar positions (Figure 5.3.5c,d). These scenarios suggest that water molecules and H_3O^+ form two types of hydrogen-bond networks: one within which

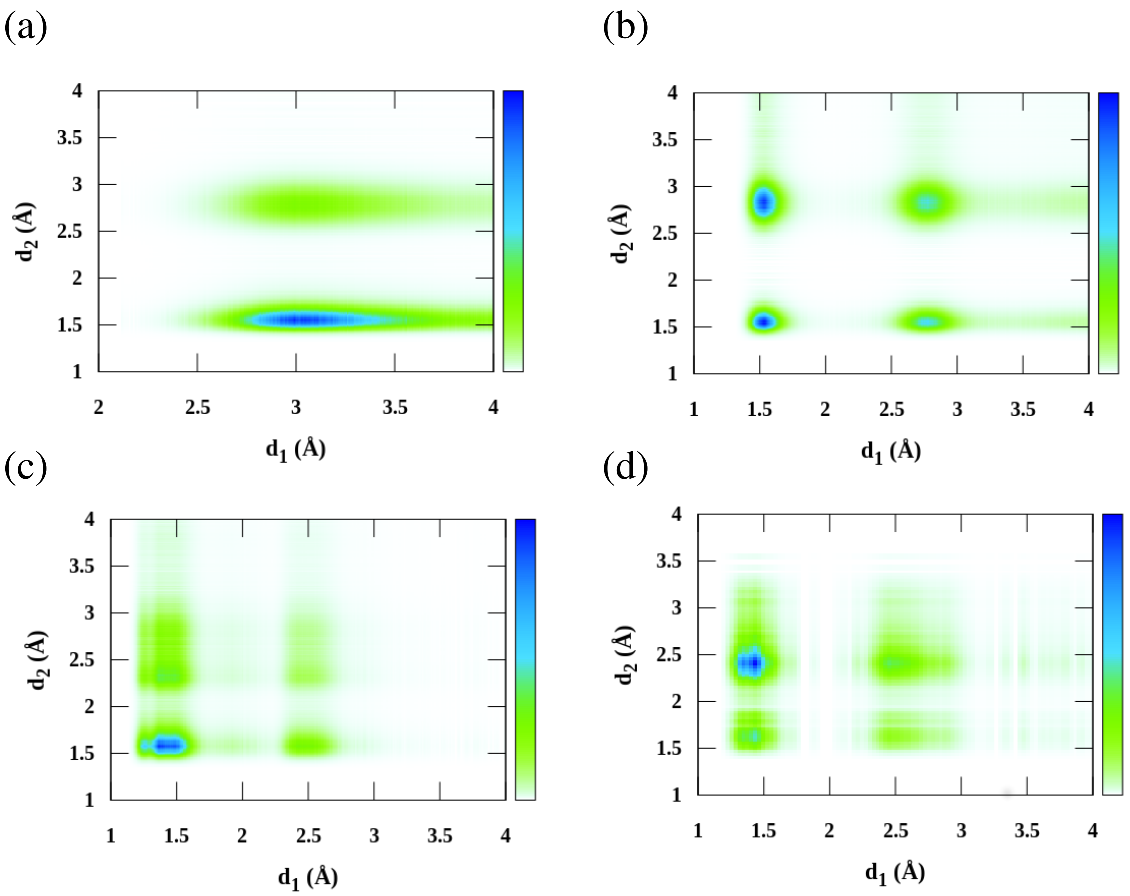

Figure 5.3.5: CDFs of P_2W_{18}-H_3O^+ interaction for **(a)** POM^{6-}, **(b)** POM^{10-}, **(c)** POM^{18-}, and **(d)** POM^{24-}. d_1 is the distance between the POM terminal oxygen and hydrodium hydrogen O_{POM}-H_3O^+. The d_2 is the distance between the water oxygen and hydrodium hydrogen O_{water}-H_3O^+. The color-coded box indicates a low value (white) to high value (blue) of CDF.

POMs are more likely solvated by $H_2O_5^+$ ions, and another in which the H_3O^+ interact with the water molecules through longer range hydrogen bonds. The competition between $H_2O_5^+$ and H_3O^+ solvations has also been highlighted by Wipff *et al.*, [51] who showed that $H_2O_5^+$ ions increased the agglomeration of 10 % compared to that obtained by H_3O^+ ions for Keggin-type polytungstanates. As explained in the computational details, the number of H_3O^+ ions in the simulations corresponds to the POM charge such that the total system is neutral. For instance, for the 12 POM^{q-} with $q = 24$, 288 H_3O^+ ions have been added to the system. One might think that changing the number of H_3O^+ ions could give more information about the pH effect on the agglomeration, however, it has been repeatedly shown that the MD simulations of charged systems suffer from high instabilities. [7] This is mostly due to the use of the Ewald sum algorithm (see Section 2.5.5), which formally converges only if the net charge of the total system is zero. Therefore, it is always recommended to run MD simulations on neutral systems.

5.3.4 Redox Potentials

The previous section has outlined the importance of agglomeration for these POMs in solution, in this section we shed insight into its effect on the redox potentials. It is important to stress that calculating the redox potentials of the entire aggregate is well beyond the limits of DFT and so we have focused instead on dimers.

Using the thermodynamic cycle, we computed the standard redox potentials U^o_{red} for both single or multiple ET and PCET occuring to $\mathbf{P_2W_{18}}$. As outlined in previous sections, Cronin *et al.* showed that 2 mM of POM firstly undergoes two single ET, while the additional two reductions are PCETs at pH = 4, resulting in a total reduction of POM by 6 e^-. However, in their work, the CV becomes more complex when pH and POM concentration are respectively lowered and increased, and it is believed that the POM can be reduced by up to 18 e^-. This high number of electrons and few redox peaks in the CV make the determination of the number of electrons and protons belonging to each reduction peaks difficult. For this reason, we only focused upon the first four reductions, specifically, U^o_{red} are computed for the first two reductions occurring both via ET, while the the two more additional reductions are PCETs. The two ETs and PCETs occur consecutively, and they correspond respectively to Eq. 5.2.1 and Eq. 5.2.2. These are listed in Table 5.3.1.

Table 5.3.1: U^o_{red}vs NHE (V) values calculated for a single $\mathbf{P_2W_{18}}$ and two $\mathbf{(P_2W_{18})_2}$ units, using PBE and PBE0 *x-c* functionals. Here, the ETs and PCETs refer respectively to Eq. 5.2.1 and 5.2.2.

	$\mathbf{P_2W_{18}}$		$\mathbf{(P_2W_{18})_2}$		**Exp.**
Reaction type	**PBE**	**PBE0**	**PBE**	**PBE0**	**2 mM**[a]
$1e^-$	1.64	1.01	1.21	1.01	0.35
$1e^-$	0.83	0.609	1.01	0.59	0.18
$2(H^+ + e^-)$	-0.36	-0.404	0.19	0.10	-0.22
$2(H^+ + e^-)$	-0.92	-0.88	-0.578	-0.67	-0.50

[a] Ref. [27], P_2W_{18} in a solution with pH = 4

From Table 5.3.1 one can see that for the first ET reduction the PBE gives a U^o_{red} with a deviation of over ~ 1 V from experimental data. Whereas, better results are given by the PBE0, whose deviation is about 0.7 V. In the case of the 2nd ET, the PBE0 still performs better than the pure GGA functional with an uncertainty of 0.4 V, however, the deviation of U^o_{red} from the PBE is halved with respect to the 1st ET. In contrast with the first two ET reductions, a small impact of the *x-c* functional is observed for the PCETs. Indeed, PBE and PBE0 return U^o_{red} values for both 1st and 2nd PCET with deviation ranging between 0.1-0.4 V. These U^o_{red} estimations are consistent with the previous theoretical studies, which showed that similar uncertainties are mainly due to the limits of the implicit solvation in the computation of accurate solvation energies. [46,48]

Since the CV changes shape as the $\mathbf{P_2W_{18}}$ concentration increases, [27] we also investigated the effect of the POM agglomeration on the redox potential by computing the U^o_{red} value for the same reactions occurring at $\mathbf{(P_2W_{18})_2}$. In the PBE case, the U^o_{red} uncertainty drops of about 0.4 V for the 1st reduction, while it increases of 0.2 V for the 2nd reduction compared to the single POM unit. On the other hand, for both 1st and 2nd reduction the PBE0 give U^o_{red} values very close to the ones in the case of a single POM unit. While for the two PCETs, the PBE and PBE0 results are more consistent with each other, and differ more from the U^o_{red} values of $\mathbf{P_2W_{18}}$, i.e., both functionals give a more positive U^o_{red} for the 1st and 2nd PCET. Therefore, our results show that the first ETs are independent from the POM-POM interactions, whereas these latter become important during the PCETs, as reflected by the different U^o_{red} values. As shown in Chapter 3, further improvement in the computation of the redox potentials can be achieved by optimizing the structures with larger basis set, and by including an explicit solvation. The size of POMs in the present work, and especially the incorporation of aggregation effects, means that these effects need to be balanced against the computational expense. Therefore, these calculations aim to qualitatively show the effect of close contacts among POMs on their electrochemistry, rather than giving a direct comparison to experiment.

Finally, it is worth noting that $\mathbf{P_2W_{18}}$ reduction through PCETs are pH-dependent. And, it has been shown that further corrections can be obtained by accounting for individual ET and proton transfer occurring for each individual redox intermediate. [103] However, accounting for all possible redox intermediates becomes extremely computationally expensive for systems like $\mathbf{P_2W_{18}}$. Besides, the uncertainty of the computed U^o_{red} values are in agreement with limits of the implicit solvation models, which have largely been discussed in literature, [103, 189] and thus we do not discuss the pH dependency in this work.

5.3.5 Electronic Delocalisation

The ability of POMs to undergo numerous electron reductions is usually ascribed to an electron delocalisation all over their structure such that the electronic repulsion among metallic centers is lessened, which is particularly true for Keggin ion types. [14,48] Despite their similarities, it has previously been shown that Keggin and Well-Dawson POMs possess, however, different electronic distributions. [14] In this section, we analysed the frontier molecular orbitals (FMOs) of the $\mathbf{P_2W_{18}}$ and $\mathbf{(P_2W_{18})_2}$ redox states involved in the four reductions at both PBE and PBE0 level. As outlined in the previous section, these computations are carried out with a continuum solvation model, and therefore the role of the explicit solvent molecules, as well as of the pH is not investigated. Furthermore, hydrogen atoms are added to POM without taking into account their solvated form, i.e. the hydronium ion H_3O^+. This approach reduces possible strong SIEs arising from the use of charged molecules. [43]

For the single $\mathbf{P_2W_{18}}$ unit, the PBE and PBE0 return similar FMOs composition, and we only focus upon the PBE0.

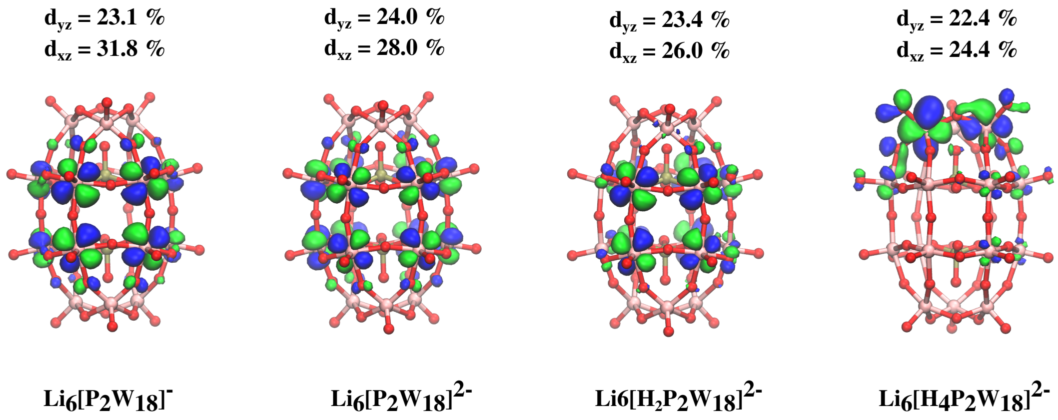

Figure 5.3.6: HOMO orbitals computed with PBE0 functional for the two ETs and PCETs of $\mathbf{P_2W_{18}}$. The Li^+ ions and the H atoms are not shown for clarity.

From Figure 5.3.6 one can see that all the HOMOs are mainly composed of a mix of d (W) and nonbonding p (O) atomic orbitals, with the metal atoms that are not totally in a perfect D_{3h} geometry, which is the idealised symmetry of each metal within the Wells-Dawson POMs. [14] Despite the deviation from the D_{3h} symmetry, the HOMOs are mainly composed of d_{xz} and d_{yz} orbitals, which in contrast to the $d_{x^2-y^2}$ orbital (whose percentage is $< 1\%$), do not point towards the oxo-ligands, and therefore, these are firstly occupied. The HOMO of $Li_6[P_2W_{18}]^-$ is spread over the twelve Mo atoms in the equatorial region of the POM. This behaviour is similarly reproduced for respectively $Li_6[P_2W_{18}]^{2-}$ and $Li_6[H_2(P_2W_{18})]^{2-}$. In contrast, the HOMO of $Li_6[H_4(P_2W_{18})]^{2-}$ is more delocalised over W atoms in one cap region. For all type of reductions, PBE0 gives a energy gap between the HOMO-1 and HOMO which is > 0.6 eV, indicating that there is no degeneracy between these orbitals.

In contrast to the single unit, the PBE and PBE0 give different HOMO distributions for the $\mathbf{(P_2W_{18})_2}$. In the PBE case, the HOMO is localised over one POM unit after the 1st ET and PCET, whereas it is distributed over two units after the 2nd ET and PCET (Figure 5.3.7b,d). On the other hand, the PBE0 gives a HOMO localised over a single unit of $\mathbf{(P_2W_{18})_2}$, regardless of the redox state (Figure 5.3.7b). The over-delocalisation is due to the typical behaviour of GGA functionals that tends to delocalise too much charge distributions. Conversely, hybdrid-GGA functionals normally give lower delocalisation errors, and therefore, more accurate electron distribution. [72,190]

For $\mathbf{(P_2W_{18})_2}$, PBE0 gives a energy gap between the HOMO-1 and HOMO which is > 0.4 eV respectively for the 1st and 2nd ET, whereas it is ≥ 0.1 eV for the PCETs reactions. Therefore, the gap between these two orbitals drops in the energy compared to the single unit, and in the last case (1st and 2nd PCET) its small value indicates that there might be some degeneracy between these orbitals, which can lead to a breaking in the symmetry due to a possible Jahn-Teller distortion. [14] This aspect will be further investigated.

Therefore, our FMOs analysis offers the following scenario: after the first two ETs, further electrons added to the $\mathbf{(P_2W_{18})_2}$ go in the equatorial region rather than on the capping atoms as occurs for $\mathbf{P_2W_{18}}$. This explains why the redox potentials of $\mathbf{P_2W_{18}}$ and $\mathbf{(P_2W_{18})_2}$ are similar for the ETs but not for the PCETs, since the reductions occur on different metallic sites.

5.3.6 Hydrogen Evolution Reaction (HER) Activity

The specificity of the adsorption site towards HER is a crucial aspect of the catalytic process, in fact, it is well-known that the efficiency of a heterogeneous catalyst strongly depends on its reaction site. [191] As shown in Figure 5.3.3, P_2W_{18} possesses different adsorption sites, however, in the previous section we show that the terminal O_t and bridging O_b oxygens are more likey to be protonated in solution. Therefore, we focus our analysis on these two

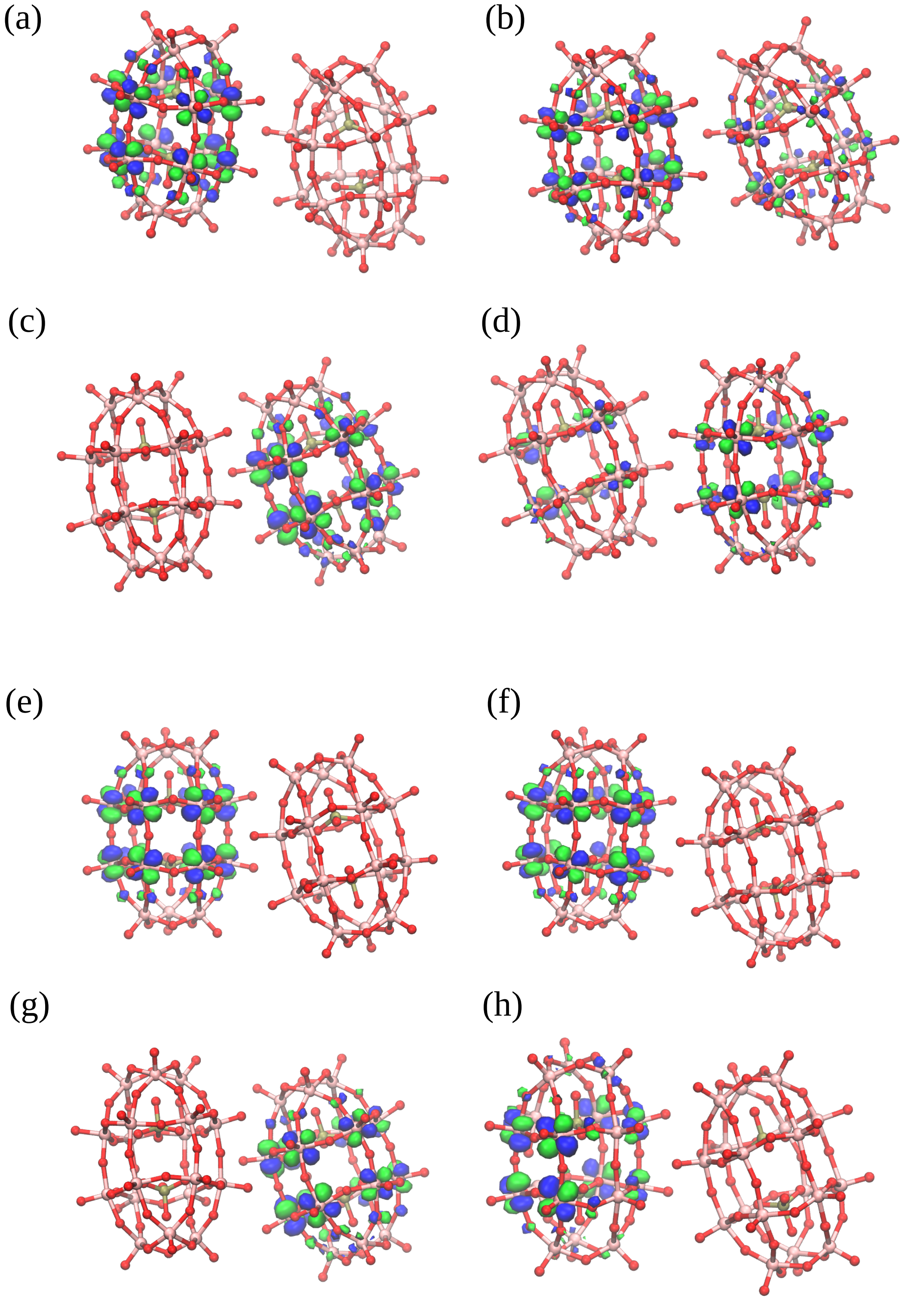

Figure 5.3.7: HOMO orbitals computed with PBE functional for $\mathbf{(P_2W_{18})_2}$ after the **(a)** 1st ET, **(b)** 2nd ET, **(c)** 1st PCET, and **(d)** 2nd PCET. HOMO orbitals computed with PBE0 functional for $\mathbf{(P_2W_{18})_2}$ after the **(e)** 1st ET, **(f)** 2nd ET, **(g)** 1st PCET, and **(h)** 2nd PCET. The Li^+ ions and the H atoms are not shown for clarity.

sites. The possible configurations that can arise from adding one hdyrogen atom to these two sites follow the series 2^n. This means that even for small values, like n $\geq$ 5, the effort to compute all possible configurations is computationally prohibitive. For this reason, we computed the ΔG_H only for n = 1, and 2 to distinguish the relative energies of each adsorption site, and on the basis of these results, we study the addition of further hydrogens to the POM.

Table 5.3.2: ΔG_H (eV) values calculated for all possible configurations arising from adding n = 1 and 2 hydrogen to O_t and O_t with PBE and PBE0 *x-c* functionals. The O_{xy-z} corresponds to the ΔG_H computed from O_{xy-z} configuration with respect to the O_z one. For example, O_{bt-b} indicates the ΔG_H due to the addition of a second hydrogen on a O_t site with a POM already hydrogenated on the O_b site.

no. H	site	PBE	PBE0
1	O_t	-0.607	0.007
	O_b	-0.872	-0.220
2	O_{bb-b}	0.102	-1.601
	O_{bt-b}	-0.123	0.022
	O_{bt-t}	0.225	-0.173
	O_{tt-t}	-0.322	-0.041

From Table 5.3.2 one can see that both PBE and PBE0 predict a too exothermic H-addition on the O_b site, while PBE0 returns a $\Delta G_H \approx 0$ for the adsorption on O_t. After the addition of a second hydrogen, ΔG_H becomes closer to zero for all the different configurations. Among the four configurations, the O_{bb-b} and O_{bt-b} display the best HER activity from the PBE results, whereas the O_{tt-t} and O_{bt-b} are the best sites from PBE0. In contrast to this, we also found that too positive (or negative) ΔG_H are shown by the O_{tt-t} (PBE) and O_{bb-b} (PBE0). Due to this opposing trend and the fact that ΔG_H of O_{bt-t} is still significantly small for the PBE0, we then chose to add further hydrogens alternatively to both terminal and bridging sites, and compute their ΔG_H. The same criteria were also applied to the study of the H-adsorption on two units $\mathbf{(P_2W_{18})_2}$.

From Figure 5.3.8a, one can see that the addition of more hydrogens to a single unit returns a ΔG_H that oscillates within the range 0.1-0.4 eV. This

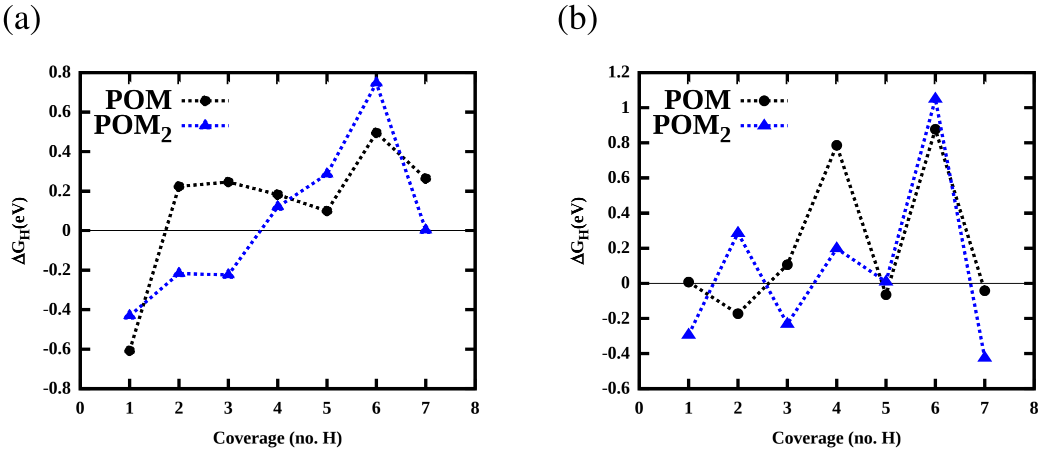

Figure 5.3.8: ΔG_H as function of the hydrogen adsorbed on a one and two POM units, computed at **(a)** PBE and **(b)** PBE0 functional. The H-adition follows Eq. 5.2.5. The dashed line are guides to visualize the patterns.

trend is found for **(P_2W_{18})$_2$**, where the energy range reaches up to 0.7 V. Figure 5.3.8b shows that PBE0 gives a **(P_2W_{18})$_2$** that possesses an opposite trend to **P_2W_{18}** for the first 3 adsorption, while they both have a similar ΔG_H pattern when further hydrogens are added. In some cases the ΔG_H is close to 0 eV, however, it is also ≥ 0.8 eV in other cases, which means that these states are too strongly endothermic to catalyse the hydrogen desorption. We also investigated the further adsorption of up to 18 hydrogens, however, an oscillating pattern can still be observed.

Therefore, our results shows that the POM-POM interaction affects the ΔG_H, however, there is not any evident improvement towards HER, regardless of the functional used.

5.4 Conclusions

In this work, we have presented a comprehensive computational study on the Well-Dawson type polyoxometalate **P_2W_{18}**, which has recently shown to be an effective electrode material in RFBs as well as proficient catalyst towards HER. [27] Our goal has been to explore the formation of POM agglomerates in solutions by rationalizing the existing relationship between its charge and the environmental factors, like solvent and counter ions. Furthermore, we aimed to investigate through first-principle calculations whether the agglomeration affects the POMs redox potential window and their efficiency towards the HER.

In the first part, we utilized the optimized DFT structures of $\mathbf{P_2W_{18}}$ as starting configuration for MD simulations. The MD outcome shows that the $\mathbf{P_2W_{18}}$ forms inorganic agglomerate at low charge states, however, as the POM charge increases, they become fully solvated. The SASA values and the RDFs of POM-water illustrate that the agglomerates are completely hydrophobic due to the small amount of solvent molecules within the clusters. In contrast, the RDF of POM-H_3O^+ shows a significant peak at 2 Å even at low charge state suggesting the important role of the hydronium ion that acts as a mediator between POMs.

The CDF analysis shows that two type of hydrogen-bond networks exist, and these can either occur via the formation of zundel ions ($H_2O_5^+$) or simply through H_3O^+ ions. The competition between $H_2O_5^+$ and H_3O^+ ions has also previously been found for Keggin-type POMs [51], which indicates that role of $H_2O_5^+$ ions must be taken into account when modelling POM in acid solution. It is worth noting that, in contrast to a single POM, the potential energy surface of a system with many POM units might possess several local minima, which could be difficult to explore. As result of this, configurations from classical MD simulations might be trapped in these minima, and therefore, unable to reach the realistic equilibrium conformations. [7]A possible solution to this would be to employ enhanced sampling techniques, like umbrella sampling or metadynamics, [7] which describe the system by biased potentials, thus allowing the overcome of many types of energy barriers. [7] Therefore, we believe that the use of these methods can give further insights into the mechanism of POM aggregation. This will be addressed in the future work.

In the second part of the work, we computed the redox potentials of a single $\mathbf{P_2W_{18}}$ and two units $\mathbf{(P_2W_{18})_2}$ by using an implicit solvent model. Generally, the results shows that PBE0 performs better than PBE functionals with an uncertainty of about 0.4 V. These deviations are within the limits of the implicit solvent model, [46,48] however, further improvements can be expected by explicitly including solvent molecules as shown in Chapter 3. [48] $\mathbf{P_2W_{18}}$ and $\mathbf{(P_2W_{18})_2}$ have similar redox potentials for the two ETs, whereas their U^o_{red} differ from each other for the PCETs, and therefore, the POM-POM interaction affects only the PCETs. This is due to the possibility of reducing the $\mathbf{(P_2W_{18})_2}$ by adding further electrons to equatorial atoms rather than capping atoms.

Furthermore, we investigated the efficiency of the $\mathbf{P}_2\mathbf{W}_{18}$ as catalyst towards HER by employing the computational hydrogen electrode (CHE) approach of Norskøv *et al.* To the best of our knowledge, this is the first study of modelling POMs for HER. We showed that both bridging and terminal oxygens can likely act as adsorption sites for the hydrogen atoms. Despite some hydrogenated species lead to almost $\Delta G_H = 0$, the remaining ones have alternating ΔG_H values for both single and two POM units, which makes a common pattern difficult to be identified. These results illustrate the limits of DFT for large inorganic systems, like POMs. For example, it has previously been shown that the contribution from explicit solvation might improve the accuracy of the solvation energy of Keggin-tpye ions, [45, 48] however, these simulations becomes extremely computationally expensive for large systems like Wells-Dawson types.

In summary, we provide a general theoretical protocol to obtain useful insights into the $\mathbf{P}_2\mathbf{W}_{18}$ agglomeration. While the size of these systems still makes first-principles simulations challenging, it is now possible to establish a direct relationship between agglomeration and electrochemistry of POMs.

Chapter 6

Thesis Summary and Outlook

6.1 Conclusion

In this PhD thesis, we have theoretically studied polyoxometalates by investigating their molecular and electronic properties in different physical environments by means of computational approaches.

Regardless of the POM type, we observe their molecular structure is not affected by the redox reductions when a relatively low number of electron are involved. In particular, the structures of $\mathbf{SiW}_{12}$ and $\mathbf{P}_2\mathbf{W}_{18}$ (after ETs) do not change after undergoing a reduction of four and six electrons, respectively. This behaviour is due to their electronic nature, i.e., after the reduction the electrons are fully delocalised over all metal atoms, and therefore, the Coulombic repulsion felt by each electron is lessened. This is no longer true when a high number of electrons are transferred to the POM as for example in the case of the super-reduced $\mathbf{PMo}_{12}$ (Chapter 4). In this case, the synergistic formation and elongation of respectively metal-metal and metal-oxygen bonds permit the transfer of many electrons to the POM. From an electronic prospective, the metal-metal bonds are guided by the formation of d-d bonding orbitals between two or three metallic centres. The Mo-Mo bonds in this POM are localised over only certain triads of the POM, resulting in a strongly asymmetric molecular structure. Thus, although all Mo atoms are formally reduced from Mo^{6+} to Mo^{5+}, only some of these, i.e. four, are reduced down to Mo^{4+}. On the other hand, the structure of $\mathbf{PV}_{14}$ is slightly influenced by a simultaneous four PCETs. However, it must be noted that in this case the HOMO is still distributed over all metal atoms, indicating that these are all involved during the reduction. The nature of the change in $\mathbf{PV}_{14}$ structure is due to the high number of PCETs. Indeed, the protonation of either a terminal or bridging oxygen of POMs leads to an elongation of the M=O double bonds, which become single bonds. [18]

Our results confirm that both GGA and hybrid-GGA functionals return similar POM geometries, which are in agreement with the experimental findings. However, these families of functionals return different answers when computing the electronic distribution of POMs. For instance, in Chapter 3, we found that PBE gives the HOMO of $Na_5[SiW_{12}O_{42}]$ being delocalised over nine out of the twelve W atoms, whereas there is a stronger localisation from PBE0 results, with the HOMO distributed only over six W atoms. This shows that for open-shell systems, like $Na_5[SiW_{12}O_{42}]$, which are intrinsically multideterminental states, the predictions of DFT might be less accurate for the low-spin open-shell states than for the high-spin and closed-shell states. [192] This observation is also in agreement with previous theoretical studies on POMs, which showed that GGAs suffer from over delocalisation due to a strong SIE. [14, 135] Difference between GGAs and hybdrid-GGAs were also observed for the Wells-Dawson $\mathbf{P_2W_{18}}$ type. In that case, PBE gives a HOMO distributed distributed over two POM units after the 2nd ET and PCET (Figure 5.3.7b,d), whereas the HOMO computed with PBE0 is localised over one unit of the system $\mathbf{(P_2W_{18})_2}$. Another interesting result is the finding of only four Mo-Mo bonds in the formally fully reduced $\mathbf{PMo_{12}}$, although PBE0 was employed. This is another manifestation of SIE, which is rather important even for hybrid-GGAs.

We demonstrated that an implicit solvent can be used to compute redox potentials of POMs with relatively good accuracy. Within this approach, POMs are fully neutralised by their counter ions, like Li^+ and Na^+, such that the influence of SIE is lessened. [46, 48] However, uncertainties can arise due to the highly charged nature of POMs that generate a strong interaction of these with surrounding solvent, which should be taken into account. Furthermore, we benchmarked different exchange-correlation functionals for the calculation of redox potentials. Our results show that the inclusion of Hartree-Fock exchange, E_{xc}^{HF}, gives better results with respect to the pure GGAs, however, errors on the computed redox potential fall within the uncertainties of the implicit solvation model (Chapter 3 and 5). Further improvement can be obtained by an explicit solvation, with a drop of the uncertainty on the redox potential down to 0.1 V. [48] This was the case for the 1st and 2nd reduction of $\mathbf{SiW_{12}}$, however, large deviations are to be expected when a large number of electrons and/or protons are involved in the reduction process. These deviations are largely due to SIE, which is particularly important for highly charged systems. This was particularly evident for the computation of VEG of $\mathbf{PV_{14}}$, which required the calculation of the energies of the systems $[H_9PV_{14}]^{4-}$ and $[H_{13}PV_{14}]^{4+}$. Indeed, a large SIE is due to the incorrect behaviour of almost all E_{xc} functionals far from a nucleus, which decay exponentially rather than asymptotically. [43]

Furthermore, the use of an explicit environment, alongside a quantum mechanical treatment of POMs, allows to gain insights into the evolution of their molecular structures in solution, and in the stability of different charge states. For instance, we showed that the breakdown of LR for $\mathbf{PV}_{14}$ is due to the change in its molecular structure after the reduction.

In addition to DFT calculations, we showed that we can gain insights into the electronic and structural changes of POMs by simulating their X-ray absorption spectra. The simulated XANES and EXAFS spectra are in perfect agreement with the experimental data suggesting, therefore, that these simulations are a powerful tool to investigate POM oxidation state. Just to give an idea, while the maximum number of Mo-Mo bonds found from DFT calculations was four, the EXAFS analysis on $\mathbf{PMo}_{12}$, constrained with Mo-Mo bonds, return a better agreement with experiment, indicating that this technique can be employed to overcome the limits of DFT mentioned above. In particular, the use of Wavelet transform permits to resolve the centres of the backscattering wave functions in both energy and distances from the absorbing atom, offering a clearer way to discriminate different neighbouring atoms. The Wavelet analysis illustrates that the EXAFS spectra are more sensitive to the Mo-O bond lengths than to the Mo-Mo bonds. The EXAFS results are supported by the XANES spectra, which are sensitive to the minimal structural change as well. Despite many examples for other systems, [117] to the best of our knowledge, this is the first time that a DNN for XAS spectra was coupled to MD simulations in order to quantitatively investigate the structural changes of POMs.

Throughout this work, we employed QM/MM MD simulations to extract the quantum-mechanical properties of POMs in an explicit environment. Besides calculating the redox potentials, our QM/MM MD simulations show that the presence of the solvent affects the molecular structures of highly charged POM (Chapter 3).These simulations explains the breakdown of linear response approximation, and therefore, they represent a further check on the accuracy of the computed redox potentials in solution. Furthermore, for highly charged POMs, like $\mathbf{PMo}_{12}$, our QM/MM simulations showed that the interaction between POMs and the counter ions become stronger, whereas the POM-solvent interaction is weakened. As result of this strong interaction, we observed that POMs and counter ions form prevalently semi-closed and closed ion pairs, with the bridging oxygens being the most basic sites. This aspect was also observed for $\mathbf{SiW}_{12}$, for which the expansion of the first solvation shell has an effect on the diffusion coefficient of POMs, and therefore, also on the kinetic and power density of RFBs.

On the other hand, classical MD helped us to investigate the macroscopic behaviour of POMs in solution. For instance, in Chapter 5, we investigate the self-assembly process of Wells-Dawson POMs. The classical MD simulations show that P_2W_{18} agglomeration strongly depends on its charge state, i.e., the higher is the charge, the more solvated is the POM. At low charge state, the POM-POM interaction is mediated by H_3O^+ and $H_2O_5^+$ ions which form a rich hydrogen bond network. Importantly, this highlights a possible competition between $H_2O_5^+$ and H_3O^+ ions, indicating that $H_2O_5^+$ ions must be taken into account when modelling POMs in acid solution. These observations were possible thanks to the computation of the SASA values and the RDFs POMs, which are indispensable tools for these types of studies. In agreement with the QM/MM calculations, at high charge states the POM-cation interactions become stronger to balance the strong POM-POM repulsion, leading to fully solvated POMs. However, in contrast to QM/MM MD of $Na_6[SiW_{12}O_{42}]$, which shows a desolvation when the POM charge increases, the classical MD results illustrate that $\mathbf{P}_2\mathbf{W}_{18}$ becomes fully solvated at high charge. This is due to the fact that classical MD and QM/MM MD handle the high repulsion of highly charged POMs in different ways. For instance, in QM/MM simulations a high excess of charge might lead to a strong overpolarization of MM region and/or to an electronic leakage of QM density (spill-out). Thus, the overpolarization leads to a larger repulsion between the electron density of QM atoms and the atomic charges of MM atoms.

In summary, it is now possible to adopt a range of computationally approaches to develop a detailed understanding of the functional properties of POMs.

6.2 Future Prospective

While DFT remains the most feasible theoretical approach to reproduce quantitatively the energies and geometries of POMs, it still has some limits. The POM elemental composition, i.e., mainly transition metals, represent a challenge for most common exchange-correlation functionals even at equilibrium geometries. To this end, the properties of POMs, like redox potential and geometries of highly charge states, need to be benchmarked in order to understand the limits and advantages of each functional in any specific case. This analysis can definitely help the community to develop better functional. For example, an important contribution is the characterization of mixed-valence POMs, especially in the study of catalytic processes. [14] In this regard, the addition of dispersion terms to local xc functionals represents a valid option to reach the so-called chemical accuracy. Among many different dispersive xc functionals, the DFT-D methods developed by Grimme *et al.* have shown to give a small mean absolute deviations for metallic clusters as well as for the dissociation of cation-anion compounds, which represent the building blocks of ionic liquids. [193, 194] For this last type of system, which is very similar to POMs and their counter ions, they found that the energy contribution of van der Waals dispersion is about 5-6 % of the equilibrium interaction energy, and therefore this term must be taken into account when ionic interactions become important. Another robust alternative are the RS hybrid functionals. In these functionals, the HF exchange is introduced by partitioning the Coulomb operator into a long-range part and a short-range part and treating one of them by local exchange and the other by HF exchange. [195, 196] This approach allows the correct description of the electron motion far from the nucleus, and therefore, it reduces the SIE effects. Grimme *et al.* showed that the performance of RS-functionals in predicting reaction profiles involving transition metals was superior to the that of local GGAs and meta-GGAs. However, there was no significant benefit over hybrid-GGAs and highly parametrized Minnesota functionals (Mxy). [151]

As outlined in the introduction, POM-based LIBs can offer a high theoretical capacity due to an incredibly high number of electrons involved in the reduction of POMs. This technology can be thought of as robust alternative to the more expensive LIBs. However, these batteries suffer from poor capacity retention due to the structural instabilities of the fully reduced POMs. Therefore, our future work will aim to study the relationship of different families of xc functionals with the elemental composition and electronic properties of POMs in order to understand how to enhance POM efficiency in LIBs.

Another important element is the account of the proton into their redox reactions. PCETs add a further degree of difficulty in the study of POMs, since these can either occur through concerted or separate PC and ET steps. The computational workload to address these aspects is almost prohibitive, even when a small number of protonation steps are involved in the reactions, however, a full ab initio MD can be used to explore the kinematic behaviour of the proton. Besides the understanding of the role of the proton, the use of free energy sampling techniques, like TI and FNE, alongside AIMD simulations, can give a quantitative description of the electron (proton) transfer rates during the charging/discharging processes of POM-based RFBs and LIBs. This is extremely important, since the rates are associated with the power density of the batteries. To the best of our knowledge, there are no computational studies regarding the electron transfer rates for POMs, and therefore, this research will help to establish the limits and advantages with respect to QM/MM and the implicit solvent model.

The great advantage of RFBs over the common LIBs is that an increase of volume, and thus of the concentration, of electrolytes improves the theoretical energy density of the battery. As observed by Cronin, [27] an increase of POM concentration in solution increases the number of electrons reducing the POMs themselves (Chapter 5). However, the mechanism behind the aggregation of POMs and to what extend this can change the number of electrons is not clear yet. Given the POMs size, the classical MD simulations remain the main tool to explore POM self-assembly processes. However, their bottleneck lies in the fact that there are high-energy barriers separating different structural configurations so that the transition between them is unlikely to happen. This problem has recently been addressed by using the so-called enhanced sampling techniques, like umbrella sampling or metadynamics. For instance, by employing the metadynamics method, Duffy *et al.* have been able to observe crystallization of calcium carbonate nanoparticles under physically realistic conditions, inaccessible to standard MD. [197] In addition, metadynamics can offer a way to understand how POMs form. An example is the recent study of Iannuzzi *et al.*, who showed that metadynamics simulations of 2-D and 3-D MOFs can offer a detailed understanding of the key elements controlling their formation. [198] Inspired by these studies, in future work we will carry out enhanced sampling simulations to understand the small details that control the aggregation (formation) of highly concentrated solution (solids) of POMs. From this research we expect to be able to provide a theoretical recipe for modelling POM aggregates in several physical contexts.

Appendix A

Bibliography

[1] Z. Yang, J. Zhang, M. C. Kintner-Meyer, X. Lu, D. Choi, J. P. Lemmon, and J. Liu, "Electrochemical energy storage for green grid," *Chem. Rev.*, vol. 111, no. 5, pp. 3577–3613, 2011.

[2] J. Winsberg, T. Hagemann, T. Janoschka, M. D. Hager, and U. S. Schubert, "Redox-flow batteries: From metals to organic redox-active materials," *Angew. Chem. Inter. Ed.*, vol. 56, no. 3, pp. 686–711, 2017.

[3] J. P. Perdew and K. Schmidt, "Jacob's ladder of density functional approximations for the exchange-correlation energy," in *AIP Conference Proceedings*, vol. 577, pp. 1–20, American Institute of Physics, 2001.

[4] J. P. Perdew, K. Burke, and M. Ernzerhof, "Generalized gradient approximation made simple," *Phys. Rev. Lett.*, vol. 77, no. 18, p. 3865, 1996.

[5] F. Jensen, *Introduction to computational chemistry*. John wiley & sons, 2017.

[6] M. P. Allen and D. J. Tildesley, *Computer simulation of liquids*. Oxford university press, 2017.

[7] L. Monticelli and E. Salonen, *Biomolecular Simulations: Methods and Protocols*, vol. 924. Springer, 2013.

[8] W. et al., "In operando x-ray absorption fine structure studies of polyoxometalate molecular cluster batteries: Polyoxometalates as electron sponges," *J. Am. Chem. Soc.*, vol. 134, no. 10, pp. 4918–4924, 2012.

[9] J. Friedl, M. V. Holland-Cunz, F. Cording, F. L. Pfanschilling, C. Wills, W. McFarlane, B. Schricker, R. Fleck, H. Wolfschmidt, and U. Stimming, "Asymmetric polyoxometalate electrolytes for advanced redox flow batteries," *Energy Environ. Sci.*, vol. 11, no. 10, pp. 3010–3018, 2018.

[10] A. Müller, E. Beckmann, H. Bögge, M. Schmidtmann, and A. Dress, "Inorganic chemistry goes protein size: A Mo_{368} nano-hedgehog initiating nanochemistry by symmetry breaking," *Angewandte Chemie International Edition*, vol. 41, no. 7, pp. 1162–1167, 2002.

[11] D.-L. Long, E. Burkholder, and L. Cronin, "Polyoxometalate clusters, nanostructures and materials: From self assembly to designer materials and devices," *Chemical Society Reviews*, vol. 36, no. 1, pp. 105–121, 2007.

[12] L. Vilà-Nadal, A. Rodríguez-Fortea, and J. M. Poblet, "Theoretical analysis of the possible intermediates in the formation of $[W_6O_{19}]^{2-}$," *European Journal of Inorganic Chemistry*, vol. 2009, no. 34, pp. 5125–5133, 2009.

[13] Y.-F. Song, *Polyoxometalate-Based Assemblies and Functional Materials*, vol. 176. Springer, 2018.

[14] X. López, J. J. Carbó, C. Bo, and J. M. Poblet, "Structure, properties and reactivity of polyoxometalates: A theoretical perspective," *Chem. Soc. Rev.*, vol. 41, no. 22, pp. 7537–7571, 2012.

[15] L. Vilà-Nadal, A. Rodríguez-Fortea, L.-K. Yan, E. F. Wilson, L. Cronin, and J. M. Poblet, "Nucleation mechanisms of molecular oxides: a study of the assembly–dissassembly of [w6o19] 2- by theory and mass spectrometry," *Angewandte Chemie International Edition*, vol. 48, no. 30, pp. 5452–5456, 2009.

[16] H.-Y. Chen, J. Friedl, C.-J. Pan, A. Haider, R. Al-Oweini, Y. L. Cheah, M.-H. Lin, U. Kortz, B.-J. Hwang, M. Srinivasan, *et al.*, "In situ x-ray absorption near edge structure studies and charge transfer kinetics of $Na_6[V_{10}O_{28}]$ electrodes," *Physical Chemistry Chemical Physics*, vol. 19, no. 4, pp. 3358–3365, 2017.

[17] R. Errington, C. Lax, D. Richards, W. Clegg, and K. Fraser, "New aspects of non-aqueous polyoxometalate chemistry," in *Polyoxometalates: From Platonic Solids to Anti-Retroviral Activity*, pp. 105–114, Springer, 1994.

[18] A. J. Bridgeman and G. Cavigliasso, "Towards an understanding of the bonding in polyoxometalates through bond order and bond energy analysis," *Faraday Discuss.*, vol. 124, pp. 239–258, 2003.

[19] H. El Moll, B. Nohra, P. Mialane, J. Marrot, N. Dupré, B. Riflade, M. Malacria, S. Thorimbert, B. Hasenknopf, E. Lacôte, *et al.*, "Lanthanide polyoxocationic complexes: experimental and theoretical stability studies and lewis acid catalysis," *Chemistry–A European Journal*, vol. 17, no. 50, pp. 14129–14138, 2011.

[20] X. López, C. Bo, and J. M. Poblet, "Electronic properties of polyoxometalates: Electron and proton affinity of mixed-addenda Keggin and Wells-Dawson anions," *Journal of the American Chemical Society*, vol. 124, no. 42, pp. 12574–12582, 2002.

[21] F.-Q. Zhang, W. Guan, L.-K. Yan, Y.-T. Zhang, M.-T. Xu, E. Hayfron-Benjamin, and Z.-M. Su, "On the origin of the relative stability of Wells–Dawson isomers: A DFT study of α-, β-, γ-, α*-, β*-, and γ*-$[(PO_4)_2W_{18}O_{54}]^{6-}$-anions," *Inorganic Chemistry*, vol. 50, no. 11, pp. 4967–4977, 2011.

[22] P. Alotto, M. Guarnieri, and F. Moro, "Redox flow batteries for the storage of renewable energy: A review," *Renewable and Sustainable Energy Reviews*, vol. 29, pp. 325–335, 2014.

[23] Q. Wang, P. Ping, X. Zhao, G. Chu, J. Sun, and C. Chen, "Thermal runaway caused fire and explosion of lithium ion battery," *Journal of power sources*, vol. 208, pp. 210–224, 2012.

[24] H. Alt, H. Binder, A. Köhling, and G. Sandstede, "Investigation into the use of quinone compounds-for battery cathodes," *Electrochimica Acta*, vol. 17, no. 5, pp. 873–887, 1972.

[25] H. D. Pratt III, W. R. Pratt, X. Fang, N. S. Hudak, and T. M. Anderson, "Mixed-metal, structural, and substitution effects of polyoxometalates on electrochemical behavior in a redox flow battery," *Electrochimica Acta*, vol. 138, pp. 210–214, 2014.

[26] Y. Liu, S. Lu, H. Wang, C. Yang, X. Su, and Y. Xiang, "An aqueous redox flow battery with a tungsten–cobalt heteropolyacid as the electrolyte for both the anode and cathode," *Advanced Energy Materials*, vol. 7, no. 8, p. 1601224, 2017.

[27] J.-J. Chen, M. D. Symes, and L. Cronin, "Highly reduced and protonated aqueous solutions of $[P_2W_{18}O_{62}]^{6-}$ for on-demand hydrogen

generation and energy storage," *Nat. Chem.*, vol. 10, no. 10, pp. 1042–1047, 2018.

[28] N. Nitta, F. Wu, J. T. Lee, and G. Yushin, "Li-ion battery materials: present and future," *Materials today*, vol. 18, no. 5, pp. 252–264, 2015.

[29] "Https://www.nobelprize.org/prizes/chemistry/2019/summary/,"

[30] N. Williard, W. He, C. Hendricks, and M. Pecht, "Lessons learned from the 787 dreamliner issue on lithium-ion battery reliability," *Energies*, vol. 6, no. 9, pp. 4682–4695, 2013.

[31] N. Boaretto, I. Garbayo, S. Valiyaveettil-SobhanRaj, A. Quintela, C. Li, M. Casas-Cabanas, and F. Aguesse, "Lithium solid-state batteries: State-of-the-art and challenges for materials, interfaces and processing," *Journal of Power Sources*, p. 229919, 2021.

[32] P. Knauth, "Inorganic solid li ion conductors: An overview," *Solid State Ionics*, vol. 180, no. 14-16, pp. 911–916, 2009.

[33] T. Famprikis, P. Canepa, J. A. Dawson, M. S. Islam, and C. Masquelier, "Fundamentals of inorganic solid-state electrolytes for batteries," *Nature materials*, vol. 18, no. 12, pp. 1278–1291, 2019.

[34] A. Yamada and J. B. Goodenough, "Keggin-type heteropolyacids as electrode materials for electrochemical supercapacitors," *Journal of the Electrochemical Society*, vol. 145, no. 3, p. 737, 1998.

[35] E. Ni, S. Uematsu, Z. Quan, and N. Sonoyama, "Improved electrochemical property of nanoparticle polyoxovanadate $K_7NiV_{13}O_{38}$ as cathode material for lithium battery," *Journal of nanoparticle research*, vol. 15, no. 6, p. 1732, 2013.

[36] S. Hartung, N. Bucher, H.-Y. Chen, R. Al-Oweini, S. Sreejith, P. Borah, Z. Yanli, U. Kortz, U. Stimming, H. E. Hoster, *et al.*, "Vanadium-based polyoxometalate as new material for sodium-ion battery anodes," *Journal of Power Sources*, vol. 288, pp. 270–277, 2015.

[37] Y. Nishimoto, D. Yokogawa, H. Yoshikawa, K. Awaga, and S. Irle, "Super-reduced polyoxometalates: Excellent molecular cluster battery components and semipermeable molecular capacitors," *J. Am. Chem. Soc.*, vol. 136, no. 25, pp. 9042–9052, 2014.

[38] J. Blumberger, I. Tavernelli, M. L. Klein, and M. Sprik, "Diabatic free energy curves and coordination fluctuations for the aqueous Ag^+/Ag^{2+} redox couple: A biased born-oppenheimer molecular dynamics investigation," *J. Chem. Phys.*, vol. 124, no. 6, p. 064507, 2006.

[39] W. Koch and M. C. Holthausen, *A chemist's guide to density functional theory*. John Wiley & Sons, 2015.

[40] M. Bühl and H. Kabrede, "Geometries of transition-metal complexes from density-functional theory," *Journal of Chemical Theory and Computation*, vol. 2, no. 5, pp. 1282–1290, 2006.

[41] Y. Minenkov, Å. Singstad, G. Occhipinti, and V. R. Jensen, "The accuracy of DFT-optimized geometries of functional transition metal compounds: A validation study of catalysts for olefin metathesis and other reactions in the homogeneous phase," *Dalton Transactions*, vol. 41, no. 18, pp. 5526–5541, 2012.

[42] H. B. Shore, J. Rose, and E. Zaremba, "Failure of the local exchange approximation in the evaluation of the H-ground state," *Physical Review B*, vol. 15, no. 6, p. 2858, 1977.

[43] D. Lee, F. Furche, and K. Burke, "Accuracy of electron affinities of atoms in approximate density functional theory," *The Journal of Physical Chemistry Letters*, vol. 1, no. 14, pp. 2124–2129, 2010.

[44] F. Jensen, "Describing anions by density functional theory: Fractional electron affinity," *Journal of chemical theory and computation*, vol. 6, no. 9, pp. 2726–2735, 2010.

[45] P. A. Aparicio, X. Lopez, and J. M. Poblet, "Ability of DFT calculations to correctly describe redox potentials and electron (de) localization in polyoxometalates," *J. Molec. Eng. Mater.*, vol. 2, no. 01, p. 1440004, 2014.

[46] A. Kremleva, P. A. Aparicio, A. Genest, and N. Rösch, "Quantum chemical modeling of tri-Mn-substituted W-based Keggin polyoxoanions," *Electrochim. Acta*, vol. 231, pp. 659–669, 2017.

[47] A. Kremleva and N. Rösch, "Modeling the effect of the electrolyte on standard reduction potentials of polyoxometalates," *J. Phys. Chem. C*, vol. 122, no. 32, pp. 18545–18553, 2018.

[48] E. Falbo and T. Penfold, "Redox potentials of polyoxometalates from an implicit solvent model and QM/MM molecular dynamics," *The Journal of Physical Chemistry C*, vol. 124, no. 28, pp. 15045–15056, 2020.

[49] X. López and J. M. Poblet, "DFT study on the five isomers of $PW_{12}O_{40}^{3-}$: Relative stabilization upon reduction," *Inorganic chemistry*, vol. 43, no. 22, pp. 6863–6865, 2004.

[50] X. Lopez, C. Nieto-Draghi, C. Bo, J. B. Avalos, and J. M. Poblet, "Polyoxometalates in solution: Molecular dynamics simulations on the α-$[PW_{12}O_{40}]^{3-}$ Keggin anion in aqueous media," *J. Phys. Chem. A*, vol. 109, no. 6, pp. 1216–1222, 2005.

[51] A. Chaumont and G. Wipff, "Ion Aggregation in Concentrated Aqueous and Methanol Solutions of Polyoxometallates Keggin Anions: The Effect of Counterions Investigated by Molecular Dynamics Simulations," *Physical Chemistry Chemical Physics*, vol. 10, no. 46, pp. 6940–6953, 2008.

[52] F. Leroy, P. Miró, J. M. Poblet, C. Bo, and J. Bonet Ávalos, "Keggin polyoxoanions in aqueous solution: Ion pairing and its effect on dynamic properties by molecular dynamics simulations," *J. Phys. Chem. B*, vol. 112, no. 29, pp. 8591–8599, 2008.

[53] A. Sole-Daura, A. Notario-Estevez, J. J. Carbo, J. M. Poblet, C. de Graaf, K. Y. Monakhov, and X. Lopez, "How does the redox state of polyoxovanadates influence the collective behavior in solution? a case study with $[I@\ V_{18}O_{42}]^{q-}$ (q = 3, 5, 7, 11, and 13)," *Inorganic chemistry*, vol. 58, no. 6, pp. 3881–3894, 2019.

[54] R. Brodbeck, T. Tönsing, D. Andrae, and D. Volkmer, "Molecular dynamics simulations of dendrimer-encapsulated α-Keggin ions in trichloromethane solution," *J. Phys. Chem. B*, vol. 112, no. 16, pp. 5153–5162, 2008.

[55] B. Courcot and A. J. Bridgeman, "Optimization of a molecular mechanics force field for polyoxometalates based on a genetic algorithm," *J. Comput. Chem.*, vol. 32, no. 2, pp. 240–247, 2011.

[56] C. Menke, E. Diemann, and A. Müller, "Polyoxovanadate clusters and cages: Force-field parameterization," *J. Mol. Struct.*, vol. 436, pp. 35–47, 1997.

[57] C. Rovira, B. Schulze, M. Eichinger, J. D. Evanseck, and M. Parrinello, "Influence of the heme pocket conformation on the structure and vibrations of the fe-co bond in myoglobin: a qm/mm density functional study," *Biophysical journal*, vol. 81, no. 1, pp. 435–445, 2001.

[58] C. de Graaf, X. López, J. L. Ramos, and J. M. Poblet, "Ab initio study of the antiferromagnetic coupling in the wheel-shaped $[Cu_{20}Cl(OH)_{24}(H_2O)_{12}(P_8W_{48}O_{184})]^{25-}$ -anion," *Physical Chemistry Chemical Physics*, vol. 12, no. 11, pp. 2716–2721, 2010.

[59] A. Szabo and N. S. Ostlund, *Modern quantum chemistry: introduction to advanced electronic structure theory*. Courier Corporation, 2012.

[60] W. Kohn and L. J. Sham, "Self-consistent equations including exchange and correlation effects," *Physical review*, vol. 140, no. 4A, p. A1133, 1965.

[61] P. Hohenberg and W. Kohn, "Inhomogeneous electron gas," *Physical review*, vol. 136, no. 3B, p. B864, 1964.

[62] J. P. Perdew, R. G. Parr, M. Levy, and J. L. Balduz Jr, "Density-functional theory for fractional particle number: derivative discontinuities of the energy," *Phys. Rev. Lett.*, vol. 49, no. 23, p. 1691, 1982.

[63] R. G. Parr, "Density functional theory of atoms and molecules," in *Horizons of quantum chemistry*, pp. 5–15, Springer, 1980.

[64] D. M. Ceperley and B. J. Alder, "Ground state of the electron gas by a stochastic method," *Physical Review Letters*, vol. 45, no. 7, p. 566, 1980.

[65] J. M. Poblet, X. López, and C. Bo, "Ab initio and dft modelling of complex materials: towards the understanding of electronic and magnetic properties of polyoxometalates," *Chem. Soc. Rev.*, vol. 32, no. 5, pp. 297–308, 2003.

[66] S. Wen, W. Guan, J. Wang, Z. Lang, L. Yan, and Z. Su, "Theoretical investigation of structural and electronic propertyies of $[pw_{12}o_{40}]^{3-}$ on graphene layer," *Dalton Transactions*, vol. 41, no. 15, pp. 4602–4607, 2012.

[67] A. D. Becke, "Density-functional exchange-energy approximation with correct asymptotic behavior," *Physical review A*, vol. 38, no. 6, p. 3098, 1988.

[68] A. Becke, "Density-functional thermochemistry. iii. the role of exact exchange (1993) j," *Chem. Phys*, vol. 98, p. 5648.

[69] C. Lee, W. Yang, and R. G. Parr, "Development of the colle-salvetti correlation-energy formula into a functional of the electron density," *Physical review B*, vol. 37, no. 2, p. 785, 1988.

[70] C. Adamo and V. Barone, "Toward reliable density functional methods without adjustable parameters: The PBE0 model," *J. Chem. Phys.*, vol. 110, no. 13, pp. 6158–6170, 1999.

[71] J. P. Perdew and A. Zunger, "Self-interaction correction to density-functional approximations for many-electron systems," *Physical Review B*, vol. 23, no. 10, p. 5048, 1981.

[72] A. J. Cohen, P. Mori-Sánchez, and W. Yang, "Challenges for density functional theory," *Chemical reviews*, vol. 112, no. 1, pp. 289–320, 2012.

[73] F. Weigend and R. Ahlrichs, "Balanced basis sets of split valence, triple zeta valence and quadruple zeta valence quality for H to Rn: Design and assessment of accuracy," *Phys. Chem. Chem. Phys.*, vol. 7, no. 18, pp. 3297–3305, 2005.

[74] A. Sartorel, M. Carraro, A. Bagno, G. Scorrano, and M. Bonchio, "Asymmetric tetraprotonation of γ-$[(\mathrm{sio}_4)\mathrm{w}_{10}\mathrm{o}_{32}]^{8-}$ triggers a catalytic epoxidation reaction: Perspectives in the assignment of the active catalyst," *Angewandte Chemie International Edition*, vol. 46, no. 18, pp. 3255–3258, 2007.

[75] M. Dolg, H. Stoll, and H. Preuss, "Energy-adjusted ab initio pseudopotentials for the rare earth elements," *J. of Chem. Phys.*, vol. 90, no. 3, pp. 1730–1734, 1989.

[76] J. C. Phillips, D. J. Hardy, J. D. Maia, J. E. Stone, J. V. Ribeiro, R. C. Bernardi, R. Buch, G. Fiorin, J. Hénin, W. Jiang, *et al.*, "Scalable molecular dynamics on cpu and gpu architectures with namd," *J. Chem. Phys.*, vol. 153, no. 4, p. 044130, 2020.

[77] X. Lopez, C. Nieto-Draghi, C. Bo, J. B. Avalos, and J. M. Poblet, "Polyoxometalates in solution: Molecular dynamics simulations on the α-$\mathrm{PW}_{12}\mathrm{O}_{40}^{3-}$-Keggin anion in aqueous media," *J. Phys. Chem. A*, vol. 109, no. 6, pp. 1216–1222, 2005.

[78] H. J. Berendsen, J. v. Postma, W. F. van Gunsteren, A. DiNola, and J. R. Haak, “Molecular dynamics with coupling to an external bath,” *J. Chem. Phys.*, vol. 81, no. 8, pp. 3684–3690, 1984.

[79] S. Nosé, “A unified formulation of the constant temperature molecular dynamics methods,” *J. Chem. Phys.*, vol. 81, no. 1, pp. 511–519, 1984.

[80] L. Verlet, “Computer "experiments" on classical fluids. I. thermodynamical properties of lennard-jones molecules,” *Physical review*, vol. 159, no. 1, p. 98, 1967.

[81] K. Vanommeslaeghe, E. Hatcher, C. Acharya, S. Kundu, S. Zhong, J. Shim, E. Darian, O. Guvench, P. Lopes, I. Vorobyov, *et al.*, “CHARMM general force field: A force field for drug-like molecules compatible with the CHARMM all-atom additive biological force fields,” *Journal of computational chemistry*, vol. 31, no. 4, pp. 671–690, 2010.

[82] D. A. Case, V. Babin, J. Berryman, R. Betz, Q. Cai, D. Cerutti, T. Cheatham Iii, T. Darden, R. Duke, and H. Gohlke, “Amber 14,” 2014.

[83] W. L. Jorgensen and J. Tirado-Rives, “The opls [optimized potentials for liquid simulations] potential functions for proteins, energy minimizations for crystals of cyclic peptides and crambin,” *Journal of the American Chemical Society*, vol. 110, no. 6, pp. 1657–1666, 1988.

[84] J. W. Ponder, C. Wu, P. Ren, V. S. Pande, J. D. Chodera, M. J. Schnieders, I. Haque, D. L. Mobley, D. S. Lambrecht, R. A. DiStasio Jr, *et al.*, “Current status of the AMOEBa polarizable force field,” *The journal of physical chemistry B*, vol. 114, no. 8, pp. 2549–2564, 2010.

[85] A. E. Allen, M. C. Payne, and D. J. Cole, “Harmonic force constants for molecular mechanics force fields via hessian matrix projection,” *J. Chem. Theory Comput.*, vol. 14, no. 1, pp. 274–281, 2017.

[86] A. K. Rappé, C. J. Casewit, K. Colwell, W. A. Goddard III, and W. Skiff, “UFF, a full periodic table force field for molecular mechanics and molecular dynamics simulations,” *J. Am. Chem. Soc.*, vol. 114, no. 25, pp. 10024–10035, 1992.

[87] F. Neese, “The ORCA program system,” *Wiley Interdiscip. Rev. Comput. Mol. Sci.*, vol. 2, no. 1, pp. 73–78, 2012.

[88] D. Frenkel and B. Smit, *Understanding Molecular Simulation: From Algorithms to Applications*, vol. 1. Elsevier, 2001.

[89] T. Darden, D. York, and L. Pedersen, "Particle mesh ewald: An n log(n) method for ewald sums in large systems," *J. Chem. Phys.*, vol. 98, no. 12, pp. 10089–10092, 1993.

[90] J. Åqvist and A. Warshel, "Simulation of enzyme reactions using valence bond force fields and other hybrid quantum/classical approaches," *Chem. Rev.*, vol. 93, no. 7, pp. 2523–2544, 1993.

[91] M. J. Field, P. A. Bash, and M. Karplus, "A combined quantum mechanical and molecular mechanical potential for molecular dynamics simulations," *J. Comput. Chem.*, vol. 11, no. 6, pp. 700–733, 1990.

[92] X. Zeng, H. Hu, X. Hu, A. J. Cohen, and W. Yang, "Ab initio quantum mechanical/molecular mechanical simulation of electron transfer process: Fractional electron approach," *J. Chem. Phys.*, vol. 128, no. 12, p. 124510, 2008.

[93] K. Stroobants, E. Moelants, H. G. T. Ly, P. Proost, K. Bartik, and T. N. Parac-Vogt, "Polyoxometalates as a novel class of artificial proteases: Selective hydrolysis of lysozyme under physiological ph and temperature promoted by a cerium (iv) keggin-type polyoxometalate," *Chemistry–A European Journal*, vol. 19, no. 8, pp. 2848–2858, 2013.

[94] V. M. Jayasinghe-Arachchige, Q. Hu, G. Sharma, T. J. Paul, M. Lundberg, D. Quinonero, T. N. Parac-Vogt, and R. Prabhakar, "Hydrolysis of chemically distinct sites of human serum albumin by polyoxometalate: a hybrid qm/mm (oniom) study," *Journal of computational chemistry*, vol. 40, no. 1, pp. 51–61, 2019.

[95] P. Amara and M. J. Field, "Evaluation of an ab initio quantum mechanical/molecular mechanical hybrid-potential link-atom method," *Theoretical Chemistry Accounts*, vol. 109, no. 1, pp. 43–52, 2003.

[96] C. M. Baker, "Polarizable force fields for molecular dynamics simulations of biomolecules," *Wiley Interdisciplinary Reviews: Computational Molecular Science*, vol. 5, no. 2, pp. 241–254, 2015.

[97] V. Théry, D. Rinaldi, J.-L. Rivail, B. Maigret, and G. G. Ferenczy, "Quantum mechanical computations on very large molecular systems: The

local self-consistent field method," *Journal of computational chemistry*, vol. 15, no. 3, pp. 269–282, 1994.

[98] N. Ferré, X. Assfeld, and J.-L. Rivail, "Specific force field parameters determination for the hybrid ab initio QM/MM LSCF method," *Journal of computational chemistry*, vol. 23, no. 6, pp. 610–624, 2002.

[99] C. P. Kelly, C. J. Cramer, and D. G. Truhlar, "Aqueous solvation free energies of ions and ion-water clusters based on an accurate value for the absolute aqueous solvation free energy of the proton," *The Journal of Physical Chemistry B*, vol. 110, no. 32, pp. 16066–16081, 2006.

[100] W. R. Fawcett, "The ionic work function and its role in estimating absolute electrode potentials," *Langmuir*, vol. 24, no. 17, pp. 9868–9875, 2008.

[101] S. Trasatti, "The absolute electrode potential: An explanatory note (recommendations 1986)," *Pure and Applied Chemistry*, vol. 58, no. 7, pp. 955–966, 1986.

[102] R. Ramette, "Outmoded terminology: The normal hydrogen electrode," *Journal of Chemical Education*, vol. 64, no. 10, p. 885, 1987.

[103] A. V. Marenich, J. Ho, M. L. Coote, C. J. Cramer, and D. G. Truhlar, "Computational electrochemistry: Prediction of liquid-phase reduction potentials," *Phys. Chem. Chem. Phys.*, vol. 16, no. 29, pp. 15068–15106, 2014.

[104] R. Peverati and D. G. Truhlar, "Improving the accuracy of hybrid meta-gga density functionals by range separation," *J. Phys. Chem. Lett.*, vol. 2, no. 21, pp. 2810–2817, 2011.

[105] T. Zhu, J. Li, G. D. Hawkins, C. J. Cramer, and D. G. Truhlar, "Density functional solvation model based on CM2 atomic charges," *The Journal of chemical physics*, vol. 109, no. 20, pp. 9117–9133, 1998.

[106] M. Born, "Volumen und hydratationswärme der ionen," *Zeitschrift für Physik*, vol. 1, no. 1, pp. 45–48, 1920.

[107] D. Armstrong, Q. Sun, and R. Schuler, "Reduction potentials and kinetics of electron transfer reactions of phenylthiyl radicals: Comparisons with phenoxyl radicals," *The Journal of Physical Chemistry*, vol. 100, no. 23, pp. 9892–9899, 1996.

[108] V. Tipmanee, H. Oberhofer, M. Park, K. S. Kim, and J. Blumberger, "Prediction of reorganization free energies for biological electron transfer: A comparative study of ru-modified cytochromes and a 4-helix bundle protein," *J. Am. Chem. Soc.*, vol. 132, no. 47, pp. 17032–17040, 2010.

[109] R. W. Zwanzig, "High-temperature equation of state by a perturbation method. i. nonpolar gases," *J. Chem. Phys.*, vol. 22, no. 8, pp. 1420–1426, 1954.

[110] W. L. Jorgensen and C. Ravimohan, "Monte carlo simulation of differences in free energies of hydration," *The Journal of chemical physics*, vol. 83, no. 6, pp. 3050–3054, 1985.

[111] W. Libby, "Theory of electron exchange reactions in aqueous solution," *The Journal of Physical Chemistry*, vol. 56, no. 7, pp. 863–868, 1952.

[112] L.-P. Wang and T. Van Voorhis, "A polarizable QM/MM explicit solvent model for computational electrochemistry in water," *J. Chem. Theory Comput.*, vol. 8, no. 2, pp. 610–617, 2012.

[113] R. A. Marcus, "On the theory of oxidation-reduction reactions involving electron transfer. I," *The Journal of chemical physics*, vol. 24, no. 5, pp. 966–978, 1956.

[114] G. Bunker, *Introduction to XAFS: A Practical Guide to X-Ray Absorption Fine Structure Spectroscopy*. Cambridge University Press, 2010.

[115] J. A. Van Bokhoven and C. Lamberti, *X-Ray Absorption and X-Ray Emission Spectroscopy: Theory and Applications*, vol. 1. John Wiley & Sons, 2016.

[116] S. A. Guda, A. A. Guda, M. A. Soldatov, K. A. Lomachenko, A. L. Bugaev, C. Lamberti, W. Gawelda, C. Bressler, G. Smolentsev, A. V. Soldatov, *et al.*, "Optimized finite difference method for the full-potential xanes simulations: Application to molecular adsorption geometries in mofs and metal–ligand intersystem crossing transients," *Journal of chemical theory and computation*, vol. 11, no. 9, pp. 4512–4521, 2015.

[117] Y. Joly, "X-ray absorption near-edge structure calculations beyond the muffin-tin approximation," *Physical Review B*, vol. 63, no. 12, p. 125120, 2001.

[118] J. D. Bourke, C. T. Chantler, and Y. Joly, “FDMX: Extended x-ray absorption fine structure calculations using the finite difference method,” *Journal of Synchrotron Radiation*, vol. 23, no. 2, pp. 551–559, 2016.

[119] A. Tougerti, E. Berrier, A.-S. Mamede, C. La Fontaine, V. Briois, Y. Joly, E. Payen, J.-F. Paul, and S. Cristol, “Synergy between XANES spectroscopy and DFT to elucidate the amorphous structure of heterogeneous catalysts: TiO_2-supported molybdenum oxide catalysts,” *Angewandte Chemie International Edition*, vol. 52, no. 25, pp. 6440–6444, 2013.

[120] D. Cabaret, A. Bordage, A. Juhin, M. Arfaoui, and E. Gaudry, “First-principles calculations of x-ray absorption spectra at the k-edge of 3d transition metals: an electronic structure analysis of the pre-edge,” *Physical Chemistry Chemical Physics*, vol. 12, no. 21, pp. 5619–5633, 2010.

[121] O. Bunău and Y. Joly, “Full potential x-ray absorption calculations using time dependent density functional theory,” *Journal of Physics: Condensed Matter*, vol. 24, no. 21, p. 215502, 2012.

[122] B. Dunn, H. Kamath, and J.-M. Tarascon, “Electrical energy storage for the grid: A battery of choices,” *Sci.*, vol. 334, no. 6058, pp. 928–935, 2011.

[123] W. Wang, Q. Luo, B. Li, X. Wei, L. Li, and Z. Yang, “Recent progress in redox flow battery research and development,” *Adv. Funct. Mater.*, vol. 23, no. 8, pp. 970–986, 2013.

[124] M. Skyllas-Kazacos, M. Rychcik, R. G. Robins, A. Fane, and M. Green, “New all-vanadium redox flow cell,” *J. Electrochem. Soc.*, vol. 133, p. 1057, 1986.

[125] D. A. Johnson and M. A. Reid, “Chemical and electrochemical behavior of the Cr(III)/Cr(II) half-cell in the iron-chromium redox energy storage system,” *J. Electrochem. Soc.*, vol. 132, no. 5, p. 1058, 1985.

[126] K. Gong, F. Xu, J. B. Grunewald, X. Ma, Y. Zhao, S. Gu, and Y. Yan, “All-soluble all-iron aqueous redox-flow battery,” *ACS Energy Lett.*, vol. 1, no. 1, pp. 89–93, 2016.

[127] J. Suttil, J. Kucharyson, I. Escalante-Garcia, P. Cabrera, B. James, R. Savinell, M. Sanford, and L. Thompson, “Metal acetylacetonate complexes for high energy density non-aqueous redox flow batteries,” *J. Mater. Chem. A*, vol. 3, no. 15, pp. 7929–7938, 2015.

[128] K. Lin, Q. Chen, M. R. Gerhardt, L. Tong, S. B. Kim, L. Eisenach, A. W. Valle, D. Hardee, R. G. Gordon, and M. J. Aziz, "Alkaline quinone flow battery," *Sci.*, vol. 349, no. 6255, pp. 1529–1532, 2015.

[129] J. Friedl, M. A. Lebedeva, K. Porfyrakis, U. Stimming, and T. W. Chamberlain, "All-fullerene-based cells for nonaqueous redox flow batteries," *J. Am. Chem. Soc.*, vol. 140, no. 1, pp. 401–405, 2018.

[130] P. Leung, A. Shah, L. Sanz, C. Flox, J. Morante, Q. Xu, M. Mohamed, C. P. de León, and F. Walsh, "Recent developments in organic redox flow batteries: A critical review," *J. Power Sources*, vol. 360, pp. 243–283, 2017.

[131] E. Papaconstantinou and M. T. Pope, "Heteropoly blues. III. preparation and stabilities of reduced 18-molybdodiphosphates," *Inorg. Chem.*, vol. 6, no. 6, pp. 1152–1155, 1967.

[132] M. Sadakane and E. Steckhan, "Electrochemical properties of polyoxometalates as electrocatalysts," *Chem. Rev.*, vol. 98, no. 1, pp. 219–238, 1998.

[133] M. T. Pope and G. M. Varga Jr, "Heteropoly blues. I. reduction stoichiometries and reduction potentials of some 12-tungstates," *Inorg. Chem.*, vol. 5, no. 7, pp. 1249–1254, 1966.

[134] F.-Q. Zhang, H.-S. Wu, X.-F. Qin, Y.-W. Li, and H. Jiao, "On the α/β-[alw12o40] 5- stability: Revisited," *Journal of Molecular Structure: THEOCHEM*, vol. 755, no. 1-3, pp. 113–117, 2005.

[135] P. A. Aparicio, J. M. Poblet, and X. López, "Tungsten redox waves in $[XMW_{11}O_{40}]^{n-}$ (X = P, Si, Al and M= W, Mo, V, Nb, Ti) Keggin compounds–effect of localised/delocalised charges," *Eur. J. Inorg. Chem.*, vol. 2013, no. 10-11, pp. 1910–1916, 2013.

[136] L. Parent, P. A. Aparicio, P. de Oliveira, A.-L. Teillout, J. M. Poblet, X. López, and I. M. Mbomekallé, "Effect of electron (de) localization and pairing in the electrochemistry of polyoxometalates: Study of Wells-Dawson molybdotungstophosphate derivatives," *Inorg. Chem.*, vol. 53, no. 12, pp. 5941–5949, 2014.

[137] A. Klamt and G. Schüürmann, "COSMO: A new approach to dielectric screening in solvents with explicit expressions for the screening energy and its gradient," *J. Chem. Soc., Perkin Trans. 2*, no. 5, pp. 799–805, 1993.

[138] V. Barone and M. Cossi, "Quantum calculation of molecular energies and energy gradients in solution by a conductor solvent model," *J. Phys. Chem. A*, vol. 102, no. 11, pp. 1995–2001, 1998.

[139] C. J. Cramer and D. G. Truhlar, "Implicit solvation models: Equilibria, structure, spectra, and dynamics," *Chem. Rev*, vol. 99, no. 8, pp. 2161–2200, 1999.

[140] L. E. Roy, E. Jakubikova, M. G. Guthrie, and E. R. Batista, "Calculation of one-electron redox potentials revisited. is it possible to calculate accurate potentials with density functional methods?," *J. Phys. Chem. A*, vol. 113, no. 24, pp. 6745–6750, 2009.

[141] C. P. Kelly, C. J. Cramer, and D. G. Truhlar, "Single-ion solvation free energies and the normal hydrogen electrode potential in methanol, acetonitrile, and dimethyl sulfoxide," *J. Phys. Chem. B*, vol. 111, no. 2, pp. 408–422, 2007.

[142] V. N. Staroverov, G. E. Scuseria, J. Tao, and J. P. Perdew, "Comparative assessment of a new nonempirical density functional: Molecules and hydrogen-bonded complexes," *J. Chem. Phys.*, vol. 119, no. 23, pp. 12129–12137, 2003.

[143] P. Mori-Sánchez, A. J. Cohen, and W. Yang, "Many-electron self-interaction error in approximate density functionals," 2006.

[144] D. W. Smith, "Ionic hydration enthalpies," *J. Chem. Educ.*, vol. 54, no. 9, p. 540, 1977.

[145] D. J. Price and C. L. Brooks III, "A modified TIP3P water potential for simulation with Ewald summation," *J. Chem. Phys.*, vol. 121, no. 20, pp. 10096–10103, 2004.

[146] A. W. Götz, M. A. Clark, and R. C. Walker, "An extensible interface for QM/MM molecular dynamics simulations with AMBER," *J. Comput. Chem.*, vol. 35, no. 2, pp. 95–108, 2014.

[147] J.-P. Ryckaert, G. Ciccotti, and H. J. Berendsen, "Numerical integration of the cartesian equations of motion of a system with constraints: Molecular dynamics of n-alkanes," *J. Comput. Phys*, vol. 23, no. 3, pp. 327–341, 1977.

[148] A. Selling, I. Andersson, L. Pettersson, C. M. Schramm, S. L. Downey, and J. H. Grate, "Multicomponent polyanions. 47. the aqueous vanadophosphate system," *Inorg. Chem.*, vol. 33, no. 14, pp. 3141–3150, 1994.

[149] B. Keita and L. Nadjo, "New aspects of the electrochemistry of heteropolyacids: Part IV. acidity dependent cyclic voltammetric behaviour of phosphotungstic and silicotungstic heteropolyanions in water and n, n-dimethylformamide," *J. Electroanal. Chem. Interf. Electrochem.*, vol. 227, no. 1-2, pp. 77–98, 1987.

[150] C. M. Isborn, B. D. Mar, B. F. Curchod, I. Tavernelli, and T. J. Martinez, "The charge transfer problem in density functional theory calculations of aqueously solvated molecules," *J. Phys. Chem. B*, vol. 117.

[151] M. Seth, T. Ziegler, M. Steinmetz, and S. Grimme, "Modeling transition metal reactions with range-separated functionals," *Journal of chemical theory and computation*, vol. 9, no. 5, pp. 2286–2299, 2013.

[152] N. Ree, C. L. Andersen, M. D. Kilde, O. Hammerich, M. B. Nielsen, and K. V. Mikkelsen, "The quest for determining one-electron redox potentials of azulene-1-carbonitriles by calculation," *Physical Chemistry Chemical Physics*, vol. 20, no. 11, pp. 7438–7446, 2018.

[153] A. Boruah, M. P. Borpuzari, Y. Kawashima, K. Hirao, and R. Kar, "Assessment of range-separated functionals in the presence of implicit solvent: Computation of oxidation energy, reduction energy, and orbital energy," *The Journal of chemical physics*, vol. 146, no. 16, p. 164102, 2017.

[154] P. Le Magueres, L. Ouahab, S. Golhen, D. Grandjean, O. Pena, J.-C. Jegaden, C. Gomez-Garcia, and P. Delhaes, "Diamagnetic and paramagnetic keggin polyoxometalate salts containing 1-d and 3-d decamethylferrocenium networks: Preparation, crystal structures and magnetic properties of $[Fe(C_5Me_5)_2]_4(POM)(Solv)_N$ ($POM=[SiMo_{12}O_{40}]^{4-}$,$[SiW_{12}O_{40}]^{4-}$,$[PMo_{12}O_{40}]^{4-}$,$[HFeW_{12}O_{40}]^{4-}$; solv= H_2O, C_3H_7ON, CH_3CN)," *Inorg. Chem.*, vol. 33, no. 23, pp. 5180–5187, 1994.

[155] M. Kozik, N. Casan-Pastor, C. F. Hammer, and L. C. Baker, "Ring currents in wholly inorganic heteropoly blue complexes. evaluation by a modification of evans' susceptibility method," *J. Am. Chem. Soc.*, vol. 110, no. 23, pp. 7697–7701, 1988.

[156] E. Bominaar, C. Achim, S. Borshch, J.-J. Girerd, and E. Münck, "Analysis of exchange interaction and electron delocalization as intramolecular determinants of intermolecular electron-transfer kinetics," *Inorg. Chem.*, vol. 36, no. 17, pp. 3689–3701, 1997.

[157] V.-T. Pham, T. J. Penfold, R. M. van der Veen, F. Lima, A. El Nahhas, S. L. Johnson, P. Beaud, R. Abela, C. Bressler, and I. Tavernelli, "Probing the transition from hydrophilic to hydrophobic solvation with atomic scale resolution," *J. Am. Chem. Soc.*, vol. 133, no. 32, pp. 12740–12748, 2011.

[158] J. Blumberger, "Free energies for biological electron transfer from Qm/Mm calculation: Method, application and critical assessment," *Phys. Chem. Chem. Phys.*, vol. 10, no. 37, pp. 5651–5667, 2008.

[159] J. Cheng, M. Sulpizi, and M. Sprik, "Redox potentials and pKa for benzoquinone from density functional theory based molecular dynamics," *J. of Chem. Phys.*, vol. 131, no. 15, p. 154504, 2009.

[160] D. Linden and T. Reddy, "Handbook of batteries third ed," 2002.

[161] N. Sonoyama, Y. Suganuma, T. Kume, and Z. Quan, "Lithium intercalation reaction into the keggin type polyoxomolybdates," *Journal of Power Sources*, vol. 196, no. 16, pp. 6822–6827, 2011.

[162] E. Ni, S. Uematsu, and N. Sonoyama, "Lithium intercalation into the polyoxovanadate $K_7MnV_{13}O_{38}$ as cathode material of lithium ion batteries," *Solid State Ionics*, vol. 268, pp. 222–225, 2014.

[163] C.-C. Lin, W.-H. Lin, S.-C. Huang, C.-W. Hu, T.-Y. Chen, C.-T. Hsu, H. Yang, A. Haider, Z. Lin, U. Kortz, *et al.*, "Mechanism of sodium ion storage in $Na_7[H_2PV_{14}O_{42}]$ anode for sodium-ion batteries," *Advanced Materials Interfaces*, vol. 5, no. 15, p. 1800491, 2018.

[164] B. M. Azumi, T. Ishihara, H. Nishiguchi, and Y. Takita, "Electrochemical intercalation of li into heteropoly 12-molybdophosphoric acid ion-exchanged with Cs," *Electrochemistry*, vol. 70, no. 11, pp. 869–874, 2002.

[165] C. D. Rankine, M. M. Madkhali, and T. J. Penfold, "A deep neural network for the rapid prediction of x-ray absorption spectra," *The Journal of Physical Chemistry A*, 2020.

[166] D. Andrae, U. Haeussermann, M. Dolg, H. Stoll, and H. Preuss, "Energy-adjusted ab initio pseudopotentials for the second and third row transition elements," *Theor. Chim. Acta*, vol. 77, no. 2, pp. 123–141, 1990.

[167] J. J. Rehr, J. J. Kas, F. D. Vila, M. P. Prange, and K. Jorissen, "Parameter-free calculations of x-ray spectra with FEFF9," *Physical Chemistry Chemical Physics*, vol. 12, no. 21, pp. 5503–5513, 2010.

[168] T. Penfold, I. Tavernelli, C. Milne, M. Reinhard, A. E. Nahhas, R. Abela, U. Rothlisberger, and M. Chergui, "A wavelet analysis for the x-ray absorption spectra of molecules," *The Journal of chemical physics*, vol. 138, no. 1, p. 014104, 2013.

[169] T. Rossi, T. Penfold, M. Rittmann-Frank, M. Reinhard, J. Rittmann, C. Borca, D. Grolimund, C. Milne, and M. Chergui, "Characterizing the structure and defect concentration of ZnO nanoparticles in a colloidal solution," *The Journal of Physical Chemistry C*, vol. 118, no. 33, pp. 19422–19430, 2014.

[170] M. M. Madkhali, C. D. Rankine, and T. J. Penfold, "The role of structural representation in the performance of a deep neural network for x-ray spectroscopy," *Molecules*, vol. 25, no. 11, p. 2715, 2020.

[171] M. Gastegger, L. Schwiedrzik, M. Bittermann, F. Berzsenyi, and P. Marquetand, "WACSF—weighted atom-centered symmetry functions as descriptors in machine learning potentials," *The Journal of chemical physics*, vol. 148, no. 24, p. 241709, 2018.

[172] K. Hansen, G. Montavon, F. Biegler, S. Fazli, M. Rupp, M. Scheffler, O. A. Von Lilienfeld, A. Tkatchenko, and K.-R. Muller, "Assessment and validation of machine learning methods for predicting molecular atomization energies," *Journal of Chemical Theory and Computation*, vol. 9, no. 8, pp. 3404–3419, 2013.

[173] S. Liu, C. Wang, H. Zhai, and D. Li, "Hydrolysis of n, n-dimethylformamide catalyzed by the keggin $H_3[PMo_{12}O_{40}]$: Isolation and crystal structure analysis of $[(CH_3)_2NH_2]_3$ $[PMo_{12}O_{40}]$," *Journal of molecular structure*, vol. 654, no. 1-3, pp. 215–221, 2003.

[174] J. Wienold, O. Timpe, and T. Ressler, “In situ investigations of structure–activity relationships in heteropolyoxomolybdates as partial oxidation catalysts,” *Chemistry–A European Journal*, vol. 9, no. 24, pp. 6007–6017, 2003.

[175] T. Heaton-Burgess and W. Yang, “Structural manifestation of the delocalization error of density functional approximations: C_{4N+2} rings and C_{20} bowl, cage, and ring isomers,” *The Journal of chemical physics*, vol. 132, no. 23, p. 234113, 2010.

[176] N. J. Blackburn, M. E. Barr, W. H. Woodruff, J. van der Ooost, and S. de Vries, “Metal-metal bonding in biology: Exafs evidence for a 2.5. Ang. Copper-copper bond in the CuA center of cytochrome oxidase,” *Biochemistry*, vol. 33, no. 34, pp. 10401–10407, 1994.

[177] N. R. Shiju, A. J. Rondinone, D. R. Mullins, V. Schwartz, S. H. Overbury, and V. V. Guliants, “XANES study of hydrothermal Mo-V-based mixed oxide m1-phase catalysts for the (amm) oxidation of propane,” *Chem. Mater.*, vol. 20, no. 21, pp. 6611–6616, 2008.

[178] M. Segado, M. Nyman, and C. Bo, “Aggregation patterns in low-and high-charge anions define opposite solubility trends,” *The Journal of Physical Chemistry B*, vol. 123, no. 49, pp. 10505–10513, 2019.

[179] J. Rossmeisl, Z.-W. Qu, H. Zhu, G.-J. Kroes, and J. K. Nørskov, “Electrolysis of water on oxide surfaces,” *Journal of Electroanalytical Chemistry*, vol. 607, no. 1-2, pp. 83–89, 2007.

[180] E. Skúlason, G. S. Karlberg, J. Rossmeisl, T. Bligaard, J. Greeley, H. Jónsson, and J. K. Nørskov, “Density functional theory calculations for the hydrogen evolution reaction in an electrochemical double layer on the Pt (111) electrode,” *Physical Chemistry Chemical Physics*, vol. 9, no. 25, pp. 3241–3250, 2007.

[181] S. Piccinin and S. Fabris, “a First Principles Study of Water Oxidation Catalyzed by a Tetraruthenium-Oxo Core Embedded in Polyoxometalate Ligands,” *Physical Chemistry Chemical Physics*, vol. 13, no. 17, pp. 7666–7674, 2011.

[182] M. Blasco-Ahicart, J. Soriano-López, J. J. Carbó, J. M. Poblet, and J.-R. Galan-Mascaros, “Polyoxometalate electrocatalysts based on earth-abundant metals for efficient water oxidation in acidic media,” *Nature Chemistry*, vol. 10, no. 1, pp. 24–30, 2018.

[183] William Humphrey and Andrew Dalke and Klaus Schulten, "VMD – Visual Molecular Dynamics," *Journal of Molecular Graphics*, vol. 14, pp. 33–38, 1996.

[184] P. Yin, D. Li, and T. Liu, "Solution Behaviors and Self-Assembly of Polyoxometalates As Models of Macroions and Amphiphilic Polyoxometalate-Organic Hybrids As Novel Surfactants," *Chemical Society Reviews*, vol. 41, no. 22, pp. 7368–7383, 2012.

[185] Z. Liu, T. Liu, and M. Tsige, "Elucidating the Origin of the Attractive Force Among Hydrophilic Macroions," *Scientific reports*, vol. 6, p. 26595, 2016.

[186] E. Nikoloudakis, K. Karikis, M. Laurans, C. Kokotidou, A. Solé-Daura, J. J. Carbó, A. Charisiadis, G. Charalambidis, G. Izzet, A. Mitraki, *et al.*, "Self-Assembly Study of Nanometric Spheres from Polyoxometalate-Phenylalanine Hybrids, an Experimental and Theoretical Approach," *Dalton transactions*, vol. 47, no. 18, pp. 6304–6313, 2018.

[187] N. I. Hammer, E. G. Diken, J. R. Roscioli, M. A. Johnson, E. M. Myshakin, K. D. Jordan, A. B. McCoy, X. Huang, J. M. Bowman, and S. Carter, "the Vibrational Predissociation Spectra of the $H_2O_5^+ \cdot RG_n$ (RG = Ar, Ne) Clusters: Correlation of the Solvent Perturbations in the Free OH and Shared Proton Transitions of the Zundel Ion," *The Journal of chemical physics*, vol. 122, no. 24, p. 244301, 2005.

[188] H.-P. Cheng, R. Barnett, and U. Landman, "All-quantum simulations: H_3O^+ and $H_5O_2^+$," *Chemical physics letters*, vol. 237, no. 1-2, pp. 161–170, 1995.

[189] N. Lespes and J.-S. Filhol, "Using implicit solvent in ab initio electrochemical modeling: investigating li+/li electrochemistry at a li/solvent interface," *Journal of chemical theory and computation*, vol. 11, no. 7, pp. 3375–3382, 2015.

[190] J. Autschbach and M. Srebro, "Delocalization error and "functional tuning" in kohn–sham calculations of molecular properties," *Accounts of chemical research*, vol. 47, no. 8, pp. 2592–2602, 2014.

[191] "Identification of Active Edge Sites for Electrochemical H_2 Evolution from MoS_2 Nanocatalysts, author = Jaramillo, Thomas F and Jørgensen, Kristina P. and Bonde, Jacob and Nielsen, Jane H. and Horch,

Sebastian and Chorkendorff, Ib, journal = science, year = 2007, number = 5834, pages = 100–102, volume = 317, publisher = American Association for the Advancement of Science,"

[192] S. Luo, B. Averkiev, K. R. Yang, X. Xu, and D. G. Truhlar, "Density functional theory of open-shell systems. the 3d-series transition-metal atoms and their cations," *Journal of chemical theory and computation*, vol. 10, no. 1, pp. 102–121, 2014.

[193] S. Grimme, W. Hujo, and B. Kirchner, "Performance of dispersion-corrected density functional theory for the interactions in ionic liquids," *Phys. Chem. Chem. Phys.*, vol. 14, no. 14, pp. 4875–4883, 2012.

[194] S. Grimme, J. Antony, S. Ehrlich, and H. Krieg, "A consistent and accurate ab initio parametrization of density functional dispersion correction (dft-d) for the 94 elements h-pu," *The Journal of chemical physics*, vol. 132, no. 15, p. 154104, 2010.

[195] T. Yanai, D. P. Tew, and N. C. Handy, "A new hybrid exchange–correlation functional using the coulomb-attenuating method (cam-b3lyp)," *Chemical physics letters*, vol. 393, no. 1-3, pp. 51–57, 2004.

[196] W. Zhang, D. G. Truhlar, and M. Tang, "Tests of exchange-correlation functional approximations against reliable experimental data for average bond energies of 3d transition metal compounds," *Journal of chemical theory and computation*, vol. 9, no. 9, pp. 3965–3977, 2013.

[197] D. Quigley, P. Rodger, C. Freeman, J. Harding, and D. Duffy, "Metadynamics simulations of calcite crystallization on self-assembled monolayers," *The Journal of chemical physics*, vol. 131, no. 9, p. 094703, 2009.

[198] R. Koitz, J. Hutter, and M. Iannuzzi, "Formation and properties of a terpyridine-based 2d mof on the surface of water," *2D Materials*, vol. 3, no. 2, p. 025026, 2016.

[199] M. Abadi, A. Agarwal, P. Barham, E. Brevdo, Z. Chen, C. Citro, G. S. Corrado, A. Davis, J. Dean, M. Devin, *et al.*, "Tensorflow: Large-scale machine learning on heterogeneous distributed systems," *arXiv preprint arXiv:1603.04467*, 2016.

[200] K. Burke *et al.*, "The abc of Dft," *Department of Chemistry, University of California*, p. 40, 2007.

[201] M. Cossi, N. Rega, G. Scalmani, and V. Barone, “Energies, structures, and electronic properties of molecules in solution with the C-PCM solvation model,” *Journal of computational chemistry*, vol. 24, no. 6, pp. 669–681, 2003.

[202] C. J. Dickson, L. Rosso, R. M. Betz, R. C. Walker, and I. R. Gould, “GAFFlipid: A general amber force field for the accurate molecular dynamics simulation of phospholipid,” *Soft Matter*, vol. 8, no. 37, pp. 9617–9627, 2012.

[203] E. Engel and R. M. Dreizler, “Exchange-correlation energy functional,” in *Density Functional Theory*, pp. 109–217, Springer, 2011.

[204] S. Ganapathy, M. Fournier, J. Paul, L. Delevoye, M. Guelton, and J. Amoureux, “Location of protons in anhydrous Keggin heteropolyacids $H_3PMo_{12}O_{40}$ and $H_3PW_{12}O_{40}$ by $^1H\{^{31}P\}/^{31}P\{^1H\}$ REDOR NMR and DFT quantum chemical calculations,” *J. Am. Chem. Soc.*, vol. 124, no. 26, pp. 7821–7828, 2002.

[205] M. Henry, “Quantitative modelization of hydrogen-bonding in polyoxometalate chemistry,” *J. Clust. Sci.*, vol. 13, no. 3, pp. 437–458, 2002.

[206] M. H. V. Huynh and T. J. Meyer, “Proton-coupled electron transfer,” *Chemical Reviews*, vol. 107, no. 11, pp. 5004–5064, 2007.

[207] M. Karplus and J. A. McCammon, “Molecular dynamics simulations of biomolecules,” *Nature structural biology*, vol. 9, no. 9, pp. 646–652, 2002.

[208] G. King and A. Warshel, “Investigation of the free energy functions for electron transfer reactions,” *J. Chem. Phys.*, vol. 93, no. 12, pp. 8682–8692, 1990.

[209] J. G. Kirkwood, “Statistical mechanics of fluid mixtures,” *J. Chem. Phys.*, vol. 3, no. 5, pp. 300–313, 1935.

[210] I. Lage-Estebanez, A. Ruzanov, J. M. G. de la Vega, M. V. Fedorov, and V. B. Ivaništšev, “Self-interaction error in DFT-based modelling of ionic liquids,” *Phys. Chem. Chem. Phys.*, vol. 18, no. 3, pp. 2175–2182, 2016.

[211] J. E. Lennard-Jones, “Cohesion,” *Proc. Phys. Soc.*, vol. 43, no. 5, p. 461, 1931.

[212] K. Maeda, S. Himeno, T. Osakai, A. Saito, and T. Hori, "A voltammetric study of keggin-type heteropolymolybdate anions," *J. Electroanal. Chem.*, vol. 364, no. 1-2, pp. 149–154, 1994.

[213] P. Mori-Sánchez, A. J. Cohen, and W. Yang, "Localization and delocalization errors in density functional theory and implications for band-gap prediction," *Phys. Rev. Lett.*, vol. 100, no. 14, p. 146401, 2008.

[214] P. Mori-Sánchez, A. J. Cohen, and W. Yang, "Many-electron self-interaction error in approximate density functionals," 2006.

[215] M. A. Olsson and U. Ryde, "Comparison of QM/MM methods to obtain ligand-binding free energies," *J. Chem. Theory Comput.*, vol. 13, no. 5, pp. 2245–2253, 2017.

[216] D. J. Price and C. L. Brooks III, "A modified TIP3P water potential for simulation with ewald summation," *J. Chem. Phys.*, vol. 121, no. 20, pp. 10096–10103, 2004.

[217] T. H. Rod and U. Ryde, "Accurate QM/MM free energy calculations of enzyme reactions: Methylation by catechol o-methyltransferase," *J. Chem. Theory Comput.*, vol. 1, no. 6, pp. 1240–1251, 2005.

[218] D. R. Roe and T. E. Cheatham III, "PTRAJ and CPPTRAJ: Software for processing and analysis of molecular dynamics trajectory data," *J. Chem. Theory Comput.*, vol. 9, no. 7, pp. 3084–3095, 2013.

[219] M. Heshmat, "Alternative pathway of co2 hydrogenation by lewis-pair-functionalized uio-66 mof revealed by metadynamics simulations," *The Journal of Physical Chemistry C*, vol. 124, no. 20, pp. 10951–10960, 2020.

[220] L. Rulísek, "On the accuracy of calculated reduction potentials of selected group 8 (Fe, Ru, and Os) octahedral complexes,"

[221] B. H. Solis and S. Hammes-Schiffer, "Proton-coupled electron transfer in molecular electrocatalysis: Theoretical methods and design principles," *Inorg. Chem.*, vol. 53, no. 13, pp. 6427–6443, 2014.

[222] C. Steinmann, M. A. Olsson, and U. Ryde, "Relative ligand-binding free energies calculated from multiple short QM/MM MD simulations," *J. Chem. Theory Comput.*, vol. 14, no. 6, pp. 3228–3237, 2018.

[223] W. C. Still, A. Tempczyk, R. C. Hawley, and T. Hendrickson, "Semianalytical treatment of solvation for molecular mechanics and dynamics," *Journal of the American Chemical Society*, vol. 112, no. 16, pp. 6127–6129, 1990.

[224] A. Togo, I. Tanaka, K. Murase, T. Yamamoto, T. Suga, and E. Matsubara, "Atomic and electronic structures of hydrated polymolybdates by first principles calculations," *Mater. Trans.*, vol. 45, no. 7, pp. 1982–1986, 2004.

[225] G. M. Torrie and J. P. Valleau, "Nonphysical sampling distributions in monte carlo free-energy estimation: Umbrella sampling," *J. Comput. Phys*, vol. 23, no. 2, pp. 187–199, 1977.

[226] D. G. Truhlar, C. J. Cramer, A. Lewis, and J. A. Bumpus, "Molecular modeling of environmentally important processes: Reduction potentials," *J. Chem. Educ.*, vol. 81, no. 4, p. 596, 2004.

[227] S.-H. Wang, S. A. Jansen, and D. J. Singh, "Substitution and stability effects in heteropolyacids: A theoretical analysis of the diversity of the keggin ion," *J. Catal.*, vol. 154, no. 1, pp. 137–150, 1995.

[228] T. Wang, G. Brudvig, and V. S. Batista, "Characterization of proton coupled electron transfer in a biomimetic oxomanganese complex: Evaluation of the DFT B3LYP level of theory," *J. Chem. Theory Comput.*, vol. 6, no. 3, pp. 755–760, 2010.

[229] A. Warshel, "Dynamics of reactions in polar solvents. semiclassical trajectory studies of electron-transfer and proton-transfer reactions," *J. Phys. Chem.*, vol. 86, no. 12, pp. 2218–2224, 1982.

[230] A. Warshel and M. Levitt, "Theoretical studies of enzymic reactions: Dielectric, electrostatic and steric stabilization of the carbonium ion in the reaction of lysozyme," *Journal of molecular biology*, vol. 103, no. 2, pp. 227–249, 1976.